Antarctic Meteorites XXIX

Papers presented to the Twentyninth Symposium on Antarctic Meteorites

June 7-9, 2005

NATIONAL INSTITUTE OF POLAR RESEARCH
TOKYO

29th Symposium on Antarctic Meteorites
June 7–9, 2005
National Institute of Polar Research, Tokyo, Japan

Tuesday, June 7, 2005

0930–1200 Registration Auditorium (6th Floor)

Oral sessions will be held in the auditorium, 6th floor of the Main Building
* *denotes speaker*

0955–1000 **Shiraishi K.** (Head, AMRC, NIPR)
Opening Address

Chairs: Fagan T. and Kaiden H.

1000–1015 **Kobayashi S.*, Tonotani A., Sakamoto N., Nagashima K., Krot A. N. and Yurimoto H.** 30
Abundances of presolar silicates in primitive carbonaceous chondrites Yamato-81025, ALHA77307, Adelaide and Acfer 094

1015–1030 **Yada T.*, Stadermann F. J., Floss C., Zinner E., Olinger C. T., Graham G. A., Bradley J. P., Dai Z. R., Nakamura T. and Noguchi T.** 94
The stellar origins of presolar silicates discovered in Antarctic micrometeorites

1030–1045 **Tazawa Y.*, Fukuoka T., Fukushi Y., Saito Y., Sakurai H., Suzuki Y., Noguchi T. and Yada T.** 84
Classification of Antarctic Micrometeorites based on their abundance patterns

1045–1100 **Fagan T. J.*, Nagashima K., Rost D., Vicenzi E. P., MacPherson G. J. and Yurimoto H.** 12
Oxygen isotopic gradient in melilite in a fine-grained Efremovka CAI: Aqueous alteration or nebular effect ?

1100–1115 **Komatsu M.*, Krot A. N., Miyamoto M. and Keil K.** 34
Mineralogical study of amoeboid olivine aggregates with low-Ca pyroxenes in Y-81020

1115–1130 **Yamashita K.*, Ueda T., Nakamura N., Kita N. and Heaman L. M.** 100
Chromium isotopic study of mesosiderite and ureilite: Evidence for ε^{54}Cr deficit in differentiated meteorites

1130–1145 **Jagoutz E.*, Dreibus G., Jotter R., Kubny A. and Zartman R.** 27
Significance of Pb-Pb isochrons produced by stepwise dissolution of meteorites

1145–1200 **Sugiura N.*** 77
^{60}Fe-^{60}Ni systematics of some achondrites measured with an ion probe

1200–1215 **Yamamoto Y.*, Okazaki R. and Nakamura T.** 98
Drastic changes of mineralogy and noble gas compositions in carbonaceous chondrite Ningqiang during experimental aqueous alteration

1215–1330 —Lunch—

Chairs: Yada T. and Tomioka N.

1330–1345 **Rubin A. E.*, Trigo-Rodríguez J. M. and Wasson J. T.** 73
Progressive aqueous alteration of CM chondrites

1345–1400 **Ohnishi I.* and Tomeoka K.** 61
Hydrothermal alteration experiments of the Allende CV3 chondrite under highly alkaline conditions

1400–1415 **Noguchi T.*, Nakamura T., Kimura M., Bischoff A., Osawa T. and Imae N.** 55
Mineralogy of heavily hydrated clasts in Asuka 881020, Acfer 182, and NWA 470 CH chondrites

1415–1430 **Nagao K.* and Honda M.** 49
Noble gas measurement of Gibeon iron meteorites

1430–1445 **Honda M.* and Nagao K.** 21
History of Gibeon meteorite in space

1445–1500 **Kusakabe M.*, Maruyama S. and Kojima H.** 36
Re-evaluation of SMOW-scale for reporting oxygen isotopic ratios of silicate minerals and $^{17}O/^{16}O$ and $^{18}O/^{16}O$ ratios of some Antarctic meteorites

1500–1530 —Coffee Break—

1530–1545 **Chen M.*, El Goresy A. and Gillet P.** 8
Natural intracrystalline transformation of olivine to ringwoodite in a shocked L6 chondrite

1545–1600 **Tomioka N.*, Tomeoka K. and Nakamura K.** 88
Transmission electron microscopy of experimentally shocked Murchison CM chondrite

—Special Talk (I)—

Chair: Kimura M.

1600–1700 **Rubin A. E.*** 71
An evaluation of asteroidal heat sources

1715–1915 Welcome Party (6th Floor)

Wednesday, June 8, 2005

Chairs: Burbine T. and Arai T.

1000–1015	**Arai T.*, Shimoda H., Kita N. and Morishita Y.** Petrogenesis of basaltic clasts with extreme compositional variations in a brecciated lunarmeteorite EET 87521	1
1015–1030	**Koizumi E.*, Chokai J., Mikouchi M. and Miyamoto M.** Crystallization experiment on lunar mare basalt LAP 02205	32
1030–1045	**Terada K.* and Sano Y.** In-situ U-Pb dating of phosphates in lunar basaltic breccia EET87521 and EET96008	86
1045–1100	**Yamaguchi A.*, Takeda H., Karouji Y., Ebihara M., Nyquist L. E., Bogard D. D., Shih C.-Y. and Reese Y.** Yamato-86032 lunar meteorite: Implication for impact history of the highland crust	96
1100–1115	**Nyquist L.*, Yamaguchi A., Bogard D., Shih C.-Y., Reese Y. and Takeda H.** Feldspathic clasts in Yamato 86032: Remnants of a feldspathic lunar crust 4.4 Ga ago	57
1115–1130	**Tamaki M.*, Yamaguchi A, Misawa K. and Ebihara M.** Highly siderophile elements in silicate clast of Mount Padbury	80
1130–1145	**Misawa K.*, Yamaguchi A. and Kaiden H.** Zr/Hf fractionation during crystallization of basaltic eucrites: Implication for U-Pb isotopic systematics of eucritic zircons	43
1145–1200	**Nakashima D.*, Herrmann S., Ott U., Nakamura T. and Noguchi T.** Noble gas study of the Dhofar 018 howardite	53
1200–1215	**Burbine T. H.*, O'Brien K. M. and Buchanan P. C.** Determining the possible chondritic building blocks of asteroid 4 Vesta	7

1215–1330 —Lunch—

Chairs: Mikouchi T. and Imae N.

1330–1345	**Nakamuta Y.*, Owaki R. and Takeda H.** Plagioclase thermometry of Caddo County IAB iron meteorite	51
1345–1400	**Takeda H.*, Yamaguchi A., Otsuki M. and Ishii T.** Mineralogy of four new Dhofar ureilites with reference to their pairing and origin	78
1400–1415	**Imae N.* and Ikeda Y.** Petrology of MIL 03346	23
1415–1430	**Mikouchi T.*, Koizumi E., Ueda Y., Miyamoto M. and McKay G.** On the relationship between mineralogical characteristics and relative burial depths of nakhlites	41
1430–1445	**Grady M. M.*, Anand M., Bridges J., Pearson V., Verchovsky A. B. and Franchi I. A.** Aqueous alteration of nakhlites: Results from Y 000593 and MIL 03346, and implications for water on Mars	17
1445–1500	**Fritz J.*, Greshake A. and Stöffler D.** Brecciation of Y-793605: Indication for two impact events ?	14
1500–1515	—Coffee Break—	
1515–1530	**Wang D.* and Chen M.** Evidence for the shock metamorphism of GRV 99027	92
1530–1545	**McKay G.* and Schwandt C.** The Europium oxybarometer: Can it be applied to nakhlites ?	39
1545–1600	**Berczi Sz.*, Horvath A., Nagy B., Kereszturi A., Sik A., Pócs T., Gesztesi A., Gánti T. and Szathmary E.** Comparisons of Martian flow-streaks with DDS origin and their probable counterparts on Antarctica	3
1600–1615	**Dreibus G.*, Jagoutz E., Brückner J. and the Athena Science Team** Results of the Mars Exploration Rovers: Chemistry of rocks and soils at Gusev crater and Meridiani Planum	10

—Special Talk (II)—

Chair: Kojima H.

1615–1715	**Grady M. M.* and Wright I. P.** The carbon cycles of Earth and Mars: How have they evolved ?	16

Thursday, June 9, 2005

Chairs: Nakamura T. and Tachibana S.

1000–1015	**Uesugi M.* and Sekiya M.** Formation process of compound chondrules in primitive solar nebula	90
1015–1030	**Ozima M.*** Terrestrial atmospheric N and light noble gases in lunar soils: Non-magnetic Earth ?	65
1030–1045	**Seki K.*, Terada N., Shinagawa H. and Ozima M.** On contribution of terrestrial ion flows to non-solar components in lunar soils: Iontransportation rates from non-magnetic Earth	75
1045–1100	**Ozono Y., Nakamura T.*, Miyamoto T. and Kusakabe M.** Matrix olivine as a carrier of large $\Delta^{17}O$ in the NWA 753 R3.9 chondrite	67
1100–1115	**Kimura M.*, Grossman J. N., Weisberg M. K. and Nakajima H.** Fe-Ni metal and spinel group minerals in LL3 chondrites: Metamorphic conditions of highly primitive chondrites	28
1115–1130	**Okazaki R.* and Nakamura T.** Oxygen isotopes and REE abundances of lithic materials in the Begaa LL3 chondrite	63
1130–1145	**Oba Y.* and Naraoka H.** Carbon and hydrogen isotopic compositions of acetic acid derived from macromolecular organic matter in the Murchison	59
1145–1200	**Nagahara H.*, Ozawa K. and Tomomura S.** The role of condensation kinetics of silicate melt on the chemical variation of chondrule compositions	47
1200–1215	**Tatsumi K., Tachibana S.*, Nagahara H. and Ozawa K.** Experimental study on growth kinetics of metallic iron in vacuum	82
1215–1230	**Ishida Y.*, Ninagawa K., Sakamoto M., Toyoda S., Nishido H. and Gucsik A.** Thermoluminescence studies of shocked minerals and rocks	25
1230–1245	**Miura Y.* and Kato T.** Fe-Ni-Co-bearing grains and crystallized diaplectic plagiocalses: Evidence of large global impact	45

Poster Session

Bérczi Sz., Józsa S., Kovács Zs., Lukács B. and Szakmány Gy. 5
Cross sections of chondritic asteroids: Evolutionary stages on the basis of studies of the NIPR Antarctic Meteorite Thin Section Set

Hargitai H. I. and Berczi S. 19
Meteorite craters and planetary surface evolution: An educational approach

Abstract only

Marakushev A. A., Bobrov A. V., Zinovieva N. G. and Granovsky L. B. 37
Origin of SNC meteorites

Park J., Okazaki R., Nagao K., Bartoschewitz R., Kusakabe M. and Kimura M. 69
Noble gas and oxygen isotopes of new CH chondrite, SaU 290 with abundant solar gases

ABSTRACTS

Petrogenesis of basaltic clasts with extreme compositional variations in a brecciated lunar meteorite EET 87521. T. Arai[1], H. Shimoda[2], N. Kita[2,3], Y. Morishita[2]. [1]Antarctic Meteorite Research Center, National Institute of Polar Research, Kaga, Itabashi, Tokyo 173-8515, Japan (tomoko@nipr.ac.jp), [2]Geological Survey of Japan, AIST, Tsukuba, Ibaraki, 305-8567, Japan, [3]Department of Geology and Geophysics, University of Wisconsin, Madison 1215 W. Dayton Street Madison, WI 53706-1692, USA.

Introduction: A lunar meteorite Elephant Moraine (EET) 87521 is a fragmental breccia dominantly composed of coarse-grained very low-Ti (VLT) mare basalts [1]. An extreme degree of compositional variation has been reported for the bulk-rock composition [e.g. 2]. Since this wide range of composition shows a linear trend where the factor of two in FeO concentration is correlated with other lithophile elements, mixing of differentiates of a basaltic liquid is suggested [2]. In this study, major, minor - elements and REEs compositions of pyroxenes in three representative basalt clasts with different FeO concentrations, designated as primitive [P], moderate [M] and evolved [E] clasts respectively, are investigated to understand the petrogenetic relationship of the basaltic clasts and the reason of the extreme variation of the bulk-regolith composition.

Sample and method: A polished thin section EET87521, 55, provided by NASA JSC, was studied. Analyses of pyroxene REE compositions were done by Cameca imf-1270 ion microprobe at the Geological Survey of Japan. Major and minor-elements of pyroxenes were analyzed by a JEOL733 electron microprobe at the Ocean Research Institute, the University of Tokyo.

Petrography: The thin section consists of two lithologies based on the breccia texture: (1) coarse-grained large basalt clast (up to 2 mm across) preserved original igneous texture with moderate shock features and (2) fragmental breccia with finer-grained smaller basalt clasts and mineral fragments of mare derivation. While the lithology (1) is composed of only the clast M, the clasts P and E are distributed in lithology (2). Pyroxene and plagioclase are dominant for both lithologies. Mesostasis phase are distinct between clast M and E. The clast M contains ilmenite, silica, fayalite, while the clast E includes whitlockite, ilmenite, FeS, FeNi, and immiscible liquids (Fe-rich and silica-rich). Any late stage mineral is not present in the clast P. The pyroxenes of clast M contain fine exsolution in a few micron scales.

Major-element compositions: Fig. 1 shows the Ca-Mg-Fe compositions of pyroxenes for the three clasts. Compositional variations are distinct from each other: a chemical zoning from a Mg and Ca-rich core to an Fe-rich and Ca-poor rim is present in the clast P. In the clast M, the Wo content is relatively constant with unsystematic variation from Mg-rich core to Fe-rich rim due to the complex Ca variation and the fine exsolution. In the clast E, the Wo content decreases only for Fe-depleted compositions, and then abruptly increases to the rim adjacent to the mesostasis. In this plot, pyroxene composition of the clasts P seemingly merges into the compositional range of the clast M. In contrast, pyroxenes in the clasts M and E represent the two distinct trends having distinct Ca variations for the similar Fe# [=Fe/(Fe+Mg)] values. Pyroxenes in crystalline mare basalts tend to show a single continuous crystallization trend with or without some gaps generated by incoming of plagioclase precipitation, with an exception of those in Apollo 17 and Luna 24 VLT basalt which display two or three different trends within a single basalt [3]. Luna 24 pyroxenes include two separated trends of Ca enrichment and Ca depletion toward the rims [3]. Two discrete trends observed in the clasts M and E might be the same case as those of Luna 24 VLT basalts. The distinct mesostasis phases found in clasts M and E might be products of such late-stage heterogeneous fractionation within a single basaltic liquid.

Minor-element compositions: Ti/(Ti+Cr) ratios [=Ti#] of pyroxenes are plotted against Fe# (Fig. 2). Pyroxenes in the three clasts show a linear trend from lower Fe# and Ti# to higher ones. In this plot, data from the clast M and clast E are nearly overlapped with one another, in contrast to the distinction in major-element compositions. The clast P represents a distinct trend with slightly Ti-enriched composition, compared to those in the clast M and P. The core-rim Fe# range (Fe# =0.34 - 0.64) of the clast P is comparable to those of the clast M and P (Fe# = 0.52 – 0.84), while the core and rim of the clast P are more Mg-rich than those of the other two. Pyroxenes in mare basalts generally constitute a single continuous trend reflecting their bulk-TiO_2 abundance [1]. Thus, the clast P is derived from a distinct magma which is slightly more enriched in TiO_2 and much more enriched in MgO than those for the clasts M and E.

REE compositions: We analyzed a core and a rim

of pyroxene of the clasts P and E, and a core, a rim and an intermediate point of the clast M, due to the larger grain size than those of the other two. All the seven analyses show similar REE pattern normalized by CI chondrite [4] with positive slopes from La to Sm, almost flat for HREE, and similar depth of negative Eu anomaly (Fig. 3). The analysis data with lower REE abundance tend to show steeper positive slope from La to Sm. The REE concentrations become enriched from cores to rims for all the pyroxenes. The Wo content is not much different for most of the points except the clast P core and the clast E rim (Fig. 1).

The pyroxene core of the clast P shows higher REE abundance with a factor of 4 in La and a factor of 2 in Dy than that of the clast M, in spite of the much lower Fe#. This is probably due to the more Ca-rich composition of the pyroxene core of the clast P than that of the clast M, because the crystal structure of the Ca-enriched pyroxene can accommodate more REE than Ca-poor one [5]. The pyroxene rim of the clast P also shows higher REE abundance with a factor of 12 in La and a factor of 2 in Dy than the pyroxene mid of the clast M of which major-element composition is comparable. The pyroxenes in the clast E show an extreme enrichment of the REE abundance within a small clast (1 mm across) having an elevation of a factor of 5 in La and a factor of 10 in Dy from a core to a rim. Compared to the rim of the clast M with comparable Fe# to the rim of the clast E, the REE abundance is extremely enriched with a factor of 25 in La and a factor of 20 in Dy. While it can be due to the extreme Ca-enriched composition of the rim of the clast E, the distinction in the magma composition and fractionation crystallization path inferred from the difference of chemical trend in the major-element pyroxene composition of the clast M and E considered might be also involved.

Petrogenesis: Based on the major-element compositions and the REE compositions, it is not definitive whether or not the pyroxenes in the clasts P and M are crystallized in the fractionation of a single melt where the REE abundance becomes gradually enriched when fractional crystallization proceeds. However, the distinct Ti# vs. Fe# trend from the clasts M and E clearly indicates the clast P is originated from a different magma slightly more titanian and much more magnesian than those for clasts M and E. Although the clast E is more enriched in the REE abundance than the clast M, the difference in the Ca-Mg-Fe compositional trend and the nearly identical Ti# vs Fe# trend for the two clasts leave following two possibilities: derivation either from two melts with different compositions (Ca, REE, P - rich melt for clast E and Fe - rich one for clast M) generated from a single magma during the differentiation, or from two different magmas with almost identical TiO_2 and FeO concentration, but different fractional crystallization sequence and probably cooling rate. The first scenario seems more likely because of the similarity to the case of Luna 24 VLT basalt. Thus, EET 87521 includes VLT basalts probably derived from two different magmas.

References: [1] Arai T. et al. (1996) *Meteorit. Planet. Sci.* **31**, 877-892. [2] Korotev R. L. et al., (2003) *Antarct. Meteorite Res.* **16**, 152-175. [3] Papike J. J. and Vaniman D. T. (1978) *Mare Crisum: the view from Luna 24*, 371-401. [4] Anders E. and Grevesse N.(1989) *GCA*, **53**, 197-214. [5] Shearer C. K. et al. (1989) *GCA*, **53**, 1041-1054.

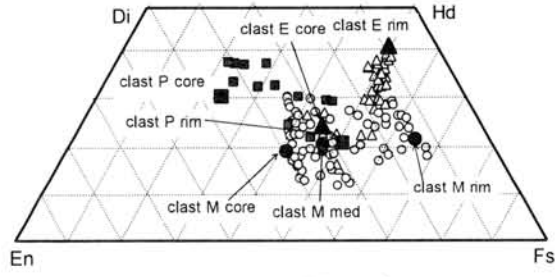

Fig.1 Major element compositions of pyroxene. Square: clast P, circle: clast M, triangle: clast E. Large symbols show compositions of the points analyzed by ion probe [same as Fig. 2].

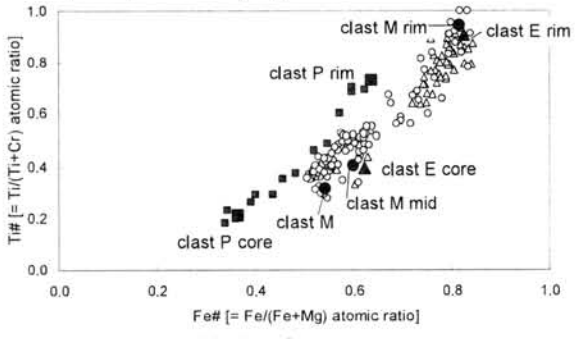

Fig. 2 Fe# vs. Ti# plot of pyroxenes.

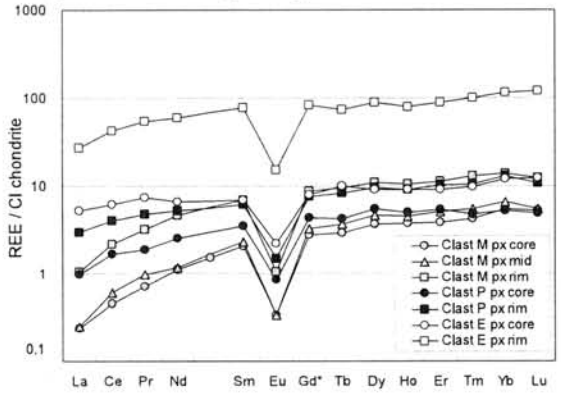

Fig. 3 REE abundance of pyroxenes.

COMPARISONS OF MARTIAN FLOW-STREAKS WITH DDS ORIGIN AND THEIR PROBABLE COUNTERPARTS ON ANTARCTICA. ***Sz. Berczi (1, 2), A. Horvath (1, 3, 4), B. Nagy (5), A. Kereszturi (1), A. Sik (1, 5), T. Pócs (1, 6), A. Gesztesi (4), T. Gánti (1), E. Szathmary (1,7)*** (1) Collegium Budapest (Institute for Advanced Study), 2 Szentháromság, H-1014 Budapest, (esa@colbud.hu); (2) Eötvös University, Dept. G. Physics, Cosmic Mat. Sp. Res. Gr. H-1117 Budapest, Pázmány 1/a. (bercziszani@ludens.elte.hu); (3) Konkoly Observatory, H-1525 Budapest Pf. 67; (4) Budapest Planetarium of Society for Dissemination of Scientific Knowledge, H-1476 Budapest Pf. 47, (planet@mail.datanet.hu); (5) Eötvös University, Dept. of Physical Geography, H-1117 Budapest, Pázmány 1/c; (6) Eszterházy Károly College, Dept. of Botany, H-3301 Eger Pf. 43., (7) Eötvös University, Dept. of Plant Taxonomy and Ecology, H-1117 Budapest, Pázmány 1/c; Hungary.

Introduction

For terrestrial counterparts of the Martian surface processes the main continent is Antarctica. This is true especially for investigations to find recent activity and effect of water on the atmospheric and soil conditions of Mars [1-3]. Our group has analyzed various slope streaks in order to elucidate if they could be the result of liquid water flows on Mars. We also compared our Martian flows to similar defrosting flows on Antarctica.

MOC image studies

We studied various slope streaks and flow markings on MGS MOC images of Mars. On the basis of albedo differences, annual changes/return, streak/environment relations in their morphology three classes were distinguished: 1) *gullies* are characterized by slope dependent flows with sharp relief from middle to high latitudes [1,4,5], 2) *dark slope streaks* are distinguished by their albedo difference, curved flow pattern, reliefless characteristics and their presence at lower latitudes [6-8], 3) *DDS-seepages* are seepage-type flows found only on DDS populated frosted Polar Regions [9-13].

To make terrestrial observations in Antarctica one of us (B.N.) visited King George Island and observed defrosting of the frost and snow covered surfaces in the period between January and February 2005.

Interpreting the Martian observations the *gullies* were found to represent streaks of water (brine) flows produced from melted snow packs where larger transported mass of material was capable of cutting relief (valley) into the soil layer. The *dark slope streaks* were interpreted as dry granular flows transporting fine grained materials (either small grain sized dust or brine materials), however, several authors suggest the contribution of water to their formation. The reliefless character is explained by the small amount of the transported material. We prefer in this interpretation the near-surface water-seepage model.

DDS seepage studies

In the case of the *DDS-seepages* we found that the Dark Dune Spots themselves were the sources of streaks. The observed morphology shows diverging, converging, downward thinning streak structures, often with accumulated ponds at their end.

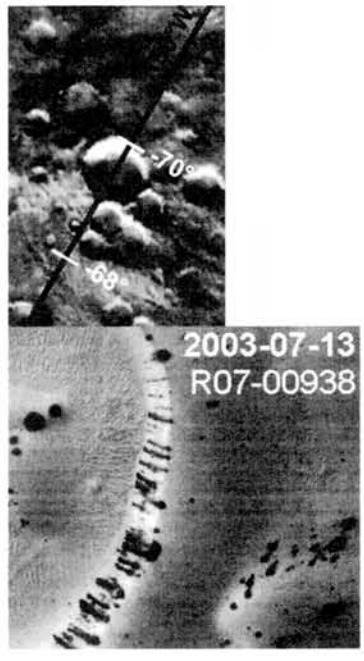

Fig. 1. The locality of the dark dune field where we found DDS-seepages flows (left) and the section of the slope, where DDS-seepages form slope-streaks.

The morphometrical analysis suggests that the size of ponds is smaller than the size of their source area. This and other statistical data on morphological characteristics of DDS-seepages

show that the liquid water transport model may give better explanation than the theories without liquid water. As a result we interpret this third group of streaks as seepages of liquid water below the CO_2/H_2O ice cover.

Comparison of origin theories of various streaks may explain the difference between the formation of seepage-like streaks on dry and polar frosted regions. Water flowing out of DDSs lends support to the idea which originally explained the formation process of these spots [11-13]. That hypothesis suggests that these spots could be habitats for extraterrestrial life. This hypothesis has been encouraged by new data from Mars Express on water ice distribution and signs of recent volcanic activity producing substantial water vapor supply.

Antarctic defrosting flows under frost cover

King George Island has a frost cover during the Antarctic winter and this frost cover regularly begins to defrost in middle of November. However in the winter season of 2004-2005 large spots of snow covered the island even in February.

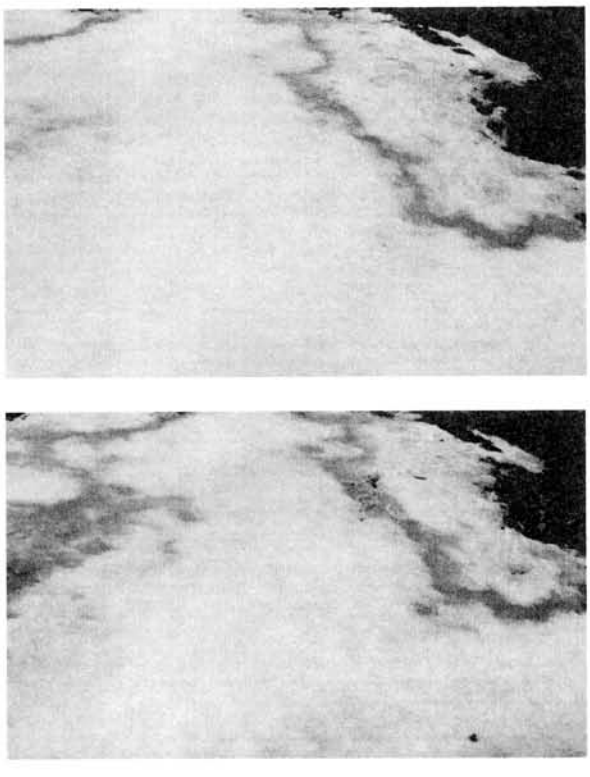

Fig. 2. Water flow below the frost cover in Antarctica, King George Island. Flows produced by release of water subsurface of the frost are seeping from the higher positions (top side of the image, width ca. 15 m) help melting and thinning the frost cover.

Summary

Martian slope streaks were found on dark dunes and they were compared with terrestrial analogue sites in an Antarctica. In terrestrial conditions water ice melts gradually seasonally. The melting of frost cover on Mars needs special conditions. In our defrosting model there is a thin water ice layer below the CO_2 ice. Release of water by life activity of Martian surface organisms (MSO) contributes to the defrosting process. This water may migrate below the frost downwards. This movement of water forms the seepages initiated from DDS on Mars and the seepages from molten water on Earth.

Acknowledgments: Collegium Budapest Mars Astrobiology Group thanks the ESA ECS-project No.98004. funding and also for supports by the Hungarian Space Office.

References: [1] Malin, M. C. and Edgett, K. S. (2000) Evidence for recent groundwater seepage and surface runoff on Mars, *Science* **288**, 2330-2335. [2] Boynton, W. V. et al (2002), Distribution of Hydrogen in the Near-Surface of Mars: Evidence for Subsurface Ice Deposits, *Science* **297**, 81-85. [3] Bibring, J.-P. et al (2004) Perennial water ice identified in the south polar cap of Mars, *Nature* **428**, 627-630. [4] Costard, F., Forget, F., Mangold, N., Peulvast, J. P. (2002) Formation of Recent Martian Debris Flows by Melting of Near-Surface Ground Ice at High Obliquity, *Science,* **295**, 110-113. [5] Christensen, P. R. (2003) Formation of recent martian gullies through melting of extensive water-rich snow deposits, *Nature* **422**, 45-48. [6] Treiman, A. H. (2004) Martian slope streaks and gullies: origin as dry granular flows, *Lunar Planet. Sci. XXXIV*, #1323. [7] Miyamoto, H., Dohm, J. M., Beyer, R. A., Baker, V. R. (2004) Fluid dynamical implications of anastomosing slope streaks on Mars, *Journal of Geophysical Research*, **109**, E6, CiteID E06008. [8] Motazedian, T. (2003) Currently Flowing Water on Mars, *Lunar Planet. Sci. XXXIV*, #1840. [9] Edgett, K.S., Supulver, K. D. and Malin, M. C. (2000), Spring defrosting of Martian polar regions: Mars Global Surveyor MOC and TES monitoring of the Richardson Crater dune field, 1999-2000, *Mars Polar Sci. and Explor.* **II**, #4041. [10] Bridges, N. T.., Herkenhoff, K. E., Titus, T. N., and Kieffer H. H. (2001) Ephemeral dark spots associated with Martian guillies. *Lunar Planet. Sci.* XXXII, #2126. [11] Horváth, A., Gánti, T., Gesztesi, A., Bérczi, Sz., Szathmáry, E. (2001) Probable evidences of recent biological activity on Mars: appearance and growing of dark dune spots in the South Polar Region. *Lunar Planet. Sci. XXXII*, #1543, LPI, Houston. [12] Gánti, T., Horváth, A., Bérczi, Sz., Gesztesi, A., Szathmáry E. (2003) Dark Dune Spots: Possible Biomarkers on Mars? *Origins of Life and Evolution of the Biosphere* **33**: 515-557, Kluwer Academic Publishers, Netherlands. [13] Horváth, A., Bérczi, Sz., Kereszturi, Á., Pócs, T., Gesztesi, A., Gánti, T., Szathmáry, E. (2004) Annual change of outflows from Dark Dune Spots in the Southern Polar Region of the Mars, *IV. European Workshop on Exo-Astrobiology (EANA),* Great Britain, 25 November 2004, *Abstr.Vol., p. 91.*

CROSS SECTIONS OF CHONDRITIC ASTEROIDS: EVOLUTIONARY STAGES ON THE BASIS OF STUDIES OF THE NIPR ANTARCTIC METEORITE THIN SECTION SET. Sz. Bérczi[1], S. Józsa[2], Zs. Kovács[3], B. Lukács[4], Gy. Szakmány[2],. [1]Eötvös University, Faculty of Science, Department of General Physics, Cosmic Materials Space Research Group, H-1117 Budapest, Pázmány Péter sétány 1/a, Hungary, (bercziszani@ludens.elte.hu). [2]Eötvös University, Faculty of Science, Department of Petrology and Geochemistry, H-1117 Budapest, Pázmány Péter sétány 1/c, Hungary, [3]Berzsenyi College, Department of Technology, H-9700 Szombathely, Károlyi G. tér 4, Hungary, [1]Central Research Institute for Physics, RMKI, H-1525 Budapest-114. P. O. Box 49. Hungary.

Introduction: The rich collection of the NIPR is based on the systematic search for meteorites since 1969 on Antarctica [1]. The educational set loaned to Eötvös University opened extraordinary possibility of the synthetic overview of the thermal evolution of the chondritic parent body. Recently more and more works synthetise such chondritic parent body studies by reconstructing the final stage of thermal evolution of meteorite groups having similar oxygene isotopic ratios [2,3,4]. We also formulated the synthetic picture of our studies on NIPR Antarctic meteorite set in such evolutionary form. Specific stages of the chondritic parent body evolution were reconstructed in the form of the cross sections of the corresponding stratified asteroidal body. We show cross sections regardless of impact distortions, which may strongly modify this picture.

Fig. 1. A very much differentiated chondritic parent body cross section with a characteristic layering given in the text.

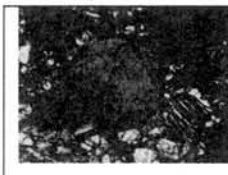	H-3, Yamato 791428
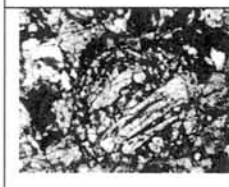	H-4, ALHA 77233
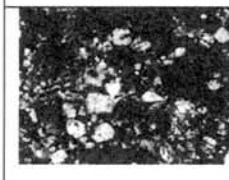	H-5, Yamato 74079
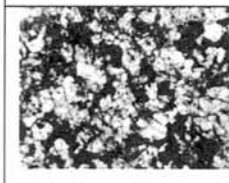	H-6, Yamato 74014

Two stages of thermal evolution, onion-shell models: The chondritic parent body thermal evolution begins with thermal metamorphism which forms a layered onion-shell stratified body with higher temperatures in the core regions and lower temperatures at the margin of the body. For the H, L and LL groups of chondrites the NIPR SET allows comparisons of the H, L and LL sequences because they are all represented by thin sections from 3 to 6 petrologic types.

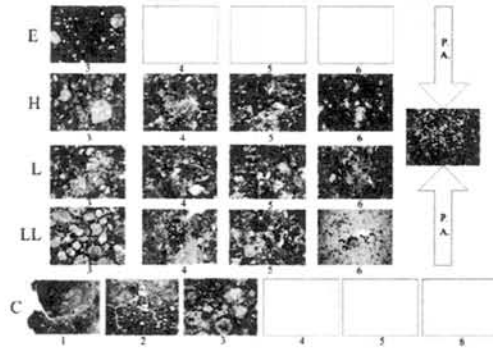

Fig. 3 Thin section images from the NIPR educational set on their corresponding matrix place in the VSW table.

CROSS SECTIONS OF CHONDRITIC ASTEROIDS: EVOLUTIONARY STAGES ON THE BASIS OF STUDIES OF THE NIPR ANTARCTIC METEORITE THIN SECTION SET. Sz. Bérczi, S. Józsa, Zs. Kovács, B. Lukács, Gy. Szakmány

They are represented by the 15, 16, 17 and 18 thin sections for H3 to H6 (Fig. 2.) [5], by the 19, 20, 21 and 22 thin sections for L3 to L6, and by the 23, 24, 25 and 26 thin sections for LL3 to LL6 metamorphic chondritic stages (Fig. 3.)

After thermal metamorphism Ostwald maturing results in the lost of the chondritic texture. Further heating causes partial melting and the consequent differentiation inside the parent chondritic body.

Transitional and differentiation layers inside the body. In the NIPR SET thin section of No. 13. represents the primitive achondrites transitional to the differentiated meteorites. Acapulcoite, lodranite, winonaite are also members of this primitive achondritic stage. Yanai [8] asserted two types of textures of them: small grain size characterizes mostly the acapulcoites, larger grain size is characteristic to the lodranites. However, the two lithologies occurring together can be found among late metamorphic type chondrites, too. In the NIPR Tokyo collection Yamato-74036, (H6) and Yamato-75300, (E6) chondrites were observed to contain these two lithologies in the same sample.

Layers of differentiation: The period of differentiation in the chondritic parent body consists of partial melting of two main components. First the metallic/sulfide melt segregates and migrates to collect into great blocks and toward the depths to form a core. The second part of differentiation is characterized by the partial melting of lower melting point silicates, forming basaltic melts. This second process produces the basaltic achondrites on the surfaces visible only in the evolved asteroidal body of Vesta and on some Vesta-like fragmented asteroids [9].

As a result of differentiation the following layering characterizes an evolved asteroidal body: Iron in the core, pallasite and upper mesosiderite layers, ureilite layers in high carbon bodies, primitive achondritic layers together with some remnants of the chondritic material below the subsurface and the basaltic achondritic upper crust (Fig. 1. body). In all cases surface regolith with brecciated materials close the sequence of textural strata in evolved chondritic bodies.

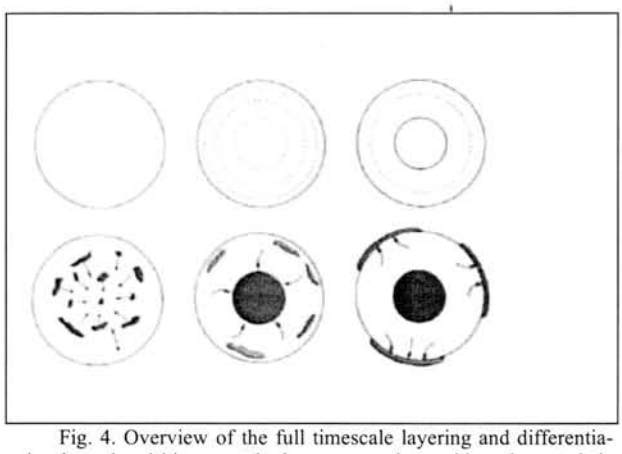

Fig. 4. Overview of the full timescale layering and differentiation in a chondritic parent body: cross sections with a characteristic onion-shell layering. Upper row: metamorphism, lower row: iron core and basaltic achondritic layers differentiating.

Summary: The Antarctic Meteorite Thin Section Educational Set (NIPR), Tokyo, Japan, is a valuable source for synthesis studies of a chondritic parent body. Cross sections of evolved chondritic parent bodies give overview and global picture of the thermal evolution of the chondritic parent bodies and give synthesis of the main processes. NIPR books [1,6,10] also help its use for universities and researchers.

Eucrite, Yamato 791195

Ureilite, ALHA-77257

Pallasite, Yamato 8451

Fig. 5. Thin section images from the NIPR educational set from upper (basaltic achondrite) and deeper (ureilite, pallasite) layers of a differentiated, originally chondritic parent body.

Acknowledgments: The loan of the NIPR Antarctic meteorite thin section set No. 3. and the fund of the Hungarian Space Office No. 154/2004 and 2005 is highly acknowledged.

References: [1] Yanai, K., Kojima, H., Haramura, H. (1995): *Catalog of the Antarctic Meteorites*, NIPR, Tokyo; [2] Bunch, T. E.; Irving, A. J.; Larson, T. E.; Longstaffe, F. J.; Rumble, D., III; Wittke, J. H. (2005): "Primitive" and Igneous Achondrites Related to the Large and Differentiated CR Parent Body. *LPSC XXXVI*, #2308, LPI, Houston; [3] Grimm, R. E.; Bottke, W. F.; Durda, D. D.; Enke, B.; Scott, E. R. D.; Asphaug, E.; Richardson, D. (2005): Joint Thermal and Collisional Modeling of the H-Chondrite Parent Body. *LPSC XXXVI*, #1798, LPI, Houston; [4] Zolensky, M. E.; Abell, P. A.; Tonui, E. K. (2005): Metamorphosed CM and CI Carbonaceous Chondrites Could be from the Breakup of the Same Earth-crossing Asteroid. *LPSC XXXVI*, #2084, LPI, Houston; [5] Lux, G. Keil, K. Taylor G. J. (1980): Metamorphism of the H-group chondrites. *GCA*, **44**, 841-855 [6] Yanai, K., Kojima H. (1987): *Photographic Catalog of the Antarctic Meteorites.* NIPR. Tokyo, [7] Yanai, K., Kojima H. (1991): *Proc. NIPR Symp. Antarct. Meteorites*, **4**. 70-90. [8] Yanai, K. (2001): Lodranites and Their Subgroups Related with Some Acapulocoites. *LPSC XXXII*, #1665, LPI, Houston, (CD-ROM). [9] Gaffey et al., (1989): Reflectance spectroscopy and asteroid surface mineralogy. (In *Asteroids II*, Eds. R. P. Binzel & al.), p. 98-127. Univ. of Arizona Press, Tucson [10] Yanai, K., Kojima H. (1987): *Photographic Catalog of the Antarctic Meteorites.* NIPR. Tokyo.

Determining the possible chondritic building blocks of asteroid 4 Vesta. T. H. Burbine[1], K. M. O'Brien[2] and P. C. Buchanan[3], [1]Astronomy Department, Mount Holyoke College, South Hadley, MA 01075, USA (tburbine@mtholyoke.edu), [2]11152 Wallingsford Road, Los Alamitos, CA 90720, USA, [3]2401 Elgem Street, Tyler, TX 75701-4901, USA.

Introduction:

All planetary bodies in our solar system are believed to have condensed out of material from the solar nebula. Chondritic meteorites represent samples of this "primitive" material. However, none of the terrestrial planets in our solar system appears to be an 'exact" isotopic and compositional match for any single chondrite type.

One other planetary body with detailed compositional information is asteroid 4 Vesta, the probable parent body of the howardite, eucrite, and diogenite meteorites (HED). Vesta is an excellent spectroscopic match to HED meteorites [1] in the visible and near-infrared wavelength regions.

We evaluated ~225 million combinations of the 13 chondritic groups in an attempt to determine the best oxygen isotopic and compositional matches to Vesta using a method used previously for Earth and Mars [2]. No combination of chondritic meteorites match the oxygen and chemical composition of Earth while a number of combinations match the composition of Mars.

Procedure:

A computer program [2] was developed that inputs average oxygen isotopic values as well as average compositional data for each chondritic group and compares combinations of these data with compositional and oxygen isotopic characteristics of HED meteorites and Vesta. Aggregate oxygen isotopic and compositional values for every possible combination of these meteorites at mass increments of 5% were computed. Elements and compounds (e.g., H_2O, FeO) were combined linearly except for the oxygen isotopic values, which were weighted by the oxygen content of each meteorite. Redox reactions were used to determine the FeO content of each matching combination.

To determine possible matches, we used oxygen isotopic and compositional constraints derived from HED meteorites. Oxygen isotopic values were taken from Clayton and Mayeda [3] and Wiechert et al. [4]. The bulk FeO content of Vesta was calculated to be 15.6 ± 1.6 wt.% after correcting for the presence of a metallic iron core.

Results:

The number of matching combinations is dependent on the values and uncertainties chosen for the assumed oxygen isotopic composition and bulk FeO content of Vesta. For realistic values and uncertainties, only a small percentage (~0.03%) of the possible combinations matches the oxygen isotopic and bulk FeO content of Vesta.

The ordinary chondrites (H, L, or LL) might comprise up to ~75% of a mixture, but carbonaceous chondritic material is also necessary to match Vesta's oxygen isotopic composition and FeO content. This result is similar to the conclusions of Boesenberg and Delaney [5].

CM2 and CR2 fragments are found in howardites [6] and have been proposed as possible building blocks of Vesta. Among our matching combinations, CR2 material can comprise up to ~50% of a mixture, but CM2 material can only represent up to ~10%.

Other types of carbonaceous chondritic material can be some of the building blocks of Vesta. Up to ~5% of a mixture can be CI material, up to ~25% can be CK material, up to ~30% can be CO material, and up to ~30% can be CV material. The biggest carbonaceous component can be CH material, which can comprise up to ~60% of a mixture.

Future Work:

We are looking for additional compositional constraints to limit the number of possible matches to Vesta. The upcoming Dawn mission to Vesta should help us better constrain its bulk chemical composition. We also plan on looking at the possible building blocks of the parent body of Northwest Africa 011 [7], a eucrite with an oxygen isotopic composition similar to CR chondrites.

References:

[1] Hiroi T. et al. (1994) *Meteoritics, 29,* 394-396. [2] Burbine T. H. and O'Brien K. M. (2004) *Meteorit. Planet. Sci., 39,* 667-681. [3] Clayton R. N. and Mayeda T. K. (1996) *Geochim. Cosmochim. Acta, 60,* 1999-2017. [4] Wiechert U. H. (2004) *Earth Planet. Sci. Lett., 221,* 373-382. [5] Boesenberg J. S. and Delaney J. S. (1997) *Geochim. Cosmochim. Acta, 61,* 3205-3225. [6] Buchanan P. C. et al. (1993) *Meteoritics, 28,* 659-669. [7] Yamaguchi A. et al. (2002) *Science, 296,* 334-336.

Natural intracrystalline transformation of olivine to ringwoodite in a shocked L6 chondrite. M. Chen[1], A. El Goresy[2] and P. Gillet[3]. [1]Guangzhou Institute of Geochemistry, Chinese Academy of Sciences, 510640 Guangzhou, China; [2]Max-Planck-Institut für Chemie, 55128 Mainz, Germany; [3]Ecole Normale Supérieure de Lyon, 46 allée d'Italie, 69364 Lyon Cedex 7, France.

Introduction :

Olivine is the most abundant mineral in Earth's upper mantle and it transforms to its high-pressure polymorphs wadsleyite and ringwoodite below 410 km in the transition zone. The transformation of olivine to ringwoodite can proceed by incoherent intercrystalline diffusion-controlled [1,2] or interface-controlled [3,4] mechanism, as well as coherent intracrystalline martensitic transformation [5,6] or nucleation and growth [7] mechanism. Natural ringwoodite had been found in many shocked chondritic meteorites, in which the ringwoodite occurs mainly as fine-grained polycrystalline aggregates formed through a phase transition of olivine during exogenous dynamic events on the parent asteroids [8-9]. No natural occurrence of ringwoodite lamellae was found so far either in the shocked meteorites or in exhumed subducted slabs. Recently, natural occurrence of ringwoodite lamellae in olivine was reported in the Sixiangkou meteorite [10].

Meteorite

Sixiangkou meteorite is a shock -metamorphosed L6-chondrite with a number of shock-produced veins up to several millimeters in thickness. The shock veins contain abundant high-pressure minerals including ringwoodite, majorite, majorite-pyrope garnet and magnesiowüstite, for which the shock-produced pressure and temperature of about 20 GPa and 2000°C were inferred. Polycrystalline aggregates of ringwoodite and majorite up to 100 μm in size, and fragments of olivine and pyroxene up to 1.5 mm in size distribute throughout the shock veins and are enclosed in the fine-grained matrix consisting of magnesiowüstite, majorite-pyrope garnet, metal and troilite crystallized from a shock-induced chondritic melt at high pressures.

Results and discussion

In addition to polycrystalline aggregate of ringwoodite related incoherent intercrystalline transformation inside the shock veins, we also found the lamellar ringwoodite in olivine within and neighboring the shock veins. However, the lamellar textures are distinct between two kinds of occurrence of olivine. Inside the veins where pressure and temperature were higher than elsewhere the ringwoodite lamellae formed parallel to {101} planes of olivine whereas outside they lie parallel to (100) plane of olivine. Widths of lamellae are up to 2 μm, mostly 0.5 μm. Figure 1 displays a fragment of olivine inside the shock vein, in which two sets of lamellae can be recognized. Individual olivine grain can be replaced by these ringwoodite lamellae from a few percent to complete. Two sets of ringwoodite lamellae lay parallel to {101} crystallographic planes of olivine, i.e. (101) and (10 $\bar{1}$), respectively. Figure 2 shows an olivine crystal in the chondritic portion at a distance about 150 μm away from the shock vein, from which only one set of lamellae can be observed. Olivine grains with one set of lamellae distribute mainly in the chondritic area close to the shock veins in a zone with a width less than 300 μm. Complete replacement of lamellae in the host olivine was not observed in this type of olivine grain, and these grains contain less than 10 vol. % lamellae. The ringwoodite lamellae lay parallel to (100) crystallographic planes of olivine.

Both kinds of lamellae occur as straight thin platelets from a few to several hundred micrometers in length. The interfaces of lamellae with neighboring olivine matrix are distinct and become locally broaden. FeO-content of lamellae is slightly but systematically higher (22.51 wt.%) than that of olivine matrix (21.86 wt.%). Relatively higher FeO-contents in ringwoodite lamellae in comparison to a lower FeO-content in olivine matrix demonstrate a Fe-Mg interdiffusion during nucleation and growth of ringwoodite.

Formation of these lamellae relates to a diffusion-controlled nucleation and growth of ringwoodite along shear-induced planar defects including stacking faults and planar fractures in olivine. We have optically observed planar fractures parallel to {101} planes that associate with ringwoodite lamellae along the same orientations. According to the occurrence and mineral assemblages of shock veins, it appears that the planar defects and ringwoodite lamellae parallel to {101} planes of olivine should have been produced in higher shear stress and temperature region than those parallel to (100) plane.

We have estimated the time duration for intracrystalline growth of ringwoodite lamellae in olivine based on the calculation of the growth rates of ringwoodite [11]. Our results indicate that the P-T condition available for an intracrystalline olivine-ringwoodite transformation during the shock metamorphism of this meteorite might last at least for several seconds. The formation of ringwoodite lamellae in olivine experienced a longer duration than previously assumed of high pressure and temperature locally prevailed in the shocked meteorite, especially along the shock veins. It was

considered that olivine might survive metastablely in the wedge-shaped region within the cold subducting lithospheric slabs at depths from 400 to 700 km [12]. These new data should bring new insight into mechanisms of olivine-ringwoodite phase transitions in the lower mantle and subducting lithosphere.

References:

[1] Sung C. M. and Burns R. G. (1976) *Earth Planet. Sci. Lett.* **32**, 165-170. [2] Vaughan P. J. et al. (1982) *Nature* 298, 357-358. [3] Liu M. et al. (1998) *J. Geophys. Res.* 103, 23897-23909. [4] Mosenfelder J. L. et al. (2001) *Phys. Earth Planet. Inter.* 127. 165-180. [5] Poirier J. P. (1981) *Phys. Earth Planet. Inter.* 26, 179-187. [6] Burnley P. C. & Green H. W. (1989) *Nature* 338, 753-756. [7] Kerschhofer L. et al. (1996) *Science* 274, 79-81. [8] Price G. D. et al. (1979) *Contrib. Mineral. Petrol.* 71, 211-218. [9] Chen M. et al. (1996) *Science* **271**, 1570-1573. [10] Chen M. et al. (2004) *Proc. Natl. Acad. Sci. USA* 101, 15033–15037. [11] Kerschhofer L. et al. (2000) *Phys. Earth Planet. Inter.* **121**, 59-76. [12] Frohlich, C. (1994) *Nature* **368**, 100-101.

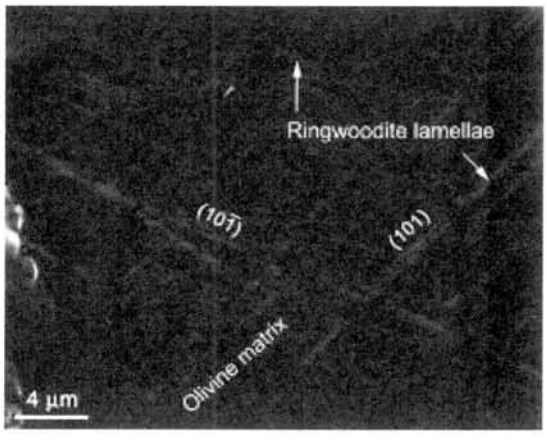

Figure 1. Back-scattered electron image of ringwoodite lamellae parallel to {101} planes of olivine inside the shock vein.

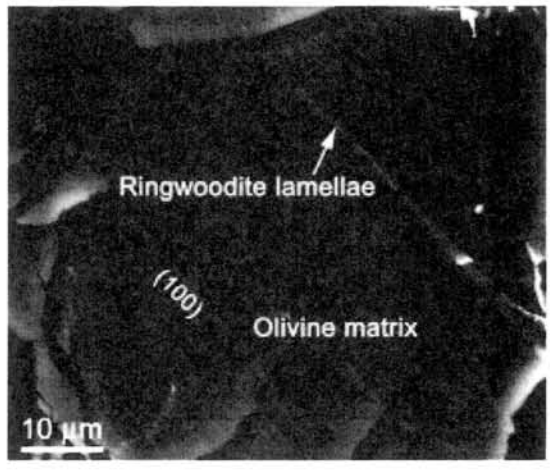

Figure 2. Back-scattered electron image of ringwoodite lamellae parallel to (100) plane of olivine in the chondritic portion of meteorite.

Results of the Mars Exploration Rovers: Chemistry of Rocks and Soils at Gusev Crater and Meridiani Planum. G. Dreibus[1], E. Jagoutz[1], J. Brückner[1], and the Athena Science Team, [1]Max-Planck-Institut f. Chemie, P.O. BOX 3060, D-55020 Mainz, Germany.

Introduction:

Searching for signs of ancient water on Mars was the mission goal of the two Mars Exploration Rovers (MER). In this respect, the two landing sites, Gusev crater for MER A (Rover Spirit) and Meridiani Planum for MER B (Rover Opportunity), were selected. Part of the Athena Science Instrument Payload is mounted on the robotic arm of the rovers. Two instruments, the Alpha Particle X-ray Spectrometer (APXS) and the Mössbauer Spectrometer (MB), provided geochemical and mineralogical information that indicates a variety of aqueous processes and various degrees of alteration at the two landing sites. The chemistry of hematite-rich spherules, found on the Opportunity landing site, provides insight in their formation process.

Gusev crater:

During the first 90 sols in the Gusev crater, only weak signs of water could be observed. The chemical composition of soils measured by the APXS is similar to those at other landing sites, i.e. a basaltic soil with 2 wt. % S and 0.4 wt. % Cl. Fresh surfaces of rocks, which were abraded by the rock abrasion tool (RAT), resemble primitive basalts with low K and an Mg number of about 0.50 [1]. The occurrence of iron-bearing minerals and the ratio of $Fe^{3+}/Fe_{(total)}$ could be determined by the MB [2]. On the rock Mazatzal, hematite was discovered on its undisturbed surface [2]. High abundance of Br relative to Cl was found on its abraded surface that contained a large vein. Probably, Br is enriched in this vein [1]. These observations indicate alteration of rocks during a past period of aqueous activity in Gusev crater. While traveling across the plains towards the Columbia Hills, a positive correlation of Mg and SO_3 was observed inside a trench that was excavated with the rover wheels in the subsurface soil. Such a positive correlation was known from the Pathfinder landing site, but not for the Gusev crater until recently. At the foot of the Columbia Hills, the MB discovered hematite in a highly altered basaltic rock, called Pot of Gold. Also a soft rock, called Clovis, revealed clues to Mars' aqueous past. On the abraded surface of this rock, the APXS found much higher concentrations of S, Br and Cl compared to basaltic or volcanic rocks at Gusev. In addition, MB discovered goethite, an iron oxide-hydroxide that forms by precipitation from liquid water. This might indicate that Clovis was chemically altered, and that fluids once flowed through the rock depositing these elements.

Meridiani Planum:

The water rich past of Mars was definitely confirmed by the MER B mission in Meridiani Planum. The crater Eagle, the landing place of Rover Opportunity, contains soils that resemble those at Gusev crater; however, their Fe, Ni and Cr contents are higher [3]. The enrichment of Fe results from an admixture of hematite (α-Fe_2O_3) as determined in-situ by the MB. Hematite was also detected at Meridiani Planum from orbit by the TES of the Mars Global Surveyor [4]. The formation of hematite is an indicator for aqueous activities under oxidizing conditions. The highest portion of this mineral was found in spherical grains, nicknamed blueberries, which cover the landing site. Surprisingly, the undisturbed surface of the outcrops discovered in Eagle crater have a factor of 2 to 3 higher S content compared to soils, whereas Cl is not enriched. After abrading their surfaces with the RAT the S contents increase up to values of about 9.5 wt. % (24 wt. % SO_3) [3]. Assuming all SO_3 is bound to $MgSO_4$ and, according to the MB, to Jarosite and ferric sulfates, the evaporite-rich rocks of Eagle crater contain about 40 wt. % sulfates. Also, high abundances of Br in some excavated soils and partly in sedimentary rocks point to ancient occurrence of acidified water and the formation of brines, which could have been precipitated according to their solubility as sulfates, chlorides and bromides. Interestingly, Br seems to be decoupled from Cl. In the case of high Br concentrations Cl is not enriched. And vice versa, enrichment of Cl in some layers of outcrops in the Endurance crater is not accompanied by bromine.

Possible formation process of hematite:

The chemical composition and mineralogy of the spherules could be constrained using a favorable location. A small concave depression on an outcrop, called Berry Bowl, was filled with a large number of spherules. Here, APXS and MB measurements were carried out at the position of the accumulated spherules ('Berry Bowl full') and offset at a place free of spherules ('Berry Bowl empty') [3,5].

There is a significant difference in Fe mineralogy for Berry Bowl Full and Berry Bowl empty. In Berry Bowl full, 64 % of total Fe content is associated with hematite [5] (Fig. 1). Based on the total Fe content of 23.0 wt %, as determined by the APXS, the hematite (Fe_2O_3) content is 21 wt. %. Assuming that pure hematite spherules in the Berry Bowl cover not more than 50 % of the field of view of the APXS, the hematite content of Berry Bowl full would increase to a value of 48 wt. % considering 12.3 wt. % Fe content of Berry Bowl empty. Simultaneously, the Mn content would decrease from 0.21 wt. % to 0.16 wt. %, resulting in an Fe/Mn ratio of 210 for 48 % hematite compared to the measured Fe/Mn ratio of 110. The measured Fe content of 23.0 wt. % would be off by a factor of 2. Either the

spherules are not made of pure hematite or are covered by air fall dust. If such a thin dust layer was present, the Fe signal from the spherules, as measured by the APXS, could be a lower limit. The APXS data evaluation does not correct for a layering case. The average sampling depth of the APXS measurements is about 20 μm for Fe and Mn radiation.

It should be noted that for other hematite-rich soils on plains in Meridiani Planum like 'JackRussell' and 'Fred Ripple', similar amounts of hematite were determined as for Berry Bowl full [3,5]. The target area of JackRussell is covered by about 30 % spherules and FredRipple is dominated by about 60 % subangular fragments from basalts or spherules. However, the radial efficiency dependence of the APXS measurement has to be taken into account. In the field of view of JackRussell more spherules are in the center compared to BerryBowl full.

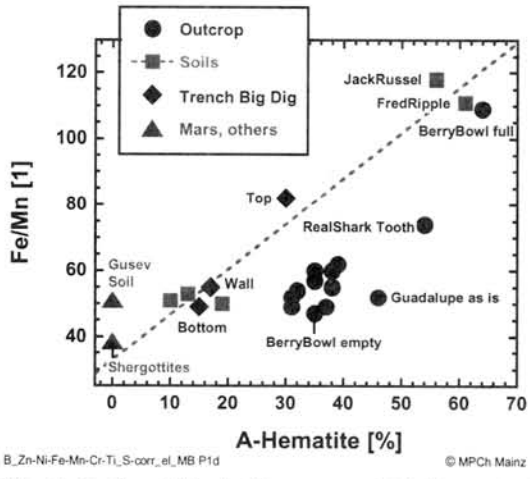

Fig. 1. Ratio of Fe to Mn versus total Fe content (weight %). Full names 'feature, target' together with sol numbers (martian day of APXS integration) of Meridiani samples are: 'DogPark, JackRussell' (Sol 80), 'DogPark, FredRipple' (Sol 91), 'Berry Bowl, Empty' (Sol 48), 'Berry Bowl, Rubel' (full) (Sol 46), 'RealShark Tooth, Enamel1' (Sol 51), Trench: 'Hematite Slope, Hema2' (= Top) (Sol 23), 'Big Dig, Hematrench1' (= Bottom) (Sol 25), and 'Big Dig, Hematrenchwall2 (= Wall)' (Sol 26). 'Shergottites' are martian meteorites.

The Fe/Mn ratios of Berry Bowl full and of the above mentioned hematite-rich soils (Fe/Mn = 114) are higher than the ratios measured in other soils and outcrops (Fe/Mn ~ 50) (Fig. 1). Because Mn^{2+} has chemical characteristics similar to Fe^{2+}, a high Fe/Mn ratio can result from the presence of oxidized Fe^{3+}-bearing minerals.

Except for the five times enrichment of S in the ratted outcrops, soils and outcrops show similar chemical compositions. However, the MB results [5] indicate a different mineralogy between hematite-poor soils (high Fe^{2+}) and outcrops (high Fe^{3+}). On the basis of similar Fe/Mn ratios in rocks and these soils (Fig. 1), the difference in mineralogy can be explained by an isochemical change resulting from a change in the oxidation state of iron.

All high hematite bearing soils are top surface samples, while subsurface soil samples and soils disturbed by rover wheels have low hematite contents.

The spherules with a restricted grain size between 4 and 6 mm, which are strewn across most soils inside Eagle crater and on the surrounding plains, appear to be the primary carrier of the coarse-grained gray hematite that was detected form orbit [4]. Small quantities of similar spherules (2 vol. %) were found in rock exposures in Eagle crater. The hematite-rich spherules are interpreted as concretions that formed by diagenesis subsequent to formation of the sulfate-rich outcrops [6]. Analogous to Earth [7] concretions could be formed in a porous matrix by dissolution of Fe^{2+} components, changing the redox and pH of the Fe-rich fluids, and subsequent hematite precipitation as spherical concretions. The precipitation of Fe_2O_3 from the Fe^{3+} solution started at a low pH; the same holds for NiO, whereas formation of MnO requires a pH higher than 5. The acidic conditions during the formation of the hematite spherules in the outcrops allow a co-precipitation of Fe_2O_3 and NiO but not of MnO. As a result, high Fe/Mn ratios of above 100 are found. The good correlation of Fe with Ni in hematite-rich and hematite-poor soils, spherules, and outcrops confirms the ancient acidic environment.

Meridiani Planum is a Noachian cratered terrain with a high erosion rate [8]. Therefore, the hematitic spherules could be weathered out of the sulfate-rich outcrops by physical, aeolian erosion and are now concentrated in the near-surface soils. Similar chemical compositions of the hematite-rich concretions and the different types of hematite-rich soils point to the same original source.

References:

[1] Gellert, R. et al. (2004) *Science, 305*, 829-832. [2] Morris, R. V. et al. (2004) *Science, 305*, 833-836. [3] Rieder, R. et al. (2004) *Science, 306,* 1746-1749. [4] Christensen, P. R. et al. (2000) *JGR, 105*, 9623-9642. [5] Klingelhöfer, G. et al. (2004) *Science, 306,* 1740-1745. [6] Squyres, S, et al. (2004) *Science, 306,* 1698-1703. [7] Chan M. A. et al. (2004) *Nature 429,* 731-734. [8] Golombek M. P. et al. (2005) *LPS XXXVI, # 1539, abstract.*

OXYGEN ISOTOPIC GRADIENT IN MELILITE IN A FINE-GRAINED EFREMOVKA CAI: AQUEOUS ALTERATION OR NEBULAR EFFECT? T. J. Fagan*[1,2], K. Nagashima[3], D. Rost[2], E. P. Vicenzi[2], G. J. MacPherson[2] and H. Yurimoto[3]. [1]Dept. Earth Sciences, School of Education, Waseda University, Tokyo, Japan (*fagan@waseda.jp). [2]Dept. Mineral Sciences, U. S. National Museum of Natural History, Smithsonian Institution, Washington, DC, USA. [3]Dept. Earth and Planetary Sciences, Tokyo Institute of Technology, Tokyo, Japan.

Introduction: Oxygen isotope systematics of coarse-grained Ca-Al-rich inclusions (CAIs) in CV chondrites indicate that these refractory objects formed initially in a ^{16}O-rich setting and were altered in a ^{16}O-poor setting [1,2] (Fig. 1A). Spinel and fassaite typically retain the ^{16}O-rich signal, whereas melilite and, in most cases, anorthite have exchanged oxygen with a ^{16}O-poor reservoir. It has been inferred that short-term heating events in the nebula, possibly involving disequilibrium melting, resulted in this alteration pattern [3,4].

In contrast, melilite from a fine-grained CAI (designated FGI-12) in the CV chondrite Efremovka exhibits a range in O-isotopic composition from ^{16}O-rich to moderately ^{16}O-poor [5] (Fig. 1A). In order to evaluate the setting and physical conditions of this distinct alteration event, we used secondary ion mass spectroscopy (SIMS) to map the distribution of O-isotopes and a large set of elements in a melilite-rich portion of FGI-12. Goals were to determine: (1) the pattern of O-isotopic variation in melilite; and (2) possible correlations between elemental and O-isotopic compositions. In particular, we anticipated a link between O-isotopes and alkalis suggestive of alteration by aqueous fluid.

Background and Methods: FGI-12 is composed of nodules of spinel surrounded by melilite and Al-diopside [5]. In one nodule, melilite with a constant major element composition ($Ak_{\sim 12}$) exhibits a range in O-isotopic composition of ~25‰ along CCAM over a distance of ~40μm (Fig. 1). A fringe of porous fassaite occurs along the boundary between melilite and spinel in one portion of the nodule.

Oxygen isotopic imaging. Maps of oxygen isotopes, Si and Al were determined for an area of ~ 40x40μm in a melilite-rich nodule using the CAMECA IMS-1270 ion microscope and SCAPS imaging system at TiTech [6,7]. A Cs+ primary ion beam (20 keV, 0.5 nA) was rastered over the area. Secondary ions of $^{27}Al^-$, $^{28}Si^-$, $^{16}O^-$ and $^{18}O^-$ were collected under conditions described previously [6,7]. The raw SCAPS oxygen data (collected without determining instrumental mass fractionation) were converted to the SMOW scale by comparison of SCAPS results with previously collected point analyses [5].

Elemental imaging. Elemental images were collected using time-of-flight secondary ion mass spectroscopy (ToF-SIMS) [8] at the Smithsonian Institution. A pulsed primary ion beam (Ga^+, 25KeV) was used to produce secondary atomic and molecular ions with a spatial resolution of ~300nm.

Results and Discussion: The SCAPS data for oxygen are consistent with previously collected point analyses and show a gradient from relatively ^{16}O-poor compositions in the center of the nodule to ^{16}O-rich compositions near the fassaite fringe (Fig. 2A). The formation of fassaite in this texture has been attributed to reactions between melilite and vapor in a cooling system while still at high temperature [9]. If so, the fassaite-forming reaction appears to be independent of the O-isotopic alteration of FGI-12, as the more ^{16}O-rich compositions occur adjacent to fassaite.

Formation of the O-isotopic gradient by reaction with an aqueous fluid is not supported by the ToF-SIMS data. No correlations between elemental composition and O-isotopic composition in the melilite were detected. A hint of aqueous alteration is suggested by the distribution of Na (Fig. 2B) and K, which exhibit high abundances in patchy domains in the porous fassaite. The Na- and K-highs may be due to precipitation from a fluid in fassaite pores. However, these patches of elevated Na and K do not correlate with the O-isotopic gradient in melilite.

These results suggest the following history for FGI-12: (1) initial formation in a ^{16}O-rich setting; (2) reaction of some melilite to fassaite in a ^{16}O-rich setting; (3) O-isotopic alteration of melilite in a ^{16}O-poor setting with low $P(H_2O)$; (4) precipitation of Na-bearing phases from aqueous fluid. Stages 1-3 are nebular, whereas stage 4 may have occurred on the Efremovka parent body. Our data are consistent with the interpretation that the O-isotopic composition of melilite was altered independently, without significant shifts in elemental composition or mineral reactions.

References: [1] Clayton R.N. (1993) Ann. Rev. Earth Planet. Sci. 21, 115-149. [2] Yurimoto H. et al. (1994) EPSL 128, 47-53. [3] Yurimoto H. et al. (1998) Science 282, 1874-1877. [4] Greenwood J.P. (2004) *LPSC XXXV*, Abstract #2132. [5] Fagan T.J. et al. (2004) MaPS 39, 1257-1272. [6] Nagashima K. et al. (2004) Nature 428, 921-924. [7] Kunihiro T. et al. (2005) GCA 69, 763-773. [8] Stephan T. (2001) Planet. Space Sci. 49, 859-906. [9] Krot A.N. et al. (2004) MaPS 39, 1517-1553.

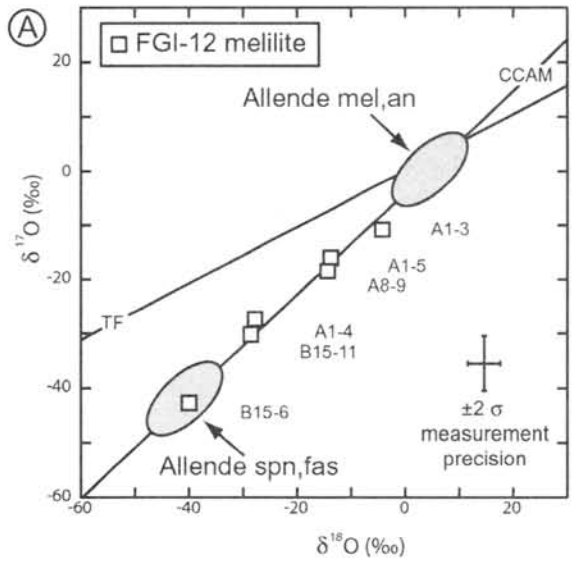

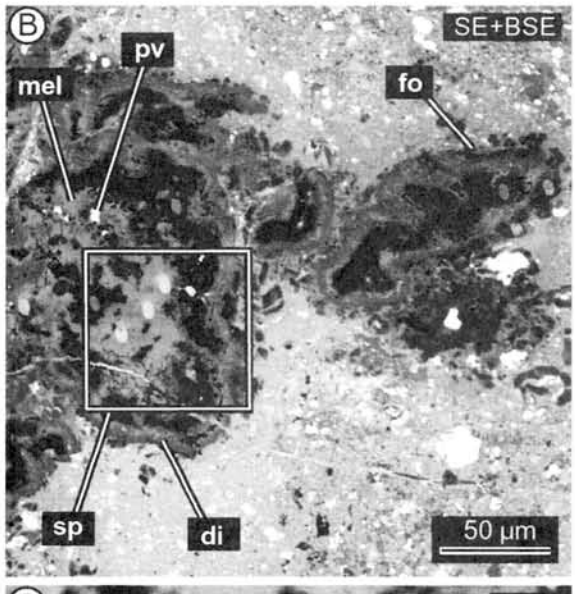

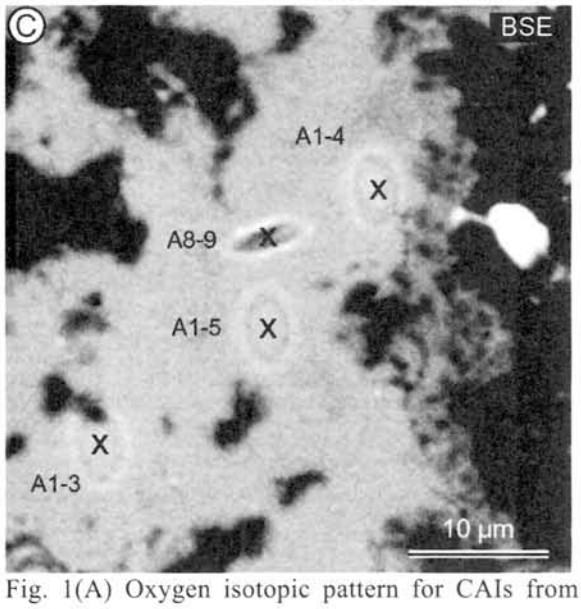

Fig. 1(A) Oxygen isotopic pattern for CAIs from Allende and compositions of melilite from Efremovka FGI-12 [5]. Analysis labels are listed to the right of plotted compositions. (B) Composite SE/BSE image of a portion of FGI-12. Bright ovals reflect high SE contrast of SIMS craters. (C) BSE image of melilite-rich region and SIMS analysis locations. Abbreviations: an, anorthite; di, diopside; fas, fassaite; fo, forsterite; mel, melilite; pv, perovskite; sp, spinel.

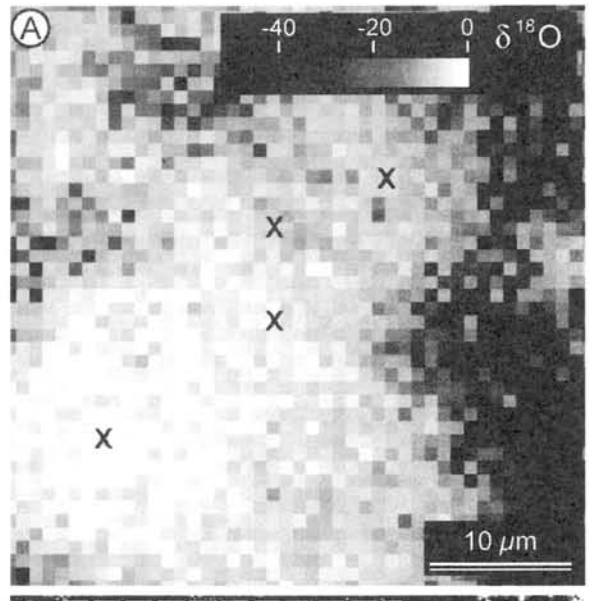

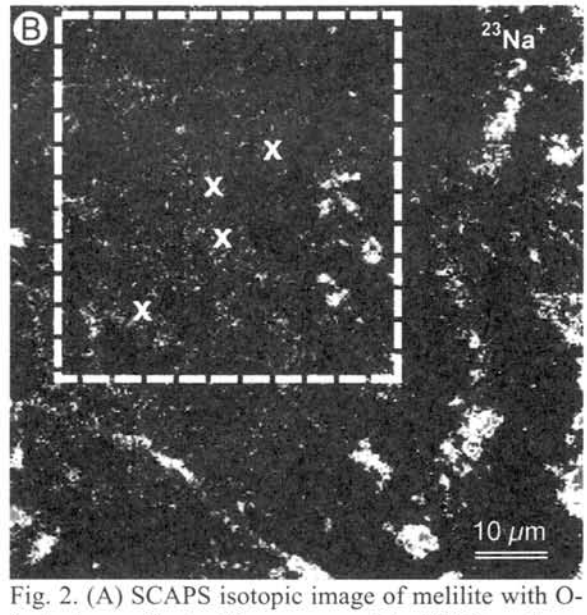

Fig. 2. (A) SCAPS isotopic image of melilite with O-isotopic gradient. X's correspond to SIMS analyses (Fig. 1C). (B) Na distribution in vicinity of melilite-rich nodule. Data collected by ToF-SIMS. Dashed white box highlights area shown in (A).

Brecciation of Y-793605: Indication for two impact events? J. Fritz, A. Greshake, and D. Stöffler. Institut für Mineralogie, Museum für Naturkunde, Humboldt-Universität zu Berlin, Invalidenstrasse 43, 10115 Berlin, Germany.

Introduction:

The conditions for the transfer of rocks from Mars to Earth are well established [1] and documented by a suite of 32 Martian meteorites. As reported previously [2] these meteorites were subjected to shock pressures in the range of 5 to 55 GPa. However, so far only two Martian meteorites, ALH 84001 [3] and Y-793605 [4], represent breccias which may have a multiple impact history.

Based on the monomict brecciation and the deposition of pre-terrestrial carbonates in the granular zones, a multistage impact history has been proposed for ALH 84001 [3, 5]. This leaves the lherzolitic shergottite Y-793605 the only Martian meteorite that was possibly brecciated in the ejection event. Therefore, this meteorite was investigated in this study with respect to indications for more than one shock event.

Analytical Procedures:

Thin sections of the lherzolitic shergottite Y-793605 were studied by optical microscopy. Back-scattered images were obtained using a JEOL-JSM 6300 Scanning Electron Microscope (SEM). To measure the modal composition and grain size distribution, digital image analysis was performed. The mineral composition was determined using a JEOL-JXA-8800L electron microprobe (EMP) with an acceleration voltage of 15 kV and a probe current of 15 nA. The beam size was defocused to 3 µm to minimize the loss of Na and K in plagioclase analyses.

Results:

The lherzolitic shergottite Y-793605 represents a cumulate textured ultramafic plutonic rock. It is composed of poikilitic and non-poikilitic lithologies.

Table 1: Modal composition based on digital image analysis of backscattered images.

	Px[1]	Ol[2]	Pl[3]	opaques[4]
Y-793605	56,3	37,3	4,9	1,4

[1]pyroxene; [2]olivine; [3]plagioclase; [4]opaque phases

The poikilitic lithologies consist of euhedral to subhedral chromite and rounded olivine poikilitically enclosed by large pyroxenes. Additionally, plagioclase appears in the non-poikilitic lithology.

Olivine (Fo_{65-71}) ranges in size up to 1.8 mm with an average size of ~270 µm. In transmitted light, the rounded olivine generally displays an unusual yellow color. Shock effects in olivine are planar microstructures and strong mosaicism.

Poikilitic pyroxene forming large crystals not completely exposed in the thin sections has compositions of $En_{50-77}Fr_{16-31}Wo_{3-34}$. Shock effects are undulatory extinction, mosaicism and planar deformation features.

In Y-793605, all plagioclase (An_{47-58}) is transformed by shock into maskelynite. Raman spectroscopic investigations indicate a shock pressure in the range of 40 to 45 GPa for this meteorite [6].

In addition to the shock metamorphic effects in the constituent minerals, the texture of the rock displays strong mechanical and thermal alterations. In contrast to the lherzolitic shergottites ALH 77005 and LEW 88516, which host large and complex textured melt-pockets, Y-793605 contains only small melt pockets and few melt veins [2]. Adjacent to a melt vein, the olivine displays an unusual brown color. The brown color is similar to the one of olivine in ALH 77005 and was formed by shock [7].

Y-793605 is cross-cut by granular bands (Figs 1a-b; 2a). The granular bands exhibit no porosity and are composed of fragments set in a aphanitic matrix. Some fragments inside the granular bands show resorbed grain boundaries, flow texture and recrystallization features. In some areas of the granular bands, the adjacent minerals recrystallized (Figs. 1 a-b). The aphanitic lithology is reported to account for ~30% of the meteorite [4].

Olivine fragments in the granular band lack the yellow color that is characteristic for the olivine of the host rock (Fig.2 a). Granular bands cross-cut earlier melt veins. Some irregular fractures propagate from the surrounding minerals into the granular bands and the incorporated fragments.

The poikilitic pyroxene crystals in Y-793605 are fractured (Fig. 2 b). These fractures are decorated with birefringent crystals that are a few microns in size. This is a unique feature in Martian meteorites. Additionally a brownish color, probably representing weathering products, can be seen on these fracture planes.

Discussion:

Because of the similar petrologic characteristics, the lherzolitic shergottites Y-793605, ALH 77005 and LEW 88516 were most probably derived from the same igneous complex on Mars [8]. Therefore, despite the higher cosmic ray exposure (CRE) age of Y-793605 compared to ALH 77005 and LEW 88516 these rocks were ejected from Mars in the same impact event [9]. The differences in CRE ages of the lherzolitic shergottites are interpreted to be due to a multi-stage exposure history of Y-793605, possibly implying irradiation by cosmic rays at a shallower depth on Mars [10]. This, however, implies that the plutonic rock was emplaced on the surface of Mars by a secondary process, i.e. erosion, volcanism, or impact cratering.

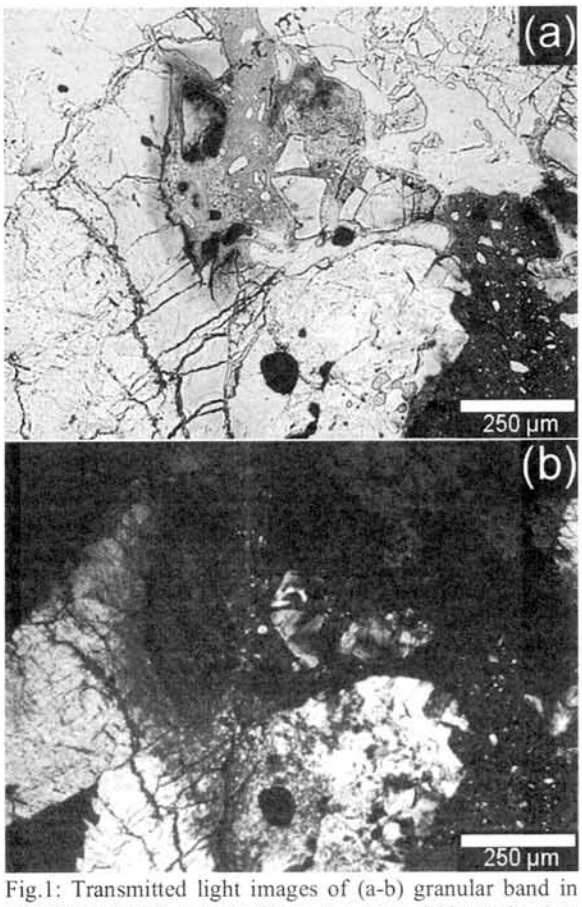

Fig.1: Transmitted light images of (a-b) granular band in Y-793605 which contain fragments up to 200 µm in size. Fragments and adjacent minerals display recystallisation texture. (a) parallel polarizers; (b) crossed polarizers.

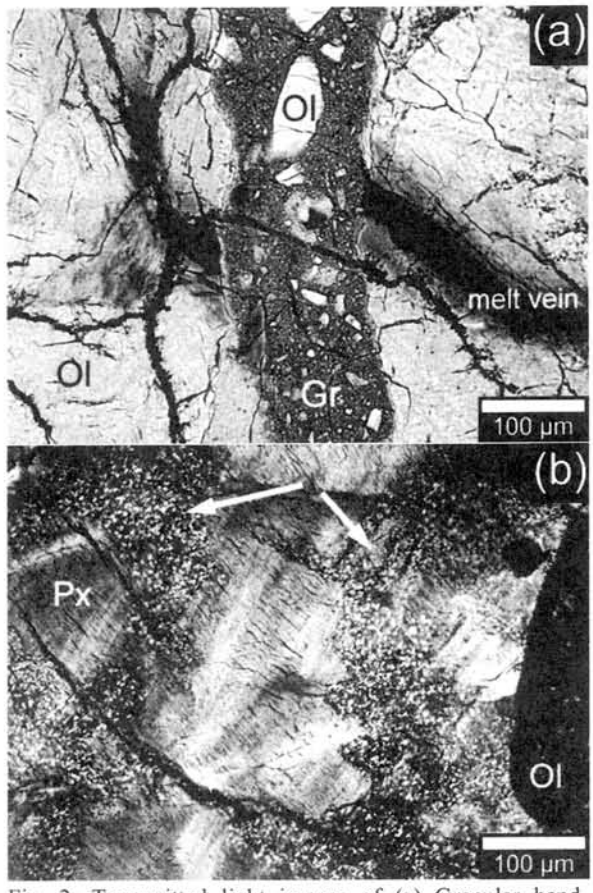

Fig. 2: Transmitted light images of (a) Granular band crosscutting a melt vein, and (b) small birefringent crystals on fractures in poikilitical pyroxene. (a) parallel polarizers; (b) crossed polarizers. Ol = olivine; Gr = granular band.

Isotopic studies of Y-793605 indicate, that after crystallization at 173 ± 14 Ma (Rb-Sr age) the U-Pb system was disturbed, and possibly dates an impact event [11]. The strong mechanical and thermal modifications documented in the rock by granular bands that cross-cut melt veins and alterations on fracture planes in pyroxene are compatible with a multi-stage impact history. Several alteration phases have been identified in Y-793605, unfortunately, none of them could unambiguously be identified as pre-terrestrial [12, 13].

Conclusion:

Several textural, geochemical, and shock characteristics of the lherzolitic shergottite Y-793605 are only compatible with a multi-stage impact history. It is also questionable that this rock could have been brecciated in the spallation zone of an impact crater and strongly shocked and ejected in the same event and then remained rigid enough to withstand the atmospheric drag during ejection from Mars. We propose that Y-793605 was brecciated at depth and ejected from its deep plutonic environment to the surface by a first impact event. It got reimpacted in a second event which formed the maskelynite and ejected the rock fragment into an Earth-crossing orbit.

Acknowledgement:

The authors are grateful for the sample that was supplied by the National Institute of Polar Research, Tokyo.

References:

[1] Artemieva N. and Ivanov B. (2004) *Icarus,* 171, 84-101. [2] Fritz J. et al. (2005) Ejection of Martian meteorites. *Meteorit. Planet. Sci.,* accepted. [3] Treiman A. H. (1998) *Meteorit. Planet. Sci.,* 33, 753-764. [4] Kojima H. et al. (1995) *Antarct. Meteorite Res.,* 10, 3-12. [5] Greenwood J. P. and McSween H. Y. Jr. (2001) *Meteorit. Planet. Sci.,* 36, 43-61. [6] Fritz J. et al. (2005) *Antarct. Meteorite Res.,* 18, in press. [7] Ostertag R. et al. (1984) *EPSL,* 67, 162-166. [8] Mikouchi T. and Miyamoto M. (1997) *Antarct. Meteorite Res.,* 10, 41-60. [9] Eugster et al. (2002) *Meteorit. Planet. Sci.,* 37, 1345-1360. [10] Nagao K. et al. (1997) *Antarct. Meteorite Res.,* 10, 125-142. [11] Morikawa N. et al. (2001) *Antarct. Meteorite Res.,* 14, 47-60. [12] Ikeda Y. (1997) *Antarct. Meteorite Res.,* 10, 13-40. [13] Mittlefehldt D. W. (1997) *Antarct. Meteorite Res.,* 10, 109-124.

The Carbon Cycles of Earth and Mars: how have they evolved? Monica M. Grady and I. P. Wright. Planetary and Space Sciences Research Institute, The Open University, Walton Hall, Milton Keynes, MK7 6AA, U.K. (m.m.grady@open.ac.uk).

It is well known that on Earth there is a dynamic interaction between four main reservoirs: the atmosphere, hydrosphere, lithosphere and biosphere. This has led to the operation of both non-biological and biological carbon cycles. In the former, carbon (in various species) is transferred through a series of processes, including sedimentary rock formation, weathering of rocks, subduction at active plate boundaries and magmatic degassing. The biological cycle intersects with the abiological cycle during sedimentary rock formation. The system is not closed: carbon is added to the Earth by meteorites and micrometeorites. The cycles are complex but fairly well understood, with end-members defined in terms of carbon speciation and isotopic composition.

Mars is a rocky planet, similar in many respects to the Earth. We know that Mars has two definite reservoirs, its atmosphere and lithosphere, and that there is evidence that in the past Mars has had a hydrosphere, even if this reservoir is now very limited. The existence of a martian biosphere is debatable, but its presence, or even its absence, is of enormous interest in the context of Solar System life studies.

Knowledge of the terrestrial carbon cycle has been built up over many years by careful, direct analyses of physical materials. How can we attempt a similar exercise for Mars, when we do not know the relative abundances of carbon in the end-member reservoirs, its speciation or isotopic composition? The martian cycle must be less complex than that of Earth, given that Mars does not have an active tectonic plate system. Indeed, the lack of both a hydrosphere and an internal heat source implies that any abiological carbon cycle must now be almost static.

Martian meteorites are igneous rocks, and so contain primary magmatic carbon. This represents the lithospheric reservoir. Many martian meteorites have suffered alteration by aqueous fluids at Mars' surface, and so contain secondary carbonates and clay minerals. These components represent the hydrosphere. Most martian meteorites also contain pockets of gas trapped within impact-generated melt. Because the gas was trapped from the martian atmosphere during ejection of the meteorites from the surface of the planet, it represents the atmospheric reservoir. Taking these data from martian meteorites gives end-member compositions that, taking analogies with the Earth's system, can be modelled to produce a carbon cycle for Mars. We can then interrogate this model, to determine whether or not there is any evidence within it for a martian biosphere.

Aqueous alteration of nakhlites: results from Y 000593 and MIL 03346, and implications for water on Mars. Monica M. Grady[1], M. Anand[2], J. Bridges, V. Pearson[1], A. B. Verchovsky[1] and I.A. Franchi[1]. [1]Planetary and Space Sciences Research Institute, The Open University, Walton Hall, Milton Keynes MK7 6AA, UK; [2]Dept. Mineralogy, The Natural History Museum, Cromwell Road, London SW7 5BD, UK. E-Mail: m.m.grady@open.ac.uk.

Introduction: The nakhlites are all clinopyroxenites that vary mainly in grain size rather than composition. They are almost unshocked rocks that formed at or near the Martian surface in a slowly-cooled, thick cumulate pile, with the various members of the group deriving from different depths within the intrusion [1]. Although they solidified from melts about 1.3 billion years ago, and were ejected from the planet about 10–12 million years ago [2], the rocks still bear traces of low temperature aqueous processes that can be used to infer conditions on the Martian surface. The meteorites have been altered by weathering, leading to the production of secondary minerals (clays, carbonates and sulphates; ref. 3, 4) associated with which are low concentrations of Martian organic material [5]. As of March 2005, there were seven individual nakhlites. The largest is the pairing group Yamato 000593/749/802 (15 kg in total), whilst the most recently recovered is MIL 03346 (712 g in size).

Several parameters have been employed to infer a differential alteration sequence amongst the nakhlites. Bridges et al. (ref. 4) modelled an evaporation sequence for nakhlites on the basis of mineral assemblages present in the three non-desert nakhlites. Mikouchi et al. (ref. 6) used olivine core and rim compositions to deduce a depth of crystallisation within the nakhlite magma pile. We have taken these two models, and applied them to Y 000593 and MIL 03346, in order to determine how they compare with the other nakhlites, and whereabouts in the crystallisation sequence the meteorites fit.

Results: Like the other nakhlites, the dominant mineralogy of Y 000593 is clinopyroxene, with around 15% olivine plus accessory minerals (apatite, sulphides, etc). As shown by other authors [6, 7], olivine compositions vary from core to rim from ~ Fa_{65} to Fa_{80}. MIL 03346 contains a much lower volume percentage of olivine; the few grains that are present are zoned from Fa_{56} in the core to Fa_{87} in the rim. In both meteorites, the olivine grains are cut by veins of preterrestrial secondary alteration products, the fine-grained mixed layer clay mineral iddingsite. Carbonates and sulphates are also present, but occur as in-fill between augite grains and in cracks in augite and mesostasis. Dissolution of 50 mg of powdered Y 000593 in 100% orthophosphoric acid liberated ~ 150 ppm

Fe-rich carbonate with $\delta^{13}C$ = +38‰ (PDB) and $\delta^{18}O$ = +39‰ (SMOW). This is the highest amount of carbonate found in a martian meteorite, apart from the orthopyroxenite ALH 84001. Combustion of Y 000593 gave 177ppm carbon, with total $\delta^{13}C$ = +21‰. At least some of this carbon is from organic material, although its martian or terrestrial origin is not yet known. A similar combustion experiment on MIL 03346 yielded 62 ppm carbon, with $\delta^{13}C$ = -20‰, indicating the greater influence of organic material on the total isotopic composition, and a much lower carbonate abundance.

Discussion: the close similarities in mineralogy and mineral chemistry amongst the nakhlites imply that they are all derived from the same magma body, whilst petrographic variations suggest that they are derived from different depths within the cumulate pile. The extent of equilibration of within individual ferromagnesian silicate grains has been recognised as a marker for depth of derivation [1,b6], and on that basis, since MIL 03346 contains the least equilibrated of all silicates, it most probably derives from the outermost edge of the intrusion, perhaps even a chill margin. Increasing depth within intrusion does not, however, correlate with decreasing extent of secondary alteration. There are at least two populations of martian weathering products within nakhlites: (1) clay minerals formed *in situ* within olivines, by the alteration and hydration of silicates and (2) precipitation of carbonates and sulphates within cracks. MIL 03346, which, on the basis of olivine composition, seems to derive from the outer edge of the intrusion, contains only sparse carbonates, although its olivine grains are broken by clay veinlets. It is possible that the outer edge that MIL 03346 represents is at the bottom of the intrusion, and not the top.

Acknowledgements: We thank the NIPR and the AMWG for generous provision of samples. This research is funded by grants from the PPARC to MMG and IAF.

References: [1] Lentz R. C. F., Taylor G. J. and Treiman A. H. (1999). Meteorit. Planet. Sci. 34, 919-932; [2] Nyquist L. E., Bogard D. D., Shih C.-Y., Greshake A., Stoffler D. and Eugster O. (2001). In: Chronology and Evolution of Mars. Eds. R. Kallenbach et al., Kluwer, Dordrecht. 96, 105-164; [3] Bridges J. C. and Grady M. M. (1999). Meteorit. Planet. Sci. 34, 407-416; [4] Bridges J. C. and Grady M. M. (2000). Earth Planet. Sci. Lett. 176, 267-279; [5] Carr R. H., Grady M. M., Wright I. P. and Pillinger C. T. (1985). Nature 314, 248-250; [6] Mikouchi T., Koizumi E., Monkawa A., Ueda Y. and Miyamoto M. (2003). Antarct. Met. Res. 16, 34-57; [7] Imae N., Ikeda Y., Shinoda K., Kojima H. and Iwata N. (2003). Antarct. Met. Res. 16, 13-33.

Meteorite craters and planetary surface evolution: an educational approach. Henrik I. Hargitai[1], Szaniszló Bérczi[1] [1]Eötvös Loránd University, Cosmic Materials Space Research Group, 1117 Budapest, Pázmány P. sétány 1/A E-mail: hargitai@emc.elte.hu

Introduction. Cratering is the most common surface modification process in the Solar System. It can be used for dating surfaces [1]. It also shows the meteoroid inventory of the particular region at the particular time. (Most) craters are created by meteoroid impacts (from micrometeorites to large asteroids) therefore the process is mutual: small planetary bodies are both receivers and (later) makers of impacts.
We have developed an educational diagram series (fig. 1.) that shows the interconnections of cosmic, planetary external and internal processes, focusing only on cratering. Impact craters play a central role in forming the surface, and they can also be used as indicators not only of the relative age of the particular surface but also of the processes operating on a planet. The diagram is part of the textbook series "Encyclopaedia of the Solar System: Cratering".

Early impacts In the early Solar System impacts played a major role of forming planetary bodies. By the size and total mass of the impacted (concreted) bodies they have pre-determined their (auto-geothermic) active lifespan (the case of moons close to gas giants are different). Impacts from icy bodies may have contibuted to the total surface water content of the Earth or other planets thus creating a hydro- and criosphere that changed their future geologic, atmospheric and biologic evolution. All previous craters have been erased when irregular planetary bodies heated to became spherical objects. During the Late Heavy Bombarment they may have exterminated life on one or more worlds; and they may be responsible for the loss of atmosphere of Mars. Impacts are also interfering the later biological evolution by making some species extint, this way allowing others to occupy new niches; and by „stirring the stand water": creating a demand for (evolutional) change [2].

Impacts during „main sequence" phase As planetary evolution changes the surface characteristics of a planetary body, the more active a planet the less crater can be found on its surface. Both internal and external forces „eat up" the crater inventory. On geolgically not active planets continuous micrometeoritic bombardment creates a very fine dusty regolith (that may endanger future human expeditions). On active planets atmosphere or surface water effectively prevents such micrometeorites to reach the surface. As planetary evolution progresses, resurfacing from magmatic and volcanic processes buries craters on a local, regional or even global scale (thus „reseting" the age of the surface). Such examples for the latter situation are Io and Venus 0.7 Ga ago. If plate tectonics is operateing, subduction effectively erases all traces of craters that are found on the relatively new basaltic crust of the planet, while at convergent plates mountain building is the crater consuming process. On continental areas water and atmosphere erodes craters, while aeolian dust, fluvial deposits or inland ice buries them. In permafrost regions the freezing -thawing cycle or glacier activity largely modifies their morphology.

Impacts at the end of planetary evolution At the end of the thermal evolution of a planetary body, geologic activity slowly ceases. Since no more resurfacing event is taking place and probably the atmophere is also disappearing because of the loss of its source, cratering again is the major surface forming process - provided there still are enough meteoroids in the Solar System. The cratering rate has been constant during the last 3 Ga [3], and it is not known when it will start to decline.

Educational material The above mentionned evolutional process is displayed on a diagram that also points out the connecting processes and their impact. As our experience shows, the knowledge of most students consists of separated „knownlegde-univeses" that are not connected. Making congnitive connection of processes and surface features, in both time

and space allow students better understand present day geographic and geologic features and the importance of meteorites. Diagrams like this make it easier to *oveview* the variuos processes controlling the surface characteristics of a planet.

This diagram was specially developed for helping introductory university lectures on Planetary Science at the Cosmic Materials Space Research Group in 2005.

References

[1] Neukum G and Wise, D. U. 1976 Mars: a standard crater curve and possible new time scale. Science 194 1381-7

[2] Ward P and Brownlee D: 2000 Rare Earth. Copernicus.

[3] Hartmann W.K. 2005: Moons and Planets.

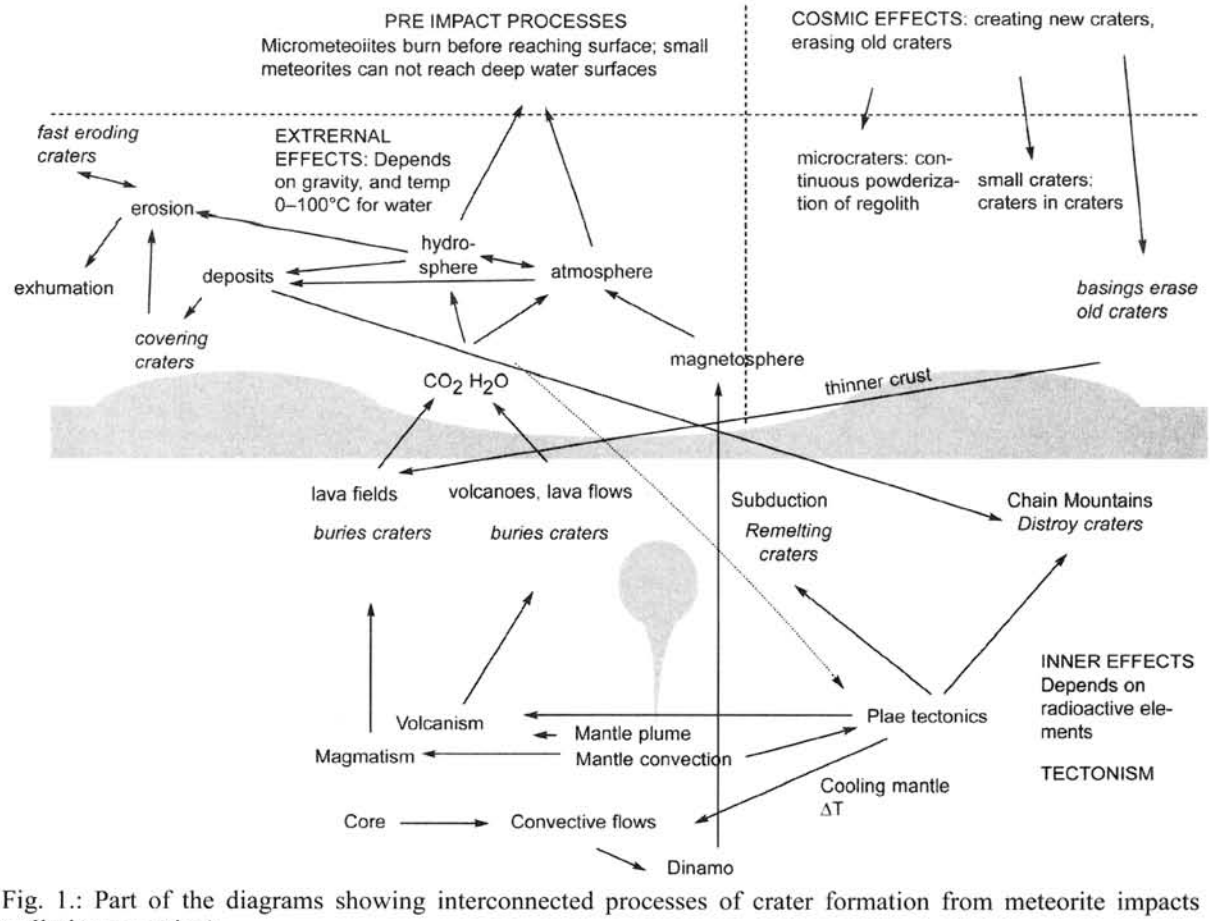

Fig. 1.: Part of the diagrams showing interconnected processes of crater formation from meteorite impacts (preliminary version)

History of Gibeon Meteorite in Space. M. Honda[1] and K. Nagao[2], [1]Department of Chemistry, Nihon University, Setagaya-ku, Tokyo 156-0045, Japan, [2]Laboratory for Earthquake Chemistry, Graduate School of Science, University of Tokyo, Bunkyo-ku, Tokyo 113-0033, Japan.

Introduction:

Fragments of the Gibeon iron meteorite, IVA, first found in 1836, fell over the world's largest strewn field, a dispersion ellipse with principal axes measuring at least 275 x 100 km in central Namibia [1]. We have measured cosmogenic nuclear species, as well as radionuclides [2] and stable nuclides [3] on many different fragments collected randomly. Because of the large size of the original iron meteoroid, of which 21 tons have been recovered, the contents of various cosmogenic nuclides vary widely from specimen to specimen. We found strong contrasts between the sets of stable and radionuclides, which only can be understood in terms of multiple break-ups in space before in atmosphere. Such complex histories of multi stage exposures have been studied for some stony meteorites [4], but not as extensively for irons.

In the simplest case, the exposure age of the meteorite can be calculated by the contents of the stable nuclides such as cosmogenic ^{36}Ar divided by the disintegration rate of ^{36}Cl, which has been assumed as saturated for a longer irradiation relative to the life time. A production rate of ^{36}Ar can be obtained accurately by the application of a small correction factor to the disintegration rate of ^{36}Cl. For this estimation we have to assume the simplest history for the meteorite in space. These assumptions can be allowed in some cases, but not necessarily in general.

Gibeon Meteorite Samples:

The first discovery of cosmogenic ^{3}He was reported in 1952 by Paneth et al. [5] on two samples of Bethany, which is a synonym of Gibeon. Today, Gibeon samples are popular among collectors and specimens are widely available at reasonable prices, such as 1$/g. However, well documented samples from specific locations are not easily available. Therefore, we decided to obtain our samples from various sources in the U.S.A. and Germany. This may be a non-systematic way of sampling, but by this method we obtained a great variety of specimens and measured the ^{10}Be and others contents of more than 60 of them.

Cosmogenic Nuclides:.

At the first stage, we determined the contents in each sample of ^{10}Be (half life: 1.5E6 y.), ^{26}Al (7E5 y), ^{36}Cl (3E5 y), and ^{53}Mn (3.7E6 y). For activities of Be, Cl and Al, AMS methods have been employed after additions of respective reagent carriers. Some inclusions like troilite are useful for studying the enhanced production of ^{26}Al in sulfur atoms. The most sensitive determinations can be performed for ^{10}Be. For ^{26}Al the sensitivity can not be compared with that of ^{10}Be. For ^{36}Cl, constant ratio of ^{36}Cl /^{10}Be = 5.9, σ = 0.4 (n=10), was available in a wide range of ^{36}Cl covering 7 - 0.001 dpm/kg.

For stable nuclides, we employed sensitive mass spectrometry for the light noble gases, He, Ne, and Ar, and an entirely different picture was available from the data set of the radionuclides. When we started this work, we expected to find data from deep within the iron. That was achieved with ^{10}Be, down to 6E-5 dpm/kg such as, in sample 103. On the other hand, the lowest content of ^{3}He was also found at 4E-13 cc/g in the sample 003, which seems to be the lowest record of the data in any iron meteorite. The samples from near the surface of primary body of, Amalia and the following members, seem these data to have relatively high ratios of ^{3}He /^{4}He at about 0.2 or more, so the whole preatmospheric body must have been larger in radius than 4000 g/cm^2 which may be estimated to be larger than 10 meters in diameter.

This figure was not only the lowest we found but it also indicated that we should conclude there were complex features in the history of Gibeon. We can interpret these data on two sets of cosmogenic nuclides as being the result of multiple exposures of the Gibeon meteoroid. Although sources of our collection of the fragments have been limited to a very small fraction of the total body, many samples contain extremely low ^{3}He /^{4}He even lower than 0.001 such as in samples C4 and 003, which could be attributed by non-cosmogenic or natural radiogenic ^{4}He at the level of 0.1E-8 cc/g. In fact, these low ratios are useful to judge the classifications of sub groups. The multiple exposure history is the most important feature of the Gibeon meteorite. These aspects may not apply only to Gibeon but will be relatively common features among large size iron meteorites.

The typical data of ^{10}Be and about 20 data of ^{3}He obtained in this work and the reported ones have been compiled and plotted in a two dimensional plane (Fig. 1). The variations of ^{3}He/^{4}He have also been indicated showing the variable historical records. So far all data can be classified into 4 different subgroups. When we can collect more samples the plot may be extended more than current area but essentially homogeneously, because the breaks might have occurred at any time and at any place. In this figure the lowest group, the latest break

products, seems to have the youngest history, giving an unsaturation for the products of longer lived activities. The plots for Amalia (Krantz) and Harvard, have not been directly supported by ^{10}Be data, but they can be estimated reasonably from ^{3}He/^{4}He.

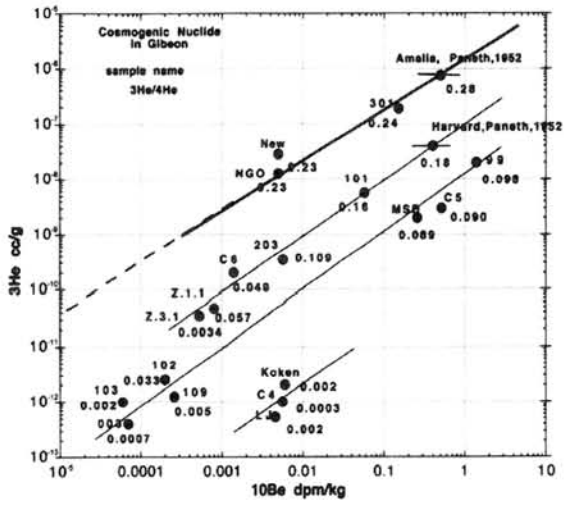

Fig. 1 ^{3}He vs ^{10}Be , and 3He/4He in Gibeon

References:

[1] V. Buchwald, V. (1975) *Handbook of Iron meteorites Vol.2*, 584-593; [2] Noguchi, M. et al. (2004) *Symposium NIPR. June 3,* Tokyo; Noguchi, M. et al. (2003) *13th. Goldschmidt Symposium, S.49.* Sept. 11, Kurashiki, Japan; [3] Nagao, K. and Honda, M. (2005) Noble gases of GIBEON iron meteorite. this symposium; [4] Honda, M. et al. (1980) *Geochemical J.* ***14***, 83; [5] Paneth, F.A. et al. (1952) *Geochim. Cosmochim. Acta,* ***2***, 300; [6] Honda, M. et al. (2002) *Meteoritics* ***37***, 1711; [7]. Liberman, R.G. et al. (2001) *Meteoritics* ***36***, 298.

Petrology of MIL 03346. N. Imae[1] and Y. Ikeda[2], [1]National Institute of Polar Research, 9-10, Kaga 1-chome, Itabashi-ku, Tokyo 173-8515, Japan, [2]Department of Material and Biological Sciences, Ibaraki University, Mito 310-8512, Japan.

Introduction:

MIL 03346 is the seventh nakhlite and the second Antarctic nakhlite [1]. We studied this new sample petrographically and petrologically using optical microscope and an electron probe microanalyzer (JXA-8200).

Petrography:

MIL 03346 consists of augite phenocrysts (1×0.5 mm or less in size), mesostasis and minor magnesian olivine grains. Modal compositions of augite phenocrysts, mesostasis and magnesian olivine grains are 67.7, 31.5 and less than 1 vol%, respectively.

Augite phenocrysts: The augite phenocrysts have magnesian core (56.5 vol%) and ferroan rim (11.2 vol%). The augite core composition is homogeneous ($En_{36-38}Fs_{24-22}Wo_{40}$), while rims with ~20 μm in average show chemical zoning, where Fs and Al_2O_3 contents increase up to ~50 mol% and 10 wt.% outwards, respectively (Fig. 1). The Fe-rich rim is divided into two layers toward the boundary with mesostasis; the 1st layer and the 2nd layer (Fig. 1). The Fs content of the 1st layer increases rapidly. The 2nd layer is rich in CaO and hedenbergitic. Magmatic inclusions (~100 μm in diameter) are found in augite phenocrysts. They are much larger than those in augites of Yamato nakhlites (Y000593, Y000749 and Y000802), and are texturally different.

Mesostasis: Mesostasis consist of cryptocrystalline materials with abundant dendritic fayalites (Fa_{92-95}), and skeletal or tiny titanomagnetites. The modal compositions of cryptocrystalline materials, dendritic fayalites and skeletal titanomagnetites are 82.4, 10.5 and 7.1 vol%, respectively. Titanomagnetites accompany thin ilmenite lamellae with the thickness of 0.2 μm or less. Silica minerals, pyrrhotites ($Fe_{0.85-0.95}S$), chalcopyrites and acicular phosphates occur, but plagioclase is not found.

Magnesian olivine grains: Olivine grains, 0.5 × 0.5 mm or less in size, are very minor in amounts. The core is magnesian (Fa_{55-57}) and the rim is ferroan ($Fa_{<85}$). Symplectites and lamellae which are observed in olivine of Yamato nakhlites [2] are not observed.

Petrology:

Intercumulus melt composition of MIL 03346 (MIM) was estimated from the mass balance calculation by substraction of augite core (56.5 vol%) from the whole rock composition. The MIM is richer in aluminum, sodium and potassium, and poorer in calcium in comparison with the intercumulus melt composition of Yamato nakhlite (YIM) [3] (Table 1).

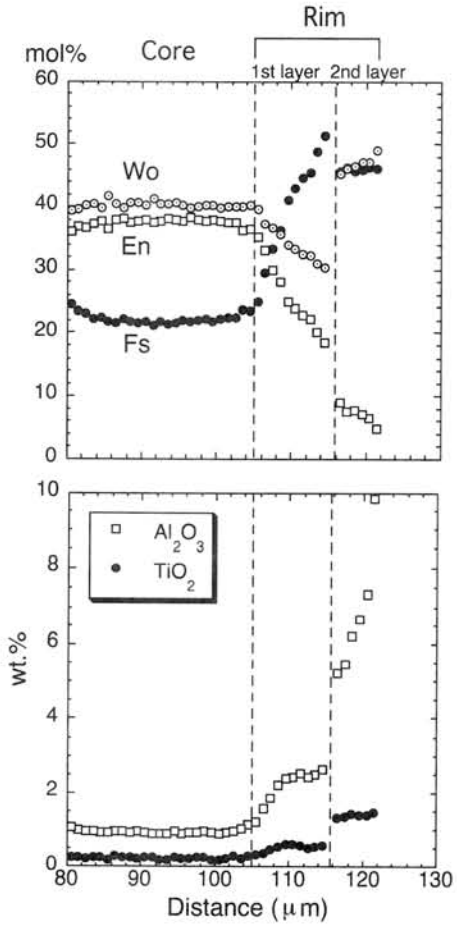

Fig. 1. The chemical zoning profile near a grain surface in the augite phenocryst.

Trapped melt composition was estimated from inclusions in augite phenocryst cores. We obtained the averaged bulk composition of five inclusions consisting of mesostasis (49 vol%), ferroan augite (43 vol%), titanomagnetites (6 vol%), fayalite (1 vol%) and hydrous phase (2 vol%) (Table 1). We corrected apparent composition of magmatic inclusions (MI^{app} in Table 1) adding wall augite composition in order to satisfy the Fe/Mg partitioning between the augite phenocryst core and the trapped melt composition. The corrected composition (MI^{cor}) is given by MI^{app}:wall-augite =80.5 vol%:19.5 vol%, is shown in Table 1 and is plotted in Fig. 2. The obtained trapped melt composition (MI^{app} and MI^{cor}) is slightly depleted in normative olivine compared with the intercumulus melt composition (MIM in Table 1).

Crystallization process to form MIL 03346 is as follows. Phenocryst augite cores accumulated in a magma chamber. Auigte rims rapidly crystallized surrounding phonocrystic augite cores during the rapid cooling. The decrease of Fs component in the 2nd layer may be due to fayalitic olivine crystallization in mesostasis. The very fine grained mesostasis suggests that the interstitial melt more severely supercooled than that of Yamato nakhlites [4]. The supercooled melt crystallized fayalite, titanomagnetite and cryptocrystalline phases in the mesostasis.

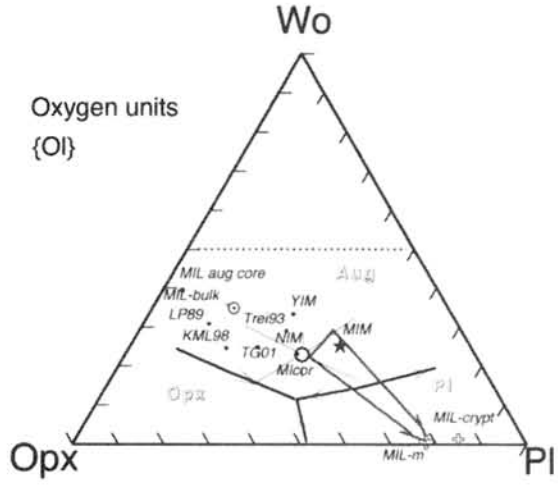

Fig.2. The pseudo ternary phase diagram of Wo-Opx-Pl system showing the crystallization from the intercumulus melt of MIL 03346 to form the mesostasis. MIM: calculated intercumulus melt composition for MIL 03346. MIL-bulk: the bulk composition of MIL 03346 [3]. MIL-m: the bulk composition of mesostasis consisting of cryptocrystalline materials, dendritic fayalites and skeletal titanomagnetites. MIL 03346. MIL-crypt: cryptocrystalline composition in mesostasis. MI^{cor}: corrected bulk composition of inclusions in augite phenocryst cores MIL 03346. MIL aug core: core composition of phenocrystic augite. LP89 [5], NIM [6], Trei93 [7], KML98 [8] and TG01 [9] are the parent magma of Nakhla.

Table 1. Bulk composition of the interstitial melt, the inclusion in augite phenocryst cores, and bulk composition of mesostasis for MIL 03346, with the reference data for intercumulus melt composition of Yamato nakhlites.

	MIM[*1)]	MI^{app}[*2)]	MI^{cor}[*3)]	Cryp[*4)]	M[*5)]	YIM[*6)]
SiO_2	46.95	48.01	48.81	59.01	50.18	47.26
TiO_2	-	2.21	1.82	0.55	2.35	0.60
Al_2O_3	7.35	10.17	8.33	17.61	14.25	5.12
FeO	27.06	23.45	21.58	8.46	22.16	20.19
Fe_2O_3	-	-	-	-	-	5.90
MnO	0.52	0.44	0.44	0.11	0.33	1.15
MgO	5.05	2.19	4.28	0.21	0.40	3.66
CaO	9.81	8.86	10.91	4.34	3.44	12.42
Na_2O	2.06	2.27	1.87	5.78	4.53	1.88
K_2O	0.69	1.51	1.21	1.15	0.91	0.59
P_2O_5	0.51	0.54	0.43	1.14	0.91	0.67
Cr_2O_3	0.01	0.04	0.07	0.02	0.02	0.18
SO_3	-	0.25	0.20	0.64	0.49	-
NiO	-	0.06	0.05	0.04	0.03	-
Total	100.01	100.00	100.00	99.06	100.00	99.62

[*1)]MIM: Interstitial melt composition for MIL 03346. [*2)]MI^{app}: Averaged apparent composition from five magmatic inclusions in augites in MIL 03346. [*3)]MI^{cor}: Corrected MI for the Fe/Mg partitioning. [*4)]Cryp: Cryptocrystalline phase in mesostasis. [*5)]M: Bulk composition of mesostasis consisting of cryptocrystalline phase, dendritic fayalites and skeletal titanomagnetites. Composition of cryptocrystalline phase was determined using defocused beam (10 μm) of an electron probe microanalyser. [*6)]YIM: Interstitial melt composition for Yamato nakhlites [4].

Acknowledgment:

We are grateful to NASA, Johnson Space Center for the loan of the polished thin section for the present study.

References:

[1] Antarctic Meteorite Newsletter (2004) Vol 27, No. 2. [2] Imae N. et al. (2003) *AMR, 16, 13-33.* [3] Anand M. et al. (2005) LPSC XXXVI. #1639. [4] Imae N. et al., in submission. [5] Longhi and Pan (1989). [6] Harvey R. P. and McSween H. Y. Jr. (1992) EPSL, 111, 467-482. [7] Treiman A. H. GCA, 57, 4753-4767. [8] Kaneda K. et al. (1998) LPSC XXVIIII. #1620. [9] Treiman A. H. and Goodrich C. A. (2001) LPSC XXXII. #1107.

Thermoluminescence Studies of Shocked Minerals and Rocks. Y. Ishida[1], K. Ninagawa[1], M. Sakamoto[2], S. Toyoda[1], and H. Nishido[1], A. Gucsik[3]. [1]Okayama University of Science, [2]Neba Elementary School, [3]Univ. West Hungary

Introduction:

A semi-circular topographical feature (approximately 900 meters in diameter) is located in the eastern side of Mt. Oikeyama on Shirabiso Highland, which lies in the southern part of the Akaishi Mountains, Nagano Prefecture. Planar microdeformations of the quartz was found in sandstone from this area [1]. These planar microdeformations might be so-called planar deformation features (PDFs) that were formed by the impact more than 10GPa, suggesting that this structure also formed hypervelocity impact event. [1-4]. In the present study, thermoluminescence (TL) of following three samples was measured to confirm the evidence of impact shock metamorphism. (1) Sandstone collected from outside of the crater, (2) Sandstone experimentally shocked by railgun experiments at 10GPa (abbreviated to railgun sandstone.), (3) Metamorphic sandstone collected from inside of the crater at Mt. Oikeyama (Fig.1).

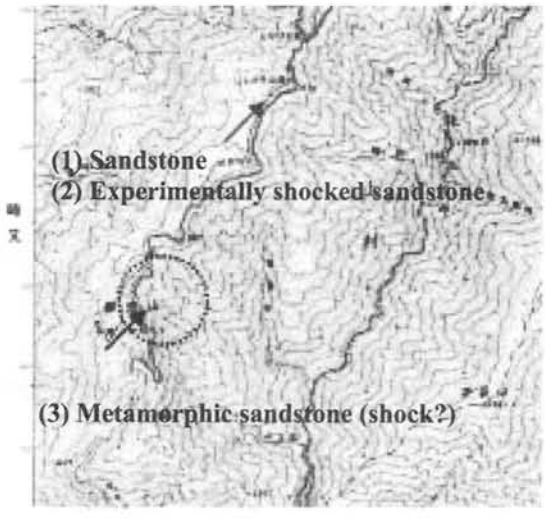

Figure 1. Sampling location

Thermoluminescence:

Three samples were gently powdered to measure TL. Induced TL was measured after a dose of 250Gy ^{60}Co gamma ray irradiation. Figure 3 shows TL glow curves of them. TL intensity is normalized by peak intensity at 150 °C. A new, relatively large peak appeared at 350 °C in the TL glow curve of the railgun sandstone, compared with that of the sandstone collected from the outside of the impact crater (Fig.2). There is a slight bulge at 350 °C in the metamorphic sandstone (Fig.3).

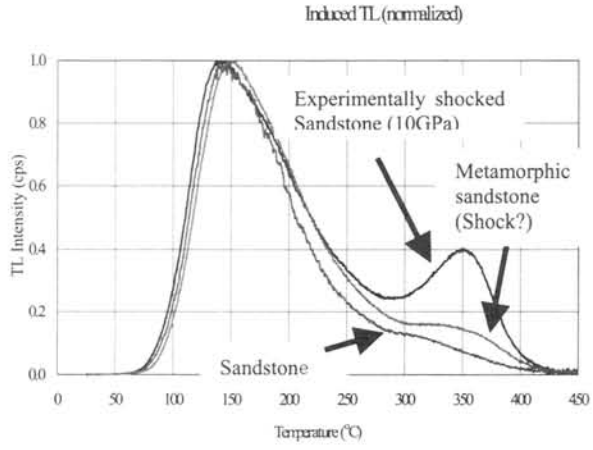

Figure 2. TL glow curves

2D TL and compositional analysis:

Firstly, 2 dimensional TL measurement and the compositional analysis on the metamorphic sandstone were done to determine the mineral responsible for the above TL peak at 350 °C. The metamorphic sandstone was cut to a plate of 350μm in thickness, and was polished for 2D TL measurement and compositional analysis. 2D TL measurement was done after a dose of 10kGy ^{60}Co gamma ray irradiation. Some parts of the sandstone, which are responsible for the TL at 150 and 350°C, were specified. Each part of the specified positions was compositionally analyzed by an EDS. As a result, the mineral responsible for the above TL at 150 °C was potassium feldspar. On the other hand, the mineral responsible for the peak at 350 °C was albite.

Next, 2 dimensional TL measurement and the compositional analysis on the railgun sandstone were done. This sample had been already powered by the railgun experiment. Then the powdered sample was fixed with a silver paste to specify the luminescence parts. As a result, potassium feldspar and albite were also responsible for the TL at 150 and 350 °C, respectively, just like the metamorphic sandstone.

TL spectra analysis:

The TL spectral measurements of them were carried out for the three samples (Figure 3-1 and 3-2). The x-axis is wavelength from 324 to 708 nm, and the y-axis is temperature from 0 to 448 °C. TL

intensity is displayed by pseudocolor. The TL spectra of some temperature regions are displayed in the upper part, and the TL glow curves of some wavelength regions are displayed in the right part. A new TL peak at about 350 °C and 380nm is produced for the railgun sandstone, comparing with sandstone.

TL spectra of shock and unshocked single crystals of albite, sanidine, bytownite, and quartz were also carried out to investigate whether a similar spectral change is produced by shock or not. However, a new peak was not observed in albite though the TL intensity decreased overall after the railgun shock experiment (Figure 5-1, and 5-2). There was no spectral difference except decrease of TL intensity for the other three single crystals.

Conclusions and discussion:

The metamorphic sandstone collected from the inside of the crater rim shows a weak TL peak at 350 °C emitted from albite grain. Also the railgun sandstone has an apparent TL peak at 350 °C where albite contributes to such emission.

These facts imply that the metamorphic sandstone might have a record of shocked metamorphism by hypervelocity impact event. Monocrystalline albite, however, did not show any emission peak at around 350 °C even if experimentally shocked at 10 GPa by railgun.

There are several types of polymorph and many domain structures in albite due to different formation temperature and various quenching processes. It is necessary to verify whether monocrystalline albite employed for railgun experiment corresponds to the same mineralogical type of albite in the sandstone from Mt. Oikeyama, and whether the new peak appears or not by higher pressure shocked experiments.

References:

[1] Sakamoto M. *et al.* (2001): *Abstract on 2001 Annual Meeting of Japanese Society for Planetary Sciences (Okayama)*, 56pp.

[2] French B.M. (1998): *Traces of Catastrophe: A handbook of shock-metamorphic effects in terrestrial meteorite impact structures. LPI, Houston*, 120 pp.

[3] Sakamoto M. *et al.* (2003): *Evolution of Solar System Materials: A New Perspective from Antarctic Meteorites*, 124 pp.

[4] Sakamoto M. *et al.* (2005) *LPSC, XXXVI Abstract*#1242.

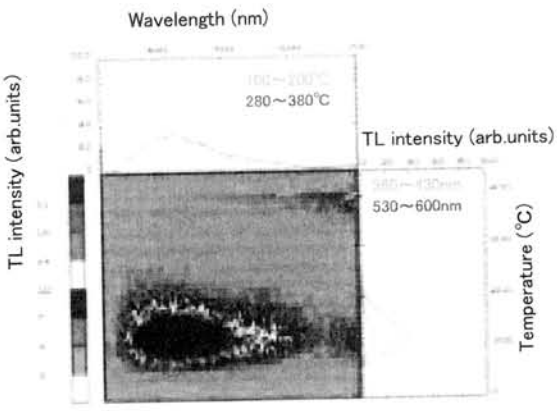

Figure 3-1. TL spectra of Sandstone

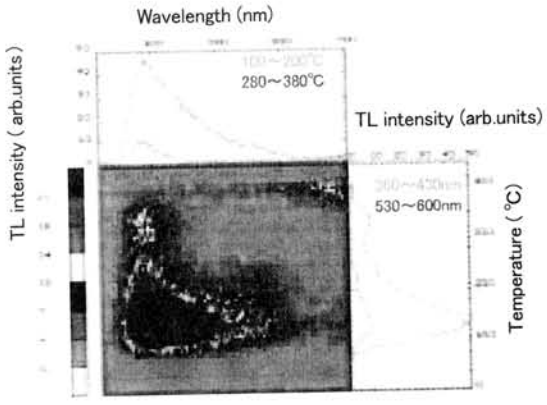

Figure 3-2. TL spectra of Railgun Sandstone

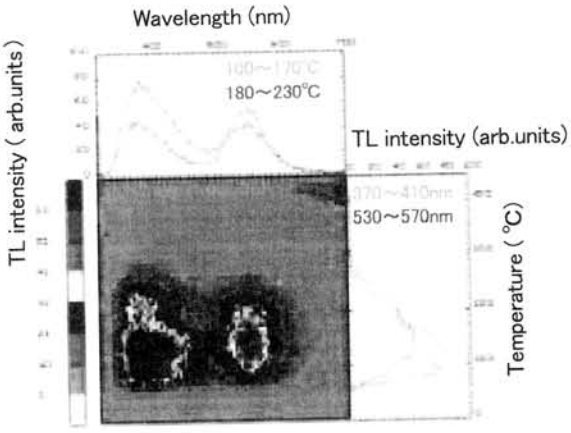

Figure 4-1. TL spectra of albite

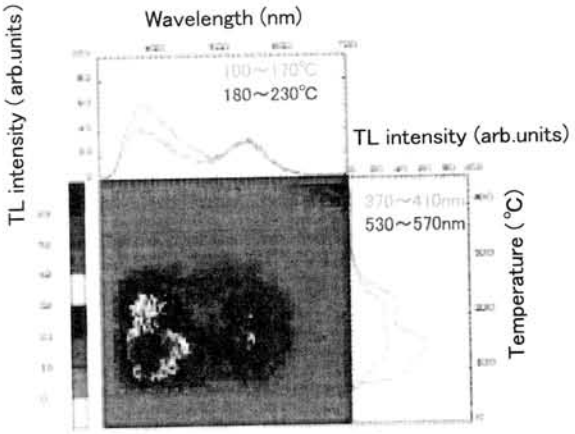

Figure 4-2. TL spectra of albite (Experimentally shocked at 10GPa)

Significance of Pb-Pb isochrons produced by stepwise dissolution of meteorites.

E. Jagoutz, G. Dreibus, R. Jotter, A. Kubny, R. Zartman
Max Planck Institut für Chemie Mainz Saarstrasse 23. jagoutz@mpch-mainz.mpg.de

A stepwise dissolution technique was applied to several nakhlite, angrite, and chondrite meteorites that were heavily contaminated by terrestrial Pb. Pulverized samples were subjected to three acid leaches of increasing strength followed by HF-HNO3 digestion of the remaining residue.

Leach 1 (L1): Ultrasonic in cold 0.02N HCl
Leach 2 (L2): Heat at 80° C
in 3N HCl for 4 hours.
Leach 3 (L3): Heat at 50°C
in 7N HNO3 and HF (7:3 ratio) for 2 hours
Residue (Res): Heat at 80°C in HF and 7N HNO3 (4:1 ratio) until completely dissolved.

Using this procedure the major portion of the terrestrial contamination was removed in Leaches 1 and 2, while essentially uncontaminated Pb was recovered in Leach 3 and the Residue. We give further details here about some of the insights gained from this improved ability to distinguish between the primary and terrestrial Pb components in meteorites.

A) Nakhlites: Firstly, we ran one sample of Nakhla as a test of the procedure. The result showed L1 and L2 to be mainly dominated by terrestrial Pb while L3 yielded Pb close to the initial Pb of other nakhlites. The Pb in the Res, however, was very radiogenic and had a 206Pb/204Pb relative to 207Pb/204Pb indicating a drastic increase of the U/Pb at 1.3 Ga. Furthermore, the relatively unradiogenic 208Pb/204Pb suggested that there might be zircon or other high U/Th mineral in the Res. An in-depth study with an electron microscope of a thin-did indeed reveal a number of tiny, 10m grains of baddeleyite. The same dissolution technique was then applied to other nakhlites from the Antarctic NIPR collection with similar results, indicating that all nakhlites may have the same age. In addition, an identical initial Pb isotopic composition indicates that all of these meteorites were derived from the same homogeneous source. Moreover, it is strongly suggested by their initial Pb that the "olivine shergotites", like SAU, DAG, Que, and Y, likewise come from this Nakhla source.

B) Angrites: The stepwise dissolution technique was applied to the angrite, D'Orbigny, and a detailed report on that study is being published elsewhere. We mention here only that the stepwise dissolution technique allowed us to determine a very precise isochron age of 4563 ±2 My based on whole-rock and pyroxene analyses.

C) Chondrites: Perhaps our main finding with chondrites analyzed by the stepwise dissolution technique is that they do not give simple results. Chondrites are essentially sediments containing a mixture of components of different ages and origin. However, there is a paradox in chondrites; i.e., although most chondrites are composed of fragments that are variable in their chemical composition, the whole rock chemical composition is amazingly uniform within a single meteorite and also among different meteorites. Analyzing individual fragments might thus give important information on localized processes, such as the time of chondrule and CAI formation. Alternatively, the whole-rock potentially contains isotopic information on more general processes, such as the fractionation of volatiles. From our work several generalities seem to be valid: (1) Some fragments have very low U/Pb and contain predominantly CD Pb (CD = Canyon Diablo Solar System initial Pb isotopic composition). (2) Many fragments with high U/Pb consist of a mixture of CD and radiogenic Pb in which the radiogenic Pb is mainly caused by the in situ decay of U. (3) In some samples, however, significant amounts of unsupported radiogenic Pb are also found, but often such Pb appears to be of terrestrial origin. (4) Only in a few cases of chondrite breccias have we observed disrupted U-Pb isotope systematics where open-system behavior has occurred at some intermediate time in the meteorite's history. Otherwise, variations in the U/Pb within the meteorite and between meteorites are almost exclusively caused by variation in the Pb concentration, while the U concentration is remarkably uniform. This variation in the Pb concentration, which correlates with other volatile elements, is caused primarily by variation in the concentration of CD Pb.

Fe-Ni metal and spinel group minerals in LL3 chondrites: Metamorphic conditions of highly primitive chondrites. M. Kimura[1], J. N. Grossman[2], M. K. Weisberg[3,4] and H. Nakajima[1], [1]Faculty of Science, Ibaraki University, Mito 310-8512, Japan, [2]US Geological Survey, 954 National Center, Reston, VA 20192, USA, [3]Department of Physical Sciences, Kingsborough College of the City University of New York, Brooklyn, NY 11235, [4]Department of Earth and Planetary Sciences, American Museum of Natural History, New York, NY10024, USA.

Introduction:

Unequilibrated ordinary chondrites are classified into petrologic types 3.0-3.9 [1]. Chondrites of lower types, especially 3.0, are important, because of their primordial isotopic compositions and petrologic features [e.g., 2,3]. However, mineralogical criteria used to distinguish the lowest types are not well established because mineral chemistry, especially of silicates, is not sensitive to metamorphism at low temperatures.

Grossman and Brearley [4] recently showed that the distribution of Cr in olivine changes systematically as metamorphism increases between type 3.0 and 3.2. Additionally, alkali elements are mobilized from the matrix and enter chondrules during the early stages of metamorphism. These metamorphic trends can be used to refine classification schemes for chondrites and to distinguish the most primitive ordinary chondrites. Cr distributions in olivine are a highly effective tool for assigning petrologic types, and can be used to divide types 3.0 and 3.1 into 3.00 through 3.15 [4].

In addition, Kimura et al. [5] showed that the chemical compositions of spinel group minerals are related to petrologic type in LL chondrites. Kimura and Weisberg [6] suggested that the characteristic features of Fe-Ni metal are highly sensitive not only to thermal metamorphism, but also to host chondrule chemistry.

Here we report the relationships between petrologic type and the characteristic features of spinel group minerals and Fe-Ni metal, in LL3 chondrites. Our goals are to explore the metamorphic conditions of the highly primitive chondrites.

Mineralogy of Fe-Ni metal and spinel group minerals:

After the method for olivine analysis by [4], we reclassified Y-74660 from LL3.0 to LL3.15. Including it, here we studied an LL3.00 (Semarkona), 1 LL3.15, 3 LL3.2, 1 LL3.3 and 1 LL3.5.

Fe-Ni metal occurs as spherical grains in chondrules, and as irregularly shaped grains on chondrule surfaces and as isolated grains in the matrix [6]. The texture of Fe-Ni metal in Semarkona depends on the occurrence; Chondrule metal typically shows a plessitic intergrowth (Fig. 1a), as noticed by [7], whereas metal on chondrule surfaces and as isolated grains always seems to be homogeneous and often shows an intergrowth of kamacite and Ni-rich metal. Fe-Ni metal in the other LL3 chondrites does not show plessitic intergrowth in any occurrence. Chondrule metal in LL3.15-3.5 chondrites typically shows an intergrowth of kamacite and Ni-rich metal (Fig. 1b).

The composition of Fe-Ni metal in Semarkona and Y-74660 depends on the occurrence: the metal in chondrules usually contains 1.3-50.6% Ni and 0.1-0.6% Co. On the other hand, metals on chondrule surfaces and as isolated grains are enriched both in Ni (51.2-68.5%) and Co (0.5-3.4%) (Fig. 2). In LL3.2-3.5 chondrites, all kamacite has a higher Co content than Ni-rich metal, in spite of its occurrence.

The abundance of spinel group minerals is lower in LL3 chondrites than in LL4-6 [5]. The average grain size in the samples is 11-17 μm, and is not related to petrologic type. However, the chemical compositions of spinel group minerals systematically change with type; The atomic Mg/(Mg+Fe) ratios range from 0.01 to 1.00 in types 3.0-3.3, and narrows to 0.04-0.61 in type 3.5. In types 3.00-3.3, nearly pure chromite (<0.5% Al2O3 and <0.5 MgO) occurs, typically as isolated minerals in the matrix, often in close association with Fe-Ni metal and troilite.

Discussion:

The composition and plessitic intergrowth of Semarkona metal are evidently distinct from those of higher petrologic type LL3 chondrites. Metal in Semarkona chondrules records the earliest stages of metal decomposition. Kimura and Weisberg [6] suggested that Semarkona metal, especially in chondrules, preserves primordial textural and chemical features, e.g., a positive correlation between Ni and Co. On the other hand, metal in the other chondrites was modified by metamorphism on the parent body. Y-74660 (LL3.15) partly lost its primordial features, e.g., it lacks plessitic intergrowth and has completely exsolved into high- and low-Ni phases. The intergrowth of kamacite and Ni-rich metal in chondrules of Y-74660 shows temperatures of 410-540°C, as calculated using the method of [8], which seems to be consistent with olivine-spinel geothermometry, much lower than 600°C, for some LL3.15-3.4 chondrites [9]. It is probable that LL3.15 chondrite experienced metamorphism under such low-temperature conditions.

Alexander et al. [10] suggested that the metamorphic temperature for Semarkona did not exceed 250°C. This is much lower than the temperature estimated for metal in LL3.15. Thus,

Fe-Ni metal is a sensitive indicator for the lowest grades of metamorphism. Semarkona is the most primitive, consistent with [4], and its metal and other minerals mostly preserve the primordial features before accretion to the parent body.

Despite the changes occurring in metal, the characteristic features, such as grain size and composition, of spinel group minerals remain unchanged in types 3.00-3.3. The differences between these minerals through petrologic types 3.00 to 3.3 may reflect differences in their diffusion rates; The diffusion rate for metal is much higher than that for spinel [11,12].

References: [1] Sears D.W. et al. (1980) Nature, 287, 791-795. [2] Kita N.T. et al. (2000) GCA, 64, 3913-3922. [3] Brearley A.J. and Jones R.H. (1998) in Planetary Materials, Mineral. Soc. America. [4] Grossman J.N. and Brearley A.J. (2005) Meteori. Planet. Sci., 40, 87-122. [5] Kimura M. et al. (2003) Meteori. Planet. Sci., 38, A33. [6] Kimura M. and Weisberg M.K. (2004) Meteorit. Planet. Sci., 39, A53. [7] Reisener R.J. and Goldstein, J.I. (1999) LPS XXX, Abstract #1868. [8] Afiattalab F. and Wasson J.T. (1980) GCA, 44, 431-446. [9] Johnson C.A. and Prinz M. (1991) GCA, 55, 893-904. [10] Alexander C.M.O. et al. (1989) GCA, 53, 3045-3057. [11] Dean D.C. and Goldstein J.I. (1986) Met. Trans. 17A, 1131-1138. [12] Freer R. and O'Reilly W. (1980) Mine. Mag., 43, 889-899.

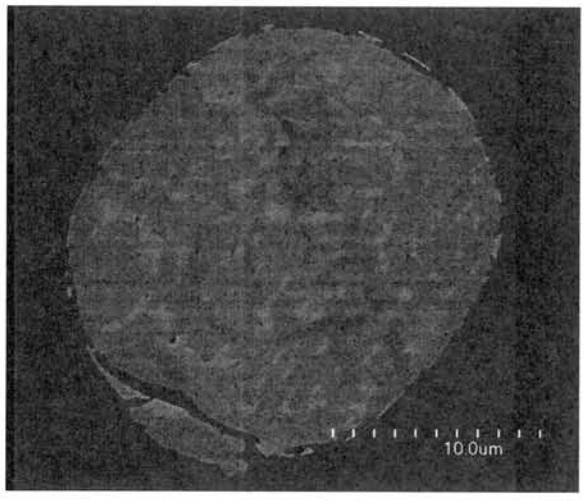

Fig. 1a. Metal spherule in chondrule of Semarkona (LL3.00), showing a plessitic intergrowth. Back-scattered electron image by FE-SEM. Width is 26 microns.

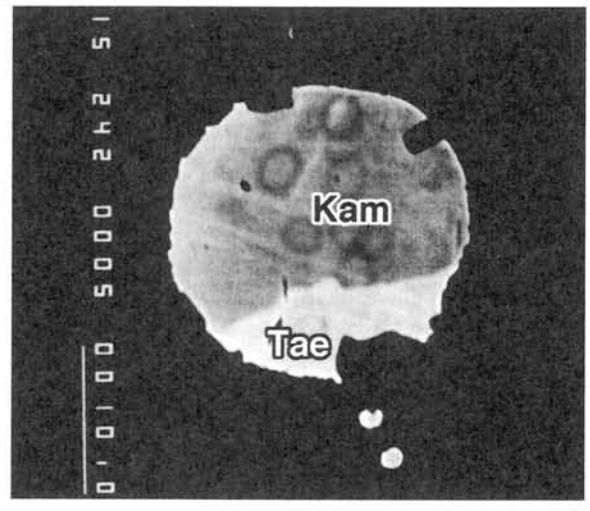

Fig. 1b. Metal spherule in chondrule of Y-74660 (LL3.15), showing kamacite-taenite intergrowth. Back-scattered electron image. Width is 40 microns.

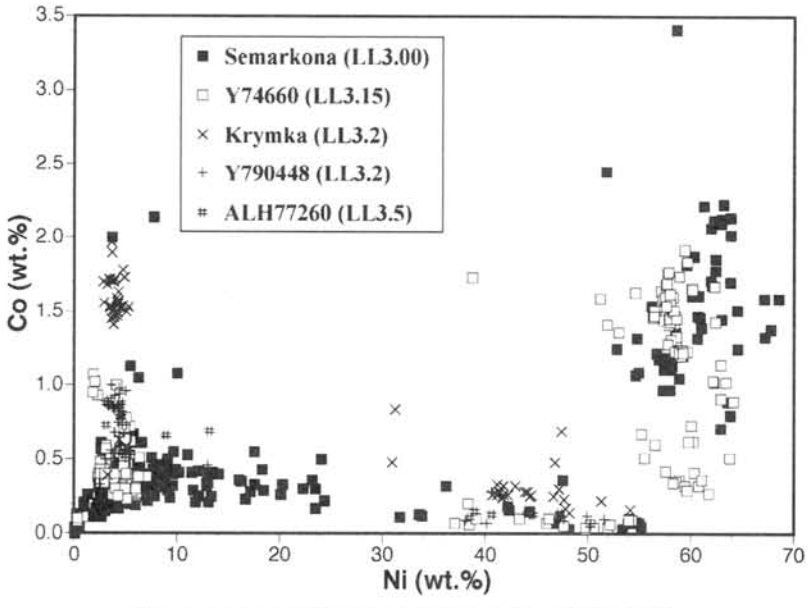

Fig. 2. Ni vs. Co plot of Fe-Ni metal in LL3.00-3.5.

Abundances of presolar silicates in primitive carbonaceous chondrites Yamato-81025, ALHA77307, ADELAIDE and ACFER 094. S. Kobayashi[1], A. Tonotani[1], N. Sakamoto[1], K. Nagashima[1], A. N. Krot[2], and H. Yurimoto[1], [1]Department of Earth and Planetary Sciences, Tokyo Institute of Technology, Ookayama 2-12-1, Meguro, Tokyo 152-8551, Japan. (sachio@geo.titech.ac.jp), [2]Hawai'I Institute of Geophysics and Planetology, School of Ocean and Earth Science and Technology, University of Hawai'i at Manoa, Honolulu, HI 06822, USA.

Introduction:

Recently presolar silicates were found in a few meteorites, Acfer 094 (ungrouped type 3), NWA 530 (CR2), Bishunpur (LL3.1) and Semarkona (LL3.0) [1-6]. Acfer 094 which is thought to be the most pristine chondrite represents the highest abundance of 176 ppm [6].

Some researchers suggest that there are some effects of alteration and metamorphism in matrix even in the petrologic subtype 3.0 chondrites [e.g., 7]. Therefore, it is unclear for the effect of alteration and metamorphism against the submicron order of presolar silicates even in type-3 chondrites.

In this study we report the presolar silicates from the least altered and metamorphosed carbonaceous chondrites, Y-81025 (CO3.0) [8], ALHA77307 (CO3.0) [9], Adelaide (ungrouped, linked to CO-CM) [10] and Acfer 094 (ungrouped, linked to CO-CM) [11], which there are some agreement that they are one of the most pristine chondrites [12].

Experimental:

The polished thin sections of Y-81025 (paired of Y-81020), ALHA77307, Adelaide and Acfer 094 were selected in this study. Petrography and mineralogy were studied using scanning electron microscope (JEOL JSM-5310LV) equipped with energy dispersive X-ray spectrometer (Oxford LINK ISIS).

Isotope images (isotopographs) were obtained by the TiTech isotope microscope (Cameca ims-1270 + SCAPS [13]). The analytical techniques are mostly same as [2] but different in several conditions. A 50 μm contrast aperture (CA) was used as well as a 150 μm one in order to obtain higher lateral resolution. Lateral resolution of isotopograph is ~1 μm by the 150 μm CA, and ~0.4 μm by the 50 μm CA. The Cs^+ beam of 0.3 nA was rastered over area of 75 x 75 μm^2 and image size is corresponding to ~60 x 60 μm^2 on the sample surface. The typical acquisition sequence for secondary ion images was $^{12}C^-$, $^{13}C^-$, $^{12}C^-$, $^{27}Al^-$, $^{28}Si^-$, $^{16}O^-$, $^{18}O^-$, $^{16}O^-$, $^{17}O^-$ and $^{16}O^-$ (150 μm CA used for C-isotopes and 50 μm CA for the others). Total integration time for one analysis was ~1 hour with sputtering depth of less than 100 nm. The digital image processing using a moving average of 3 x 3 pixels (corresponding to 0.6 x 0.6 μm^2) was applied to simple isotope ratio image (isotopograph) in order to reduce the statistical error. The scale of O-isotopograph is normalized to O isotopic compositions of each meteorite.

The selection criterion for isotopically anomalous presolar grain candidates is that the isotopic composition is 2σ away from 3σ ellipse of the distribution of the normal matrix materials.

Matrix-normalized abundances of presolar silicates are expressed as ppm and grain density (number of grains per analyzed area). The abundance is calculated assuming the grains are 0.3 μm in diameter that is an average size of presolar silicate grains reported to date.

Results:

Total analyzed areas, number of presolar silicate grains, abundance (ppm) and grain density for each meteorites are shown in Table 1. Three O-isotope diagram of presolar silicate grains is shown in Fig. 1. Numbers of 20, 8, 8 and 14 presolar silicates were identified in isotopographs (Fig. 2) of ~34,000 μm^2 (11 matrix areas), ~25,000 μm^2 (8 matrix areas), ~14,000 μm^2 (5 matrix areas) and ~166,000 μm^2 (40 matrix areas) for Y-81025, ALHA77307, Adelaide and Acfer 094, respectively. Matrix-normalized abundances of presolar silicates were respectively, calculated to be 53, 29, 51 and 8 ppm (assuming 0.3 μm in diameter).

Discussion:

The abundances of presolar silicates in the least metamorphosed and altered chondrites are ~10-55 ppm and are higher than those of most type of presolar phases. The high abundances of presolar silicates in these chondrites could be due to the nature of the least metamorphosed and altered chondrites. Among these chondrites, the abundance of presolar silicates in Y-81025 is the highest and is ~55 ppm. The second highest abundance is ~50 ppm in Adelaide and third is ~30 ppm in ALHA77307. Acfer 094 represents the lowest abundance of ~10 ppm among chondrites used in this study. The TEM studies of matrix materials in Acfer 094, Adelaide, and ALHA77307 suggest that the matrix in Acfer 094 largely escaped aqueous alteration and thermal metamorphism [11] and seem to be more pristine

than that of Adelaide [12]. The matrix of ALHA77307 seems to be more pristine than that of Adelaide [10] and has some similarities with that of Acfer 094 [10, 11]. Although Y-81025 has not been investigated by TEM, Y-81025 is probably more primitive than ALHA77307 based on the elemental distributions among matrix materials and opaque minerals [9]. Although the chondrites used in this study show slight differences of the degree of aqueous alteration and thermal metamorphism, such differences are inconsistent with the abundances of presolar silicates. The lowest abundance in Acfer 094 with most pristine matrix could exclude the possibility that the differences of presolar silicates between primitive chondrites resulted from destruction of presolar silicates by thermal metamorphism and aqueous alteration processes. The difference of the abundance of presolar silicates among the least metamorphosed and altered chondrites suggest that the presolar silicates were heterogeneously distributed among chondrite forming regions in the solar nebula.

The abundance of presolar silicates in Acfer 094 is estimated to be 130-176 ppm by recent NanoSIMS study [5, 6]. This contrasts with the abundance in this study. However, the discrepancy is likely to be systematic. If this is valid to estimate true abundances, the true abundance of presolar silicates should be more than ~18 times higher than that in this study. The true abundances of presolar silicates in Y-81025 may be more than several hundred ppm comparable to that of IDPs estimated from [14, 15].

References:

[1] Nguyen A. N. and Zinner E. (2004) *Science, 303*, 1496-1499. [2] Nagashima K. et al. (2004) *Nature, 428*, 921-924. [3] Mostefaoui S. and Hoppe P. (2004) *ApJ, 613*, L149-L152. [4] Mostefaoui S. et al. (2003) *Meteorit. Planet. Sci., 38*, A99. [5] Hoppe P. et al. (2005) *LPS, XXXVI*, Abstract#1301. [6] Nguyen A. N. et al. (2005) *LPS, XXXVI*, Abstract#2196. [7] Grossman J. N. and Rubin A. E. (1999) *LPS, XXX*, Abstract#1639. [8] Kojima T. et al. (1995) *NIPR, 8*, 79-96. [9] Brearley A. (1993) *GCA, 57*, 1521-1550. [10] Brearley A. (1991) *LPSC XXII, 22*, 133-134. [11] Greshake A. (1997) *GCA, 61*, 437-452. [12] Greshake A. et al. (2004) *Workshop on Chondrites and Protoplanetary Disk*, 9041. [13] Yurimoto H. et al. (2003) *Appl. Surf. Sci., 203-204*, 793. [14] Messenger S. et al. (2003) *Science, 300*, 105-108. [15] Floss C. and Stadermann F. J. (2004) *LPS, XXXV*, Abstract#1281. [16] Nittler L. R. et al. (1997) *ApJ, 483*, 475-495.

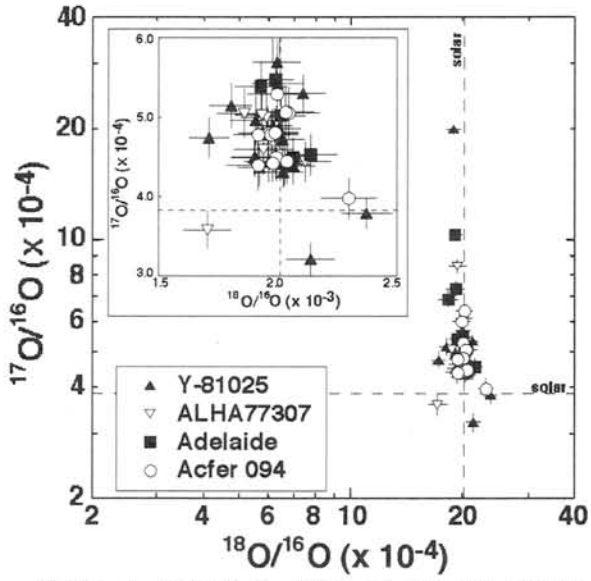

Figure 1. O-isotopic ratios of presolar silicate grains from Y-81025, ALHA77307, Adelaide and Acfer 094. Errors are 2σ. Inset figure shows the same data at an expanded scale around the solar O-isotope ratio. Note that inset figure is linear scale. O-isotopic ratios of presolar silicates represent similar distribution in different chondrites. Forty-six grains belong to group 1, one grain belongs to group 3, and three grains belong to group 4 grains of presolar oxide grains [16].

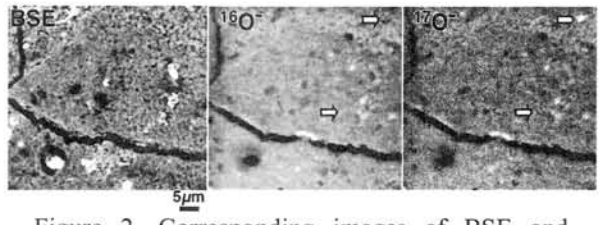

Figure 2. Corresponding images of BSE and secondary ion ($^{16}O^-$ and $^{17}O^-$). White allows indicate locations of presolar grains.

Table 1: Matrix-normalized abundances of presolar silicates.

Meteorite	class	Analyzed area (μm^2)	No. of silicates	Abundance (ppm)	Grain density (No./mm^2)
Y-81025	CO3.0	34,000	20	53	588
ALHA 77307	CO3.0	25,000	8	29	320
Adelaide	C-3 ungrouped	14,000	8	51	571
Acfer 094	C-3 ungrouped	166,000	14	8	84

Crystallization experiment on lunar mare basalt LAP 02205. E. Koizumi[1], J. Chokai[1], T. Mikouchi[1] and M. Miyamoto[1], [1]Dept. of Earth and Planetary Science, University of Tokyo, Hongo, Bunkyo-ku, Tokyo 113-0033, Japan. (koi@eps.s.u-tokyo.ac.jp)

Introduction:

LAP02205 (LAP) and its paired samples (02224/02226/02436/03632) are lunar meteorites recently discovered in LaPaz Ice Field in Antarctica. LAP is the largest mare-basalt meteorite with a total weight of 1.23 kg. Although most lunar meteorites are brecciated, LAP is a crystalline rock showing a basaltic texture, thus offering useful information to understand crystallization of lunar mare basalt. In this study, we performed crystallization experiments to investigate the formation history of this fifth lunar mare basalt. We also calculated its phase assemblages by using MELTS software.

Petrology and mineralogy:

LAP mainly consists of medium-grained pyroxene, plagioclase and olivine (Fig. 1a). There are abundant areas (~a few %) of mesostasis mainly composed of fayalite with Si-, K-rich glass, ilmenite, silica, Fe sulfide and apatite. This meteorite contains abundant plagioclase and does not show a cumulate texture. Therefore, it is likely that the bulk composition of LAP is close to its parent melt composition.

Most pyroxenes are subhedral and extensively zoned. The zoning pattern in a single grain is irregular, but the most inner core is usually pigeonite ($En_{55}Fs_{30}Wo_{15}$) and partly mantled by augite ($En_{40}Fs_{25}Wo_{35}$). Then, outer parts are zoned to nearly Mg-free compositions (some are probably pyroxferroite) (Fig. 2a). Olivine grains are rounded and up to 1 mm in size. They are usually present as clusters of a few grains. Olivine grains are zoned from Fo_{67} to Fo_{48} (Fig. 2a). LAP is similar to Apollo 12 ilmenite basalt with its texture, mineral phases and mineral composition [1].

MELTS calculation:

We calculated equilibrium mineral assemblages by the MELTS program [2] with the bulk composition of LAP [3] at the oxygen fugacity of $\log fO_2$=IW-1. According to the calculation results, the liquidus phase of this bulk composition is olivine at 1137 °C and its composition is Fo_{55}. This composition is more Fe-rich than the core composition of LAP. Then, olivine immediately disappears and pigeonite ($En_{53}Fs_{36}Wo_{11}$) starts crystallizing at 1134 °C. Plagioclase appears at 1123 °C. Spinel and augite ($En_{36}Fs_{28}Wo_{36}$) start crystallizing at 1109 °C and 1096 °C, respectively. Calculated compositions of both pigeonite and augite are similar to those of LAP, implying that both pyroxenes crystallized from the parent melt that has a similar composition to the bulk composition of LAP.

Crystallization experiment:

We prepared a starting material having the LAP bulk composition [3] and adopted our usual wire loop technique to perform crystallization experiment [4]. The charges homogenized at 1160 °C for 48 hours were cooled from 1160 °C to 1000 °C at various cooling rates (1, 2.5, 5, 10 and 20 °C/hr). We used CO_2-H_2 gas mixture to keep oxygen fugacity at IW-1.0 during the experiment.

Pyroxene, olivine, plagioclase, ilmenite and Fe-Ni metal crystallized in all cooling rate experiments, and their textures are generally similar to that of LAP (Fig. 1a-d). Only 20 °C/hour cooling experiment produced a very fine-grained texture clearly different from LAP.

The zoning sequences of pyroxenes from 1 °C/hr and 5 °C/hr experiments are most similar to that of LAP (Fig. 2b-c), although synthetic pigeonites have slightly different core compositions. Pyroxene from 1 °C/hr cooling experiment lacks in the Mg-rich pigeonite that is seen in LAP. However, magnesian pigeonite core is present in the pyroxene from 5 °C/hr cooling run. The pyroxene composition from the 20 °C/hr cooling run differs from those of slower cooling rate runs since pyroxene from 20 °C/hr cooling run has no low-Ca pyroxene at the Fe-rich rim (Fig. 2d).

The largest difference seen in experimental charges is olivine petrology. Although 5 °C/hr and faster cooling experiments crystallized abundant olivine, it was rare in the 1 °C/hr cooling run (Fig. 1b-d). The olivine compositions from faster cooling run products have wider ranges than that of 1 °C/hr cooling run as shown in Fig. 2b-d. Comparing with LAP, synthetic olivine compositions are more Fe-rich than that of LAP, which indicates that some olivine grains in LAP would be xenocrysts.

Implications for crystallization of LAP 02205:

As is suggested by MELTS and experimental crystallization, some Mg-rich olivines seem to be xenocrysts. However, it is also obvious that olivine is the liquidus phase of the LAP parent melt. We propose the following crystallization history. At first, small amounts of olivine were incorporated into the LAP parent melt as xenocrysts. During cooling, olivine phenocrysts started crystallizing. Some olivine would overgrew on xenocrysts. Olivine crystallization immediately ended and magnesian pigeonite started crystallizing. Then, crystallizing pyroxene is changed by augite. The MELTS calculation result suggests that plagioclase started crystallizing earlier than augite. However, textural features show the prior augite crystallization. This is probably due to the crystallization difficulty of plagioclase, and fast cooling would suppress the plagioclase crystallization. After the onset of the

plagioclase crystallization, Fe-rich pigeonite started crystallizing. The ilmenite texture suggests that ilmenite would crystallize prior to Fe-rich pyroxenes. Finally, the mesostasis formed to crystallize various late-stage phases (fayalite and Si-, K-rich glass).

The texture and mineral chemistry of LAP suggest fairly fast cooling history typical for lunar mare basalts. The olivine petrology and pyroxene composition from crystallization experiments show that LAP is most similar to the experiment of 5 °C/hr cooling. Olivine is the first phase appears in LAP melt during cooling, but it is not stable at the temperature at which pyroxene crystallizes. Results of crystallization experiments and MELTS calculation show that olivine would start melting after the onset of pyroxene crystallization, and it would be completely melted away under slow cooling condition. Therefore, LAP should have cooled fast enough to leave olivine without melting.

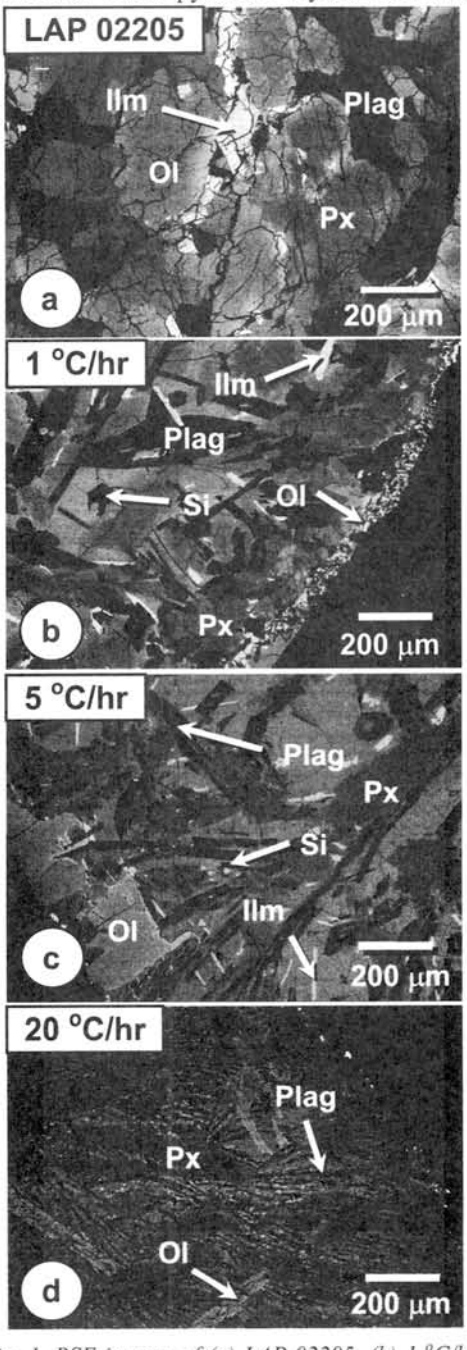

Fig. 1. BSE images of (a) LAP 02205, (b) 1 °C/hr cooling experiment, (c) 5 °C/hr cooling experiment and (d) 20 °C/hr cooling experiment . Ol: olivine, Px: pyroxene, Plag: plagioclase, Ilm: ilmenite, Si: Silica.

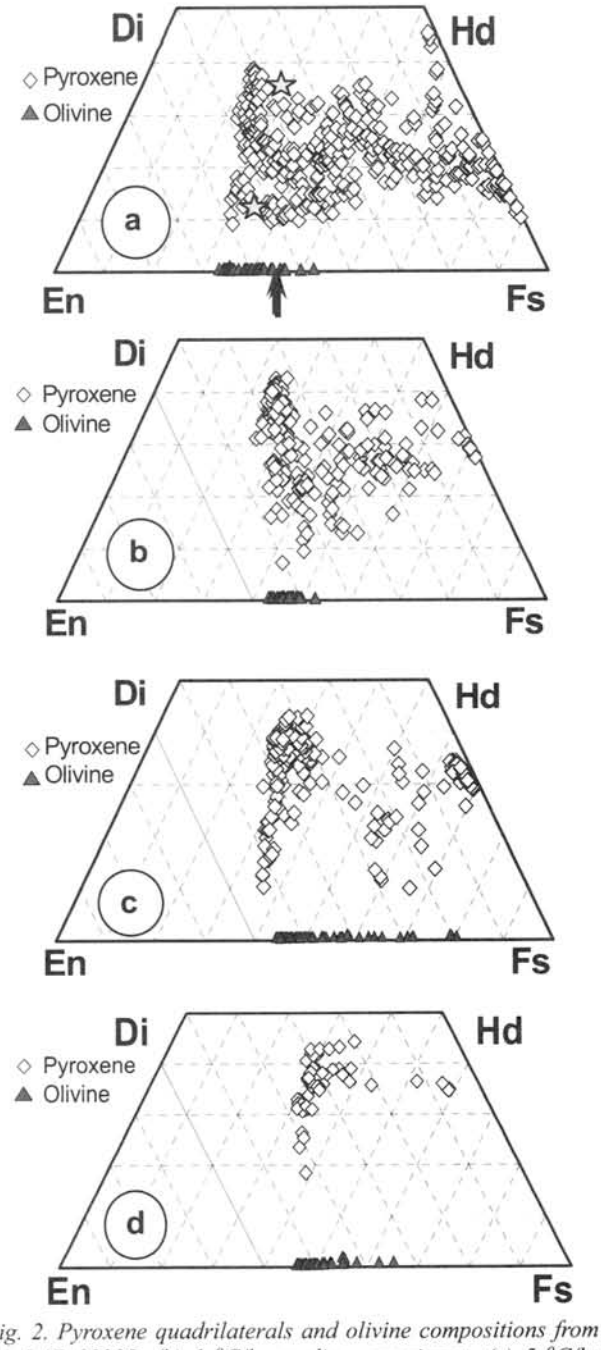

Fig. 2. Pyroxene quadrilaterals and olivine compositions from (a) LAP 02205, (b) 1 °C/hr cooling experiment, (c) 5 °C/hr cooling experiment and (d) 20 °C/hr cooling experiment. Arrow and Stars in (a) is the calculated compositions of liquidus olivine, pigeonite and augite by MELTS.

References:

[1] Mikouchi T. et al. (2004) *35th LPSC*, #1548. [2] Ghiorso M. S. and Sack R. O. (1995) *Contrib. Mineral Petrol,* 119, 197-212. [3] Anand M. et al. (2004) *35th LPSC*, #1626. [4] McKay G. et al. (1994) *GCA, 58*, 2911-2919.

Mineralogical study of amoeboid olivine aggregates with low-Ca pyroxenes in Y-81020.

M. Komatsu[1], A. N. Krot[2], M. Miyamoto[3], and K. Keil[2], [1]The University Museum, University of Tokyo, Japan (mutsumi@um.u-tokyo.ac.jp), [2]Hawai'i Institute of Geophysics & Planetology, SOEST, University of Hawai'i at Manoa, USA. [3]Department of Earth & Planetary Science, University of Tokyo, Japan.

Introduction: Amoeboid olivine aggregates (AOAs) are irregularly-shaped objects composed of fine-grained forsteritic olivine, minor Fe,Ni-metal, and a refractory component consisting of spinel, Al-diopside, anorthite, ±melilite. Although among other refractory inclusions, AOAs are mineralogically and chemically most similar to magnesian, olivine-rich (Type I) chondrules, they have lower contents of SiO_2, Cr_2O_3, MnO, and Na_2O, and generally lack low-Ca pyroxene. Recently, Krot et al. [1, 2] reported that ~ 10% of AOAs in primitive carbonaceous chondrites contain low-Ca pyroxene ($Fs_{1-3}Wo_{1-5}$). It is found in three major textural occurrences: (*i*) thin (<15 μm) discontinuous layers around forsterite grains or along forsterite grain boundaries in AOA peripheries; (*ii*) 5-10-μm-thick haloes and subhedral grains around Fe,Ni-metal nodules in AOA peripheries, and (*iii*) shells of variable thickness (up to 70 μm), commonly with abundant tiny (3-5 μm) inclusions of Fe,Ni-metal grains, around AOAs. Forsterite grains in AOAs with low-Ca pyroxene have ^{16}O-rich isotopic compositions ($\Delta^{17}O$ < -20‰). Low-Ca pyroxenes of the textural occurrences (*i*) and (*ii*) are ^{16}O-rich ($\Delta^{17}O$ < -20‰), whereas those of (*iii*) are ^{16}O-depleted ($\Delta^{17}O$ = -6‰ to -4‰). Based on these observations, Krot et al. [1,2] concluded that AOAs are aggregates of solar nebular condensates formed in an ^{16}O-rich gaseous reservoir, in the CAI-forming region(s). Solid or incipiently melted forsterite in some AOAs reacted with gaseous SiO in the same nebular region to form low-Ca pyroxene. Some other AOAs accreted ^{16}O-poor pyroxene-normative dust and experienced varying degrees of melting, most likely in chondrule-forming region(s). In order to understand the thermal history of AOAs with and without low-Ca pyroxenes, we performed the mineralogical and structural study of AOAs in the CO3.0 carbonaceous chondrite Yamato-81020, one of the most primitive CO chondrites [3], using electron back-scattering diffraction (EBSD) technique which can provide crystallographic information of micron-sized regions on the surface of a polished thin section.

Methods: Polished thin section of Y-81020 was studied in reflected and transmitted light using optical microscopy and mapped in Ca, Al, Mg, Ti and Na Ka X-rays with resolution of 5-10 μm (1 μm for individual AOAs) using the JEOL JXA 8900L electron microprobe. Mineral compositions were analyzed using JEOL JX-733 electron microprobe. A NORAN phase ID EBSD system and forescatter detector (VG system Japan Co.) attached to a HITACHI S-4500 scanning electron microscope (SEM) were used to analyze crystallographic orientation and grain-sizes of AOAs. In SEM, orientation contrast (OC) imaging in backscattered electron (BSE) mode is possible in mounting a solid-state BSE detector underneath the EBSD detector, i.e. in the forward-scattered position [4]. In the resulting image of the contrast is related to the orientation of the grain. By combining the orientation contrast images with EBSD patterns, individual grains were determined.

Results and discussion: AOA #1 is a compact object, 450×450 μm in size, composed of nearly pure forsterite ($Fo_{99.5-99.9}$), Fe,Ni-metal nodules, and a refractory component (Fig. 1). EBSD study shows that forsterite grains range in size from 2 to 20 μm (Fig. 2b). Forsterite grains are overgrown by porous Al-diopside (4-20 wt% Al_2O_3), which is 2-10 μm in width and 2-5 μm in length; it also forms discontinuous layers (< 1μm) around Fe,Ni-nodules. Occasionally, low-Ca pyroxene ($Fs_{1.3-5.1}Wo_{1.2-1.4}$) replaces forsterite around Fe-metal nodules. It is similar to the type (*ii*) of low-Ca pyroxene described in [1,2]. FeO-free spinel (< 5μm) is enclosed within fine-grained (2-10 μm) anorthite.

AOA #2 is an irregularly shaped object, 300×400 μm in size, consisting of forsterite ($Fa_{99.5-100}$), Fe,Ni-metal, and a refractory component. The outer portion of the AOA is replaced by low-Ca pyroxene ($Fs_{0.5-2.5}Wo_{2.9-9.7}$) (Figs. 1, 3a). The AOA probably belongs to the textural type (*iii*) of low-Ca pyroxene in AOA [1,2]. Fe,Ni-metal nodules are preferentially concentrated in low-Ca pyroxene. Occasionally, low-Ca pyroxene encloses fine-grained high-Ca pyroxenes (relict Al-diopside?) that are too fine-grained for microprobe analysis. EBSD study shows that individual low-Ca pyroxenes in this region are much smaller (< 1 μm) than those in other regions (2-10 μm; Fig. 3b).

AOA #3 is a compact AOA, 250×400 μm in size. AOA #3 consists of forsterite, irregularly shaped Al-diopside-anorthite-spinel inclusions, and FeNi-metal nodules. EBSD study shows that forsterite grains are ~10 μm. No low-Ca pyroxene was found in this AOA.

Our study shows that type (*i*) low-Ca pyroxenes in AOA #2 have relatively higher CaO content than those from other groups (CR, CV, CM, Acfer 094 and Adelaide) [1], while type (*ii*) low-Ca pyroxenes in AOA #1 and other minerals have similar composition to those from other groups. (Table 1) There are no mineral size differences in between AOAs with (AOA #1, #2) and without (AOA #3) low-Ca pyroxene. Krot et al. [1] concluded that some of the AOAs with low-Ca pyroxene experienced melting to a small degree. The presence of rounded Fe,Ni-metal nodules in low-Ca pyroxene of AOA #2 is consistent with this conclusion. We infer that AOAs with

low-Ca pyroxene may provide a link between AOAs and Type I chondrules. We note, however, that although low-Ca pyroxenes in AOA #2 are chemically similar to those in Type I chondrules (Fig. 4), they are much finer-grained than in chondrules (50-200 μm) and probably formed by gas-solid condensation.

References: [1] Krot et al. (2004) *GCA, 68,* 1923-1041. [2] Krot et al. (2004) *Chem. Erde, 64,* 185-239. [3] Chizmadia et al. (2002) *MAPS, 37,* 1781-1796. [4] Prior et al. (1996) *Mineral. Mag., 60,* 859-869.

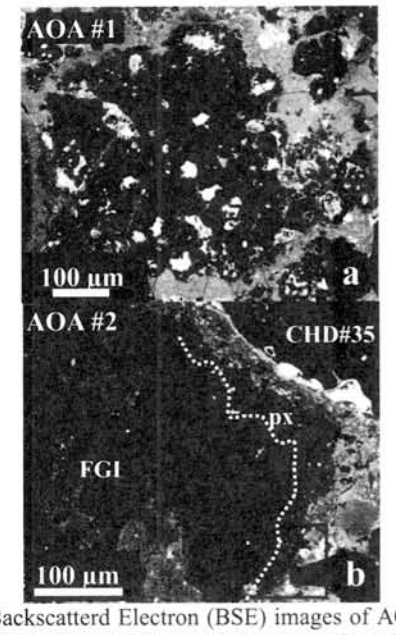

Fig. 1. Backscatterd Electron (BSE) images of AOA #1 (a) and AOA #2 (b). In AOA #2, the outer portion of the AOA is replaced by low-Ca pyroxene (px). Regions outlined in (a) and (b) are shown in detail in Fig.2 and Fig. 3, respectively. FGI – Fine-grained Ca,Al-rich inclusion.

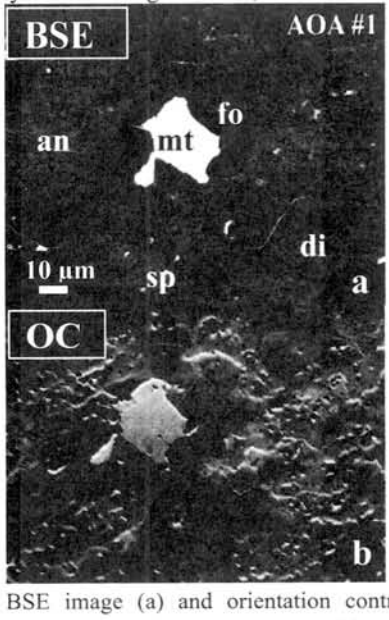

Fig. 2. BSE image (a) and orientation contrast (OC) image (b) of AOA#1. (a) AOA#1 consists of forsterite (fo), Al-diopside (di), spinel (sp), anorthite (an), and FeNi-metal (mt). (b)In the OC image, individual mineral grains with different crystallographic orientation have different contrast.

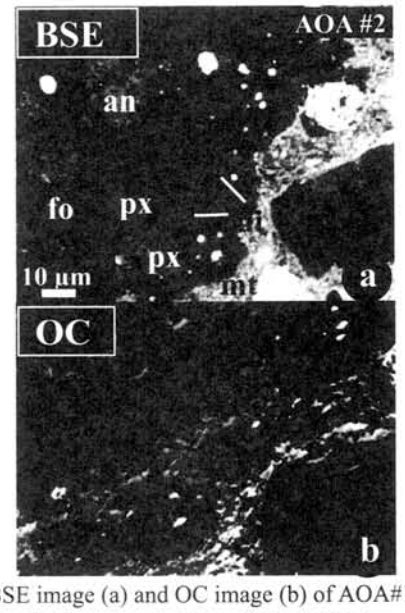

Fig. 3. BSE image (a) and OC image (b) of AOA#1. (a) Olivine in the outer portion of the AOA is replaced by low-Ca pyroxene (px). (b) Fine-grained low-Ca pyroxenes enclose tiny FeNi-metals and high-Ca pyroxenes.

Table 1. Representive electron microprobe analyses of minerals in AOAs and chondrules in Y 81020.

	AOA#1					AOA#2				AOA#3
	fo	px	cpx	an	sp	fo	px	px	cpx	fo
SiO_2	42.2	55.6	51.5	43.0	1.62	42.3	56.3	55.9	48.8	42.0
Al_2O_3	0.57	0.29	4.57	35.6	67.3	0.06	1.47	4.45	12.6	<0.03
TiO2	<0.09	0.17	1.23	<0.09	0.73	<0.09	0.56	0.28	0.79	<0.09
FeO	0.21	3.92	0.26	1.61	0.37	<0.08	0.71	0.02	0.73	0.16
MnO	0.09	0.07	0.08	<0.07	<0.07	0.39	0.46	0.69	0.17	<0.07
MgO	55.6	39.7	17.7	0.10	26.5	56.3	35.7	33.7	17.8	57.2
CaO	0.47	0.70	24.4	19.1	0.72	0.21	3.64	4.28	18.9	0.16
Na_2O	<0.06	<0.06	<0.06	<0.06	<0.06	<0.06	<0.06	<0.06	0.12	<0.06
K_2O	<0.04	<0.04	<0.04	<0.04	<0.04	<0.04	<0.04	<0.04	<0.04	<0.04
Cr_2O_3	0.13	0.33	0.16	0.03	1.85	0.50	0.79	0.76	0.27	0.08
total	99.3	100.8	100.1	99.8	99.5	99.8	99.7	100.2	100.2	99.6

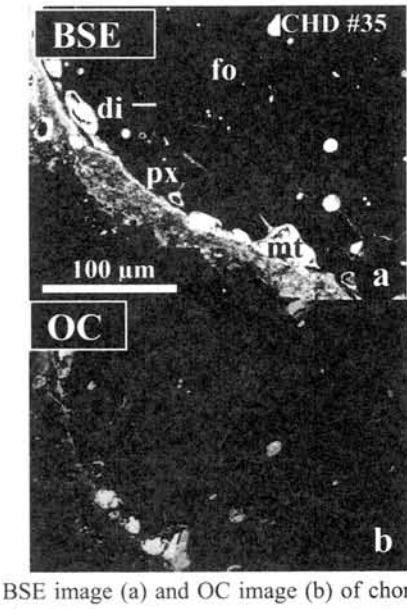

Fig. 4. BSE image (a) and OC image (b) of chondrule #35 from Y-81020. Low Ca pyroxene grains (px) are coarser than those in AOAs.

Re-evaluation of SMOW-scale for reporting oxygen isotopic ratios of silicate minerals and $^{17}O/^{16}O$ and $^{18}O/^{16}O$ ratios of some Antarctic meteorites.

M. Kusakabe[1], S. Maruyama[1], H. Kojima[2]. [1]Institute for Study of the Earth's Interior, Okayama University, Misasa, Tottori-ken 682-0193, Japan, [2]Antarctic Meteorite Research Center, National Institute of Polar Research, Tokyo 173-8515, Japan.

Re-evaluation of $\delta^{18}O$ value of NBS28 quartz:

NBS-28 quartz is often used as a reference for reporting oxygen isotopic composition of silicates and oxides. Its oxygen isotopic ratio has been assigned to 9.58‰ with respect to VSMOW based on the compilation of literature values [1]. However, individually reported values range from 8.8 to 10.0‰. This variability arises from different ways of fluorination using conventional or laser heating methods with BrF_5, ClF_3 or F_2 as a fluorination reagent. The choice of gas (CO_2 or O_2) for mass spectrometric measurement may also contribute to the variability. The VSMOW-SLAP scaling of the measured $\delta^{18}O$ values needs to be applied [1]. If oxygen isotopic ratio of CO_2 recovered from NBS-28 quartz is compared with that of CO_2 in equilibrium with VSMOW, the choice of variously reported fractionation factors between CO_2 and H_2O [2] affects the $\delta^{18}O$ value. To minimize such potential uncertainties, we directly compared oxygen isotopic ratios of O_2, liberated from silicate minerals using a laser fluorination technique with BrF_5 as a reagent [3], with those of O_2 from VSMOW prepared using the same fluorination line after minor modification for water analysis. The VSMOW-SLAP scaling was also taken into account. The $\delta^{18}O$ value of NBS-28 quartz was 9.30 ± 0.08 ‰ (n=18). $\delta^{18}O$ values close to 9.3‰ have been obtained for NBS-28 quartz by those who used O_2 as an analytical gas. The $\delta^{18}O$ values of the other international reference materials, i.e., NBS-30 biotite and UWG2 garnet were 5.01‰ (n=7), and 5.71‰ (n=85), respectively. Their $\delta^{17}O$ values were also measured with the analytical precision better than 0.1‰. The results plot on the terrestrial fractionation line approximated by $\delta^{17}O=0.511\times\delta^{18}O$, close to that defined by Clayton [4].

Oxygen isotopes of meteorites from Antarctica and other sources:

The oxygen isotopic ratios were measured for altogether ca. 100 meteorites from Antarctica and other sources (supplied by NIPR and individuals). The chondrite types include CM2 (4 samples), CO3 (8), H (6), L & LL (4), Enstatite (3), Rumuruti (2), CH (2), CK (3), CI (2), CR (1), Bencubin (1), and composite of CI and H (1). The achondrite types include SNC (12), HEDs(20), Aubrite (10), Ureilite (6), Lodranite (2), Angrite (1), CB (1), and Lunar achondrite (2). Replicate analysis was made for most of the samples with the reproducibility normally around ±0.1‰ for both $\delta^{17}O$ and $\delta^{18}O$, but much poorer for samples containing abundant hydrous minerals such as CM2-type meteorites with our laser-fluorination technique.

The results for the achondrites and chondrites are shown in Figs. 1 and 2, respectively. Most samples plot on the regions previously-known for various meteoritic types [4], confirming the classification based on the mineralogical and petrological observations. Willard (b), a brecciated ordinary chondrite (H3.5-3.6), contains clasts of carbonaceous chondrite. The $\delta^{17}O$-$\delta^{18}O$ features suggest that the clasts are of CI-type. Samples NWA-2035, -2335 and -2336 supplied by R. Bartoschewitz as CV3 do not plot close to the CO-CK-CM line but to the right of L & LL group slightly above the TF line. This is previously-unknown. Further studies are required.

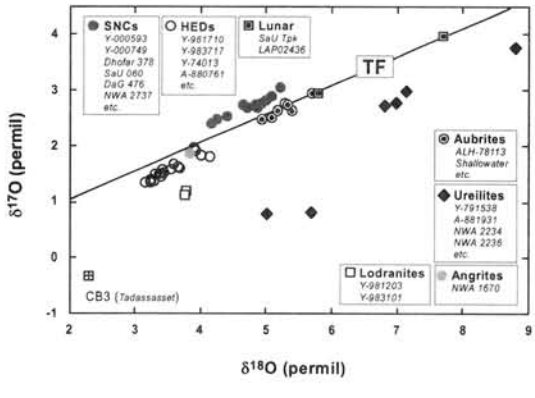

Fig. 1. A $\delta^{17}O$-$\delta^{18}O$ plot for achondrites from Antarctica and other sources.

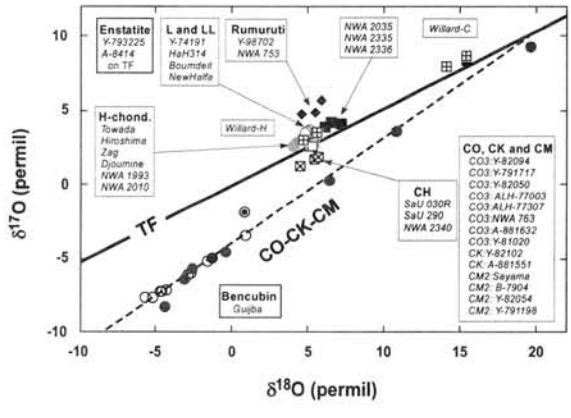

Fig. 2 A $\delta^{17}O$-$\delta^{18}O$ plot for chondrites from Antarctica and other sources.

References:

[1] Gonfiantini R., Stichler W. and Rozanski K. (1995) *IAEA-TECDOC-825*.

[2] Chako T., Cole D.R. and Horita J. (2001) *Rev. Mineral. Geochem.*, **43**, Chapt. 1.

[3] Kusakabe, M. et al. (2004) *J. Mass Spectrom. Soc. Jpn.* **52**, 205-212.

[4] ClaytonR.N. (1993) *Annual Rev. Earth Planet. Sci.* **21**, 115-149.

Origin of SNC meteorites. A. A. Marakushev, A. V. Bobrov, N. G. Zinovieva, and L. B. Granovsky, Department of Petrology, Geological Faculty, Moscow State University, Leninskie Gory, Moscow 119992, Russia

SNC meteorites (shergottites, nakhlites, and chassignites) are silicate achondrites principally different from widely abundant ordinary achondrites, such as howardites, eucrites, and diogenites (HED), not only by their limited abundance, but also by some other features (oxygen isotopes and age). HED meteorites are the oldest bodies of the solar system (4.6—3 Ga) being correlated with lunar rocks, in this respect, whereas SNC meteorites are relatively young with an age of 1.3—1.4 Ga (Shergotty, 1.34; Nakhla, 1.37; Chassigny, 1.39). Nakhlites (Yamato (Y) 000539, Y000749, Y000802) recently found in the Antarctic region were described in details in Antarctic Meteorite Research, 2003, No. 16. Additional data on Rb – Sr and Sm – Nd ages (~1.3Ga) were obtained for Y000593 meteorite; that provides evidence for relatively young age of the discussed family of meteorites. Based on this and the fact that ejection ages of nakhlites and Chassigny are the same, the authors [1] join the abundant opinion suggesting that all of nakhlites and Chassigny were ejected from Mars in a single impact cratering event" (p. 10). The main results of SNC meteorites studies are presented in the review by Yu.A.Shukolyukov [2], in which it is demonstrated that according to the composition of gases SNC meteorite have similarities with Martian atmosphere; that oxygen isotopic composition provides evidence for the formation of all SNC meteorites on the single, quite big parental body; that age of SNC meteorites excluding ALHA 84001 (3.9—4.3 Ga), is 180—1300 Ma.

Nowadays we may basically judge about Martian rocks by images of Mars surface, which provide no evidence for such a young age of Martian rocks. The southeastern part of Mars has relief analogous to the lunar one (Fig. 1) presented by old crust with numerous meteoritic craters and basaltic depressions (seas), more huge than on the Moon. To the north basaltic depressions are united in a big depression plate (it occupies the whole northwestern Mars hemisphere) where large volcanic uplifts (Olympus, Farsida and others) were formed. The images like Fig. 1 allow us to suppose that the oldest initial crust presented by leucocratic eucrites and partly replaced by basalts (similar to lunar ones) remained on Mars, as well as on the Moon. Analogously to lunar rocks and eucrites we may suppose the old age for Martian rocks (3—4 Ga) and, consequently, Mars could not be a source of SNC meteorites (1.3—1.4 Ga).

Relatively young achondrites might be genetically related to the Jupiter's system whose satellite Io has its own magnetic field and is endogenously active now. The outer part of the solar system (for example, Trojans family asteroids whose orbits are coincident

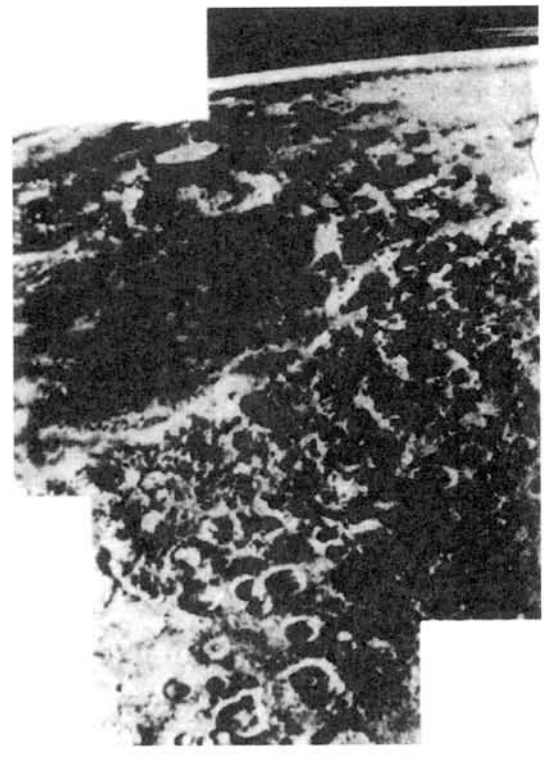

Fig. 1. The southern part of the Argir circle basin in Mars and its continental surrounding (view from the south-west). Image by Viking-1 [3]

with Jupiter's one) is the most likely to be the source of SNC achondrites. Trojans are divided almost equally in to two groups orbiting the Sun 60° ahead and behind of Jupiter and their position is controlled by so-called Lagrange points (Fig. 2). Jupiter partly degassed from its surface lost some satellites, which inherited its orbital motion around the Sun and formed the Trojans family. It is necessary to mention that the opinion about the Trojans origin at the expense of satellites lost by Jupiter was discussed in literature many years ago [5]. We consider the asteroid belt as a boundary dividing old (near-solar) iron-stony planets (4.6—3 Ga) and satellites from relatively young satellites of giants (less than 1.3 Ga) in the outer part of the solar system, the volcanism on which (Io) occurs nowadays.

According to the endogenous activity of Io the age of crystallization on it is relatively young, so that the origin of SNC achondrites at the expense of the Trojans asteroid family is well correlated with their age estimations [6].

Nakhlites being the most calcic types of achondrites crystallization of which starts with diopside and is

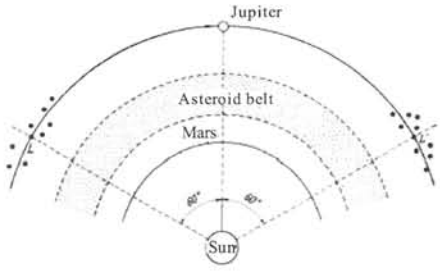

Fig 2. Relative position of the Sun and orbits of Mars and Jupiter. Lagrange points (L, L') on the Jupiter's orbit are located 60° ahead and behind of the planet. The Trojans family is divided in to two groups, accordingly [4]. This family is a source of the youngest (1.3 Ga) achondrites (shergottites, chassignites, and nakhlites)

accompanied by effective fractionation are the best studied among SNC meteorites.

Acknowledgments:

This work was supported by the Program "Support of Scientific School", grant 1301.2003.5, and the Program "Universities of Russia - Basic Researches" (grant 09.02.601).

References:

[1] Misawa K. et al. (2003) *Antarctic Meteorite Res., 16,* 1–12. [2] Shukolyukov Yu. A. (2003) *Geokhimiya, 11,* 1139-1171. [3] Sidorov Yu. I. and Zolotov M. Yu. (1989) *Porody i grunt poverkhnosti Marsa.* Moscow, Nauka-press, 222 p. [4] King E.A. (1976) *Space Geology*, John Wiley&Sons, Inc., New York – London – Sydney – Toronto. [5] Rabe E. (1954) *Astron. Jour., 59,* 433–439; [6] Marakushev A.A. et al. (2003) *Kosmicheskaya Petrologiya.* Moscow, Nauka-press, 387 p.

The Europium Oxybarometer: Can It Be Applied to Nakhlites? G. McKay[1] and C. Schwandt[2], [1]Mail Code KR, NASA Johnson Space Center, Houston, TX 77058, [2]ESC Group, NASA Johnson Space Center.

Introduction: One of the most important characteristics of a planet is the oxidation state of its mantle, as reflected in primitive basalts. On Mars, correlations have been reported between oxidation states and trace element and isotopic systematics of Martian basaltic meteorites [e.g., 1]. Thus, it is essential to the oxidation state of these samples in as much detail as possible to verify these correlations.

Petrologists have devised several methods to estimate the fO_2 under which basalts crystallized. One method that has been the subject of recent interest involves the depth of the Eu anomaly in early crystallizing minerals. This technique provides an additional means of estimating oxygen fugacity. With precious samples such as Martian meteorites, it is desirable to apply as many tools as possible.

History of the Eu Oxybarometer: Philpotts [2] first suggested that the depth of Eu anomalies reflected redox conditions. Drake [3] was the first to calibrate this oxybarometer through experimental measurement of plagioclase/melt partition coefficients, and Weill *et al.* [4] formulated a theoretical model for the expected variation of D(Eu, mineral/liquid) with fO_2.

McKay *et al.* [5] noted that the ratio of partition coefficients, e.g., D(Eu, Px/L)/D(Gd, Px/L), is less susceptible to variations in phase composition (e.g., Al content of pyroxene or melt) than are individual partition coefficients. Consequently, they recast the formulation of [4] in terms of partition coefficient ratios. They further noted that if two minerals are present that were both in equilibrium with the same liquid, the formulation could be further recast as the ratio of partition coefficients between the two minerals, thus eliminating the liquid. This is a major advantage because the REE concentrations in the parent melt of a sample are rarely known with certainty.

Experimental Calibration: In the formulation of [5], D(Eu/Gd) for a mineral varies along S-shaped curves that approach $D(Eu^{+2})/D(Gd)$ at low fO_2 and $D(Eu^{+3})/D(Gd)$ at high fO_2 (Fig. 1). The symbols in Figure 1 are experimentally determined plagioclase/melt and pyroxene/melt partition coefficient ratios (D(Eu/Gd)) measured in a system with the bulk composition of angrite LEW 86010 [5]. The curves are least-squares fits of model parameters to the observed data.

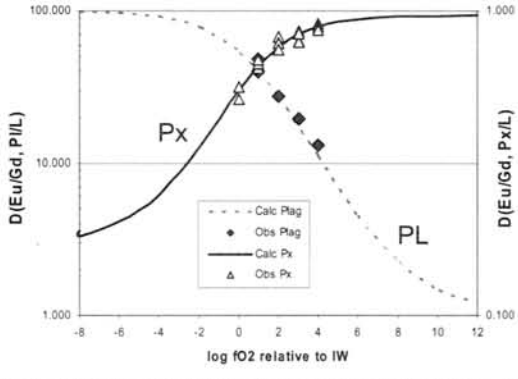

Fig 1. Calibration of D(Eu/Gd) for angritic plagioclase and pyroxene from [4].

Application to Angrites: McKay *et al.* [5] combined the curves in Fig. 1 with analyses of plagioclase and fassaite [6] to solve for the fO_2 of LEW. They concluded that LEW crystallized at log fO_2 of ~IW+1, more than two log units higher than eucrites [7]. This was the first time experimental calibrations of the Eu oxybarometer were combined with SIMS analyses of near-liquidus minerals to yield reliable quantitative oxygen fugacities.

LEW provided an ideal situation for applying the Eu oxybarometer. Experimental studies indicated that fassaite and plagioclase were near-liquidus phases. Moreover, the REE abundances in both phases indicated they were in equilibrium. Thus, the ratio of Eu and Gd between the two near-liquidus phases could be used to estimate the oxygen fugacity without uncertainties involved in estimating the Eu and Gd abundances in the coexisting melt.

Application to Shergottites: Using the pyroxene calibrations of [4], Wadhwa [1] applied the Eu oxybarometer to basaltic shergottites. Because melt composition could not be directly determined, she assumed (1) that the REE content of the bulk rocks approximated that of the melts and (2) that the pyroxene cores that she analyzed by SIMS were in equilibrium with those melts. She concluded that the fO_2 under which shergottites crystallized ranged from ~IW-1 to ~IW+2, suggesting a ~3 log unit range of oxidation states for basalt source regions on Mars. However, estimated fO_2s from this technique were 1-2 log units lower than those estimated from oxide compositions [8], although both techniques agreed on the magnitude of the variation.

Application to Nakhlites: Recently, Wadhwa et al. [9] applied the Eu oxybarometer to several nakhlites. They observed D(Eu)/D(Gd) ratios in pyroxenes that were similar to those in the nakhlite experiments of Oe *et al.* [10] run near QFM. Thus, these results suggest that Nakhlites came from much more oxidized source region than basaltic shergottites.

Two important assumptions are involved in the above conclusion: (1) Eu/Gd in the parent melt from which the nakhlite cumulus pyroxenes crystallized is the same as that of the whole rock. Close parallelism between the REE patterns calculated from pyroxene cores and those observed for the whole rock supports this notion. (2) The experimental D(Eu/Gd) ratios of [10] are applicable. However, there are two shortcomings with the experimental data. First, Eu partition coefficients were measured at only one fO_2, so that it is not possible to determine the sensitivity of D(Eu/Gd) to changes in fO_2. Hence, although it is

possible to estimate that the nakhlites formed near QFM, the uncertainties in this estimate are unknown. Second, a recent study by Prowwatke and Klemme [11] indicates that D(Sr/Gd), and by inference D(Eu/Gd), might be very sensitive to melt Al content.

For titanite/melt, they noted a strong correlation of trivalent D(REE) values with melt Alumina Saturation Index (ASI, molar $Al_2O_3/(Na_2O+K_2O+ CaO)$, a measure of the degree to which a melt is polymerized) [11]. Significantly, they observed much less correlation of monovalent, divalent and quadravalent trace elements with ASI. Thus, as ASI increased, the observed value of D(Sr)/D(Gd) decreased. Insofar as Sr is a proxy for Eu^{+2}, the magnitude of the Eu anomaly in the titanite would also change with melt composition, even when the Eu^{2+}/Eu^{3+} ratio remains constant. Thus changes in ASI affect the activity of REE in the melt. Hence these results would also be applicable to pyroxenes. In fact, we have also seen the effect of melt Al on D values for trivalent REE in our experimental studies (Fig. 2).

The most straightforward way to overcome this potential problem is to perform D(Eu/Gd) calibration experiments using an appropriate melt composition. Oe *et al.* al [10] used the estimated nakhlite melt composition of Kaneda *et al.* [12], which was derived to produce pyroxenes having major element and Al contents as those in nakhlites. However, all nakhlites known at that time had patchy, bimodal Al distributions (Fig. 3). In contrast, our recent work on the newest Antarctic nakhlite MIL 03346 [13] has shown that its cumulus augites, while similar in most respects to those of all other nakhlites, have homogeneous Al distributions.

Fig. 3 shows Al maps of MIL and Yamato000593. There are clear differences in the homogeneity and zoning patterns of Al in the cumulus pyroxenes. Histograms of Al contents in MIL and Nakhla clearly show a single mode in the former and a bimodal distribution in the latter. The origin of the Al zoning seen in Nakhla and Y000593, and the reason why it is absent in MIL are not known. MIL is the most rapidly cooled nakhlite [e.g., 13]. Could the Al zoning be a secondary feature associated with slower cooling? The Al content of the nakhlite parent melt used by Oe to measure REE partition coefficients is heavily dependent on the Al content of Nakhla pyroxenes. If the higher Al content seen in MIL pyroxenes more accurately reflects the true Al content of the nakhlite parent melt, then the composition used by Oe is significantly too low in Al. This, in turn, could have an important effect on D(Eu/Gd) based on Fig. 2 and the results of [11]. Until the origin of the Al variations in Figs. 3-4 is understood, we are no longer confident that the Al content of the melt that Oe *et al.* [10] used to measure REE partition coefficients for Nakhla is appropriate, and hence that the D(Eu/Gd) calibration are directly applicable to nakhlites.

Summary: The Eu oxybarometer offers a potentially useful way to measure the fO_2 that prevailed during the crystallization of the cores of liquidus minerals in basaltic rocks. It is less influenced by post-magmatic processes than the more commonly used oxide oxybarometer. It has been successfully applied to angrites and shergottites. However, recent results suggest it may be sensitive to melt Al content. Moreover, study of the new nakhlite MIL calls into question our understanding of Al zoning in nakhlite pyroxenes, and may render our previously estimated nakhlite parent melt composition (and thus our calibration of D(Eu/Gd)) invalid. Until further experimental studies resolve these issues, the conclusion that nakhlites formed near QFM [9] may be suspect.

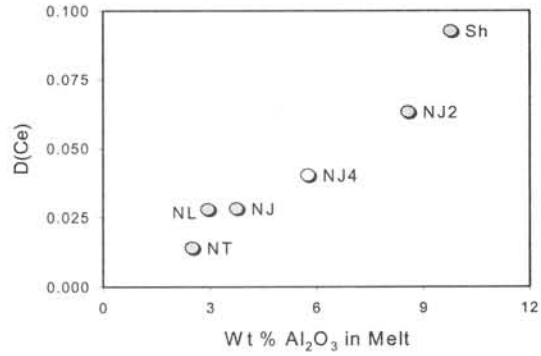

Fig.2. Variation of D(Ce, pyroxene/melt) with melt Al for a variety of experimental Martian melt compositions. Data from [10].

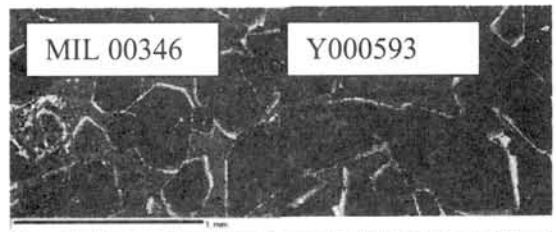

Figure 3. Al maps of pyroxenes in nakhlites MIL 03346 and Yamato 000593. Former has homogeneous Al distribution while latter has bimodal distribution.

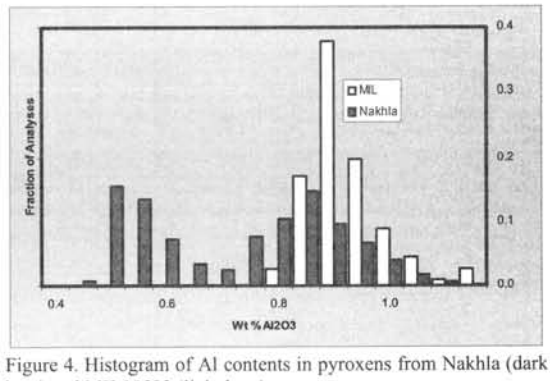

Figure 4. Histogram of Al contents in pyroxens from Nakhla (dark bars) and MIL00593 (light bars).

References: [1] Wadhwa (2001) Science 291, 1527. [2] Philpotts (1970) EPSL 9. 257. [3] Drake (1972) PhD Thesis, University of Oregon. [4] Weill *et al.* (1974) PLPSC 5th, 1337. [5] McKay *et al.* (1994) *GCA* 58, 2911. [6] Crozaz and McKay (1990) EPSL 97, 369. [7] Stolper (1977) *GCA* 41, 587. [8] Herd *et al.* (2002) GCA 66, 2025. [9] Wadhwa *et al.* (2004) AMR 17, 97. [10] Oe *et al.* (2001) LPSC 32, #2174. [11] Prowatke and Klemme (2005) GCA 69, 695. [12] Kaneda *et al.* (1998) LPSC 29, #1944. [13] McKay and Schwandt (2005) LPSC 36, #2351.

On the relationship between mineralogical characteristics and relative burial depths of nakhlites. T. Mikouchi[1], E. Koizumi[1], Y. Ueda[1], M. Miyamoto[1] and G. McKay[2], [1]Department of Earth and Planetary Science, Graduate School of Science, University of Tokyo, Hongo, Bunkyo-ku, Tokyo 113-0033, JAPAN (E-mail: mikouchi@eps.s.u-tokyo.ac.jp), [2]Mail Code KR, NASA Johnson Space Center, Houston, TX77058, USA.

Introduction:

For decades, there were only three known nakhlite samples, Nakhla (Nak), Governador Valadares (GV) and Lafayette (Laf). However, in the last several years recovery of thousands of meteorites from hot and cold deserts yielded four new nakhlite samples, NWA817 (NWA), NWA998, Y000593 (Y), and MIL03346 (MIL) [1]. Before these new samples were found, Harvey and McSween [2] proposed that Nak, GV and Laf were closely related to each other, undergoing various degrees of late-magmatic and subsolidus atomic diffusion due to different burial depths in a common cooling cumulate pile. Their identical crystallization (1.3 Ga) and ejection (10-11 Ma) ages also indicate that they originated from the same igneous body on Mars [3]. An interesting question is whether newly discovered samples can fit into this picture, even though they were recovered from different locations around the world. We studied the mineral characteristics of all nakhlites except NWA998 to determine whether they can all be related by varying burial depths in a common igneous body.

Petrographic variation:

All the nakhlites studied show an unbrecciated cumulate texture with ~75-90% augite and minor olivine set in the intercumulus groundmass (or mesostasis). The modal abundances of these three phases show slight variations from one sample to another. The abundance of the groundmass is the most variable. In Laf, Nak, and GV, the groundmass abundance is about 7-8%. Y has a slightly higher abundance of 10% and NWA and MIL have much higher abundance of 20-24%. The texture of the groundmass is related to its abundance. The groundmass of Laf, Nak, and GV is mainly composed of lathy feldspar grains (~50 μm wide). In contrast, NWA and MIL have glassy mesostasis with few or no feldspar crystals. In the latter two samples, skeletal titano-magnetite is the most abundant crystalline phase in the mesostasis with minor amounts of pyroxene and olivine. The groundmass of Y is similar to that of Laf, Nak, and GV, but plagioclase laths are thinner (~20 μm wide).

We find little difference in augite petrography among all the nakhlites studied. Augite is present as a polysynthetically twinned prismatic grains up to 1.5 mm long. Olivine abundance varies from one sample to another. MIL has the smallest olivine abundance (4%), but the relationship to the abundance of other phases is not clear. For example, Nak itself has a variation in olivine abundance (5-10%) from one thin section to another.

Mineral compositional variation:

Augite grains in all samples have an identical core composition ($En_{39}Fs_{22}Wo_{39}$). The cores are large and there are thin Fe-rich rims where augite grains abut groundmass or mesostasis. The degree of chemical zoning towards the Fe-rich rims varies from one sample to another in spite of the identical core composition (Fig. 1). In Laf, GV, Nak, Y and NWA, the interior portions of the Fe-rich rims have a fairly uniform Wo content, but the Wo contents drop at the outer edge of the grain. We found fine exsolution lamellae (~1 μm) of pyroxene at these edges except for NWA. Laf has the most Mg-rich edge composition, and Nak and GV have identical, but slightly more Fe-rich edge compositions. NWA has the most Fe-rich edge composition and Y is intermediate between Nak/GV and NWA. In contrast, MIL shows a qualitatively different zoning pattern from the others. In MIL, the Fe-rich edge is zoned to hedenbergite composition (Fig. 1). No exsolution lamellae were observed at the edge.

Olivine grains in all samples except Laf show extensive chemical zoning whose degree is clearly related to the zoning patterns in pyroxenes. MIL and NWA have the widest compositional ranges (Fa_{54-93}, Fig. 2). Y shows a similar but slightly narrower compositional range (Fa_{58-85}). Nak and GV have even narrower ranges (Fa_{58-72}), while Laf has quite homogeneous olivines (Fa_{68}). Olivines in Nak, GV and Y are also different from other samples in the presence of symplectic exsolution lamellae.

Calculated burial depths:

Chemical zoning of nakhlite olivines is useful to estimate cooling rates of these cumulate rocks. Mikouchi and Miyamoto [4] calculated cooling rates and burial depths of Nak, GV, Laf and NWA by using Fe-Mg and Ca chemical zoning profiles in the temperature range of 1100-700 °C. It is assumed that the original composition was homogeneous (Fa_{54}) as represented by the core of NWA olivine. The obtained burial depths are 1-2 m for NWA, ~10 m for Nak and GV, and >30 m for Laf. The cooling rate of Y has not been calculated, but it would be intermediate between NWA and Nak/GV, because the degree of chemical zoning is intermediate between them. MIL is similar to NWA in olivine zoning, suggesting a similar shallow burial depth, essentially at the Martian surface.

Relationship between mineralogical characteristics and burial depth:

The burial depth of each nakhlite, obtained from chemical zoning in olivine, is clearly related to the other mineralogical characteristics of that sample as described in the previous sections. If we consider that gravitational settling played a significant role in this igneous body, cumulus phases should have been more densely packed in deeper areas. This could produce loose cumulus framework for shallower samples, forming abundant groundmass or mesostasis areas. This is consistent with the observation that the shallower samples such as NWA and MIL have higher mesostasis abundances. The glassy nature of mesostasis in NWA and MIL is also consistent with fast cooling of the intercumulus melt. In contrast, the groundmass of deeper samples (Y, Nak, GV and Laf) contains crystalline feldspar grains consistent with slow cooling at depth. The degree of chemical zoning of pyroxene also varies systematically with the relative cooling rates inferred from olivine, supporting the idea that chemical zoning in pyroxene was produced by interaction between cumulus grains and evolved intercumulus melts [2,5]. Thus, all studied nakhlites appear to fit a scenario wherein they are samples of a single cumulus pile whose cumulus crystals are loosely packed near the surface and become more closely packed with increasing depth (Fig. 3). Hence nakhlites represent an excellent sampling of different depths within a Martian cumulate igneous body that has been suggested to lie within Syrtis Major [6].

References:

[1] Meyer C. (2004) *Mars Meteorite Compendium* (http://wwwcurator.jsc.nasa.gov/curator/antmet/mmc/mmc.htm) [2] Harvey R. P. and McSween H. Y. Jr. (1992) *GCA, 56*, 1655-1663. [3] McSween H. Y. Jr. (2002) *Meteorit. Planet. Sci., 37*, 7-25. [4] Mikouchi T. and Miyamoto M. (2002) *LPS XXXIII*, Abst. #1343. [5] Mikouchi T. et al. (2003) *AMR, 16*, 34-57. [6] Harvey R. P. and Hamilton V. E. (2005) *LPS, XXXVI*, Abst. #1019.

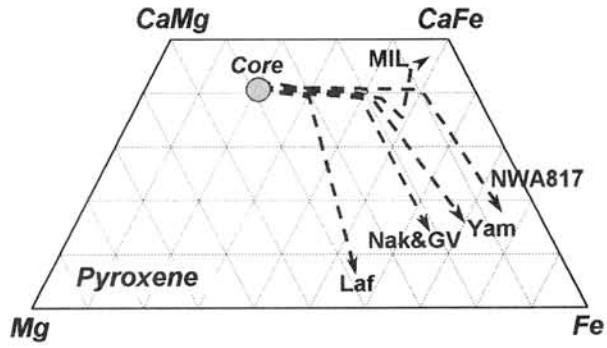

Fig. 1. Chemical zoning of pyroxenes in nakhlites plotted onto pyroxene quadrilateral. MIL pyroxene shows different zoning trends from others.

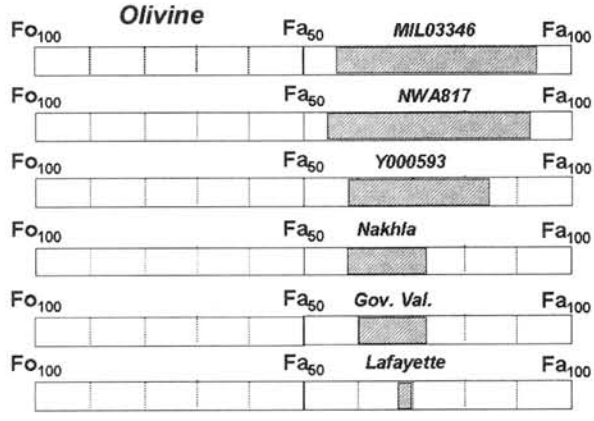

Fig. 2. Compositional variation of olivines in nakhlites. Olivines in MIL and NWA show much wider compositional ranges than others, and the most Fe-rich olivine is $Fa_{>90}$. Laf olivine is the only sample showing homogeneous composition.

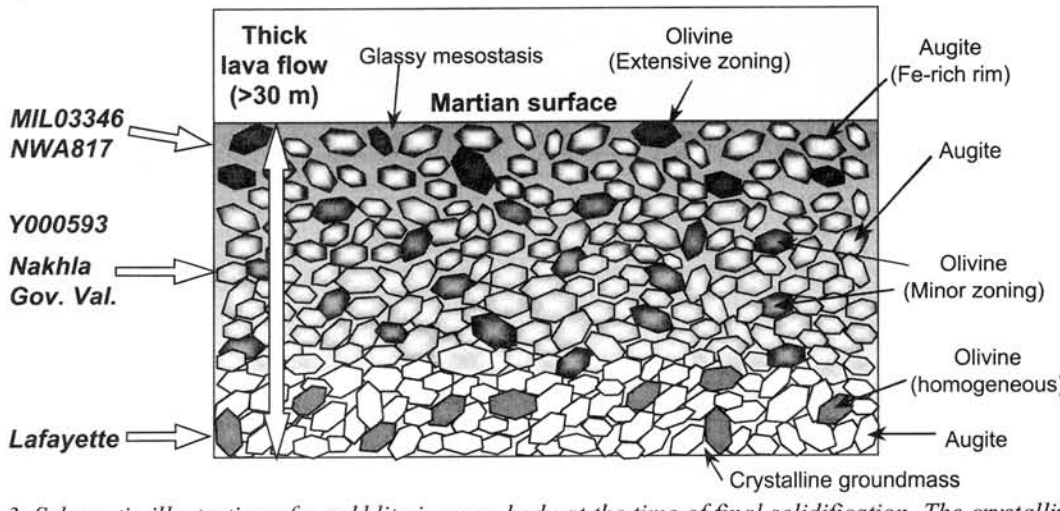

Fig. 3. Schematic illustration of a nakhlite igneous body at the time of final solidification. The crystallization should have occurred at 1.3 Ga. The burial depths are 1-2 m for MIL and NWA, ~10 m for Nak-GV and >30 m for Laf. Y is intermediate between MIL-NWA and Nak-GV, but would be closer to Nak-GV.

Zr/Hf fractionation during crystallization of basaltic eucrites: Implication for U-Pb isotopic systematics of eucritic zircons. K. Misawa, A. Yamaguchi and H. Kaiden Antarctic Meteorite Research Center, National Institute of Polar Research and Graduate University of Advanced Studies, Tokyo 173-8515. (misawa@nipr.ac.jp)

Introduction: Zircon could have formed late in the sequence of crystallization of basaltic eucrites, and is one of the most refractory minerals that incorporates U into its crystal structure and strongly excludes Pb. Several previous studies have analyzed the U-Pb isotopic systems of zircons from a variety of basaltic eucrites using ion microprobes and obtained old ages of ~4.55 Ga [1-10]. However, the implications of these data for the duration of volcanism and thermal metamorphism on the eucrite parent body (EPB) were not discussed in detail. In this study we focused on the Zr/Hf ratios of zircon and examined whether the obtained U-Pb ages of zircon reflect basalt formation or subsequent thermal metamorphism.

Experimental: We have studied sixteen samples of eucritic materials, including unmetamorphosed (Y74159, Y75011 and Y82210), metamorphosed (Y790266, Y794016, Y792150, Y82066, Juvinas and Stannern), highly metamorphosed (Y86763, A881388 and A881467) and highly shocked (Padvarninkai) eucrites. Hf contents of eucritic zircons were determined by EPMA using the Lα peak. An accelerating voltage of 15 kV, a beam current of 30 nA and integration time of 60 seconds were used for all samples. Repeated analysis of Hf in zircon 91500, from an Ontario syenite, before and after the sessions was 0.608 ± 0.061 wt.% (n = 13, error represents 1σ), which is consistent with the recommended value of Hf = 5895 ppm determined by IDMS [11].

Hf abundance in eucritic zircon: Eucritic zircon commonly contains a certain amount of Hf. The Hf contents of zircons in basaltic eucrites analyzed range from 0.54 wt.% to 1.43 wt.%. There are no systematic correlations between metamorphic grades and Hf abundances in zircon. Padvarninkai zircons have a relatively narrow range of Hf abundances (1.06-1.31 wt.%).

Zr/Hf fractionation of eucritic zircon: Zr/Hf ratios of whole-rock samples of basaltic eucrites are chondritic ($(Zr/Hf)_{CI\text{-}chondrite}$=36.3, [12]) with ± 15% variation [13-18], although some data obtained by INAA (e.g., [19]) deviate from this range, which seems to be mainly due to the relatively large uncertainty (20-50%) in Zr abundance. Because the Zr-Hf twin pairs are isovalent trace elements with very close ionic radii (Zr = 80 pm, Hf = 79 pm; [20]) and exhibit the same degree of incompatibility during petrogenetic processes, Zr and Hf should display extremely coherent behavior during igneous processes and retain their respective chondritic ratio. Eucritic zircon we studied shows a super-chondritic Zr/Hf ratio of 1.27 x CI-chondrite (range 1.01-2.49 x CI-chondrite), consistent with previous results [1,5,21] although there are some minor exceptions [1,22]. The fact suggests that Zr-Hf fractionation occurred prior to zircon crystallization. On the basis of Zr abundances in pyroxene and modal abundances of pyroxene in basaltic eucrites [23], Mittlefehldt and Lindstrom estimated that <15% of bulk Zr is contained in pyroxene [19]. Zr and Hf partition coefficients for pyroxene and plagioclase are small (<<1), and are no significant differences between them [24], Zr-Hf fractionation hardly occur in the early stage of eucritic basalt crystallization. The Zr and Hf partition coefficients between ilmenite and mare basalts are $^{ilm/liq}D_{Zr}$ = 0.332 and $^{ilm/liq}D_{Hf}$ = 0.406, respectively [25,26], thus Hf is preferentially partitioned into ilmenite relative to zirconium, and ilmenite may fractionate the Zr/Hf ratio effectively due to the higher $^{ilm/liq}D_{Zr,Hf}$ values. If this is the case, and if $^{ilm/liq}D_{Zr}$ and $^{ilm/liq}D_{Hf}$ values are applicable for basaltic eucrite petrogenesis, Zr-Hf fractionation could have occurred during ilmenite crystallization allowing the subsequent crystallization of zircon. Textural relationships between ilmenite and zircon in unmetamorphosed eucrites suggest that ilmenite crystallized from silica- and incompatible element-rich melts and that zircon then crystallized from a residual liquid.

Decomposition of oxides and re-equilibration with pyroxene during thermal metamorphism is a possible mechanism for zircon growth [27]. The Zr abundance in Ibitira (49 ppm [16]) is comparable to those in Pasamonte and Juvinas (51-59 ppm, [17]). Zr contents in the pigeonite of partially melted eucrites EET90020 [21] and Ibitira [27] are 10- to 30-fold higher than those in the pigeonite of Pasamonte, Juvinas and the granulitic eucrites A881388 and A881467 [27,28]. Thus, growth of zircon by ilmenite decomposition and pyroxene re-equilibration during thermal metamorphism may not be a plausible mechanism for the eucrites studied [10], although some eucritic zircons show recrystallization texture.

When did volcanic activities on the EPB cease? : The U-Pb ages of eucritic zircons are almost concordant [10]. A calculated upper intercept age of five eucrites studied here is 4552 ± 9 Ma (n = 49). If less precise data due to the low count rates of secondary ions for A881388 zircons are excluded, the age changes to 4555 ± 9 Ma (Fig. 1). An averaged ^{207}Pb-^{206}Pb age of zircon from five eucrites is 4554 ± 7 Ma (n = 49) and is identical, within analytical uncertainty, to the U-Pb age. Taking advantage of SHRIMP U-Pb isotopic analysis, we have determined absolute crystallization ages of basaltic eucrites. It is still hard to distinguish small time differences (<5 Ma) of fine-grained eucritic zircons using a single-collector ion microprobe. Such small time differences are resolvable on the basis of ^{26}Al-^{26}Mg, ^{53}Mn-^{53}Cr and ^{182}Hf-^{182}W systematics of whole-rock and mineral separate samples by

multicollector TIMS or by multicollector ICP-MS.

Figure 2 shows time-temperature regime of basaltic volcanism on the EPB [10]. Horizontal lines represent closure temperatures of isotopic systems and temperatures are shown in arbitrary units. The first temperature spike represents initial crystallization of basaltic lavas or shallow intrusions. The earliest volcanism may have occurred at a time during which ^{26}Al and ^{53}Mn were still alive (taking Asuka 881394 as an example [29]). The ^{26}Al-^{26}Mg (in pyroxene-plagioclase) and ^{53}Mn-^{53}Cr (in pyroxene-chromite) systems could be closed during thermal metamorphism (a and b). On the other hand, the U-Pb systems of eucritic zircon recorded initial crystallization of basaltic lavas (c). The ^{207}Pb-^{206}Pb age of eucritic zircon is 4554 ± 7 Ma (within 95% C.L.), indicating that the latest volcanism on the eucrite parent body ceased at 4547 Ma (i.e., a lower limit) [10]. Later thermal metamorphism and/or shock heating did not reset the U-Pb systems of eucritic zircons but reset or disturbed the U-Pb, Sm-Nd, Rb-Sr and K-Ar systems of silicates and phosphates. Whole-rock ^{26}Mg-^{26}Al systematics of basaltic eucrites shows a maximum range of magmatic activity of 0.85 ± 0.41 Ma [30], suggesting a brief period of magmatic activity on the EPB.

References: [1] Bukovanská M. & Ireland T.R. (1992). *DPS Meeting* **24**, 941. [2] Bukovanská M. et al. (1991) *Meteoritics* **26**, 39. [3] Bukovanská M. & Ireland T.R. (1993) *Meteoritics* **28**, 333. [4] Bukovanská M. et al. (1996a) *Meteoritics* **31**, A24. [5] Bukovanská M. et al. (1996b) *Meteoritics* **29**, 451-452. [6] Ireland T.R. et al. (1992) *Lunar Planet. Sci.* **XXIII**, 569-570. [7] Ireland T.R. & Bukovanská M. (1992) *Meteoritics* **27**, 237. [8] Ireland T.R. & Bukovanská M. (2003) *Geochim. Cosmochim. Acta* **67**, 4849-4856. [9] Srinivasan G. et al. (2004) *Lunar Planet Sci.* **XXXV**, #1709. [10] Misawa K. et al. (2005) *Geochim. Cosmochim. Acta* in revision. [11] Wiedenbeck M. et al. (1995) *Geostandards Newsletter* **19**, 1-23. [12] Jochum K.P. et al. (1986) *Geochim. Cosmochim. Acta* **50**, 1173-1183. [13] Wänke H. et al. (1977) *Proc. Lunar Sci. Conf.* **8th**, 2191-2213. [14] Warren P.H. & Jerde E.A. (1987) *Geochim. Cosmochim. Acta* **51**, 713-725. [15] Metzler K. et al. (1995) *Planet. Space Sci.* **43**, 499-525. [16] Barrat J.A.et al. (2000) *Meteoritics Planet. Sci.* **35**, 1087-1100. [17] Jochum K.P. et al. (2000) *Meteoritics Planet. Sci.* **35**, 229-235. [18] Münker C. et al. (2003) *Science* **302**, 84-87. [19] Mittlefehldt D.W. & Lindstrom M.M. (2003) *Geochim. Cosmochim. Acta* **67**, 1911-1934. [20] Whittaker E.J.W. & Muntus R. (1970) *Geochim. Cosmochim. Acta* **34**, 945-956. [21] Yamaguchi A. et al. (2001) *Geochim. Cosmochim. Acta* **65**, 3577-3599. [22] Saiki K. et al. (1991). *Proc. Lunar Planet. Sci. Conf.* **21st**, 341-349. [23] Delaney J.S. et al. (1984) *Proc. 15th Lunar Planet Sci. Conf., J. Geophys. Res.* **89**, C251-C288. [24] Fujimaki H. et al. (1984) *Proc. 15th Lunar Planet. Sci. Conf., J. Geophys. Res.* **89**, B662-B672. [25] McKay G.A. et al. (1986) *Proc. 16th Lunar Planet. Sci. Conf., J. Geophys. Res.* **91**, D229-D237. [26] Nakamura Y. et al. (1986) *Proc. 16th Lunar Planet. Sci. Conf., J. Geophys. Res.* **91**, D239-D250. [27] Hsu W. & Crozaz G. (1996) *Geochim. Cosmochim. Acta* **60**, 4571-4591. [28] Floss C. et al. (2000) *Antarctic Meteorite Res.* **13**, 222-237. [29] Nyquist L.E. et al. (2003) *Earth Planet. Sci. Lett.* **214**, 11-25. [30] Bizzarro M. et al. *Lunar Planet. Sci.* **XXXVI**, #1312.

Fig. 1. U-Pb concordia plots for zircons in basaltic eucrites (Y75011, Y792510, A881467 and Padvarninkai) [10]. Error ellipsoids represent 1σ.

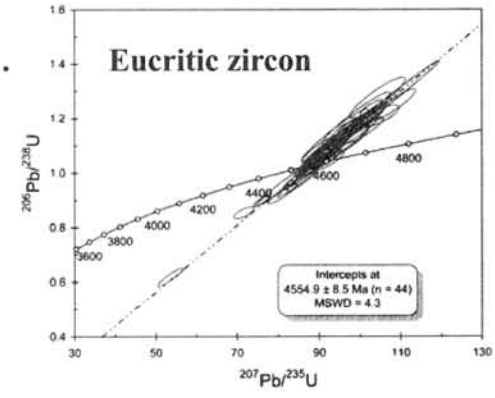

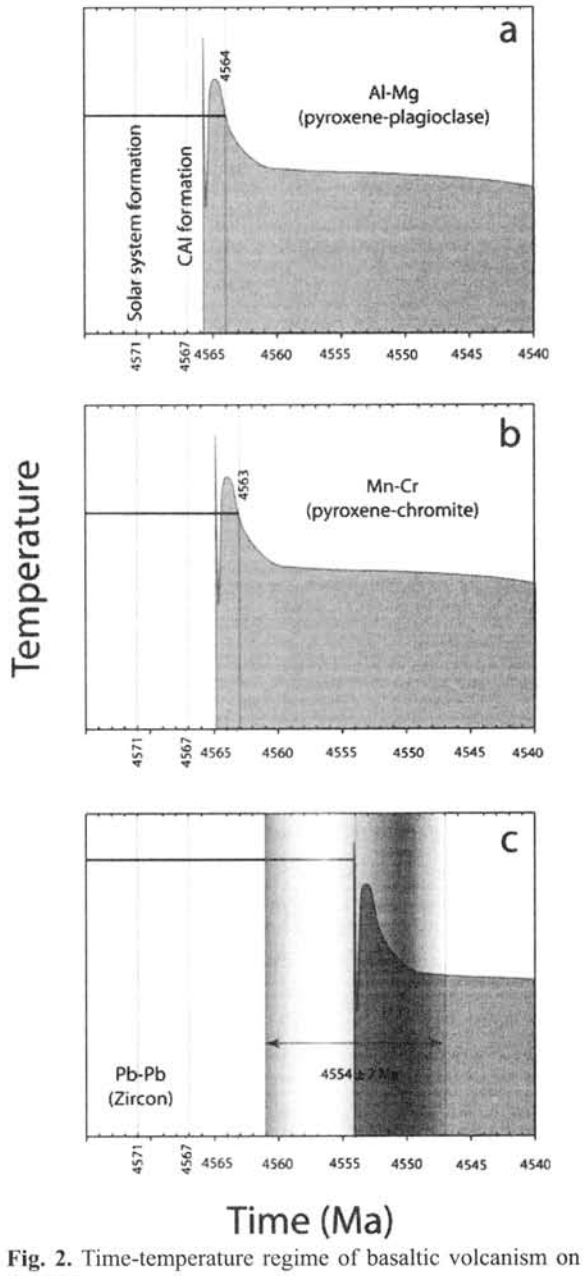

Fig. 2. Time-temperature regime of basaltic volcanism on the EPB.

Fe-Ni-Co-bearing grains and crystallized diaplectic plagiocalses: Evidence of large global impact. Y. Miura and T. Kato, Department of Earth Sciences, Faculty of Science, Yamaguchi University, Yoshida 1677-1, Yamaguchi 753-8512, Japan., Email: yasmiura @ yamaguchi-u.ac.jp

Introduction:

An intermediate plagioclase with multi-layer texture of labradorescence is studied by Miura et al. [1-4] which is considered to be re-crystallized to magmatic spinodal texture (ca.3.0Ga ago) at rim of stable continents before continental drift of the Earth. There are only several locations to find these older minerals on the Earth. Senior author recently found large samples to investigate in details on the older rocks on the Earth and to conclude that shocked diaplectic glasses can be started to crystallize to spinodal decomposition in solid-state reaction for long slow heating [5]. The main purpose of the present study is to describe crystallized shocked rocks of large global impact to the Earth.

Estimation of large global (giant) impact:

There is few material evidence of larger global impact to the primordial Earth to form the Moon and topographic surface of the Earth which is estimated by the facts of same oxygen isotope of the Moon and the Earth, and those of shocked lunar rocks with heavier elements after the impact reaction [6,7]. Previous reports with computer simulation support that Mar-size parent body hits primordial Earth to make rings of the primordial Earth to form present Moon and the Earth. However, all shocked rocks of the collided Earth are considered to be recrystallized without impact materials of global impact event. Therefore, large shocked event at global impact can be proved to be found as remnants of shocked texture and siderophile elements-rich grains.

Detailed data of shocked textures on older rock:

The following results are reported recently [5,8].

1) There is relict of shocked texture within each block of older labradorite feldspar minerals, which shows different orientations. These radiated textures are difficult to be formed by homogeneous and slow-cooling magmatic melting at gabbro or anorthosite rocks (Fig.1).
2) At global impact almost all impact materials at collided location are ejected to form lowland of sea. Shocked glasses of older rocks at global impact are found mainly at the rim of stable continents on the Earth which are mainly located at southern hemisphere.
3) Rims of the continents formed at global impact are places to be heated by igneous magma to form micro lamellar texture of spinodal decomposition under solid-solid reaction.
4) These lamellar textures are broken by later stress events to form cracks on the deep-seated older rock, which are evidences of up-lifting and flat-moving during continental uplifting and continental drift from older continental blocks at global impact.
5) Its older plutonic rocks contain siderophile element (Fe,Ni,Co)-bearing sulphide grains in the crystallized rocks which are considered to be formed during crystallization from impact breccias. Ni-rich sulphide can be formed also at Sudbury impact rock to form plutonic intrusion, which is meteoroids impact process to maintain the shocked events during magmatic reaction to the impact site.
6) Material impact signature of other feldspar and pyroxene at global impact is easily changed and discarded after crystallization from impact melt rocks during deep-seated magmatic reaction.
7) There are no regular orbital distribution on the several localities of such rocks with intermediate plagioclases with lamellar texture. Therefore, several locatities do not fit one single orbital impact (as in meteoroidal impact), but cracked places of continenets formed by global impact.
8) Magmatic melting to form magmatic solution and homogenous texture cannot found in these intermediate plagioclases which were crystallized from impact glasses to avoid pre-existed texture of shocked feature.

Comparison with lunar and Martian meteorites:

Present result of terrestrial plagioclase-rich rocks is compared with lunar and Martian rocks as follows:

1) Lunar rocks have few intermediate plagioclase feldspar so far to form such crystallized feldspar.
2) Marian meteorites have maskelynite glasses of intermediate plagioclase composition, though there are no reports of crystallized samples so far for long-time reaction at rim of broken continents if there is continental drift on Mars.
3) Meteorite from asteroids has no intermediate plagioclase composition to keep previous impact process on the parent body.
4) The terrestrial labradorite feldspar is only the case to keep previous impact history on intermediate plagioclase composition for long crystallization process.
5) The plagioclase minerals are considered to be formed at global giant or larger impact which is crystallized to magmatic spinodal texture (ca. 3.0Ga ago) at rim of stable continents before continental drift of the older Earth.

Conclusions:

The followings are summary of the present study:

1) New evidence of radiated texture and Fe-Ni-Co bearing grains in remnants of shocked impact in the older terrestrial rocks is found on intermediate plagioclases which are crystallized at rim of broken stable-continents before continental drift of the older Earth.
2) Lunar rocks and meteorites from asteroids have no intermediate plagioclase feldspar to form such crystallized feldspar with lamellar texture.
3) Martian meteorites have impact glasses of intermediate plagioclase composition without any crystallization for long-time at rim of continents on Mars so far.
4) Terrestrial labradorite feldspar with lamellar texture is only the mineral to keep previous impact history on intermediate plagioclases for long crystallization process on the Earth.
5) This plagioclase minerals are considered to be formed at global giant or larger impact which are crystallized to magmatic spinodal texture at rim of broken stable-continents before continental drift of the older Earth.
6) Impact glasses, as well as magmatic melt glasses, can form spinodal decomposition with multi-layers of labradorite feldspar minerals for long-time reaction on terrestrial history.

References:

[1] Miura Y. (1978) *Mineral.J.*, 9(2), 91-102.
[2] Miura Y. and Tomisaka T. (1978) *American Mineral.*, 63, 584-590.
[3] Miura Y., Tomisaka T. and Kato T. (1975) Mineral J., 7, 526-541.
[4] Miura Y., Tomisaka T. and Kato T. (1974) *Memoirs of Geol. Soc. Japan* (Tokyo) 11, 145-165.
[5] Miura Y. (2004): *Japan. Assoc. Mineral., Petrol. & Econ. Geol., (Okayama)* 158.
[6] Miura Y. and Graham R.A.(1994) S*hock Waves Journal* (Springer-Verlag), 3, 293-298.
[7] Miura Y. and Kato T. (1992) Celestial Mechanics and Dynamical Astronomy (Kluwer Academic), 54, 245-248.
[8] Miura Y., Takayama K. & Kato T. (2005) Proc. 2nd Int. Symposium on Interdisciplinary Shock Wave Research (COE, Tohoku Univ., Sendai), pp.2 (CD-ROM).

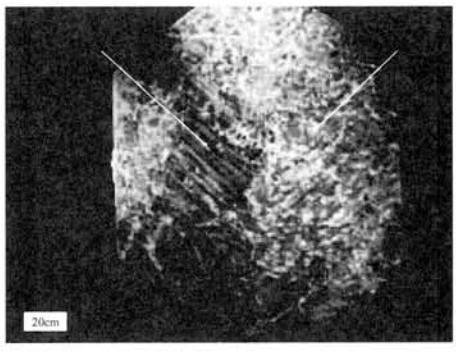

Fig.1 . Photo of large labradrite feldspar from Canada, with relicts of shocked texture.

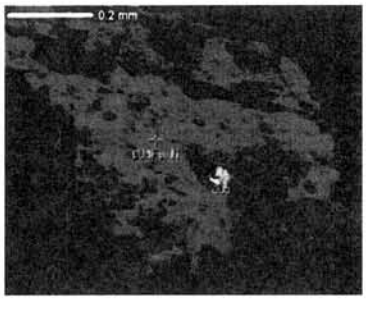

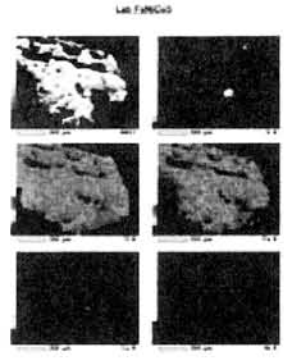

Fig.2 Fe-Ni-Co-bearing grains in labradorites with lamellar texture from Canada. BEI image (left), EPMA Color mapping (right).

The role of condensation kinetics of silicate melt on the chemical variation of chondrule compositions. H. Nagahara, K. Ozawa, and S. Tomomura, *Dept. Earth Planet. Sci., Univ. Tokyo, Hongo, Tokyo 113-0033, Japan*

Introduction:

The chemical composition of chondrules is characterized by large fractionations in major and minor elements without isotopic mass fractionation. The variation should be related to the origin of chondrules. We have obtained comprehensive bulk chemical composition of chondrules with high precision for Bishunpur and Krymka chondrites. The compositional range is much smaller than that previously reported, which were obtained by either INAA or "broad beam technique" of EPMA.

Chondrule compositions:

The bulk chemical composition of chondrules is summarized as follows: (1) most ferromagnesian chondrules are in a fairly narrow compositional range, and they appear to form a "trend", suggestive of formation by a certain common cosmochemical or physical process(es), (2) the refractory component abundance is fairly constant, which is smaller than that of CI, suggesting that fractionation of the refractory component played a role, (3) there is a large fractionation regarding Mg and Si, and the Mg/Si fractionation is over the CI ratio, suggesting the role of Mg-rich and/or Si-rich component on the fractionation. The process responsible for the Mg/Si fractionation does not accompany the refractory component fractionation, and (4) abundance of FeO varies largely, which is almost independent of the abundance of other elements, although the Mg/Si ratio of FeO-rich chondrules are lower than CI, which suggests that Mg/Si fractionation accompanies FeO fractionation.

Above observation may be explained by mixing of two solid components, which had been previously fractionated by an unknown process. It is, however, not the case, because the trend is not a straight line in the MgO-FeO-SiO2 diagram, although it is the case in the FeO - (Al2O3+CaO) - SiO2, (Al2O3+CaO) – MgO - SiO2, and FeO – MgO - (Al2O3+FeO) diagrams. The most plausible fractionation is gas – liquid (and/or solid) fractionation, in which gas coexisting with more refractory liquid (and/or solid) than CI has more volatile (SiO2 and FeO) – rich composition. The process thus is either evaporation or condensation.

Although quantitative models to investigate compositional variation of chondrules have been developed for equilibrium condensation [1] and isothermal evaporation [2], there is, however, a line of evidence that chondrules were formed in an open system through cooling. Therefore, development of a new model to explain the compositional variation of chondrules through cooing in an open system, that is, a kinetic condensation model, is necessary.

Model:

We have developed a kinetic condensation model that is based on the Hertz-Knudsen equation, which is an equation to describe the rate of condensation (or evaporation) as a function of temperature, pressure, and ambient gas composition. The model contains a critical parameter, cooling rate of ambient gas, which is the same for condensing liquid.

The initial conditions are 10^{-4} bars total pressure and 500 times dust enrichment relative to the solar. The total pressure of 10^{-4} bar is the most commonly assumed pressure for the solar nebula at 1 to 2 A.U., and the dust enrichment of 500 times solar is the condition where Mg-Si-rich silicate melt appears as a stable phase at this total pressure. The dust compositions are either CI or depleted in (Al_2O_3+CaO)- and/or FeO-depleted by 0.2, 0.5 and 0.75 times CI. The condensation and evaporation coefficients are assumed to be the same and the value of 0.2 is used for all elements [2,3]. The model assumes constant volatility for all the elements considered [4]. Pertinent model parameters (elemental fractionation factor and activation energy for evaporation) obtained by optimizing the results of evaporation experiments. In order to determine the equilibrium vapor pressures of silicate melts, solution models by [5] for CaO-MgO-Al_2O_3-SiO_2 melts and the MELTS model by [6] for FeO-bearing melts were used. Silicate melt without metal/sulfide melt was considered as a condensed phase.

Reuslts:

The effect of cooling rate, degree of supersaturation, and initial composition on the composition paths of condensing liquid and coexisting gas has been evaluated.

Comparing the calculation results with the chondrule compositions, we show that all the chondrule composition diversities (except for Al-rich ones) are well reproduced as either liquid condensates or quenched products of coexisting residual gas and that the gas should be initially depleted in the refractory component by a quarter and iron by ~80% relative to the CI ratio. The initial composition of CI does not reproduce the observed compositional variation of chondrules.

The dimensionless conditions are converted to the dimensional numbers, which results in the cooling rate of the system 0.01 - 1 °C/hour at

$P_{tot}=10^{-4}$ with dust enrichment by 500 times of CI. The cooling rate is slightly smaller than the rates previously estimated from dynamic crystallization experiments for textural reproduction. In summary, a possible scenario is as follows: dust which are enriched by 500 times relative to the CI abundance and from which some fraction of refractory component (CAIs) and most of metallic iron were fractionated was instantaneously heated to vaporize, then, the gas cooled rapidly and supersaturated partly to form liquid droplets and the residual gas also quenched to form liquid droplets with fractionated (SiO2- and FeO-rich) compositions. The condensed liquid droplets and droplets quenched from chemically fractionated gas became chondrules with wide variation in terms of Mg/Si and FeO abundance.

References:

[1] Ebel, D. S. and Grossman, L. (2000) GCA 64, 339, [2] Alexander, C. M. O'D. (2004) GCA 68, 3943, [3] Richter, F. et al. (2002) GCA 66, 521, [4] Ozawa, K. and Nagahara, H. (2001) GCA 65, 2171, [5] Berman, R. G. (1988) J. Petrol. 29, 455, [6] Ghiorso, M. S. and Sack, R. .O. (1995) CMP 119, 197.

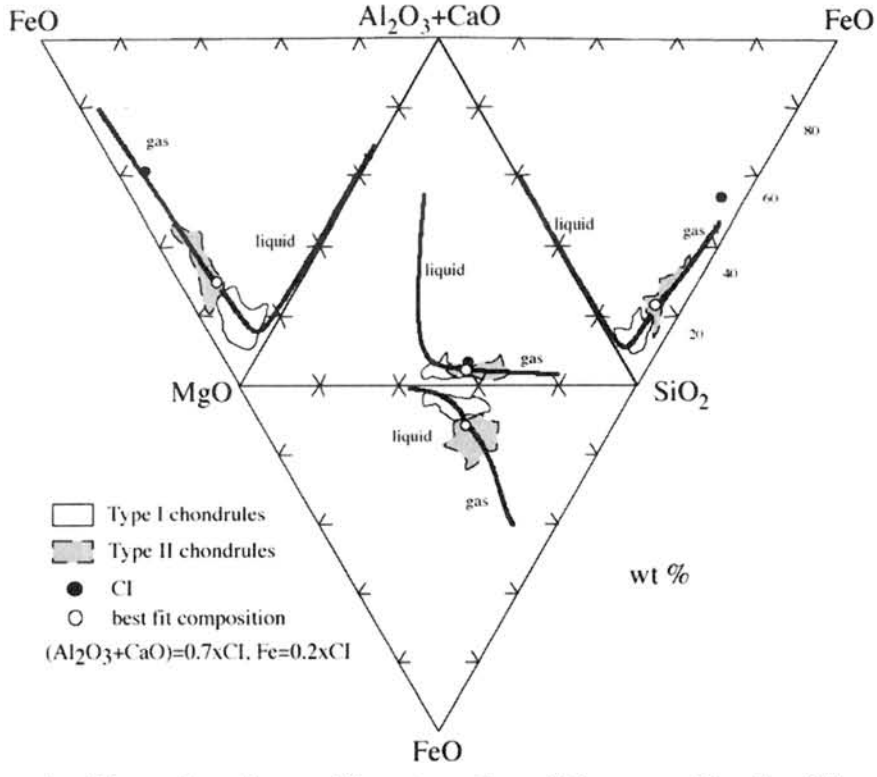

Fig. 1 The most plausible condensation conditions to produce all the compositional variation of chondrules from a common precursor (gas composition) through a common process. The initial composition is partly depleted in the refractory component and significantly in Fe, and the dimensionless cooling rate is 0.01-0.02, which corresponds to be 0.01 to 1°/hour at $P_{tot}=10^{-4}$ bar and dust enrichment by 500 times CI. Type I chondrules can be liquid condensates and type II chondrules are quenched liquid from the residual gas that are condensing Type I chondrules.

Noble gas measurement of Gibeon iron meteorites. K. Nagao[1] and M. Honda[2], [1]Laboratory for Earthquake Chemistry, Graduate School of Science, University of Tokyo, Bunkyo-ku, Tokyo 113-0033, Japan, [2]Department of Chemistry, Nihon University, Setagaya-ku, Tokyo 156-0045, Japan.

Introduction:

Gibeon iron meteorites classified as IVA have been discovered as a large number of fragments in a strewn field in Namibia, Africa. Total weight becomes about 21 tons [1]. We measured noble gases of samples taken from many fragments of the Gibeon meteorites to investigate production profile of cosmogenic nuclides under heavy shielding condition inside a large meteoroid.

Experimental method:

Meteorite pieces weighing 0.3–1.9g cut out from Gibeon fragments of various sources were washed with diluted HNO_3 in ultrasonic bath to remove weathered materials. In some cases, weathering products adhered on the samples were mechanically removed before the HNO_3 treatment. After the treatment, the samples were rinsed with acetone in ultrasonic bath. The cleaned samples were installed in a sample holder made of low He-permeability glass, and then set on an extraction furnace of the noble gas extraction and purification system. We used Al_2O_3 crucible to melt the iron meteorite samples. Before noble gas measurement, the sample holder and the purification line were baked out overnight. During the heating, the samples were heated at about 200°C to remove atmospheric contamination. The crucible in the extraction furnace was heated repeatedly at 1850-1900°C for totally 3-5 hours to reduce degassing from the crucible. Hot blank levels at 1850°C for 30 min. were $2x10^{-10}$ (^{4}He), $1\text{-}2x10^{-11}$ (^{20}Ne), $1x10^{-8}$ (^{40}Ar), $7x10^{-13}$ (^{84}Kr) and $5x10^{-14}$ (^{132}Xe) in unit of cm^{3}STP. For noble gas extraction, samples were heated at 1850°C for 30 min. In this condition metal was evaporated from the crucible and deposited on cooler wall above the crucible. Extracted noble gases were purified and separated into two fractions He-Ne and Ar-Kr-Xe for noble gas analysis. Isotopic compositions and concentrations were measured on a modified VG5400 (MS-II) mass spectrometer at the laboratory for Earthquake Chemistry, University of Tokyo. In the present condition of the mass spectrometer (MS-II), ^{21}Ne peak is interfered by $^{66}Zn^{3+}$ ions, whose intensity is equivalent to $1\text{-}2x10^{-12}$ cm^{3}STP of ^{22}Ne. Hence, the cosmogenic ^{21}Ne abundance was calculated based on $^{21}Ne/^{20}Ne$ ratio and ^{20}Ne peak intensity.

Results and Discussion:

Ar isotopic ratios are plotted in Fig. 1. Most of the data points are plotted along a straight line connecting the two noble gas components, terrestrial atmospheric Ar and cosmogenic Ar. Samples with low concentrations of cosmogenic gases tend to converge on the atmospheric composition, while those with abundant cosmogenic gases move to the point of cosmogenic Ar. Because Ar abundances evolved from sample melting are generally much larger than the blank level and the Ar with atmospheric isotopic ratios may not be trapped in the metal samples, the Ar is probably derived from Al_2O_3 crucible being attacked by some non-metallic elements contained in the meteorites. This is the reason why estimation of cosmogenic ^{38}Ar abundance was very difficult for most of the samples with low cosmogenic ^{38}Ar. The degassing of atmospheric Ar from the crucible implies that other noble gases of atmospheric origin would affect the noble gas isotopic compositions to some extent. In the future work, selection of materials resistive to liquid metal at high temperature (>1800°C) and with low gas content is the most important factor to measure noble gases of iron meteorites.

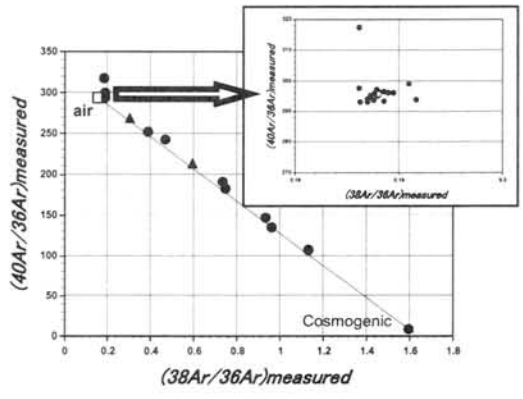

Fig. 1. Ar isotopic ratios of Gibeon and El Taco iron meteorites.

Fig. 2 shows concentrations of cosmogenic ^{21}Ne and ^{3}He for Gibeon and El Taco iron meteorite samples. El Taco is known to be a meteorite with very low concentrations of cosmogenic noble gases because of its large preatmospheric body. El Taco data by Takaoka (personal communication) are also plotted in the figure for comparison. Our data for El Taco are in good agreement with those by Takaoka. The data points for Gibeon show linear trend on the log-log plot, and cosmogenic ^{3}He and ^{21}Ne concentrations vary by almost six orders of magnitude from 10^{-13} to 10^{-7} cm^{3}STP/g and 10^{-14} to 10^{-9} cm^{3}STP/g, respectively. More than half of the Gibeon samples measured so far show much lower

concentrations of cosmogenic ^{3}He and ^{21}Ne than those for El Taco iron meteorite. This means that these samples were heavily shielded to cosmic rays in a preatmospheric body which was much larger than that of El Taco iron meteorite.

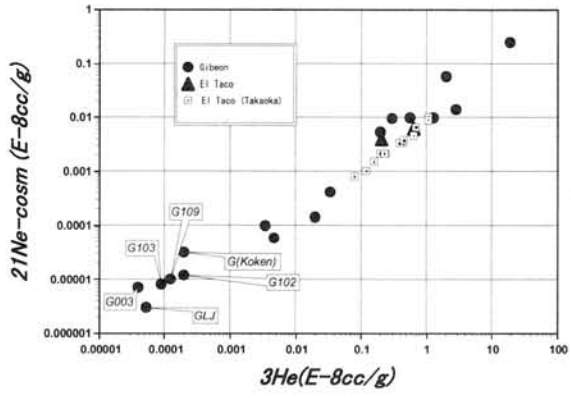

Fig. 2. Plot of cosmogenic ^{21}Ne vs. cosmogenic ^{3}He concentrations for Gibeon and El Taco iron meteorites.

Fig. 3 shows a correlation plot of cosmogenic ^{3}He and ^{38}Ar concentrations. As noted above, relatively high amount of Ar probably released from the Al_2O_3 crucible when the samples were heated to melt made it difficult to estimate small amounts of cosmogenic ^{38}Ar. The lower limit of cosmogenic ^{38}Ar abundance detected in the present study was about $1x10^{-12}$ cm^{3}STP as can be seen in Fig. 3. Linear correlation between the cosmogenic ^{38}Ar and ^{3}He can be seen. The data for El Taco are also plotted on the trend for Gibeon.

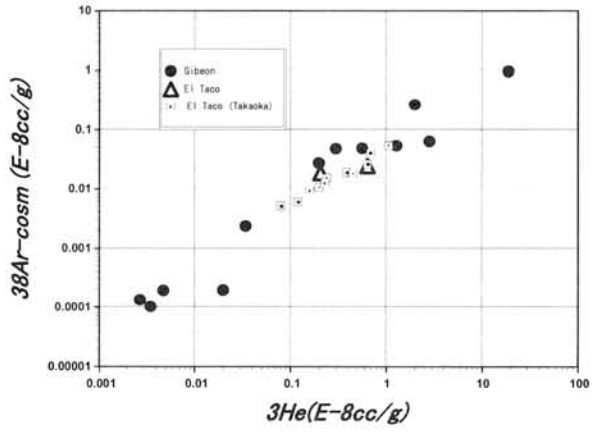

Fig. 3. Plot of cosmogenic ^{38}Ar vs. cosmogenic ^{3}He concentrations for Gibeon and El Taco iron meteorites.

Our noble gas data on cosmogenic gases along with the data on cosmogenic radioactive nuclides clearly indicate that the fragments from Gibeon iron meteorite studied in this work are the samples from various depths from surface to central part of preatmospheric body of this meteorite. Combining the stable noble isotopes and the radioactive nuclides such as ^{10}Be, history of irradiation condition of this meteorite in space will be elucidated [1].

References:

[1] Honda M. and Nagao K. (2005) Symp. Antarct. Meteorites, NIPR, this volume.

Plagioclase thermometry of Caddo County IAB iron meteorite. Y. Nakamuta[1], R. Owaki[2], H. Takeda[3], [1]Kyushu University Museum, Kyushu University, Fukuoka 812-8581, Japan (nakamuta@museum.kyushu-u.ac.jp), [2]Department of Earth and Planetary Sciences, Faculty of Sciences, Kyushu University, Fukuoka 812-8581, Japan, [3]Research Institute, Chiba Institute of Technology, Narashino 257-0016, Japan.

Introduction: IAB irons are unique among iron meteorites in containing variable types of silicate inclusions, having the compositions in the range from chondritic to andesitic ones [1-3]. These silicate inclusions were thought to have formed by inhomogneous segregation of partial melts from chondritic source materials [1].

Chronological studies of IAB irons show that the I-Xe ages of silicates in IAB irons are ~4.56 Gyr that is very near to the 4.567 Gyr Pb-Pb age of Ca, Al-rich inclusions in primitive meteorites, which are though to be the earliest condensates in the solar system [3]. In contrast to the I-Xe ages, the Ar-Ar, Rb-Sr, and Sm-Nd ages of IAB irons appear significantly younger at ~4.53-4.43 Gyr [3]. These chronological data suggest very prolonged thermal histories of the parent body of IAB iron meteorites and the thermal history of the IAB parent body has been controversial [1-3].

Coarse-grained gabbroic material rich in plagioclase and diopside was found which is not a clast within a breccia, but rather is an area with transitional margins located mainly at silicate-metal boundaries only a few cm away from fine-grained, ultramafic silicates similar to winonaites [1]. The gabbroic material was thought to have formed by inhomogneous segregation of partial melts [1].

Sodic plagioclase crystallized at a lower temperature forms a structure in which Al concentrates in one site of the four symmetrically nonequivalent tetrahedral sites of the framework, with Si in the remaining sits; whereas sodic plagioclase crystallized at high temperature of >900 °C shows the structure in which Al distributes randomly in the four tetrahedral sites. Sodic plagioclase formed at intermediate temperatures takes an intermediate structure [4-6]. The separation of the 1-31 and 131 diffraction peaks in an x-ray diffraction pattern, the Δ131 parameter, is sensitive to changes in the relative structural state of sodic plagioclase [4] and is related to temperature of synthesis of sodic plagioclase [7, 8]. In this study, the sodic plagioclase thermometer was applied to a gabbroic inclusion in the Caddo County IAB iron described by [1] in order to obtain thermal data and give a constraint on the thermal history of the IAB iron.

Experiments: Four tiny grains of plagioclase, about 1 mm in size, which were sampled from a gabbroic silicate inclusion of the Caddo County IAB iron and named as CADDO #4 by [1], were embedded in glycol phthalate and polished to thin sections. Individual grains were named as Grain 1, 2, 3, 4. Polished thin sections (PTSs) of each grain were observed by an optical microscope and their chemical compositions were analyzed by an electron-probe microanalyzer (EPMA) with a wave-length dispersive mode. Pieces of plagioclases, about a hundred μm in size, were taken out from each PTS and glued on glass fibers of 10 μm in diameter for X-ray analysis. X-ray powder diffraction patterns were taken by using a Gandolfi camera. Peak positions of 1-31 and 131 reflections of plagioclase were precisely determined by applying a profile-fitting technique. The temperature of plagioclase was determined by plotting the Δ131 parameter on the diagram relating the Δ131 and temperature of synthesis of plagioclase after correction for the crystallographic influence of the Or content.

Results: Photomicrographs of each grain are shown in Fig. 1. Grain 1 shows a conspicuous band structure

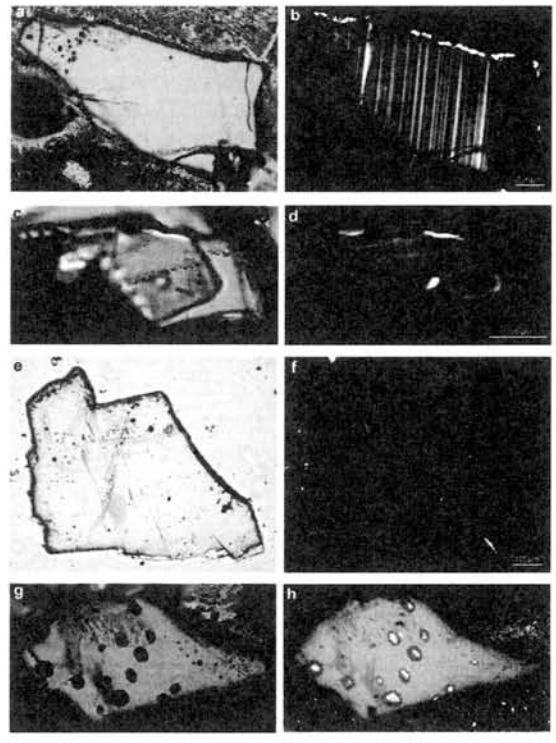

Fig. 1. Photomicrographs of each grain. **a**, **b**: transmitted light views of Grain 1 between parallel and crossed polars, respectively. **c**, **d**: transmitted light views of Grain 3 between parallel and crossed polars, respectively. **e**, **f**: transmitted light views of grain 4 between parallel and crossed polars, respectively. **g**, **h**: transmitted and reflected light views of Grain 2, respectively.

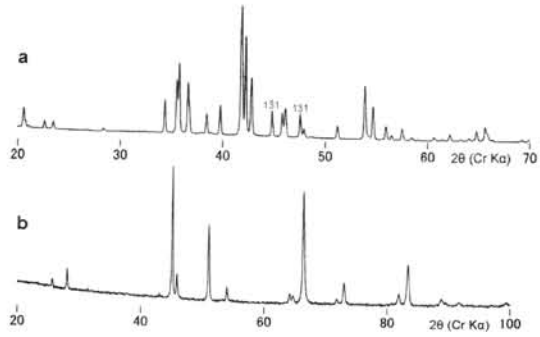

Fig. 2. X-ray powder diffraction patterns of a piece of Grain 1 (**a**) and a tiny crystal in a void of Grain 2 (**b**) taken by a Gandolfi camera.

maybe due to albite twins in a transmitted light view between crossed polars (Fig. 1b), whereas Grain 4 does not (Fig. 1f). Grain 3 shows a broader and less remarkable band structure (Fig. 1d). Grain 2 contains rounded to ovoid-shaped voids as observed in Fig. 1g, in which euhedral crystals with metallic luster occur (Fig. 1h). Each plagioclase grain is homogeneous in chemical compositions and has compositions of $An_{16.71\text{-}18.19}Ab_{80.52\text{-}78.30}Or_{2.76\text{-}2.85}$ as listed in Table 1.

An example of X-ray patterns of plagioclases taken by using a Gandolfi camera is shown in Fig. 2 together with that of a tiny crystal in a void of Grain 2. The X-ray pattern shown in Fig. 2b reveals that the crystals occurring in voids of Grain 2 are troilite. Plagioclases show sharp and well-resolved X-ray reflections as seen in Fig. 2a. The Δ131 parameters of each grain are summarized in Table 1 together with chemical compositions. The plots of plagioclases on the relation diagram between the Δ131 parameter and temperature are shown in Fig. 3. The temperatures of each plagioclase were read on the diagram and shown in Table 1.

Discussion: Temperatures estimated based on the structural states of plagioclase are in the range between 693 and 772 °C. The temperatures are much lower than the solidus of plagioclase of about 1100 °C. Melts with plagioclase compositions were thought to form by inhomogeneous segregation during partial melting of chondritic materials [1]. The view is consistent with the result of this study that euhedral troilite crystals occur in voids of Grain 2, which suggests the coexistence of plagioclase and troilite melts in the silicate inclusion. Then, following two explanations may be possible for the plagioclase temperatures, (1) ordering of Al in tetrahedral sites occurred during a prolonged cooling period, (2)

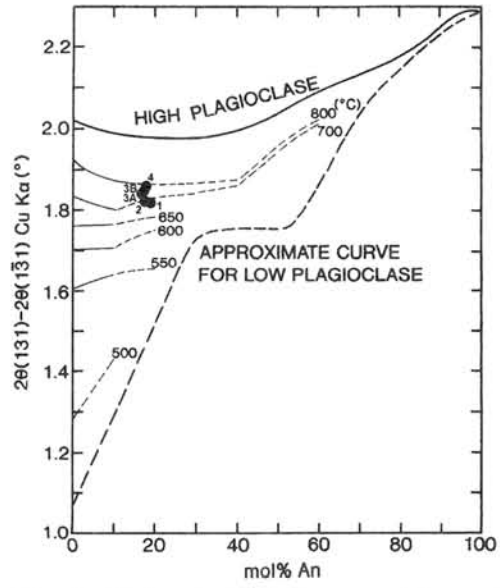

Fig. 3. Plots of plagioclase crystals on the relation diagram between the Δ131 parameter and the temperature of synthesis of plagioclase by [8]. Grain numbers are also shown on each plot.

plagioclase melts were quenched to a temperature of about 800 °C and plagioclases crystallized at the temperatures obtained in this study.

It is noticeable that Grain 1 showing the lowest temperature among studied samples shows a band structure under an optical microscope. The band structure may be attributed to albite twins formed by ordering of Al in tetrahedral sites during a prolonged cooling period. Grain 4 showing the highest temperature does not show such a band structure, and then is thought not to experience Al-ordering after crystallization. The observations may support the idea that plagioclase melts were quenched nearly to the temperature obtained by Grain 4 before crystallization of plagioclase.

References: [1] Takeda H. et al. (2000) *GCA* 64, 1311-1327. [2] Benedix, G.K. et al. (2000) *Meteorit. Planet. Sci.*, 35, 1127-1141. [3] Bogard D.D. et al. (2000) *Meteorit. Planet. Sci.*, 40, in press. [4] Smith J.R. and Yoder H.S. (1956) *Am. Mineral* 41, 632-647. [5] Bambauer H.U. et al. (1967) *Schweizer Mineral. U. Petrog. Mitt.* 47, 351-364. [6] Kroll H. and Ribbe P.H. (1980) *Am Mineral.* 65, 449-457. [7] Eberhard E. (1967) *Schweizer Mineral. U. Petrog. Mitt.* 47, 385-398. [8] Smith J.V. (1972) *J. Geol.* 80, 505-525.

Table 1. Chemical and X-ray data of plagioclase grains and estimated tmperatures.

Grain	An	Ab (mol %)	Or	Δ131 Cu Kα(degree) observed	correction	corrected	Temperature (°C)
1	18.92	78.30	2.77	1.749	0.065	1.814	693
2	17.89	79.24	2.85	1.750	0.068	1.818	696
3A	16.71	80.52	2.76	1.775	0.064	1.839	743
3B	17.03	80.26	2.70	1.776	0.064	1.840	750
4	18.17	79.03	2.79	1.780	0.066	1.846	772

Noble gas study of the Dhofar 018 howardite. D. Nakashima[1], S. Herrmann[1], U. Ott[1], T. Nakamura[2], and T. Noguchi[3] [1]Max-Planck-Institut für Chemie, Joh.-J.-Becher-Weg 27, D-55128 Mainz, Germany, [2]Department of Earth and Planetary Sciences, Kyushu University, Hakozaki, Fukuoka 812-8581, Japan, [3]Department of Materials and Biological Science, Ibaraki University, Bunkyo, Mito 310-8512, Japan.

Introduction:

Dhofar 018 was found in Oman on January 17, 2000, and was classified as a howardite [1]. This meteorite shows brecciated textures and contains several kinds of clasts such as CM and LL chondrites and an aubrite [2], indicating that Dhofar 018 is a polymict breccia. The hydrous clasts such as CM chondrites serve as an indicator of temperatures during lithification of the host meteorite [3]. We will study the host Dhofar 018 meteorite and foreign clasts mineralogically and chemically. This study can provide information on evolution processes of the regolith on the HED meteorite parent body, possibly 4 Vesta [cf. 4-5].

There have been no noble gas data for Dhofar 018 so far. Here we report the results of noble gas analysis as the beginning of the comprehensive study of the Dhofar 018 howardite.

Noble gas analysis:

We prepared the two samples, weighing 30.0mg and 8.1mg. The 30.0mg sample was used for stepwise heating analysis at 300-1700°C with 200°C intervals, whereas the 8.1mg sample was used for total extraction analysis at 1700°C. The concentrations and isotopic ratios of extracted noble gases were measured with a MAP 215-50 noble gas mass spectrometer at Max-Planck-Institut für Chemie [6].

Results and discussion:

Results of noble gas analysis are shown in Table 1. Figure 1 shows release patterns of noble gases in Dhofar 018. Most of ^{4}He and ^{20}Ne are released in 500-700°C fractions. Isotopic ratios of He and Ne in these fractions show that Dhofar 018 contains solar and cosmogenic noble gases. The presence of solar gases and the brecciated textures indicate that Dhofar 018 is a regolith breccia. Most of ^{36}Ar is released in 700-1300°C fractions. The highest amounts of ^{84}Kr and ^{132}Xe are released in the 300°C fraction. Isotopic ratios of Kr and Xe in this fraction are identical to atmospheric Kr and Xe, respectively, suggesting atmospheric gas contamination due to terrestrial weathering.

Figure 2 shows comparisons between the concentrations of ^{4}He, ^{20}Ne, and ^{36}Ar in Dhofar 018 and those in solar-gas-rich meteorites, the Kapoeta howardite [7] and Fayetteville H4 chondrite [8]. Fayetteville contains the largest concentrations of solar noble gases of all non-lunar meteorites [8-9]. The concentrations of ^{20}Ne and ^{36}Ar are higher than those in Kapoeta and Fayetteville. The ^{20}Ne/^{36}Ar ratio of Dhofar 018 is 26, which is comparable with the typical value of solar wind implanted species (^{20}Ne/^{36}Ar=26.8, lunar soil ilmenites 12001, [10]). This suggests no large diffusive loss of ^{20}Ne and ^{36}Ar from Dhofar 018. The concentrations of ^{4}He are lower than that in Fayetteville (Fig. 2). The ^{4}He/^{20}Ne ratio of Dhofar 018 is 46, which is lower than the value for lunar soil ilmenites 12001 (^{4}He/^{20}Ne=253, [10]). This suggests ^{4}He diffusive loss from Dhofar 018.

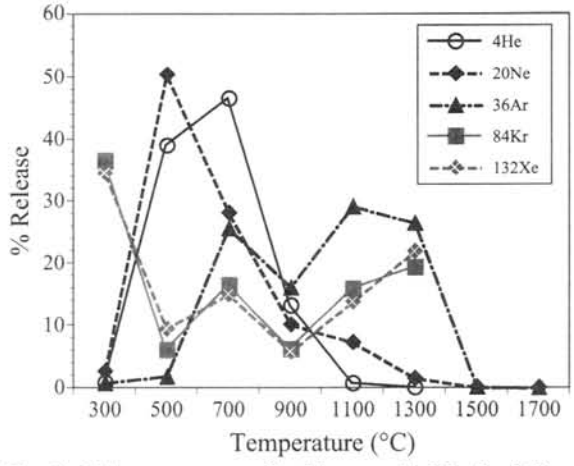

Fig. 1: Release patterns of noble gases in Dhofar 018.

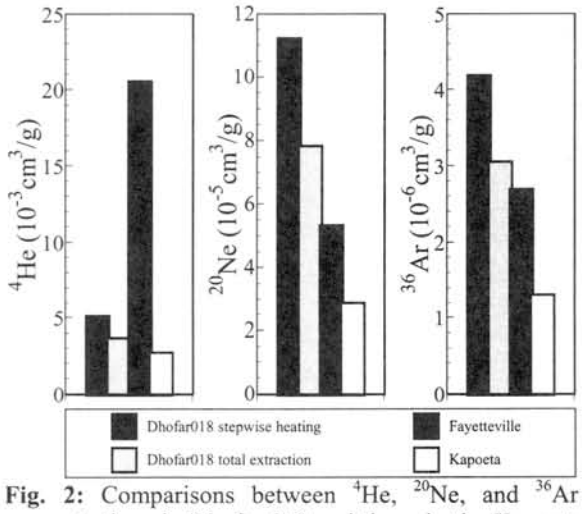

Fig. 2: Comparisons between ^{4}He, ^{20}Ne, and ^{36}Ar concentrations in Dhofar 018 and those in the Kapoeta howardite and Fayetteville H4 chondrite. The highest concentrations of ^{4}He, ^{20}Ne, and ^{36}Ar in the Fayetteville samples [8] and in the Kapoeta samples [7] are shown in this figure.

We may expect some solar Xe, because Dhofar 018 contains large amounts of solar Ne and Ar (Fig. 2). However, isotopic ratios of Xe showed that Xe is

dominated by atmospheric and cosmogenic Xe. Solar Xe can not be clearly observed.

The concentrations of cosmogenic ^{3}He (^{3}He$_C$), ^{21}Ne (^{21}Ne$_C$), and ^{38}Ar (^{38}Ar$_C$) were calculated based on the isotopic ratios (Table 2). For the calculations, we used the values, $(^3He/^4He)_{solar}$=0.0003, $(^3He/^4He)_C$ =0.2, $(^{21}Ne/^{22}Ne)_C$=0.9, $(^{38}Ar/^{36}Ar)_{trapped}$=0.188, and $(^{38}Ar/^{36}Ar)_C$=1.5. The ratios of $(^{21}Ne/^{22}Ne)_{solar}$ (=0.0311) were obtained by taking the intersection of the Ne SW-SEP line and an extension line of Ne cosmogenic in the Ne three isotope diagram (see [3]). Assuming that the meteorite was exposed to cosmic rays with 4π geometry and with an average shielding, cosmic ray exposure ages, T_3, T_{21}, and T_{38} are calculated from cosmogenic gas concentrations and production rates (Table 2, [11]). T_3 and T_{38} ages are shorter than T_{21} age (Table 2). The short T_3 age is explained by ^{3}He$_C$ diffusive loss. The short T_{38} age might be due to underestimation of ^{38}Ar$_C$ by the inaccurate correction for trapped ^{38}Ar. Another possible explanation is ^{38}Ar$_C$ loss induced by alteration on Earth. One of the main target elements of ^{38}Ar$_C$ production is Fe, which is present in Fe-sulfides. We found oxidized Fe-sulfides in the thin section of Dhofar 018. The decomposition of Fe-sulfides might cause ^{38}Ar$_C$ loss. Considering partial losses of ^{3}He$_C$ and ^{38}Ar$_C$, cosmic ray exposure age of Dhofar 018 would be around 21-24Ma, which is around the main peak at 21Ma in the exposure age distribution for HED meteorites [12].

Summary:

The concentrations and isotopic ratios of noble gases in the Dhofar 018 howardite were measured. Dhofar 018 contains solar and cosmogenic noble gases. The presence of solar gases and the brecciated textures indicate that Dhofar 018 is a regolith breccia. The concentrations of ^{20}Ne and ^{36}Ar are higher than those in Fayetteville, which contains the largest concentrations of solar noble gases of all non-lunar meteorites. On the other hand, the ^{4}He concentrations are lower than in Fayetteville. The ^{4}He/^{20}Ne ratio is lower than the value for lunar soil ilmenites 12001, which suggests diffusive loss of ^{4}He. Heavy noble gases consist of atmospheric and cosmogenic components. The presence of atmospheric components is explained by terrestrial contamination. Cosmic ray exposure ages deduced from ^{3}He$_C$ and ^{38}Ar$_C$ are shorter than that from ^{21}Ne$_C$, which can be explained by ^{3}He$_C$ and ^{38}Ar$_C$ losses. The cosmic ray exposure age of Dhofar 018 is around 22Ma.

References:

[1] Grossman J. N. (2000) *Meteorit. Planet. Sci., 35,* A199-A225. [2] Lorenz C. et al. (2001) *LPS XXXII,* #1778. [3] Nakashima D. et al. (2003) *EPSL, 212,* 321-336. [4] McCord T. B. et al. (1970) *Science, 168,* 1445-1447. [5] Consolmagno G. J. and Drake M. (1977) *GCA, 41,* 1271-1282. [6] Patzer A. and Schultz L. (2001) *Meteorit. Planet. Sci., 36,* 947-961. [7] Pedroni A. (1989) Ph. D. dissertation, ETH, Zürich. 224p. [8] Wieler R. et al. (1989) *GCA, 53,* 1441-1448. [9] Schultz L. and Franke L. (2004) Helium, neon & argon in meteorites: A data collection, *MPI für Chemie, Mainz.* [10] Eberhardt P. et al. (1972) *Proc. Lunar Sci. Conf., 3rd,* 1821-1856. [11] Eugster O. and Michel Th. (1995) *GCA, 59,* 177-199. [12] Eugster O. and Michel Th. (1993) *Meteoritics, 28,* 346.

Table 1. Concentrations and isotopic ratios of noble gases in Dhofar 018.

analysis	mass	^{4}He*	^{3}He/^{4}He	^{20}Ne*	^{20}Ne/^{22}Ne	^{21}Ne/^{22}Ne	^{36}Ar*	^{38}Ar/^{36}Ar	^{40}Ar/^{36}Ar	^{84}Kr*	^{132}Xe*
stepwise heating	30.0mg	505616	0.000377 ±0.000007	11246	12.4 ±0.1	0.0377 ±0.0004	418	0.191 ±0.001	4.70 ±0.04	2876	298
total extraction	8.1mg	365949	0.000363 ±0.000003	7808	12.3 ±0.1	0.0393 ±0.0003	305	0.192 ±0.001	15.6 ±0.2	2715	251

* ^{4}He, ^{20}Ne, and ^{36}Ar concentrations are given in 10^{-8}cm^3/g, and ^{84}Kr and ^{132}Xe concentrations are given in 10^{-12}cm^3/g.

Table 2. Cosmogenic gas concentrations and cosmic ray exposure ages of Dhofar 018.

	^{3}He$_C$	^{21}Ne$_C$	^{38}Ar$_C$	P_3#	P_{21}#	P_{38}#	T_3	T_{21}	T_{38}
	10^{-8}cm^3/g			10^{-8}cm^3/g			Ma		
stepwise heating	22.0 ±3.7	6.16 ±0.44	1.22 ±0.49	1.65	0.256	0.092	13.3 ±2.3	24.1 ±1.7	13.3 ±5.4
total extraction	11.0 ±1.2	5.42 ±0.26	1.32 ±0.50				6.7 ±0.8	21.2 ±1.0	14.4 ±5.4

Production rates for average chemical abundances of howardites and average shielding [11].

Mineralogy of heavily hydrated clasts in Asuka 881020, Acfer 182, and NWA 470 CH chondrites. Takaaki Noguchi[1*], Tomoki Nakamura[2], Makoto Kimura[1], Addi Bischoff[3], Takahito Osawa[4], and Naoya Imae[5], [1]Department of Materials and Biological Sciences, Ibaraki University, [2]Department of Earth and Planetary Sciences, Kyushu University, [3]Institut für Planetologie, Westfälische Wilhelms-Universität, [4]Japan Atomic Energy Research Institute, [5]National Institute of Polar Research (*: tngc@mx.ibaraki.ac.jp)

Introduction: Asuka 881020 (A-881020) has many petrographic features common to CH chondrites (e.g., [1,2,3]). One of the characteristic petrographic features of the CH chondrites is the presence of dark clasts, most of which experienced heavy aqueous alteration (e.g., [4]). In ALH 85085, there are at least two major types of dark clasts based on SEM observation and electron microprobe analysis; (1) C1 clasts that contain magnetite, pentlandite, merrillite, troilite, olivine, and dolomite embedded in fine-grained matrix, and (2) reduced clasts that contain Fe-Ni metal and olivine embedded in fine-grained matrix [4]. So far, only a few TEM studies of heavily hydrated clasts in some CH (and CB) chondrites were performed [5, 6]. In this study, we present mineralogical variations of the dark clasts and hydrated clasts in A-881020 and compare their mineralogical characteristics with heavily hydrated clasts in the two CH chondrites Acfer 182 and NWA 470, which were recovered from African desert [2, 7].

Sample and Experiments: We prepared polished thin sections of A-881020 and Acfer 182 and a polished slab of NWA 470. First, detailed SEM studies were performed to describe dark clasts and hydrated clasts in these meteorites. Then, microprobe analysis was done. Based on these data, some clasts were extracted from thin sections and a slab for synchrotron radiation X-ray diffraction (SR-XRD) and TEM studies. We selected representative samples for TEM analysis based on SR-XRD data. Samples were prepared by ultramicrotomy.

Results: We investigated 58, 22, and 15 dark clasts in A-881020, Acfer 182, and NWA 470, respectively, and 26 altered glass clasts (AGCs [1]) in A-881020 by SEM and microprobe. We recognized three major types of dark clasts in A-881020: (1) dark clasts that consist of magnetite (often occurring as framboidal aggregates), Fe-sulfide, Fe-Ni sulfide, dolomite, and olivine embedded in fine-grained matrix, (2) dark clasts that are similar to (1) but lack dolomite, and (3) dark clasts that contain abundant Fe-sulfide and Fe-Ni metal embedded in fine-grained matrix. In Acfer 182 and NWA 470 abundant dark clasts similar to (1) were observed. Figure 1 shows compositional variations of fine-grained matrices of the dark clasts in A-881020, Acfer 182, and NWA 470 obtained by defocused beam (5 μm in diameter) electron probe analysis. Dark clasts in Acfer 182 and NWA 470 are similar to each other. On the other hand, compositional variations of dark clasts in A-881020 are wider than within the other two meteorites.

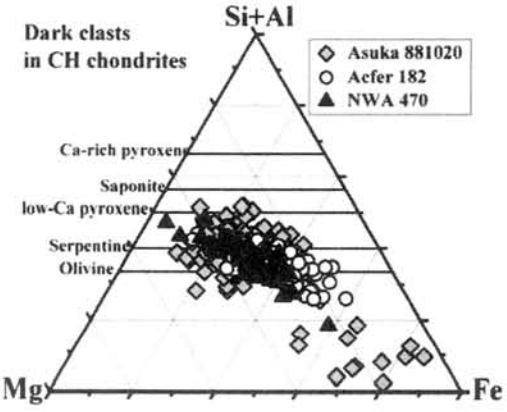

Fig. 1: Electron microprobe analyses of fine-grained matrices in dark clasts from A-881020, Acfer 182, and NWA 470.

We selected 7, 7, and 4 dark clasts from A-881020, Acfer 182, and NWA 470, respectively, and 4 AGCs from A-881020 for SR-XRD analysis. These analyses of dark clasts revealed that there are three types having different mineralogy. The most abundant type is characterized by the dominance of serpentine as the hydrated phase (serpentine-rich clasts). Major minerals include serpentine, magnetite, dolomite, pyrrhotite, kamacite, and olivine.

The next type is characterized by abundant saponite as the hydrated phase (saponite-rich clasts). This type was not found within clasts from Acfer 182 and NWA 470. Major minerals are saponite, pentlandite, pyrrhotite, olivine, magnetite, and serpentine. The third type is characterized by abundant Fe-sulfide and the absence of hydrated silicates although the clasts are mat black under optical microscope and have angular morphology that are common to the above dark and hydrated clasts. Major minerals include kamacite, pyrrhotite, olivine, low-Ca pyroxene, and magnetite.

We performed TEM observation of these three types of clasts. One clast from each type in A-881020, and a serpentine-rich one from NWA 470 were investigated. TEM observation of a serpentine-rich clast in Acfer 182 is now under way.

The TEM observations of serpentine-rich clasts in A-881020 and NWA 470 are similar to each other. In both samples, the dominating phyllosilicate is serpentine. The thickness (normal to (001)) of serpentine is often up to 10 nm. There is also a small amount of saponite that is intergrown with serpentine in both meteorites [7]. Due to the coexistence of

serpentine and saponite, compositions of phyllosilicates in these clasts obtained by analytical electron microscopy (AEM) are plotted above the solid solution line of serpentine in a (Si+Al)-Mg-Fe ternary diagram (Fig. 1). Fine-grained (<100 nm in diameter) magnetite and Fe- (and Ni-)sulfides are embedded in serpentine.

Saponite-rich clasts were found only in A-881020. The saponite-rich clast investigated is composed of fine-grained (<100 nm in diameter) Fe-(and Ni-)sulfides and magnetite embedded in saponite. The thickness normal to (001) of saponite is variable and reaches a maximum of 30 nm in some grains. Compositions of phyllosilicates obtained by AEM are plotted near the saponite solid solution line in a (Si+Al)-Mg-Fe ternary diagram (Fig. 1). Serpentine is rare.

Microprobe data of the Fe-sulfide-rich clast are plotting on the extension of the compositional trend of the saponite-rich clast. Only based on SEM and microprobe, the difference between this clast and the saponite-rich one is the relative abundance of Fe-(and Ni-)sulfides and Fe-Ni metal. However, as indicated by SR-XRD data, this clast does not contain detectable amounts of phyllosilicate. TEM observation of this clast revealed that there are poorly crystalline Si- and Fe-rich materials that fill the interstices between abundant Fe-Ni metal, sulfide, and anhydrous ferromagnesian silicates. The poorly crystalline material may be protophyllosilicate or ferrihydrite.

AGCs are unique objects found in A-881020 [3]. They are composed of a relict core of unaltered glass rimmed by altered glass. TEM observation of the altered glass in an AGC revealed that it contains poorly crystalline material. Its high-resolution TEM image suggests that it is protophyllosilicate. Most of the altered glass is poor in FeO.

Discussion and conclusions: Our data show that the most abundant type of the dark clasts is serpentine-rich. By comparing the most abundant minerals in these clasts and within the C1 clasts of [4], the latter may also belong to this type. The mineralogy of the serpentine-rich clasts determined by SR-XRD and TEM is similar to that of the heavily hydrated clasts. This is the case not only in other CHs [6], but also in the CBs [6] and CRs [8]. This study supports the idea that the most popular type of the heavily hydrated clasts in meteorites belonging to the CR clan is serpentine-rich. SR-XRD of the matrix of CRs shows variable results. Among the CRs investigated only the matrix of Renazzo contains abundant phyllosilicates. Its matrix mineralogy is similar to that of the serpentine-rich clasts. The saponite/serpentine-ratio in the Renazzo matrix is slightly higher than that in the clasts. These data suggest that serpentine-rich clasts formed under aqueous alteration conditions similar to that of the most hydrated CRs, However, the degree of aqueous alteration of the clasts was much higher than within the host CRs.

On the other hand, saponite-rich clasts were not encountered within the studied CHs except for A-881020. This type of clasts seems to be also rare in the other CHs, as well as within CBs and CRs [5, 8]. Saponite-rich clasts have higher bulk (Si+Al)/(Si+Al+Mg+Fe)-ratios than those of serpentine-rich ones. The degree of aqueous alteration of saponite-rich clasts is stronger than that of serpentine-rich ones: The former rarely contain relict ferromagnesian silicates and Fe-Ni metal. These data suggest that saponite-rich clasts were hydrated on a preexisting (precursor) parent body, which was different from that where the serpentine-rich clasts formed (see also [10]). Our data also indicate that the bulk chemistry was not greatly changed during aqueous alteration.

It is not clear, whether iron sulfide-rich clasts in this study correspond to the reduced clasts in [4] or not. If this type of clasts were formed by thermal decomposition under a reducing condition, the clasts would have been composed of a mixture of Fe-Ni metal and sulfide, magnesian olivine, and low-Ca pyroxene. In addition to these minerals, TEM observation of a clast shows that it contains Si- and Fe-rich poorly crystalline interstitial material. If the poorly crystalline material is protophyllosilicate or ferrihydrite, this type of clast may have experienced incipient aqueous alteration.

Altered glass clasts (AGCs) in A-881020 are similar to partially altered chondrules in ALH 85085 [5, 9]. However, AGCs always occur as angular and irregular shaped objects. Altered glass in AGCs is almost amorphous and richer in (Si+Al) and Mg than altered glass in the chondrules from ALH 85085. Micro-Raman spectroscopy of unaltered glass in AGCs and glassy to cryptocrystalline chondrules in the host meteorite revealed that no olivine and pyroxene Raman shift peaks were detected in the former. It means that the crystallinity of glass in AGC is systematically lower than that within the glass of the chondrules. Further detailed studies are planned in order to discuss the possibility of weak aqueous alteration on the bulk CH parent body.

References: [1] Noguchi T. et al. (2004) *Papers presented to the NIPR symposium on Antarctic Meteorites (abstract),* 62–63. [2] Bischoff A. et al. (1993) *Geochim. Cosmochim. Acta, 57,* 2631–2648. [3] Krot A. N. et al. (2002) *Meteorit. Planet. Sci., 37,* 1451-1490. [4] Grossman J. N. et al. (1988) *Earth Planet. Sci. Lett., 91,* 33-54. [5] Greshake et al. (2002) *Meteorit. Planet. Sci., 31,* 281-293. [6] Osawa T. et al. (2005) *Meteorit. Planet. Sci., 40,* 71-86. [7] Ivanova, M. A. et al. (2001) *Lunar Planet. Sci. Conf. XXXII,* #1817. [8] Endreß M. et al. (1994) *Meteoritics, 29,* 26-40. [9] Krot, A. N. (1999) *Meteorit. Planet. Sci., 35,* 1249-1258. [10] Bischoff A. (1998) *Meteorit. Planet. Sci., 33,* 1113-1122.

Feldspathic Clasts in Yamato 86032: Remnants of a Feldspathic Lunar Crust 4.4 Ga Ago.

L. Nyquist[1*], A. Yamaguchi[2], D. Bogard[1], C.-Y. Shih[3], Y. Reese[4], and H. Takeda[5], [1]Mail Code KR, NASA Johnson Space Center, Houston, TX 77058, l.nyquist@jsc.nasa.gov, [2]National Institute of Polar Research, Tokyo 173-8515, Japan, [3]Mail Code JE-23, ESCG/Jacobs Sverdrup, Houston, TX 77058, [4]Mail Code JE-23, ESCG/Muniz Engineering, Houston, TX 77058, [5]Research Institute, Chiba Institute of Technology, Narashino 257-0016, Japan.

Introduction:

Yamato 86032 is a feldspathic lunar highland breccia containing regolith and fragmental breccia components [1,2]. One ancient feldspathic clast has an Ar-Ar age of 4.35-4.41 Ga [3], and Sm-Nd isotopic systematics implying negative ε_{Nd} at that time [4], suggesting a direct link to the primordial lunar magma ocean (LMO). The absence of KREEP components [5] indicates that Y86032 may have come from regions of the moon far distant from the Procellarum KREEP Terrain (PKT) and the Apollo landing sites. White (W), light gray (LG), dark gray (DG), and impact melt (IM) bulk lithologies were identified by [6]. Six samples representing the three main lithologies were prepared by A. Yamaguchi and allocated by the NIPR for this study: LG ,28; DG ,43 ,44; IM ,33 ,30 and ,37.

Age of the protolith:

Sm-Nd analyses were made of bulk samples and mineral separates from ,28 and ,44, and of a bulk sample of ,33. Plagioclase-enriched and pyroxene-enriched samples were separated from sieved fractions <74 μm in grain size using heavy liquids of densities ρ <2.85, 2.85-3.32, and >3.32 g/cm^3. The analyses define a good isochron for an age T=4.43±0.03 Ga (Fig.1). $\varepsilon_{Nd\ CHUR}$ calculated relative to an interlaboratory-adjusted initial $^{143}Nd/^{144}Nd$ value for the **Ch**ondritic **U**niform **R**eservoir [7] is +0.19±0.13, but is more appropriately calculated as $\varepsilon_{Nd\ HED}$ = -0.64±0.13 relative to initial $^{143}Nd/^{144}Nd$ obtained in the JSC lab for HED meteorites [8]. The age is similar to the Ar-Ar age of the W lithology ,116 reported earlier [3], and to the crystallization ages of ferroan anorthosites [9]. Some uncertainty is introduced into the Ar-Ar age because ,116 is itself a feldspathic fragmental breccia [2] and contains a small amount of solar wind ^{36}Ar, and presumably lunar atmosphere ^{40}Ar. A maximum age of 4.404±0.035 Ga is obtained for ,116 if no correction is made for trapped ^{40}Ar. More probable values lie within the range 4.393±0.035 if trapped $^{40}Ar/^{36}Ar$ = 3 and 4.369±0.035 Ga if $^{40}Ar/^{36}Ar$ = 10. Because the analysed samples were breccias, both the Sm-Nd and Ar-Ar ages are lower limits to the age of the protolith; i.e., to the age(s) of the suite of rocks contributing to the breccias. However, the good linearity of the Sm-Nd isochron suggests that rocks of the protolithic suite were cogenetic, whereas the Ar-Ar age of ,116 shows the igneous formation age of the dominant component of the W lithology must be at least 4.35 Ga.

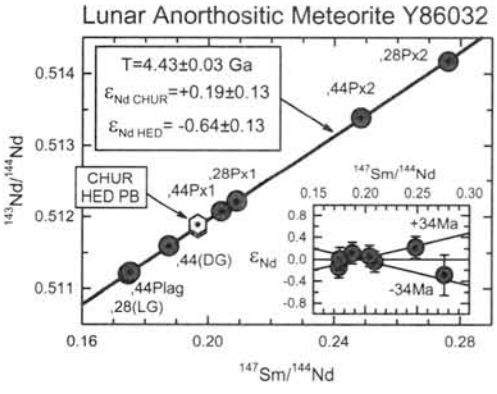

Figure 1. Sm-Nd isochron for separated phases.

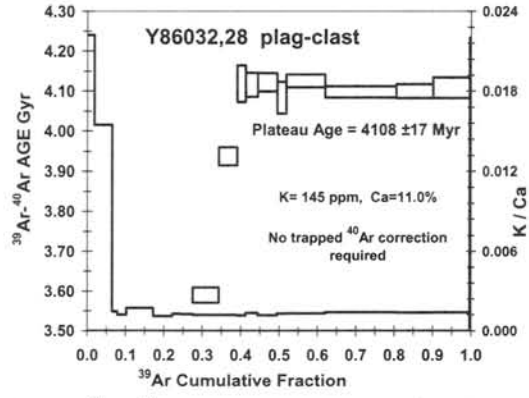

Figure 2. ^{39}Ar-^{40}Ar stepwise age spectrum for ,28.

Impact history:

^{39}Ar-^{40}Ar analysis of LG ,28 (Fig. 2) is the clue to interpreting the later impact history of Y86032.

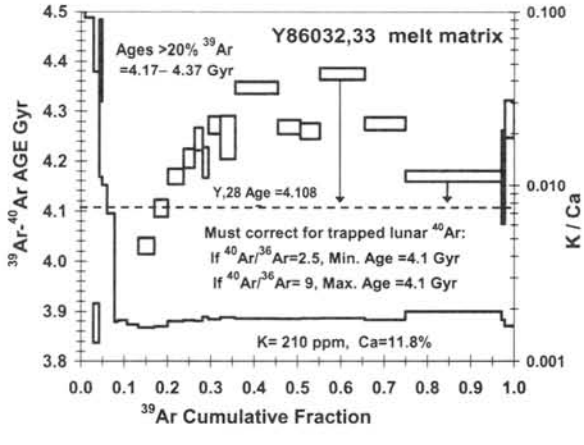

Figure 3. ^{39}Ar-^{40}Ar stepwise age spectrum for ,33.

The first ~35% of the ^{39}Ar release shows considerable diffusive loss of ^{40}Ar, but the last 6 temperature steps give constant ages averaging 4108±17 Ma. Furthermore, there is no evidence of solar wind ^{36}Ar in this lithology and no correction for trapped ^{40}Ar is required. The Ar-Ar age is interpreted as the time of brecciation of ,28, when previously accumulated radiogenic ^{40}Ar was outgassed.

The Ar release spectrum of IM ,33 is more complicated. Above ~20% ^{39}Ar release, apparent ^{39}Ar-^{40}Ar ages range from 4.17-4.37 Ga. However, ,33 contains a significant component of solar wind ^{36}Ar, indicating a prior surface history. Because IM intersects the LG lithology, the time of impact melting of ,33 can not have preceded that of LG; i.e., could not have been more than 4.1 Ga ago. To bring the maximum apparent age for ,33 down to 4.1 Gyr requires a correction for trapped ^{40}Ar assuming ^{40}Ar/^{36}Ar = 9; lower apparent ages require a smaller ^{40}Ar/^{36}Ar ratio to yield the same corrected age. We attribute the scatter in ages of individual temperature steps to in situ radiogenic ^{40}Ar not completely degassed by the event that incorporated ,33 into the breccia. The degassing time for ,33 and formation of the breccia also could, in principle, have been later than 4.1 Gyr.

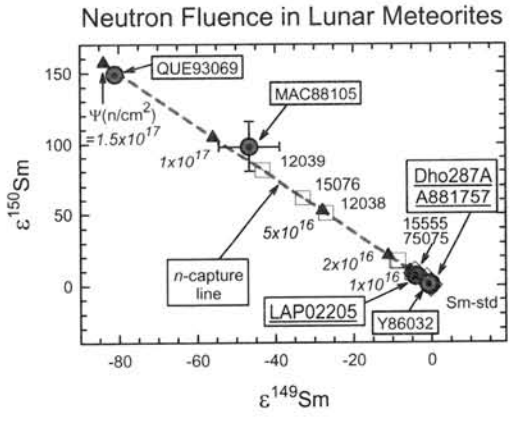

Figure 4. Sm isotopic composition of Y86032 compared to Apollo samples and other lunar meteorites as 10^{-4} deviations from terrestrial value.

Residence in a megaregolith

The Sm isotopic composition of Y86032 shows no detectable decrease in ^{149}Sm abundance due to capture of thermalized neutrons (Fig. 4). Thus, Y86032 was rather deeply buried in the megaregolith for most of its history prior to impact ejection from the lunar surface. This conclusion is consistent with near-absence of solar wind Ar from most lithologies, and near-absence of grain-surface-correlated Pb in leaches of sample ,118 from the W-lithology [10]. The U-Pb analyses of ,118 also showed this lithology was derived from a low-^{238}U/^{204}Pb source similar to that of Apollo 16 FAN 60025.

ε_{Nd} in the LMO and early lunar crust:

Our Sm-Nd age results for Y86032 confirm early formation of its protolith. Although remnants of

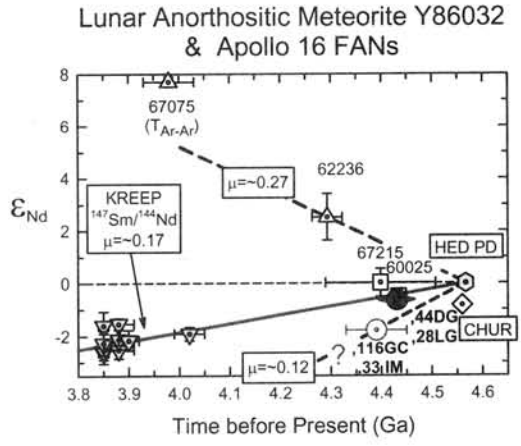

Figure 5. Evolution of ε_{Nd} with time for Y86032 lithologies, FANs, and KREEP.

different rock types are present in the breccia, the protolith was dominantly feldspathic. Modal abundances of plagioclase, olivine, low-Ca pyroxene, and augite in the LG lithology are 94.5, 4.1, 1.5, and 1.1 vol. %, respectively. With the exception of olivine and minor augite, this mineralogy closely resembles that of FANs. Furthermore, REE abundances in the W and LG litholgies are only slightly enriched relative to those in FANs [11]. Thus, it is reasonable to compare the Sm-Nd data for the Y86032 samples to those of FANs from other lunar localities, especially from the Apollo 16 site.

Fig. 5 compares ε_{Nd} from Fig. 1 to values from the literature for Apollo 16 FANs. The slightly negative value of ε_{Nd} at 4.43 Ga ago is consistent with derivation from the lunar magma ocean (LMO) following crystallization of mafic mantle cumulates.

Early crustal bombardment history:

The presence of clasts in Y86032 with different Ar-Ar ages implies multiple impact heating events, and impacts occurring during an early period of bombardment from 4.1 – 4.35 Ga ago. This observation poses the question of how these ages survived the hypothesized later cataclysmic bombardment [12]. Deep burial in the megaregolith far distant from basin-forming impacts seems a likely explanation.

References: [1] Takeda H., et al (1989) *Proc. NIPR Symp. Antarct. Met., 2,* 3-14. [2] Takeda H. et al., (2002) *LPS-XXXIII* (CD-ROM #1267). [3] Bogard D.D. et al., (2000) *LPS-XXXI* (CD-ROM #1138). [4] Nyquist L.E. et al., (2002) *LPS-XXXIII* (CD-ROM #1289). [5] Köberl C. et al. (1989) *Proc. NIPR Symp. Antarct. Met., 2,* 15-24. [6] Yamaguchi A. et al., (2004) *LPS-XXXV* (CD-ROM #1474). [7] Jacobsen S. B. and Wasserburg G. J. (1984) *EPSL 67,* 137-150. [8] Nyquist L. E. et al. (2004) *Antarct. Met., XXVIII,* 66-67. [9] Norman M. D. et al. (2003) *MAPS 38,* 645-661. [10] Tatsumoto M. and Premo W. R. al (1991) *Proc. NIPR Symp. Antarct. Met., 4,* 56-69. [11] Karouji Y. et al. (2004) *Antarct. Met., XXVIII,* 29-30. [12] Tera F. and Wasserburg G. J. (1974) *EPSL 22,* 1-21.

Carbon and hydrogen isotopic compositions of acetic acid derived from macromolecular organic matter in the Murchison. Yasuhiro Oba[1)] and Hiroshi Naraoka[2)], 1) The Graduate School of Natural Science and Technology and 2) Department of Earth Sciences, Okayama University. Okayama 700-8530, JAPAN

Introduction

Carboxylic acid is one of the most abundant solvent-extractable organic species in carbonaceous chondrites. Since the first report on meteoritic carboxylic acid in 1973 [1], a lot of attentions have been directed to the occurrence of monocarboxylic acids including acetic acid in carbonaceous chondrites [2-4]. There are some candidates for its origin and formation mechanism such as spark discharge in a molecular cloud [5], however, they have not been elucidated previously.

Besides solvent-extractable organic species, solvent-insoluble macromolecular organic matter exists as a main organic constituent, consisting more than 90% of organic matter in carbonaceous chondrites. This macromolecular organic matter is extracted by demineralization of silicate matrix. Infrared resonance (IR) and nuclear magnetic resonance (NMR) spectroscopy have revealed that it mainly consists of aromatics with many functional groups such as carboxyl and carbonyl [6, 7]. Pyrolysis of the macromolecular organic matter has been conducted to generate several polycyclic aromatic hydrocarbons [8]. So carboxylic acids may be generated by pyrolysis of macromolecular organic matter. However, such a study has not been reported previously. Stable carbon and hydrogen isotopic compositions of the carboxylic acid could have a potential to elucidate its origin and formation mechanism. The solvent-extractable carboxylic acids show ^{13}C- and D-enriched signature [2, 3]. On the other hand, bulk macromolecular organic matter is depleted in ^{13}C relative to solvent-extractable organic matter [9].

In this study, we conducted hydrous pyrolysis of macromolecular organic matter purified from the Murchison meteorite, as well as carbon and hydrogen isotopic analyses of the generated carboxylic acid. Also we conducted bulk-carbon and hydrogen isotopic analyses of macromolecular organic matter before and after the hydrous pyrolysis.

Experimental Procedures

Powdered sample of the Murchison meteorite, which was already extracted with water and organic solvent, was treated with 6M HCl and subsequently demineralized with a mixture of concentrated HF and HCl (1/1 by volume) in a Teflon^{TM} bottle by shaking at ~70°C. The residue was washed with H_2O several times to neutral pH, and subsequently washed with organic solvents. The isolated macromolecular organic matter was dried and subjected to an elemental analyzer (EA) and isotope ratio mass spectrometer (IRMS) coupled with EA to determine its CHNS concentrations and isotopic compositions, respectively. About 7mg of macromolecular organic matter was heated with 0.5ml of H_2O in a degassed Pyrex^{TM} tube at 270-330°C for 72h. After heating, the solution (pyrolysate) was separated and dried under reduced pressure in an alkaline condition. The resulting residue was dissolved in H_2O and decanted to an apparatus for cryogenic distillation. The solution was heated to ~250°C in acidic condition, transferred and trapped at nitrogen temperature.

The distillate containing carboxylic acid was analyzed by gas chromatograph (GC). Total carbon and hydrogen isotopic compositions of carboxylic acid were determined by GC/combustion and pyrolysis/IRMS, respectively. Intra-molecular carbon isotopic analysis of carboxylic acid was carried out by GC/pyrolysis/IRMS.

Results and discussion

The macromolecular organic matter contains 58.4wt% carbon with 3.02wt% hydrogen, 2.22wt% nitrogen and 10.6wt% sulfur, and the H/C atomic ratio is 0.62 before heating. After heating, the H/C atomic ratio decreases by 0.2-0.3 with increasing heating temperature, indicating that hydrogen is more thermally labile than carbon in the macromolecular organic matter. C_2-C_5 monocarboxylic acids are detected after the hydrous pyrolysis. Acetic acid (C_2) constitutes more than 90% of total mono-carboxylic acid in the pyrolysate. The amounts of generated acetic acid increase from 0.13 to 0.49 μmol/mg with increasing heating temperature (Table 1). Since the Murchison is known to contain ~1.45wt% macromolecular carbon [10], this result indicates that the macromolecule has a potential to generate ~6.7 μmol acetic acid/g meteorite. This amount is about four times higher than the amount of water-extractable acetic acid in the Murchison [2].

Bulk $\delta^{13}C$ of macromolecular organic matter decreased by ~3‰ after hydrous pyrolysis (Table 1). The generated acetic acid was ^{13}C-depleted relative to bulk macromolecular organic matter after heating, which indicate that ^{13}C-enriched components except for acetic acid were simultaneously generated during hydrous pyrolysis. Intra-molecular carbon isotopic analysis shows

that methyl group of acetic acid is enriched in ^{13}C than the carboxyl group at all temperatures. This isotopic distribution indicates that the acetic acid is generated by kinetic process, probably due to heterogeneous isotope distribution in the macromolecule.

Bulk δD of macromolecular organic matter is extremely enriched in D (~+985‰), as reported previously [9]. In contrast to bulk $\delta^{13}C$, δD of bulk macromolecular organic matter decreased dramatically after heating, down to ~+300‰ at 270°C, ~+65‰ at 300°C, and +25‰ at 330°C. This δD change implies that hydrogen of macromolecule could exchange with D-depleted water used in the hydrous pyrolysis (δD=~-70‰), or D-enriched hydrogen might be dehydrogenated preferentially from the macromolecule. δD of methyl group of acetic acid is almost the same value (~-160‰) at all temperatures, being extremely D-depleted relative to bulk macromolecular organic matter. These results also indicate that D-enriched component except for acetic acid were simultaneously generated during hydrous pyrolysis, or methyl hydrogen of acetic acid might be exchanged with H_2O hydrogen (δD=~-70‰) because α-hydrogen of carboxylic acid could partly exchange with hydrogen in the extraction water [11].

Although the extremely ^{13}C and D-enriched organic compounds in carbonaceous chondrites have been referred as interstellar origin, it should be noted that carboxylic acid formation may occur by hydrothermal activity on meteorite parent bodies.

References

[1]Yuen G.U. and Kvenvolden K.A. (1973) *Nature*, 246, 301-303. [2]Yuen G.U. et al. (1984) *Nature*, 307, 252-254. [3]Krishnamurthy R.V. et al. (1992) *GCA*, 56, 4045-4058. [4]Naraoka H. et al. (1999) *Origins Life Evol. Biosphere*, 29, 187-201. [5]Miller S.L. (1955) *J. Am. Chem.Soc.*, 77, 2351-2361. [6]Hayatsu R. et al. (1977) *GCA*, 41, 1325-1339. [7]Cody G.D. et al. (2002) *GCA*, 66, 1851-1865. [8]Sephton M.A. et al. (1998) *GCA*, 62, 1821-1828. [9] Kerridge J.F. et al. (1987) *GCA*, 51, 2527-2540. [10] Mullie F. and Reisse J. (1987) Organic matter in carbonaceous chondrites. In *Topics in Current Chemistry*, 139 (eds. M. J. S Dewer *et al.*), pp. 83–117. Springer-Verlag, Berlin, Germany. [11] Fuller M. and Haung Y. (2003) *Meteorit. Planet. Sci.*,, 38, 357-363.

Table 1 Chemical and isotopic distributions* of macromolecular organic matter and generated acetic acid from the Murchison.

	Murchison macromolecular organic matter					acetic acid				
	H(wt%)	C(wt%)	H/C	$\delta^{13}C$	δD	μmol /mg	$\delta^{13}C_{total}$	$\delta^{13}C_{methyl}$	$\delta^{13}C_{carboxyl}$	δD_{methyl}
pre-heating	3.02	58.4	0.62	-12.70	+986±3	-	-	-	-	-
270°C	1.34	38.5	0.42	-15.68	+307±17	0.13	-20.8±0.2	-19.1±0.2	-22.5±0.2	-152±9
300°C	1.74	53.0	0.39	-16.15	+64±14	0.25	-26.7±0.1	-20.1±0.6	-32.6±0.6	-167±0.4
330°C	1.83	70.8	0.31	-16.09	+25	0.48	-27.0±0.0	-25.7±0.9	-28.3±0.9	-161±6

*Standard deviations are calculated by two measurements. δD of methyl hydrogen is calculated by isotopic mass balance because carboxyl hydrogen is easily exchanged with ambient H.

Hydrothermal alteration experiments of the Allende CV3 chondrite under highly alkaline conditions. Ichiro Ohnishi[1] and Kazushige Tomeoka[1,2], [1]Graduate School of Science and Technology, Kobe University, [2]Department of Earth and Planetary Sciences, Faculty of Science, Kobe University, Nada, Kobe 657-8501, Japan. Correspondence author's e-mail address: ichiro@kobe-u.ac.jp

INTRODUCTION:

Carbonaceous chondrites of petrologic type 1-3 contain various amounts of hydrous minerals such as phyllosilicates. These hydrous minerals are regarded to have been formed largely by aqueous alteration on the meteorite parent bodies. Many workers [1-11] have conducted hydrothermal alteration experiments of meteorites to find a clue to the conditions of aqueous alteration of the meteorites. All the past experiments have been conducted exclusively under acidic and neutral conditions [1-11]. We here present the results of hydrothermal alteration experiments of the Allende CV3 chondrite performed under alkaline conditions. We intended to compare the results with those performed under acidic and neutral conditions.

EXPERIMENTAL:

Allende samples (3 mm×3 mm×10 mm in size, ~0.3 g) and 1N-NaOH solutions (pH~14, ~0.5 g) were sealed in gold capsules, loaded into an autoclave, and heated at 300 ℃ and 0.5 kb for 1 week and 7 weeks. After each run, the recovered sample was examined by a binocular optical microscope and a scanning electron microscope (SEM) (JEOL JSM-6460LAII) equipped with an energy-dispersive X-ray spectrometer (EDS). Part of the sample was crushed to powder and analyzed by an X-ray powder diffractometer (XRD) (Rigaku RINT2000). Polished sections were made from the rest part of the sample and examined with the SEM-EDS.

RESULTS:

Run duration: 1 week

The recovered sample was covered with a thin layer of powdery material. SEM observations show that the powdery material consists of fluffy aggregates (10-50 μm in size) of Mg-Fe silicate with minor amounts of small euhedral grains of Ca-phosphate (<5 μm in size). Subhedral to euhedral grains of Fe-oxide (<10 μm in size) also occur together with Mg-Fe silicate on the inside wall of the Au capsule. From XRD measurements, the Mg-Fe silicate is probably a mixture of serpentine and smectite.

XRD measurements of the recovered sample show small peaks corresponding to serpentine and smectite in addition to the peaks for natural Allende.

SEM observations of polished sections reveal that most Fe-rich olivine grains (<10 μm in size) in the matrix have been partially replaced by phyllosilicate from their outside. From composition, we identify the phyllosilicate as serpentine. Rounded aggregates of Ca-rich pyroxene and andradite, which are common in natural Allende matrix, appear to have been little affected. Bulk chemical compositions of the matrix obtained by EDS broad-beam analyses indicate that the matrix are enriched in Na, and depleted in S, Ca, Fe, and Ni compared with the matrix of natural Allende.

Mesostases of chondrules have been extensively replaced by phyllosilicate. From composition, the phyllosilicate can be identified as a mixture of serpentine and smectite. Although enstatite in chondrules has been partially replaced by serpentine, Mg-rich olivine and Ca-rich pyroxene in chondrules remain almost unaltered.

Run duration: 7 weeks

Smectite, serpentine, Ca-phosphate, and Fe-oxide occur on both the surface of the recovered sample and the inside wall of the Au capsule, as in the sample run for 1 week. The abundance of Fe-oxide is higher than that in the sample run for 1 week.

XRD measurements of the recovered sample show that diffraction peaks of serpentine and smectite are much larger than those in the sample run for 1 week, whereas peaks of olivine are smaller.

SEM observations reveal that most Fe-rich olivine grains in the matrix have been extensively replaced by serpentine. In places, relic olivine grains (<3 μm in size) remain. Aggregates of Ca-rich pyroxene and andradite have been partially replaced by serpentine. Broad-beam EDS analyses indicate that the major element abundances of the matrix are similar to those of the sample run for 1 week except that the S/Si, Fe/Si, and Ni/Si ratios are slightly lower.

The mesostases of chondrules have been extensively replaced by mixtures of serpentine and smectite. Enstatite in chondrules has been almost completely replaced by serpentine, and most of them show pseudomorph textures. However, Mg-rich olivine and Ca-rich pyroxene remain almost unaltered.

DISCUSSION:

From our experimental results, it is evident that the degree of aqueous alteration of Allende increases progressively with increasing run duration under alkaline conditions. In both samples run for 1 week and 7 weeks, the matrix has been more extensively altered than chondrules. In the sample run for 7 weeks, most of Mg-rich olivine phenocrysts in chondrules remain unaltered, whereas Fe-rich olivine

grains in the matrix have been extensively replaced by phyllosilicate. These results contrast with those of the previous hydrothermal alteration experiments of Allende carried out under acidic and neutral conditions [1-5]. In the previous experiments, the matrix shows relatively minor effects of alteration compared with chondrules and CAIs [1-5]. We suggest that the difference is probably related to the difference in resistance of olivine to aqueous alteration under different pH conditions.

Our results also reveal differences in phyllosilicate mineralogy between the runs performed under acidic/neutral conditions and alkaline conditions. Under acidic conditions, chlorite has been formed together with serpentine and talc in chondrules, whereas under neutral conditions, the dominant alteration products in both chondrules and matrix are saponite and serpentine [5]. On the other hand, under alkaline conditions, serpentine occurs predominantly in both chondrules and matrix, although minor amounts of smectite occurs together with serpentine in the chondrule mesostases. The difference in phyllosilicate mineralogy is probably related to the differences in precursor minerals altered under different pH conditions. Under acidic and neutral conditions, glass and anorthite in the chondrule mesostases are preferentially altered and Si and Al are released to aqueous solutions, thus producing a condition favorable for the formation of chlorite and saponite. On the other hands, under alkaline conditions, Fe-rich olivine in the matrix is preferentially altered and Mg, Fe and Si are released to aqueous solutions, producing a condition favorable for the formation of serpentine.

The present experimental results, combined with previous experimental results [1-5], suggest that pH value of aqueous solutions is an important factor to control both alteration degree of chondrite constituents and phyllosilicate mineralogy.

References:

[1] Tomeoka K. and Kojima T. (1995) *Papers Presented at 20th Symp. Antarctic Met.*, 251-253. [2] Tomeoka K. and Kojima T. (1995) *Meteorit.*, ***30***, 588. [3] Kojima T. and Tomeoka K. (1998) *Papers Presented at 23rd Symp. Antarctic Met.*, 58-60. [4] Kojima T. and Tomeoka K. (1999) *Meteorit. Planet. Sci.*, ***34***, A67. [5] Kojima T. and Tomeoka K. (2000) *Meteorit. Planet. Sci.*, ***35***, A90. [6] Brearley A. J. and Duke C. L. (1998) *LPS **XXIX***, #1782. [7] Duke C. L. and Brearley A. J. (1998) *Meteorit. Planet. Sci.*, ***33***, A43. [8] Duke C. L. and Brearley A. J. (1999) *LPS XXX*, #1782. [9] Jones C. L. and Brearley A. J. (2000) *LPS **XXXI***, #1204. [10] Brearley A. J. and Jones C. L. (2002), *Meteorit. Planet. Sci.*, ***37***, A23. [11] Sato K. et al. (2002), *Meteorit. Planet. Sci.*, ***37***, A126.

OXYGEN ISOTOPES AND REE ABUNDANCES OF LITHIC MATERIALS IN THE BEGAA LL3 CHONDRITE. R. Okazaki and T. Nakamura. Department of Earth and Planetary Sciences, Faculty of Science, Kyushu University, Hakozaki, Higashiku-ku, Fukuoka 812-8581, Japan (okazaki@geo.kyushu-u.ac.jp).

Introduction: The Begaa LL3 chondrite was collected from southeast Morocco in 1999 [1]. Two lithic materials, 3mm in apparent diameter, were found in a polished section. Unlike usual chondrules, these lithic materials are much larger than the mean chondrule size of LL chondrites (0.9mm [2]) and show white internal reflections under a reflected light microscope. Here we report characteristics of the two Begaa lithic materials in terms of major/minor element abundances, oxygen isotope compositions, and rare earth element (REE) abundances.

Experimental procedures: A polished section with 150 μm thick was prepared from the Begaa chondrite. The polished section was investigated with a polarizing microscope under reflected light and with a scanning electron microscope (SEM) before and after ion microprobe analyses. Chemical compositions of the two lithic materials and their constituent minerals were determined with an electron microprobe analyzer at the Kyushu Univ. Oxygen and REE measurements were performed with a cameca 6f ion microprobe at the Kyushu Univ. For the oxygen measurements, the 0.6nA Cs^+ primary ion beam was focused in aperture-illumination mode to produce a ~30μm spot. The secondary mass spectrometer was operated at 9.5kV with a mass resolving power of 5500 and a 75eV energy window. ^{16}O was measured with the faraday cup and $^{17,18}O$ were measured with the electron multiplier. The normal-incident electron flood gun was used for charge compensation. A San Carlos olivine was used for standardization. REE abundances were determined following the method described in [3]. The 2nA O^- primary beam was focused in critical-illumination mode to ~30μm. The secondary-ion mass spectrometer was operated at 9.5kV accelerating voltage, with an 80eV offset, a 50eV energy window, and a mass resolving power of ~500.

Results and discussion: The optical microscope and SEM observation revealed that the Begaa chondrite preserves the chondritic textures, not brecciated. Chondrules in the specimen are well recognized, which is consistent with the announced petrologic type of 3. Our electron microprobe analyses for matrix olivines show the coefficient of the variation in Fa# is 19%, with the mean Fa# of 30. This indicates that the subtype would be 3.8 for this meteorite [4]. Most of the chondrules are 0.5-1mm in apparent diameter, ranging within the typical chondrule size, while the two lithic materials (hereafter BLM-1 and BLM-2) are unusually large. The BLMs consist mainly of magnesian olivine, magnesian low-Ca pyroxene, and anorthitic glass or plagioclase: Fo_{82-89} and An_{87-94} for BLM-1, and Fo_{77-81} and An_{75-87} for BLM-2, respectively. The Fo#s are relatively constant at the cores and rims of the BLMs. Plagioclases are stoichiometric and could be crystalline. Chemical compositions of pyroxenes are shown in Fig. 1. The outer layers of the BLMs consist predominantly of low-Ca pyroxenes, suggesting the formation of pyroxene from interaction between olivine and Si-rich gas [5]. The bulk chemical compositions of BLMs are essentially same as those of Fe-Mg chondrules, although the presence of anorthitic glass is controversial.

Oxygen isotopic ratios were determined for olivine grains in BLM-1 and BLM-2. Most of the data plot close to the TFL (Fig. 2), suggesting that the lithic materials could originate from a gas reservoir similar to those for Earth or E-chondrite parent material. No clear ^{16}O excess was observed, which is unlike plagioclase-rich inclusions where ^{16}O excess are found in variable degrees (e.g., [6]).

Considering the modal abundances and chemical compositions of constituent minerals along with oxygen isotope compositions, we suggest that both of the BLMs may have been derived from precursory material similar to those for type IIAB chondrules. The major element abundances of the lithic materials are close to the typical compositions of type IIAB chondrules but apparently depleted in Na and K (Na_2O=0.05 and 0.25wt%, K_2O=0.03 and 0.04wt% for BLM-1 and BLM-2, respectively). Thus the important question to be addressed is how the Na and K were depleted. REE abundances of anorthitic glass (or crystalline plagioclase) in the BLM-2 exhibit a fractionated REE pattern: LREE>HREE fractionation with positive Eu anomaly (Fig. 3). This REE pattern is quite similar to those for igneous materials such as acapulcoites [7], but different from those for mesostasis glass of porphyritic olivine chondrules [8] in which the patterns are flat to the CI chondrite abundance. It is likely that the LREE/HREE fractionation and the positive Eu anomaly are resulted from fractional crystallization, suggesting that the Begaa lithic materials have experienced long duration heating and/or slow cooling. The compositional variation observed in pyroxene (Fig. 1) is consistent with the crystallization at slow cooling rate.

Based on the bulk compositions, the liquidus temperature of the BLMs is around 1650-1600 °C [9]. Plagioclase compositions set the lower limit for the

temperature of 1400°C during loss of Na and K. The oxygen fugacity during the heating and the cooling should be high (fO_2>10^{-11} atm; [10]) sufficient to prevent reducing olivine. To account for the depletion of Na in BLMs (only 3% and 15% of the average Na content of type II chondrules [11] for BLM-1 and BLM-2, respectively) at least 2 hours are necessary [12] even if 1530°C isothermal heating (fO_2~5x10^{-10}atm) is assumed. Again, the occurrence of low-Ca pyroxene predominantly in the outer layer of BLMs suggests that the heating episode resulting in the Na loss would have occur in the nebula, not in the Begaa meteorite parent body.

References: [1] http://www.meteorite.fr [2] Scott E. R. D. (1996) in *Chondrules and the Protoplanetary Disk* (R. H. Hewins et al., eds.), pp. 87-96. [3] Zinner E. and Crozaz G. (1986) *Intl. J. Mass Spectr. Ion Proc.* 69, 17-38. [4] Sears D. W. G. and Dodd R. T. (1988) in *Meteorites and the Early Solar System* (J. F. Kerridge et al., eds.), pp. 3-31. [5] Tissandier L. et al. (2002) *M&PS 37*, 1377-1389. [6] Maruyama S. et al. (1999) *EPSL 169*, 165-171. [7] Patzer A.et al. (2004) *M&PS* 39, 61-85. [8] Pack A. et al. (2004) *LPS XXXV*, Abstract #-2062. [9] Hewins R. H. and Radomsky P. M. (1990) *Meteoritics 25*, 309-318. [10] Yada T. et al. (1996) *Proc. NIPR Symp. Antarct. Meteorites 9*, 218-236. [11] Jones R. H. *GCA 54*, 1785-1802. [12] Yu Y. and Hewins R. H. (1998) *GCA 62*, 159-172.

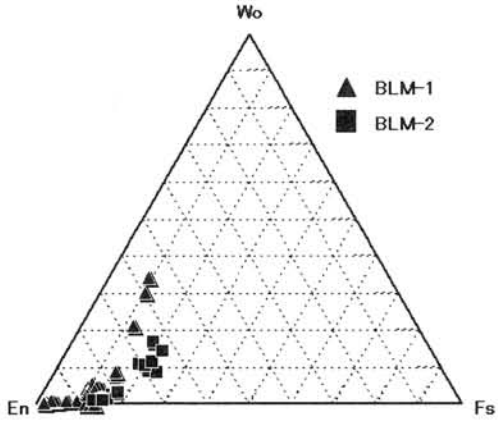

Fig. 1. Pyroxene compositions of the Begaa lithic materials (BLMs).

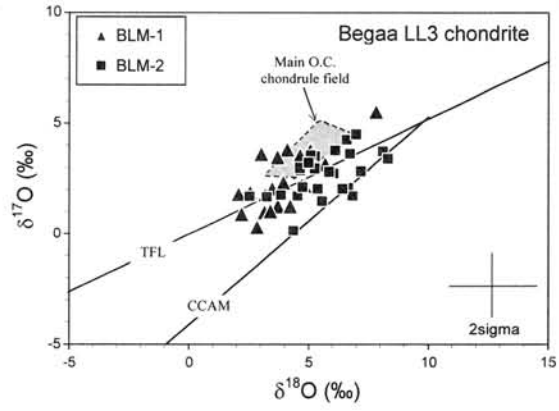

Fig. 2. Oxygen isotopic compositions for the Begaa lithic materials (BLMs). Most of the analyzed olivines in the BLMs lie on the terrestrial fractionation line (TFL).

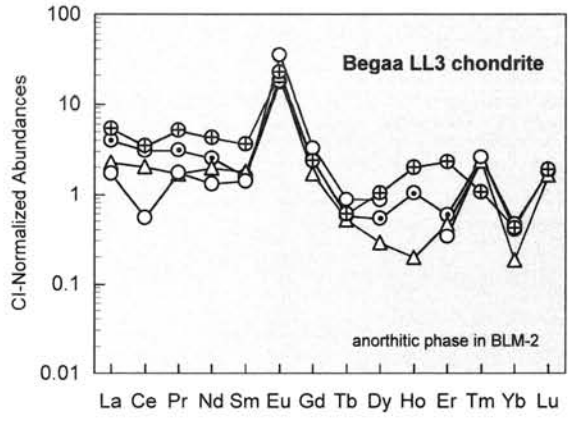

Fig. 3. REE abundances of anorthitic glass in one of the Begaa lithic materials (BLM-2).

Terrestrial atmospheric N and light noble gases in lunar soils: Non-magnetic Earth?

Minoru Ozima
Graduate School of Earth Planetary Science, University of Tokyo, Tokyo 113-0033, Japan (EZZ03651@nifty.ne.jp).

Solar wind (SW) implanted in lunar soils contains not only components from the Sun, but also non-solar components including N and light noble gases. With the use of published data [1,2], Ozima et al. [3] showed that non-solar components of N and He, Ne, Ar can be attributable to the terrestrial atmospheric components; the observed data for these elements are well explained in terms of a mixing between the terrestrial components and the solar components. From numerical calculation Seki et al. [4] showed that a substantial amount of terrestrial atmospheric N and Ar (and possibly Ne, He) can be picked up from the ionopause by the Solar Wind (SW) and transported to the moon, if there was no geomagnetic field (GMF). We therefore hypothesized that GMF was absent in an early Earth when the terrestrial N and Ar were implanted in the lunar ilmenites (Apollo 17, 14, 12). In this paper, we discuss the implications of this non-magnetic Earth hypothesis on the early evolution of the Earth.

A non-magnetic Earth – when? The non-magnetic Earth hypothesis suggests that during the time when the terrestrial components (with the SW) were implanted in the lunar soils the Earth must have been non-magnetic. Although there is no direct method to estimate the SW surface exposure age of ilmenite grains, we may impose some constraint on the age. The SW implantation age of an ilmenite grain corresponds to the time when a grain happened to be placed on the very top of the lunar soil. For this, an ilmenite grain must have in the first place been disintegrated from a host rock. All the ilmenite samples used in our study [3] are from Apollo (17, 14, 12) breccias. From a large number of high quality ^{40}Ar-^{39}Ar ages obtained for impact poikilitic melts separated from Apollo breccias, Dalrymple and Ryder [5] concluded that the Apollo breccias were essentially formed at about 3.9 Ga. We assume that the disintegration of a single ilmenite grain from a host rock and its subsequent surface exposure in general coincided with the formation of the breccias, which was about 3.9 Ga ago. In support of this assumption, we note that the Monte-Carlo simulations [6] for a trajectory of a single grain test particle initially placed in soil interior showed that chances for surface exposure of a grain becomes exponentially decreased with the initial burial depth. This suggests that SW implantation on a grain was essentially attributable to the first surface exposure event. The latter event can reasonably be attributed to the time of the breccia formation, that is, to about 3.9 Ga ago. It is then tempting to speculate that the appearance of a robust geomagnetic field was no earlier than 3.9 Ga.

N-R transition: During geomagnetic field reversal, the dipole filed is generally assumed to diminish essentially to zero. If this were the case, we would expect an enhanced flux of terrestrial components (hereafter Earth Wind or EW) during the N-R transition. The occurrence frequency of the geomagnetic field reversal is about 5 times per Ma (in the Cenozoic Era) and the N-R transition is of the order of 10^3 – 10^4 years, which are comparable to the SW exposure duration. (The SW exposure duration of an ilmenite grain can be estimated by dividing the observed amount of implanted SW in ilmenite by a SW flux.) Since the diminished GMF periods correspond to about 0.5-5% of the Cenozoic Era, the chance to see the record of a N-R

transition in a single ilmenite grain in recent soils may not be null. In this regard, it is worth noting that a Monte Carlo calculation suggests that the top 5 mm layer of the lunar regolith essentially formed in the Cenozoic Era [7, 8].

Oxygen isotopic ratios in lunar soils: Recently, Hashizume and Chaussidon [9] reported a very interesting discovery of exotic oxygen in metallic particles in Apollo breccias which is not related to the terrestrial O by a common mass-dependent isotopic fractionation. On the basis of the depth profile of the implanted O-isotopic ratios in the metal grains, they suggested that the exotic O represented the protosolar nebula. We suggest that the EW (*E*arth *W*ind) from a non-magnetic Earth might be an alternative explanation for the exotic O. In the early Earth prior to the full development biogenic O, CO was likely to be a major atmospheric constituent. It is then conceivable that photochemical dissociation of the CO in the upper atmosphere [10] gave rise to a non-mass dependent isotopic fractionation, which may explain the exotic oxygen isotopic compositions in lunar metal particles observed by Hashizume and Chaussidon [9].

References

[1] Hashizume K. et al. (2000) *Science,* **290**, 1142-1145. [2] Heber V.S. et al. (2003) *Astrophysical J.* **597**, 602-614. [3] Ozima M. et al. (2005) *Nature* (under review), [4] Seki K. et al. (2005) *NIPR Antarctic Meteorite Symposium* (this volume). [5] Dalrymple B. and Ryder G. (1996) *JGR*, **101**, 26069-26084. [6]. Borg J. et al., (1976) *EPSL*, **29**, 161-174. [7] Langevin Y. and Arnold, J.R. (1977) *Ann. Rev. Earth Planet. Sci.* **5**, 449-489. [8] Langevin Y. and Maurette, M. (1976) *Proc. Lunar Sci. Conf.* **7**, 75-91. [9] Hashizume K. and Chaussidon M. (2005) *Nature* **434**, 619-621. [10] Bally et al. (1982) *Astrophysical J.* **255**, 143-148.

Matrix olivine as a carrier of large $\Delta^{17}O$ in the NWA 753 R3.9 chondrite. Y. Ozono[1], T. Nakamura[1], T. Miyamoto[1] and M. Kusakabe[2], [1]Dept. of Earth Planet. Sci., Fac. of Sci., Kyushu Univ., Hakozaki, Fukuoka 812-8581, Japan, [2]Inst. For Study of the Earth's Interior, Okayama Univ., Misasa, Tottori 682-0193, Japan.

R chondrites are known to have oxygen isotope compositions with the highest $\Delta^{17}O$ amongst all meteorite classes [1]. Greenwood et al. [2] have conducted O isotope analysis of chondrule silicates and magnetites in PCA-91241 R chondrite and found that silicates and magnetites have O compositions similar to those in LL chondrites. Thus, they predict that the carrier of the large $\Delta^{17}O$ in R chondrites resides in matrix. In the present study, mineralogical and oxygen isotope signatures of the NWA 753 R3.9 chondrite were investigated in detail, in order to identify principal phases responsible for the high whole-rock $\Delta^{17}O$ values of R chondrites and to decipher nebular and parent-body processes that established the unique oxygen composition.

We prepared a large polished slice, with a dimension of 1 cm x 2 cm, of NWA 753 R3.9 chondrite. Although most R chondrites having been studied are breccias [3], our slice exhibits non-brecciated texture where many well-defined rounded chondrules up to 3 mm in diameter are present. Chondrule/matrix volume ratio is approximately 1. Electron microprobe analysis showed that Fa# of olivine varies between chondrules from Fa18 to Fa42 with a peak around Fa38 (Fig. 1.), confirming the weak thermal metamorphism experienced by this meteorite. Many coarse olivines of chondrules and of isolated fragments show Fe-Mg zoning. Some chondrules consist of core olivine with Fa18~20 and outer one with Fa38. Both high- and low-Ca pyroxenes occur and their Fe/Mg ratios are variable. Coarse pyrite occurs in both chondrules and matrix, while Fe-oxides are minor.

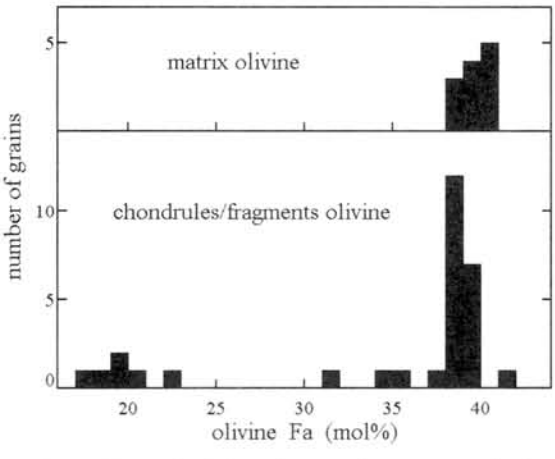

Fig. 1. Fa# of olivines in matrix and chondrules or fragments.

Synchrotron X-ray diffraction analyses, performed at photon factory of the high-energy accelerator research organization, showed that matrix consists mainly of anhydrous silicates including Fe-rich olivine, low-Ca pyroxene, and albitic plagioclase (Fig. 2). No hydrous phases are detected. Scanning electron microscope observation of the matrix revealed that it is an aggregate consisting of distinct grains of small equigranular olivines less than 1μm in size, with relatively homogeneous Fe/Mg ratios at Fa38~40 (Fig. 1). The texture differs from that of heated hydrous carbonaceous chondrites that are rich in bundles of decomposed fibrous serpentine. These facts suggest that the matrix is neither aqueous-alteration products nor dehydration products of hydrous phases.

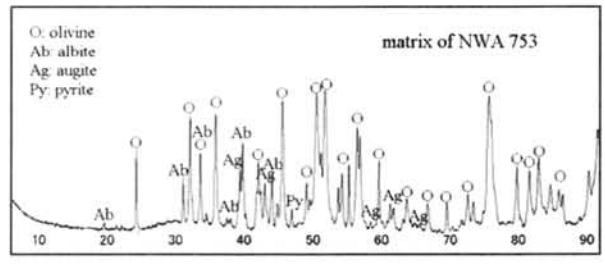

Fig. 2. X-ray diffraction pattern of a small piece of matrix.

The oxygen isotope ratios of a whole-rock meteorite were determined by a mass spectrometer with a CO_2 Laser-BrF_5 fluorination system [4] and those of silicates in both chondrules and matrix were measured by a secondary ion mass spectrometer [5]. The average whole-rock $\delta^{18}O$ and $\delta^{17}O$ values are 6.52‰ and 6.00‰, respectively, with $\Delta^{17}O$ of 2.61‰ (Fig. 3). Chondrules tend to have $\Delta^{17}O$ values lower than that of the whole rock and make clusters close to the slope-1 mixing line in the $\delta^{18}O$-$\delta^{17}O$ field (Fig. 3). On the other hand, matrix silicates have higher $\Delta^{17}O$ with an average of 3‰ (Fig. 3). The high $\Delta^{17}O$ of the matrix clearly indicates that the major contributor of the high $\Delta^{17}O$ of this R chondrite is small silicates of mainly olivine in the matrix (Fig. 4).

The high $\Delta^{17}O$ of matrix silicates could be the result of isotope exchange reactions between high-$\Delta^{17}O$ water having O composition of H_2O nebular gas [6] and low-$\Delta^{17}O$ silicates having CAI oxygen compositions [6], under a condition of water/silicate oxygen molar ratios close to 4 and temperatures around 300°C. In the calculation of

oxygen isotope fractionation at 300°C between water and olivine, fractionation factors given in [7] were used. The obtained water/silicate ratio of 4 is the highest value expected from the solar system abundance of elements. The lack of evidence of aqueous alteration in the matrix silicates requires a very low water/silicate ratio in the parent body of this meteorite. Therefore, it is suggested that the matrix silicates had already been at high $\Delta^{17}O$ at the time of the parent-body formation, in consequence of oxygen exchange reactions taken place in a hot region of the solar nebula.

References:

[1] Weisberg M. K. et al. (1991) *GCA* 57, 1079-1091. [2] Greenwood E. F. et al. (2000) *GCA 64,* 3897-3911. [3] Rubin and Kallemeyn G. H. (1994) *Meteoritics* 29, 255-264. [4] Kusakabe et al. (1994) *J. Mass Spectrom. Soc. Jpn.* 52, 205-212. [5] Akaki T. and Nakamura T. (2005) *GCA*. in press. [6] Clayton R. N. and Mayeda T. K. (1984) *EPSL* 67, 151-161. [7] Zheng Y. F. (1993) *GCA* 57, 1079-1091.

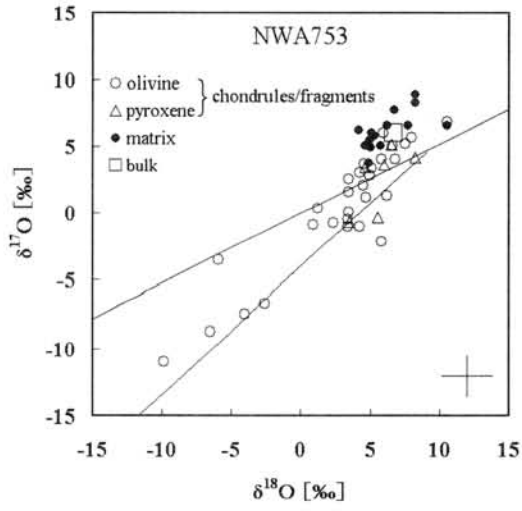

Fig. 3. Oxygen isotope ratios of a whole-rock sample (bulk) and silicates in both chondrules and matrix.

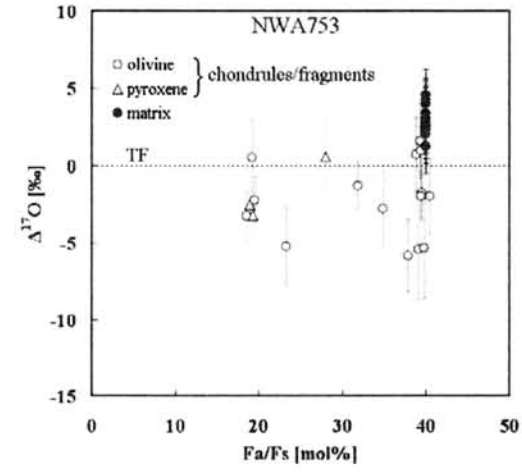

Fig. 4. Relationship between $\Delta^{17}O$ and Fa# or Fs# of olivine and low-Ca pyroxene, respectively.

Noble gas and oxygen isotopes of new CH chondrite, SaU 290 with abundant solar gases.

J. Park[1], R. Okazaki[2], K. Nagao[1], R. Bartoschewitz[3], M. Kusakabe[4] and M. Kimura[5], [1]Laboratory for Earthquake Chemistry, Graduate School of Science, University of Tokyo, Hongo, Bunkyo-ku, Tokyo 113-0033, Japan. E-mail: jisun@eqchem.s.u-tokyo.ac.jp, [2]Department of Earth and Planetary Sciences, Faculty of Sciences, Kyushu University, Hakozaki, Fukuoka 812-8581, Japan. [3]Bartoschewitz Meteorite Lab, Lehmweg 53, D-38518 Gifhorn, Germany, [4]Institute for Study of the Earth's Interior, Okayama University, Misasa, Tottori-ken 682-0193, Japan. [5]Ibaraki University, Mito 310-8512, Japan.

Introduction: A new CH-like-chondrite, Sayh al Uhaymir 290 (SaU 290, nicknamed SaU 30R) was found in Adam County, Oman, by Rainer and Claudia Bartoschewitz, 2004. They found this new chondrite on the gravel plateau of Miocene fresh-water limestone of Middle Fars group, during the natural science expedition. SaU 290 was recovered as broken 64 pieces, the total mass of 1.796 kg, within a distance of 10 m approximately. SaU 290 will be officially named in the Meteorite Bulletin, 2005 [1]. At first, it was thought as an E 3 anomalous enstatite chondrite [2]. But, SaU 290 has been classified as CH chondrite, because it has abundant 20~30-micron-sized chondrules and Fe-Ni metal grains. Its oxygen isotopic compositions plot in the area of CR-and CH-clans.

Experimental methods: SaU 290 was analyzed by using the mass-spectrometric system (modified-VG 5400 / MS-II). 0.0110 g of SaU sample was prepared for total melting experiment (TM) at the temperature of 1800 °C and 0.1173 g for stepwise heating method (SH) with 11 different temperature steps (400, 600, 700, 800, 900, 1000, 1100, 1200, 1300, 1500 and 1800 °C), in order to extract the noble gases.

Extracted gases at each temperature were purified using Ti-Zr getters heated at 750 °C. At first He and Ne were separated from Ar, Kr and Xe by retaining the heavier noble gases on a charcoal trap held at liquid N_2 temperature. After isotopic compositions of He and Ne were measured, the Ar, Kr and Xe were desorbed from the charcoal trap followed by separation using a cryogenic-trap and their isotopic compositions were determined.

Results and discussion: Table 1 shows the cosmic-ray exposure ages (T_{21}), production rate of ^{21}Ne (P_{21}), and K-Ar ages (T_{40}) from total melting and stepwise heating methods. The calculated T_{21} from TM and SH are 1.4 m.y. and 1.3 m.y., and T_{40} are 3.11 ± 0.21 b.y. and 3.09 ± 0.21 b.y. respectively.

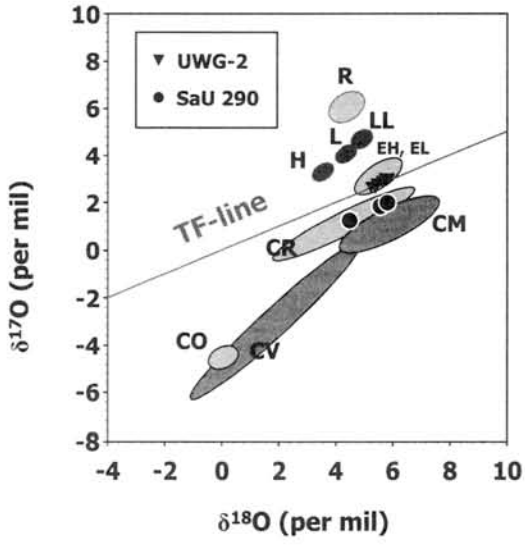

Fig 1. Oxygen isotope compositions of SaU 290. (UWG-2 is the standard terrestrial sample (garnet).

Oxygen isotope analyses of SaU 290, weighed about 2 mg, were organized three times at the Institute for Study of the Earth's Interior, Okayama University, with the mass spectrometer (modified VG-SIRA12) connected on-line to a 12W CO_2 laser extraction system (Fig 1). The $\delta^{17}O$ and $\delta^{18}O$ values are 1.83‰ and 5.58‰, 1.99‰ and 5.83‰, 1.24‰ and 4.51‰, respectively. The SaU 290 plots on the area of CR chondrite. The oxygen isotopic evidence indicates that SaU 290 belongs to CR-clan. The deviation observed in oxygen isotope graph (Fig 1.) was due to heterogeneity of the samples.

The elemental abundances of heavy noble gases in SaU 290 CH chondrite are presented in Fig 2. The observed elemental ratios $(^{36}Ar/^{132}Xe)_{trapped}$ and $(^{84}Kr/^{132}Xe)_{trapped}$ for this meteorite from total melting method is 350 and 2.23, respectively, which falls above Q gas. Data from stepwise heating method in

Table 1. Cosmic-ray exposure age (T_{21}) and K-Ar age (T_{40}) in SaU 290.

SaU 290	^{21}Ne	$(^{22}Ne/^{21}Ne)_c$	P_{21}	T_{21}	^{40}Ar	*K	T_{40}
	10^{-8} cm^{3}STP/g		10^{-8} cm^{3}STP/g/m.y.	m.y.	cc/g	ppm	b.y.
TM	0.436	1.11	0.319	1.4	1.02E-05	317.1	3.11 ±0.21
SH	0.418	1.11		1.3	1.01E-05	317.1	3.09 ±0.21

(TM: Total melting method, SH: Stepwise heating method, *K content [1], $(^{22}Ne/^{21}Ne)_c$ = 1.11 of average chondritic value and production rate of P_{21} are used from [3], Chemical composition was assumed as CV. F_{cv}=0.96 for P_{21}.)

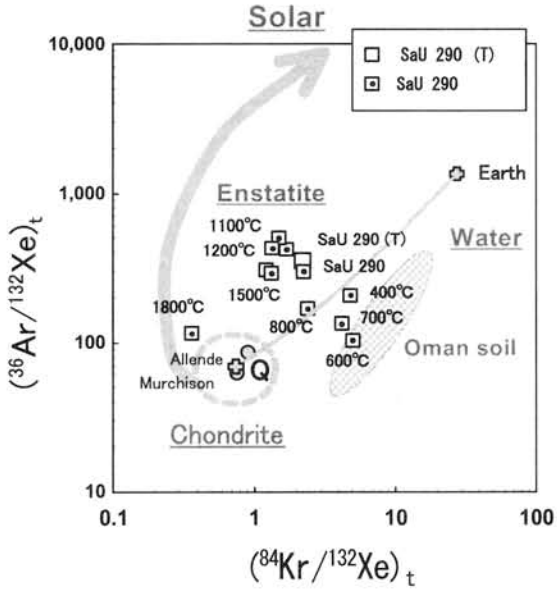

Fig 2. Elemental abundances of Ar, Kr and Xe in SaU290. Allende and Murchison (Q) are from [4,5], Earth and Mars [6]. Data of Oman soil is unpublished data..

SaU 290 are also plotted in Fig 2. The trapped heavier noble gases plot around trapped component of enstatite chondrites with subsolar gases and Q-gas (Chondrite). For the meteorites from hot desert received more weathering process severely than Antarctic meteorites, the weathering effect may be connected with the formation of oxides and hydroxides from metal [8]. Because CH chondrite, SaU 290 has contained relatively high metal and been found in Oman desert, it shows high $^{84}Kr/^{132}Xe$ ratios and atmospheric contamination. However, these data do not plot on the mixing line of Earth and Solar line. It can be explained by the process of rusty formation from metal with dissolved in water [8]. And SaU 290 from stepwise heating method at the lower temperature plot towards to Oman desert soil (unpublished data), supporting the evidence of desert weathering.

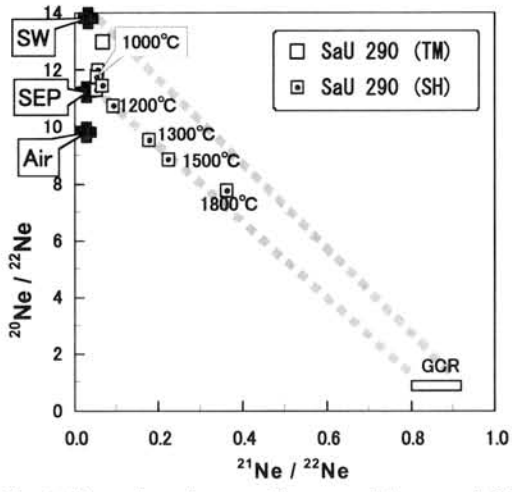

Fig 3. Neon three-isotope diagram with trapped Ne end members. SW; solar wind, SEP; solar energetic particles, Air; Earth atmosphere, GCR; galactic cosmic ray spallation-induced.

Neon three-isotope diagram is shown in Fig 3. The measured Ne composition is a mixture of cosmogenic Ne and trapped Ne, such as solar wind (SW) and solar energetic particles (SEP). The Ne isotopes of SaU 290 measured by total melt method are close to solar wind Ne composition ($^{20}Ne/^{22}Ne$ = 12.96 ± 0.23). This means that low energy solar gas is trapped in this meteorite. It is interesting that this chondrite does not show typical brecciated texture observed in ordinary chondrites.

Fig 4. shows the plots of $^{130}Xe/^{132}Xe$ versus $^{136}Xe/^{132}Xe$ in CH-chondrite, SaU 290. Component Q, solar wind (SW) and terrestrial atmosphere (Air) are plotted for comparison. Xe-data in SaU (TM) and SaU (SH) plot between SW and Q-Xe. SaU 290 shows H-Xe excess at the temperature of 900 ºC and 1000 ºC, though. This excess can be explained as that Xe-HL is degassed from the temperature of 800 to 1000 ºC, while Xe-Q is released between at 1000 to 1200 ºC [9]. The gap between total melting method and stepwise heating method is probably caused from the heterogeneous distribution of solar Xe.

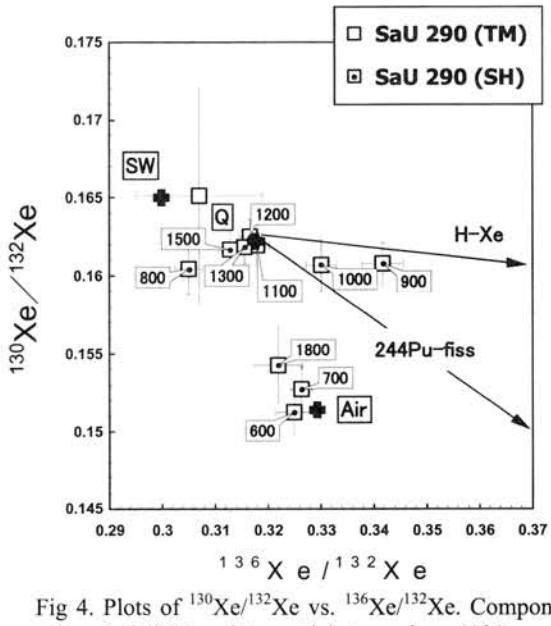

Fig 4. Plots of $^{130}Xe/^{132}Xe$ vs. $^{136}Xe/^{132}Xe$. Component Q, solar wind (SW) and terrestrial atmosphere (Air) are plotted for comparison [7]. Low temperature fractions (600-700 ºC) by stepwise heating method show terrestrial atmospheric contamination.

References: [1] Bartoschewitz R. (2005) pers. comm. [2] Park J. et al. (2005) *LPS* XXXVI, 1632. [3] Eugster O. (1988) *GCA*, 52, 1649-1662. [4] Wieler R. et al. (1991) GCA, 55, 1709-1722. [5] Wieler R. et al. (1992) GCA, 56, 2907-2921. [7] Ozima M and Podosek F. A. (2002) Noble Gas Geochemistry, 2nd edition, pp286. [8] Scherer P. and Schultz L. (2000) *MAPS*, 35, 145-153. [9] Matsuda J. et al. (1999) *MAPS*, 34,129-136.

An evaluation of asteroidal heat sources. Alan E. Rubin, Institute of Geophysics and Planetary Physics, University of California, Los Angeles, CA 90095-1567, USA. (aerubin@ucla.edu)

About 92% of the meteorites observed to fall have been appreciably heated. These include rocks that were once melted (irons, stony-irons and achondrites) and those that were significantly metamorphosed (type-4 to -6 chondrites). More than 99% of ordinary-chondrite (OC) falls are classified into types 3.6 to 6 or are type-3 breccias containing type-4 to -6 clasts. The identification of the mechanisms responsible for heating asteroids is one of the major unsolved problems in planetary science.

A large number of asteroidal heat sources have been suggested including electromagnetic induction in the protosolar wind [1-4], exothermic chemical reactions [5], FU-Orionis-type events [6], and tidal heating [7]. However, most researchers favor the decay of ^{26}Al ($t_{½}$=0.73 Ma) as the principal mechanism that heated the asteroids [8-11]. Several collisional heating models have been suggested [12-14], but many workers [15-17] have tended to dismiss these models. Nevertheless, there are reasons to question the efficacy of ^{26}Al decay as the main asteroidal heat source and there is evidence to support impact heating.

Although many refractory inclusions have initial $^{26}Al/^{27}Al$ values equal to the canonical initial ratio of $\sim 4.5\times10^{-5}$, some objects (CM2 hibonite grains and CV3 FUN inclusions) have $^{26}Al/^{27}Al$ ratios of 0, indicating the complete absence of live ^{26}Al [18]. The existence of these inclusions indicates that there was more than one aluminum-isotopic reservoir sampled by early-solar-system materials. If ^{26}Al was not uniformly distributed, there is no assurance that particular asteroids had enough of it on hand to metamorphose or melt.

In any case, refractory inclusions account for just a minor fraction of the bulk aluminum in chondrites. Of much greater importance are the chondrules, which constitute 40-80 vol.% of the rocks in most chondrite groups. The mean initial $^{26}Al/^{27}Al$ ratio of OC chondrules is 7.4×10^{-6}, about a sixth of the value in refractory inclusions [19]. If chondrules formed 1 to 2 Ma after refractory inclusions, the upper limit on the $^{26}Al/^{27}Al$ ratio in asteroids at the time of accretion would be set by the chondrules. Kunihiro et al. [20] found that chondrules in the Y81020 CO3.0 chondrite have a mean $^{26}Al/^{27}Al$ ratio of 3.8×10^{-6} (a value only about half that of OC chondrules). Thermal models by Kunihiro et al. [20] show that OC asteroids could be heated to a maximum temperature of 1100°C by ^{26}Al decay (assuming instantaneous accretion); this temperature is too low to cause silicate melting. CO asteroids could have reached a maximum temperature of only 670°C, too low to cause any melting at all. (If ^{60}Fe was also present and had an initial ratio of 1.4×10^{-7} [21], the maximum temperature reached in a CO asteroid would increase to 850°C [20], still too low to cause melting.)

These data and the resultant thermal models suggest that the decay of short-lived radionuclides was not the principal mechanism for heating asteroids. It is thus worthwhile to examine the viability of collisional heating.

Various objections have been raised against impact heating of asteroids [16]: (1) Single impacts cannot raise the global temperature of asteroid-size bodies by more than a few degrees. (2) The low surface/volume ratios of small bodies promote heat loss. (3) Typical impacts generate miniscule amounts of melt relative to the volume of impact-generated debris. (4) The low escape velocities of asteroids allow much of the impact-generated melt to escape.

However, these objections may be largely irrelevant; they pertain only to cohesive asteroids of low porosity. In contrast, the low densities (as low as 1.2 g cm^{-3}) determined recently for many asteroids [22] indicate that such bodies are highly porous piles of rubble. A high-energy impact would create a near-cylindrical depression in such a porous target. Because shock energy is attenuated rapidly in porous materials, an impact can heat localized materials very efficiently [23]. Compared to impacts into cohesive targets, more of the energy goes into crushing and heating porous target materials and less goes into ejecting debris. Although the global temperature of the asteroid would not increase appreciably, portions of the target would be significantly heated; some portions would even be melted. The meteorites that reach the Earth are preferentially from these compressed and heated regions.

There are several additional arguments in support of collisional heating:

(1) Annealed impact-melt-rock clasts occur in many OC fragmental breccias [24]. This indicates that impact events occurred before and/or at the same time as OC thermal metamorphism.

(2) There is a positive correlation in OC between petrologic type and shock stage [25,26], indicating that the more-metamorphosed OC tend to be more shocked. Data from Grady [27] on 1651 OC show that the mean shock stage increases with petrologic type: type-3 (S2.26), type-4 (S2.32), type-5 (S2.64), type-6 (S3.17) [28].

(3) There is a correlation among the three OC groups in their proportions of highly annealed (type-6 and -7) members and highly shocked (stage S4-S6) members. L chondrites have the highest proportions of both sets, H chondrites have the

lowest proportions, and LL chondrites are intermediate.

(4) Those chondrite groups with many metamorphosed (type-4 to -6) members (H, L, LL, EH, EL, CK) also have many shocked members of stage ≥S4. Chondrite groups with no metamorphosed members (CI, CM, CO, CR) have no members of shock stage ≥S4 [29]. CV chondrites follow the trend with a single exception; although there are no CV4-6 chondrites, there is one CV3 chondrite of shock-stage S4 (Efremovka) [30]. R chondrites also follow this general trend; there are few metamorphosed members and few members of shock stage ≥S4 [27].

Rubin [28] studied 53 type-5 to -6 OC of shock stage S1 (as indicated by sharp optical extinction in olivine). He found that every one of these rocks had relict shock features demonstrating that they were once shocked to stage ≥S3 and then annealed. The relict shock features include chromite veinlets, chromite-plagioclase assemblages, metallic Cu, irregular troilite grains inside metallic Fe-Ni, rapidly solidified metal-sulfide intergrowths, martensite and various types of plessite, polycrystalline troilite, metal-troilite veins, silicate melt veins, silicate melt pockets, silicate darkening (due to the dispersion of tiny metal and troilite blebs in silicate interiors), and the presence of low-Ca clinopyroxene. After these rocks were shocked to stage S3-S6, impact-induced annealing must have repaired the damage produced by shock in their olivine crystal lattices [31,32], giving these chondrites the appearance of shock-stage S1 (i.e., "unshocked") materials.

One of these equilibrated shock-stage-S1 OC (LL6 MIL 99301) has an ^{39}Ar-^{40}Ar age of ~4.23 Ga [29, 33], indicating that it was annealed ~300 Ma after accretion. This is equivalent to ~400 half-lives of ^{26}Al. Impacts constitute the only feasible mechanism that could have caused annealing at this late date. Because some shock-stage-S1 OC with relict shock features (Guareña, Kernouvé, Portales Valley [28]) were shocked and annealed 4.44-4.45 Ga ago [34,35] (during a period when impacts were prevalent and most OC were thermally metamorphosed), it follows that impact-induced annealing could have contributed significantly to OC thermal metamorphism.

References:

[1] Sonet C. P. et al. (1970) *Astrophys. Space Phys., 7,* 446-488. [2] Herbert F. and Sonett C. P. (1979) *Icarus, 40,* 484-496. [3] Herbert F. (1989) *Icarus, 78,* 402-410. [4] Herbert F. et al. (1991) In *The Sun in Time,* 710-739. [5] Clayton D. D. (1980) *Nukleonika, 25,* 1477-1490. [6] Wasson J. T. (1992) *Trans. Amer. Geophys. Union, 73,* 336. [7] Czechowski L. (1991) *Earth Moon Planets, 52,* 113-130. [8] Urey H. C. (1955) *Proc. Natl. Acad. Sci., 41,* 127-144. [9] Fish R. A. et al. (1960) *Ap. J., 132,* 243-258. [10] Lee T. et al. (1976) *GRL, 3,* 109-112. [11] Grimm R. E. and McSween H. Y. (1993) *Science, 259,* 653-655. [12] Wasson J. T. et al. (1987) *Meteoritics, 22,* 525-526. [13] Cameron A. G. W. (1990) *LPS, XXI,* 155-156. [14] Wasson J. T. and Kallemeyn G. W. (2002) *GCA, 66,* 2445-2473. [15] Wood J. A. and Pellas P. (1991) In *The Sun in Time,* 740-760. [16] Keil K. et al. (1997) *Met. Planet. Sci., 32,* 349-363. [17] McSween H. Y. et al. (2002) In *Asteroids III,* 559-571. [18] MacPherson G. J. et al. (1995) *Meteoritics, 30,* 365-386. [19] Kita N. T. et al. (2000) *GCA, 64,* 3913-3922. [20] Kunihiro T. et al. (2004) *GCA, 68,* 2947-2957. [21] Tachibana S. and Huss G. R. (2003) *Ap. J., 588,* L41-L44. [22] Veverka J. et al. (1999) *Icarus, 140,* 3-16. [23] Melosh H. J. (1989) *Impact Cratering: A Geologic Process,* 245 pp. [24] Rubin A. E. et al. (1983) *Meteoritics, 18,* 179-196. [25] Stöffler D. et al. (1991) *GCA, 55,* 3845-3867. [26] Rubin A. E. (1995) *Icarus, 113,* 156-167. [27] Grady M. M. (2000) *Catalogue of Meteorites,* 689 pp. [28] Rubin A. E. (2004) *GCA, 68,* 673-689. [29] Rubin A. E. (2002) *GCA, 66,* 3327-3337. [30] Scott E. R. D. et al. (1992) *GCA, 56,* 4281-4293. [31] Bauer J. F. (1979) *Proc. Lunar Planet. Sci. Conf., 10,* 2573-2596. [32] Ashworth J. R. and Mallinson L. G. (1985) *EPSL, 73,* 33-40. [33] Dixon E. T. et al. (2004) *GCA, 68,* 3779-3790. [34] Turner G. et al. (1978) *Proc. Lunar Planet. Sci. Conf., 9,* 989-1025. [35] Garrison D. H. and Bogard D. D. (2001) *LPS, XXXII,* 1137.

Progressive aqueous alteration of CM chondrites. Alan E. Rubin, Josep M. Trigo-Rodríguez and John T. Wasson, Institute of Geophysics and Planetary Physics, University of California, Los Angeles, CA 90095-1567, USA. (aerubin@ucla.edu)

Introduction. CM chondrites are aqueously altered rocks that contain ~9 wt.% H_2O^+ (i.e., indigenous water) [1] bound in phyllosilicate phases (mainly serpentines and montmorillonites), tochilinite (an interstratified Fe-Ni sulfide and Fe-Mg hydroxide), and hydrated Mg- and Ca-sulfates [2]. Also present are grains of carbonate (mainly calcite and aragonite [3,4]), in some cases intergrown with tochilinite, serpentine and sulfide [5]. Rare clusters of magnetite also occur [6]. Clumps of so-called "poorly characterized phases" (i.e., PCP) appear bright in BSE images of CM chondrites; the clumps consist mainly of phyllosilicate and tochilinite intergrown with pentlandite and pyrrhotite.

We studied eight CM chondrites that span the range of moderate-to-extreme aqueous alteration. Each chondrite was assigned an alteration stage (modified from those defined in [8]): QUE 97990, CM2 – stage 0-1; Murchison, CM2 – stage 1; Murray, CM2 – stage 1; Y791198, CM2 – stage 1; QUE 99355, CM2 – stage 2; Cold Bokkeveld, CM2 – stage 4; QUE 93005, CM2 – stage 4-5; LAP 02277, CM1 – stage 5. Browning et al. [7] and Hanowski and Brearley [8] identified several mineralogical and textural properties that reflect CM alteration; these include changes in hydrated mineral compositions, destruction of isolated matrix silicate grains, and alteration of mafic silicates within chondrules. We have identified additional parameters that appear to correlate with progressive alteration: (1) the modal abundance of metallic Fe-Ni, (2) the PCP texture and modal abundance of large PCP clumps, (3) the mean composition and compositional heterogeneity of PCP, (4) the presence and compositional complexity of carbonate, and (5) the compositional diversity of fine-grained mantle layers around CM chondrules.

Metallic Fe-Ni. The abundance of metallic Fe-Ni decreases as metal oxidizes during alteration [6]. QUE 97990 (stage 0-1) contains ~2 wt.% metallic Fe-Ni occurring as blebs inside porphyritic chondrules and as relatively coarse grains in the matrix. Murchison (stage 1) contains 0.13 wt.% metallic Fe-Ni [1], present both inside porphyritic chondrules and in the matrix. Murray (stage 1) contains ~0.2 wt.% metallic Fe-Ni grains occurring mainly inside low-FeO porphyritic chondrules. Y791198 (stage 1) contains 0.2-0.5 wt.% metallic Fe-Ni; a few small (ca. 10 μm) metal grains occur in the matrix, but most porphyritic chondrules do not contain significant amounts of metal blebs. QUE 99355 (stage 2) contains <0.1 wt.% metallic Fe-Ni. Metallic Fe-Ni is absent in CM chondrites of stages 3 to 5.

Large PCP clumps. The stage-1 CM chondrites typically contain 30-40 vol.% coarse (≥50 μm) BSE-bright PCP clumps consisting of 30-60-μm-size grains and grain clusters. Cold Bokkeveld (stage 4) contains similar abundances, but large PCP clumps are rare in QUE 93005 (stage 4-5) and LAP 02277 (stage 5).

PCP composition. LAP 02277 (stage 5) is at the extreme in the concentrations of many minor elements in its mean PCP composition: it has the highest concentrations of SiO_2 (27.0 wt.%), CaO (0.48 wt.%), Na_2O (0.34 wt.%), and, along with Cold Bokkeveld (stage 4), MnO (0.22 wt.%); it has the second highest concentrations (right after Cold Bokkeveld) of TiO_2 (0.11 wt.%), Al_2O_3 (2.9 wt.%) and Cr_2O_3 (0.38 wt.%); it has the lowest S concentration (1.8 wt.%), next to lowest "FeO" concentration (37.9 wt.%) (slightly higher than in Cold Bokkeveld); and the lowest ratios of S/SiO_2 (0.07) and "FeO"/SiO_2 (1.4). It appears that increasing aqueous alteration tends to cause PCP to become richer in SiO_2, TiO_2, Al_2O_3, Cr_2O_3, MnO, CaO and Na_2O and poorer in S and "FeO." (The "FeO" concentration includes FeO in phyllosilicates and Fe^{2+} in sulfide.) This trend probably reflects an increase in the phyllosilicate/sulfide ratio in PCP during alteration. Our data also show that PCP in LAP 02277 has the lowest standard deviations for many of these elements (e.g., SiO_2, Al_2O_3, "FeO," MnO, Na_2O) among the CM chondrites in our study. This suggests that, with increasing aqueous alteration, PCP becomes more uniform in composition and texture.

Carbonate. Ca carbonate occurs as 10-60-μm-size grains in QUE 97990 (stage 0-1), Murchison (stage 1), Y791198 (stage 1) and Cold Bokkeveld (stage 4). QUE 99355 (stage 2) contains only small grains of Ca carbonate. QUE 93005 (stage 4-5) contains ~8 vol.% of 20-70-μm-size carbonate grains; about 20% are nearly pure Ca carbonate, the majority being complex carbonates containing significant amounts of Ca, Mg, Fe and Mn. In some cases, the more complex carbonates form partial rims around Ca carbonate grains indicating that the Ca carbonate formed earlier. Carbonate appears to be rare or absent in LAP 02277 (stage 5).

Composition of fine-grained mantle layers around chondrules. Many CM chondrules are surrounded by fine-grained, matrix-like mantles rich in serpentine and tochilinite [9]. Some of these mantles are layered. In many cases the inner layer is lighter in BSE images and more uniform in shade. In Y791198, the outer layer tends to be speckled, with a moderately dark groundmass (in BSE images) containing coarser lumps of BSE-bright PCP and sulfide. Electron microprobe analyses show that the inner light layers and outer, dark, speckled layers in

QUE 97990 are very similar to each other in composition (although the light layers are slightly richer in S and P_2O_5 and slightly poorer in SiO_2). Major element ratios in the light and dark layers are similar: SiO_2/MgO, 1.7 and 1.9, respectively; FeO/MgO, 2.8 and 2.6; FeO/SiO_2, 1.7 and 1.4. The light layers in Y791198 are similar to the layers in QUE 97990; the SiO_2/MgO, FeO/MgO and FeO/SiO_2 ratios in Y791198 light layers are 2.0, 2.6 and 1.4, respectively. The dark, speckled layers in Y791198 differ somewhat in composition: they have a lower mean FeO content (~26 wt.%), higher SiO_2 (~30 wt.%) and higher MgO (~17 wt.%). Consequently, the FeO/MgO and FeO/SiO_2 ratios in Y791198 dark, speckled layers (1.5 and 0.87, respectively) are lower than those in the light layers in Y791198 or either layer in QUE 97990. We interpret these results to indicate that in Y791198, Fe has migrated from the adjacent fine-grained regions into small voids where it formed PCP. Because the inner light layers were more compact, these regions did not experience this process to the same degree; the dark, speckled layers were more porous and became more altered. In QUE 97990, the alteration process stopped at an earlier stage, with more of the Fe being retained in metal and primary sulfide, and PCP being formed mainly in the meteorite matrix. The dark, speckled layers in this meteorite are only slightly more altered than the inner, light layers.

Cr concentration in ferroan olivine. Grossman and Brearley [10] found that the concentration of Cr_2O_3 in ferroan (Fa13-24) olivine grains in type-3 ordinary chondrites decreases systematically with increasing metamorphism: type 3.0, ~0.50 wt.% Cr_2O_3; type-3.1, ~0.23 wt.%; type-3.2, ~0.15 wt.%; type-3.3, 0.08 wt.%. Mild thermal metamorphism in these rocks appears to be responsible for Cr leaving olivine, probably as a result of chromite exsolution. Our data on ferroan (Fa17-56) olivine grains in CM chondrites show that the Cr_2O_3 concentration (in wt.%) is independent of the degree of aqueous alteration: QUE 97990, 0.33±0.10 (n=30) (stage 0-1); Y791198, 0.32±0.11 (n=12) (stage 1); Murchison, 0.33±0.09 (n=22) (stage 1); Murray, 0.33±0.12 (n=25) (stage 1); QUE 99355, 0.33±0.15 (n=25) (stage 2); Cold Bokkeveld, 0.36±0.10 (n=12) (stage 4); QUE 93005, 0.30±0.10 (n=3) (stage 4-5). [LAP 02277 (stage 5) contains no unaltered olivine grains.] These results suggest that mild thermal metamorphism was not associated with aqueous alteration in CM chondrites.

Summary. Our study combined with literature data indicate the following trends to be reflective of progressive alteration of CM chondrites: increased formation of phyllosilicates, destruction of isolated matrix silicate grains, alteration of chondrule mesostasis, alteration of chondrule mafic-silicate phenocrysts, oxidation of metallic Fe-Ni (first from the matrix and then from porphyritic chondrules), decreased abundance of large PCP clumps, increased phyllosilicate/sulfide ratio in PCP clumps, increased uniformity of PCP composition, increased PCP formation in the outer layers of fine-grained mantles around chondrules, development of secondary sulfide, and the development of Ca carbonate, followed by the formation of complex carbonates, and ending in the near-disappearance of carbonate.

References:

[1] Jarosewich E. (1990) *Meteoritics, 25,* 323-337. [2] Zolensky M. E. and McSween H. Y. (1988) In *Meteorites and the Early Solar System*, 114-143. [3] Bunch T. and Chang S. (1980) *Geochim. Cosmochim. Acta, 44*, 1543-1577. [4] Barber D. J. (1981) *Geochim. Cosmochim. Acta, 45*, 945-970. [5] Fuchs L. H. et al. (1973) *Smithson. Contrib. Earth Sci., 10*, 1-39. [6] Tomeoka K. and Buseck P. R. (1985) *Geochim. Cosmochim. Acta, 49*, 2149-2163. [7] Browning L. et al. (1996) *Geochim. Cosmochim. Acta, 60*, 2621-2633. [8] Hanowski N. P. and Brearley A. J. (2001) *Geochim. Cosmochim. Acta, 65*, 495-518. [9] Metzler K. et al. (1992) *Geochim. Cosmochim. Acta, 56*, 2873-2897. [10] Grossman J. N. and Brearley A. J. (2005) *Meteorit. Planet. Sci., 40,* in press.

On contribution of terrestrial ion flows to non-solar components in lunar soils: Ion transportation rates from non-magnetic Earth. K. Seki[1], N. Terada[2], H. Shinagawa[2], and M. Ozima[3], [1]STEL, Nagoya University, Honohara 3-13, Toyokawa, Aichi 442-8507, Japan (seki@stelab.nagoya-u.ac.jp), [2]NiCT, Tokyo 184-8795, Japan, [3]Graduate School of Earth and Planetary Science, University of Tokyo, Tokyo 113-0033, Japan.

Introduction:

Mechanisms responsible for the atmospheric escape from a planet dramatically change with the strength of its intrinsic magnetic field [1,2]. In the present Earth, SW (solar wind) approaching to the Earth is stopped by the geomagnetic field (GMF) at the magnetopause (at about 10 Earth radii), where the magnetic pressure of the GMF balances the dynamic pressure of the SW. It is not easy to evaluate the quantitative feasibility of an atmospheric source of extrasolar N in lunar soils by implantation in the Earth's magnetotail.. However, we can at least put upper limit of the N+ flux to be $<10^3$ $cm^{-2}s^{-1}$, when we refer the recent estimations of O+ escape flux [2] and N+/O+ ratio [3] in the magnetotail. Thus it may not be negligible but also quantitatively inadequate to account for the extrasolar N flux in lunar soils.

On the other hand, when the planet has no GMF as in cases of present Mars and Venus, the SW directly interacts with the planetary upper atmosphere and may cause efficient loss of heavy atmospheric constituents such as Nitrogen and Argon under certain solar wind conditions. In this study, we estimate the escape rates of H+, He+, N+, O+, Ne+, and $^{36}Ar+$ from the non-magnetic Earth, i.e., under assumption that the Earth does not have its intrinsic magnetic field, through the solar wind induced escape. In order to access whether these escaping ions contribute to non-solar components implanted in lunar soils, fluxes of the terrestrial ions at lunar orbit are discussed.

Ion escape rate above the ionopause:

At altitudes above ~80 km, terrestrial atmosphere starts ionized by solar radiation and these atmospheric electrons and ions form the ionosphere, a dense plasma layer in the upper atmosphere. If the Earth does not posses any intrinsic magnetic field, the solar wind would approach to the Earth until its kinetic pressure was balanced by the ionospheric pressure and this boundary of the solar wind entry is called the "ionopause". Above the ionopause, the terrestrial ions are accelerated by the electric field induced by the magnetized solar wind flow and flow away from the Earth together with the diverted solar wind flow around the planet. This picked-up process can efficiently remove terrestrial ions created above the ionopause. The solar wind induced ion escape from unmagnetized planets has been observed at Mars and Venus, which have no permanent global magnetic dipole [4, 5, 6].

In order to estimate the ion escape rates due to this pick-up process above the ionopause, we first calculated the ion production rates around the Earth using MSIS00 model [7], an empirical model of the terrestrial upper atmosphere, as an input. From the given neutral atmospheric density and temperature, the ion production rate of each ion species are calculated based on previously studies of the photon ionization by solar radiation [8,9] and photoelectron impact ionization [10]. Figure 1a displays the resultant production rates for H+, He+, N+, O+, Ne+, and Ar+, respectively. If one assumes that ions produced above the ionopause escape from the Earth, the total ion escape rate can be estimated by integrating the ion production rate over the dayside Earth surface area above the ionopause.

The picked-up planetary ions flow away from the Earth with the solar wind, and spread over the "tail region" in the anti-sunward direction from the Earth. From the observations at Mars and Venus, it is known that the "tail region" has a cylinder shape with the radius of about two planetary radii [11]. Assuming a circular escape area with the radius of two Earth radii in the anti-sunward direction of the Earth, we can obtain a rough estimate of the average ion escape flux in the nightside tail region. Figure 1b shows the estimated escape flux of each ion species

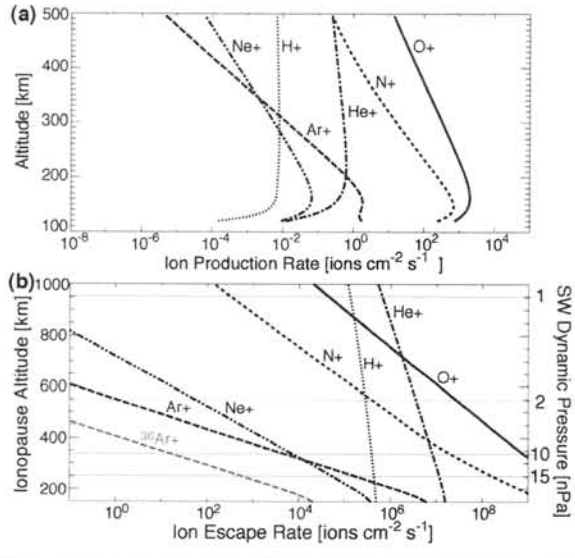

Figure 1: (a) Ion production rates calculated from an empirical model of the present Earth's atmosphere (MSIS00 model) under normal EUV flux ($F_{10.7}$ = 150) condition. (b) Escape fluxes of Ar^+, Ne^+, O^+, N^+, He^+, and H^+ ions normalized with the tail width of two Earth radii. Gray dashed line show the $^{36}Ar^+$ flux (1/300 of the total Ar^+ escape flux) for convenience of comparison with lunar samples. The ordinate represents both the ionopause altitude (left) and corresponding solar wind dynamic pressure (right) derived from IRI model.

as a function of the ionopause altitude (and also SW dynamic pressure). If we take the typical (active) solar wind conditions with solar wind dynamic pressure of 1 (15) nPa, which corresponds to velocity of 500 (1000) km/s and density of 5 (15) cm^{-3}, it would balance with the ionospheric plasma pressure estimated inferred from IRI (International Reference Ionosphere) model [12] at the altitude of 950 (250) km. As shown in Figure 1b, the escape rates of heavier ions are more sensitive to the ionopause altitude as expected.

Terrestrial ion flux at lunar orbit:

If Earth did not have no permanent global magnetic field in the past, some fraction of the escaping ions would hit the Moon, creating potentially observable effects that last even to the present day. If we assume the ionopause altitude of 500 km which is expected for the present Earth without global magnetic field under normal solar wind conditions, N^+ flux in the Earth's tail is expected to be ~10^6 ions/cm^2/s as shown in Figure 1b. Assuming 10^6 ions/cm^2/s N^+ escape flux from the early non-magnetic Earth, we next estimate the fraction of the escaping ions that will hit the lunar surface. A circular cross section with two Earth radii is assumed for the escaping area of terrestrial ions (hereafter referred as Earth's tail or tail region).

In evaluating the probability of Moon's passage through the Earth's tail, we also considered the variation of Earth-Moon distance with time. The distance between the Earth and Moon has been increasing due to tidal dissipation since the formation of the Earth-Moon system [13]. For example, the Earth-Moon distance was ~40 Earth radii about 4 Ga ago. If we take account of the fraction of time that the lunar orbit stays inside the Earth's tail, about 0.3% of the terrestrial ion flux would hit the lunar surface, i.e. it corresponds to ~3×10^3 N^+ ions/cm^2/s on average. The N^+ ions will then be implanted on lunar soils with the same velocity as that of the solar wind. As shown in an accompanied paper by *Ozima et al.* [14], the above estimated average N flux (about 3×10^3 atoms/cm^2/s) that could be transported to the Moon from the non-magnetic Earth is close to the non-solar implanted N flux observed at the lunar surface (>2×10^3 atoms/cm^2/s). It should be noted that the escape fluxes in Figure 1 may be underestimated, since terrestrial ions can escape also at and below the ionopause through other processes [1].

Figure 1b also shows that if the solar wind dynamic pressure changes from 2 to 15 nPa, the ionopause altitude decreases drastically from 500 km down to ~250 km, and accordingly the escaping ion flux, especially of heavy ions, undergo significant increase. If the solar wind pressure exceeds 15 nPa, the ionopause becomes even closer. When the ionopause altitude decreases from 500 to 200 km, for example, the average terrestrial N^+ flux at lunar surface increases from 3×10^3 to 2×10^6, Ne^+ from 0.5 to 5×10^2, and $^{36}Ar^+$ from 7×10^{-5} to 13 ions/cm^2/s, respectively. Such high solar wind pressure as assumed above is still within the present variation and hence even higher solar wind flux would be expected from an active young Sun [15]. In addition, low O_2 pressure (and possibly CO_2) in the paleoatmosphere further brings the ionopause closer to the Earth. All these factors tend to enhance the ion escape rate especially of heavy components. The high terrestrial ion fluxes from the ancient non-magnetic Earth with low atmospheric O_2 (or CO_2) pressure can be the source of non-solar components of N and light noble gases implanted in lunar soils [14].

References:

[1] Shizgal B. D. and Arkos G. G. (1996) *Rev. Geophys., 34*, 483-505. [2] Seki K. et al. (2001) *Science, 291,* 1939-1941. [3] Mall et al. (2002) *Geophys. Res. Lett., 29*, 2001GL013957. [4] Lundin R. et al., (1989) *Nature, 341*, 609. [5]Huddleston D. E. et al. (1996) *JGR, 101*, 4539-4546. [6] Brace L. H., Hartle R. E. and Theis R. E. (1995) *Adv. Spa. Res., 16(6)*, 99-112. [7] PiconeJ.M.etal.(2000)*Phys. and Chem. of the Earth, Solar-Terres., Planet. Sci., 25 (5-6)*, 537-542. [8] Richards P. G., Fennelly J. A., and Torr D. G. (1994) *JGR, 99*, 8981-8992. [9] Schunk,R.W.andNagyA.F.,(2000)*Ionospheres, Cambridge University Press*, U.K. [10] Richards P. G. and Torr D. G. (1988) *JGR, 93*, 4060-4066. [11] Dubinin E. et al. (1996) *JGR, 101*, 27061-27075. [12] Bilitza D. (2001) *Radio Science, 36(2)*, 261-275. [13] Abe M. and Ooe M. (2001) *J. Geodetic Soc. Japan, 47*, 514-520. [14] Ozima M. et al. (2005) this issue. [15] Hessler A. M. (2004) *Nature, 428*, 736-738.

^{60}Fe-^{60}Ni systematics of some achondrites measured with an ion probe. N.Sugiura, Univ. of Tokyo, Tokyo, Japan.

Introduction:

^{60}Fe is mainly produced by supernovae and not produced efficiently in AGB or by cosmic rays. Therefore, this is a crucial isotope for judging the origin of extinct nuclides in the early solar system. Detection of significant excesses in ^{60}Ni has been reported for several meteoritic samples [1,2,3,4, 5,6,7,8], whereas significant excesses in ^{60}Ni were not detected in other materials [9,10,11]. The upper limit to ^{60}Ni excess of [10] is in conflict with some of the reported ^{60}Fe/^{56}Fe initial ratios for the solar system. Therefore, although ^{60}Fe seems to have been present, its homogeneous distribution in the solar system is not well established.

Ion probe measurements:

Iron-rich olivine and pyroxene in achondrites (Stannern, Asuka 881394 and Sahara 99555) were measured with a Cameca-6f ion microprobe.

There are five Ni isotopes, 58, 60, 61, 62 and 64. Among these, 58 and 64 have interferences that cannot be resolved with the mass resolution of SIMS. Of the remaining 3 isotopes, the abundance of ^{61}Ni is the smallest, about 1/3 of ^{62}Ni. Therefore, ^{61}Ni cannot be measured precisely. ^{61}Ni is used for correction of mass fractionation which could depend on the tuning of SIMS measurement conditions. Usually a 30 minutes measurement of the Fe-Ni system of a Ni-poor sample without ^{61}Ni data gives 1 sigma error of ^{60}Ni/^{62}Ni of ~ 23 permil. In contrast, one sigma error of instrumental mass fractionation of a Ni-rich standard sample is only 1.7 permil. Therefore we measured only ^{60}Ni and ^{62}Ni for this study. Other measurement procedures are similar to that described in [9]. Corrections were made for tails of adjacent ^{44}CaO and ^{46}TiO peaks. A relative sensitivity factor of $(Ni^+/Fe^+)/(Ni/Fe)$ ~0.75 was used for both Fe-rich olivine and pyroxene. This is the same factor as that used in [9, 11].

Results:

Our preliminary results showed that all the ^{60}Ni/^{62}Ni ratios were normal, within 2 sigma errors. The upper limits to the initial ^{60}Fe/^{56}Fe were 1.4E-8, 1.2E-8 and 1.2E-8 for Stannern, Asuka 881394 and Sahara 99555, respectively. According to Al-Mg systematics [12,13,14], Asuka 881394 is about 3.9 Ma younger than CAIs whereas Sahara 99555 is about 5.1 Ma younger than CAIs. Using this chronological information, solar system initial ratios of ^{60}Fe/^{56}Fe were calculated to be less than 7.2E-8 and 1.2E-7 from Asuka 881394 and Sahara 99555, respectively. Stannern's age is much younger (and not well determined) than these two achondrites. Hence a strict limit to the initial ratio for the solar system was not obtained from Stannern.

Discussion:

The small (upper limit) excess in ^{60}Ni found in the present study is consistent with small excesses reported earlier for eucrites [2,3]. But, the small excesses of [2,3] could be considered as due to late disturbance, because those eucrites appeared to be affected by late impacts. In contrast, Asuka 881394 and Sahara 99555 are pristine samples not affected by impacts. Their ages are well determined by both Al-Mg and Mn-Cr systematics. Therefore, the present results place a strict upper limit to the solar system initial ratio of ^{60}Fe/^{56}Fe ~1E-7. This is significantly smaller than the previous upper limit of [10] and in conflict with positively determined initial ratios of >5E-7 [7].

We note that closure effects on Mn-Cr, Fe-Ni and Al-Mg systems are fairly well known. Other factors being equal, closure temperatures are probably the highest for the Mn-Cr system and lowest for the Al-Mg system. But the differences are rather small, which is consistent with the consistency of Al-Mg ages and Mn-Cr ages among angrites and eucrites. In summary, the small excesses in ^{60}Ni in achondrites cannot be attributed to late closure of the Fe-Ni system. It is not yet known if the conflict between the present results and those reported in literature is due to heterogeneous distribution of ^{60}Fe in the solar nebula.

References:

[1] Birck J.L. and Lugmair G.W. (1988) EPSL, 90, 131-143. [2] Shukolyukov A. and Lugmair G.W. (1993) Sci., 259, 1138-1142. [3] Shukolyukov A. and Lugmair G.W. (1993) EPSL, 119, 159-166. [4] Tachibana S. and Huss G.R. (2003) Astrophys. J., 588, L41-L44. [5] Mostefaoui S. et al., (2003) LPS, XXXIV, 1585.pdf. [6] Mostefaoui S. et al., (2004) LPS, XXXV, 1271.pdf. [7] Tachibana et al., (2005) LPS, XXXVI, 1529.pdf. [8] Quitte G. et al., (2005) LPS, XXXVI, 1827.pdf. [9] Kita N.T. et al., (1998) Antarc. Met. Res. 11, 1003-121. [10] Kita N.T. et al., (2000) GCA, 54, 3913-3922. [11] Mostefaoui et al., (2005) LPS, XXXVI, 1611.pdf. [12] Nyquist L.E. et al. (2003) EPSL, 11-25. [13] Wadhwa M. et al., (2005) LPS, XXXVI, 2126.pdf. [14] Spivak-Birndorf L., et al., (2005) LPS, XXXVI, 2201.pdf.

Mineralogy of four new Dhofar ureilites with reference to their pairing and origin.
Hiroshi Takeda[1*], A. Yamaguchi[2], M. Otsuki[3] and T. Ishii[3], [1]Res. Inst., Chiba Inst. of Technology, 2-17-1 Tsudanuma, Narashiro City, Chiba 275-0016, Japan (takeda@pf.it-chiba.ac.jp), [2]Natl. Inst. Polar Res., Tokyo 173-8515, Japan, [3]Ocean Res. Inst., Univ. of Tokyo, 1-15-1 Minamidai, Nakano-ku, Tokyo 164-8639, Japan.

Introduction:

Discoveries of Antarctic samples have almost tripled the number of known ureilites by 1990 [1]. Now, numbers of ureilites found in hot deserts are also increasing rapidly. All non-Antarctic ureilites described by Berkley et al. [2] contain pigeonite as a major pyroxene phase, and their compositions vary within a limited range. Antarctic samples extended their compositional ranges of minerals. Augite- or Orthopyroxene-bearing ureilites found in Antarctica and described by us in 1989, fall outside the original definition of a ureilite [3, 4]. Such mineral assemblage was found in Hughes 009 in 1994 [5]. We reported more unusual examples in the NWA ureilites [6]. Before describing such unique ureilites, we report here chemical variations of minerals in the Dhofar ureilites (4 in total), which cover more normal ranges of classical ureilites.

Samples and experimental methods:

Dhofar 836, a single stone weighing 995 g, and split into two pieces, was found by an anonymous finder in August 2000 in the Dhofar region of Oman (18°20.92' N, 54°12.84' E). Brief mineralogy and classification were reported by us in Met. Bull. [6]. Dhofar 837, a single stone weighing 900.1 g was found by an anonymous finder in 2000 spring in the Dhofar region of Oman (19°35.30' N, 54°57.10' E) [6], for which it was reported erroneously as "split into two pieces". Brief mineralogy was also reported [6]. Samples were supplied from National Sci. Museum (NSMT) in Tokyo. Dhofar 132 and 295 were listed in the Table of Met. Bull. [7, 8] and their specimens were supplied from the Planet. Materials Database Collections of Univ. of Tokyo.

The PTSs of the Dhofar ureilites were studied by an optical microscope and an electron probe micro-analyzer (EPMA) at Ocean Res. Inst. (ORI) of Univ. of Tokyo. The Area Analysis technique of the JEOL 8900 EPMA was applied to obtain elemental distribution maps at ORI. A mineral distribution map of each PTS was constructed by combining the elemental maps. The modal abundance (vol. %) of silicate minerals was derived from these maps. Chemical compositions of minerals were obtained with EPMA, JEOL JCXA-733 at ORI with WDS.

We studied all four ureilites found in the Dhofar region. The location of find of Shisr 007 is within this region. Dhofar 837 as well as Dho 295 look also similar in texture to Hajmah (a), which was named after the Hajma oil bore company. The meteorite itself is not necessarily from Hajma city (the city is appr. 190 km N of Dho 295).

Results:

We report mineralogy and mineral chemistry of four Dhofar ureilites under each meteorite number.

Dhofar 836: The PTS shows a typical texture of ureilite, with medium − grained (1 − 2 mm), equigranular olivine (Fo79 core; Fo90 rim) and pigeonite. Carbonaceous matter occurs as narrow, intergranular veins. Weakly shocked (S1), with rare mosaicism in olivine, but fractures are abundant in the olivine crystals. The sample is weathered to brownish color in hand specimen, W1. The pigeonite compositions range from Ca10Mg74Fe16 to Ca11Mg71Fe19 (Fig. 1). The mineral distribution map (Fig. 2) shows that modal abundance of the olivine grains (82 vol.%) is larger than that of pigeonite (18 %).

Dhofar 837: The sample is weathered to brownish color in hand specimen, W1. A few large-grained olivine and pigeonite grains (up to 2.1 to 1.5 mm in size) are set in a texture of smaller grained minerals with carbonaceous material and fine metal veins at grain boundaries. Distribution of the carbonaceous materials are not uniform. Weakly shocked (S1-2). Olivine grains (75 vol. %) are more abundant than pigeonite (20 %). The metal veins are less than 5 vol.%. The pigeonite composition Ca5Mg76Fe19 is uniform and the Fo values of olivine range from 78 to 79.

Dhofar 132 shows a texture different from common ureilites. Carbonaceous and metalic materials at grin boundaries are not prominent in this PTS and the rims of olivine grains are decorated by minute dusty opaque inclusions. The clear olivine crystals up to maximum 1.1X1.0 mm in size have less fractures and shows very weak undulatory extinction. Dhofar 295 shows a typical texture of ureilites with carbonaceous veins. Mineral grains (1.7X1.2 to 0.8X0.5 in size) are fractured and olivine crystals show undulatory extinction. Several grains of olivine in the same orientation are joined at their corners. Mineral chemistries of Dhofar 132 we obtained, including Fo cores 84～86, rims ca. 93, Ca11.7Mg75.3Fe13.0, are within the ranges reported previously, Fa15.2, Fs12.7Wo12.0 (mol%) [7] (Fig. 1). Our data of Dhofar 295, including Fo cores 84~85, rims ca. 91, Ca5.7Mg80.4Fe13.9 also agree with the previous ones, Fa13.7, Fs13.8Wo6.13 (mol%) [8]

Discussion:

The pigeonite compositions in ureilites originally described [1, 2, 4] vary within a limited range as shown in Fig. 1. The range of chemical

compositions of olivines and pyroxenes from the Antarctic ureilites extends towards more Mg-rich, Fe-rich, and Ca-rich components. The range of Fa contents of core olivines extended from 14-22 atomic % to 3-24 atomic %. The pyroxene compositions (Fig. 1) of our four Dhofar ureilites covers four corners of the known chemical variations of the ureilite pyroxenes [1]. It is to be noted that all Dhofar ureilites are normal kinds among hot desert meteorites.

Dhofar 836 was found only 6 km NW of Dhofar 837, but they are different in texture and in composition, and so may not be paired. Dhofar 836 looks quite different in texture etc. to Shisr 007 and Dhofar 132. Dhofar 132 has much smaller olivine clasts, and the color of Shisr 007 and Dhofar 132 is very dark black-brownish while Dhofar 836 is slightly more greenish and brighter and one would be surprised if Dhofar 836 could be paired to those. Because the two specimens differ in composition and texture, they may not be paired. Dhofar 837 seems to have some similarities in texture in hand specimen to Dhofar 295. Both have unusual large clast, and Dhofar 837 was found 113 km SSE of Dhofar 295. However, because two specimens have very different Fe atomic%, they are not necessarily paired. Shisr 007 was found 61km West of Dhofar 837. Shisr 007 and Dhofar 837 look very different in texture etc. to each other. Dhofar 132 and Dhofar 295 were found only 9 km apart, but they look again extremely different in texture etc. to each other. A pairing of those ureilites can be excluded in the finder's opinion. The pyroxene compositions (Fig. 1) rule out any possibility of their pairing of the Oman ureilites.

It should be noted that large oxygen isotope anomalies were found originally in Antarctic ureilites of the magnesian subgroup with orthopyroxene (Opx) [4, 9]. Augite (Aug) was found also in the Opx ureilite (LEW85440). Olivine-Opx-Aug assemblages with essentially no carbon were reported in Fughes 009 [5] and in DaG 319 [10], but such Opx was previously reported in Y791538 and LEW85440, and Aug in LEW85440, Y74130 and MET78008 [3, 4]. We found that NWA 2236 has such assemblage, but with carbon veins as in ordinary ureilites [11]. An explanation for the scattering of ureilites along an ^{16}O mixing line rather than the fractionation line is given by us in 1989 [4], who attributed it to the anomaly left in refractory magnesian silicates inherited from the carbonaceous chondrite-like materials by a planetesimal-scale collision. A well-defined negative correlation is observed between the mg# of olivine cores and $\triangle^{17}O$ [12]. Such correlation was also found in the NWA 2234 and 2236 ureilites (Kusakabe and Yamaguchi, personal comm.) The oxygen isotope variations and mineral assemblages can be explained by an impact or collision to an internally hot planetesimal with Na-, Si-, K-rich partial melts, which escaped together with volatiles.

Acknowledgements:

We thank Dr. Yoneda of NSMT, and Univ. of Tokyo for meteorite samples and an anonymous dealer for information on their locations of finds. This works is supported in part by funds from the cooperative program (No. 14, 2005) provided by Ocean Research Inst., Univ. of Tokyo, and in part by funds from the Res. Forum of Chiba Inst. of Tech.

References:

[1] Yanai K. and Kojima H. (1995) Catalog of the Antarct. Meteorites, 230pp; Tadeda H. (1991) *GCA, 55,* 35–47. [2] Berkley J.L. et al. (1980) *GCA, 44,* 1579–1597. [3] Takeda H. et al. (1989) *Meteorit. 24,* 73-81. [4] Takeda H. (1989) *EPSL, 93,* 181-194. [5] Goodrich C. A. (1998) *LPS XXIX,* #1123. [6] Takeda H. et al. in Russell S. S. et al. (2003) *Meteorit. Bull., 87, MAPS 38,* A199. [7] Greshake A. (2001) *Meteorit. Bull., 85,* A302. [8] Lorenz C. (2002) *Meteorit. Bull., 86,* A166. [9] Clayton R. N. and Mayeda T. K. (1988) *GCA, 52,* 1313–1318. [10] Ikeda Y. and Printz M. (2001) *MAPS, 36,* 481-499. [11] Yamaguchi et al. (2004) *Meteorit. Bull., 88,* 15-16. [12] Hudon P. et al. (2004) *LPS XXXV,* #2075.

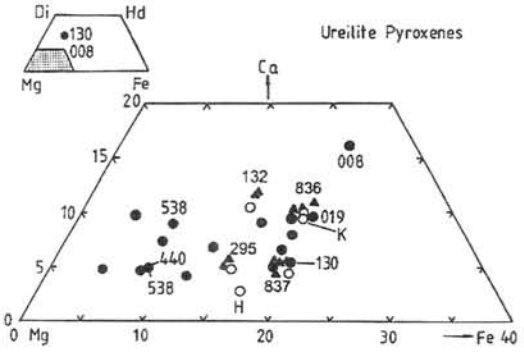

Fig. 1. Chemical compositions of ureilite pyroxenes plotted in an enlarged portion of the pyroxene quadrilateral [1]. Triangles: Dhofar ureilites; solid circles: Antarctic ureilites; open circles: non-Antarctic ureilites (H,K). Numbers represents last three digits of the meteorite numbers.

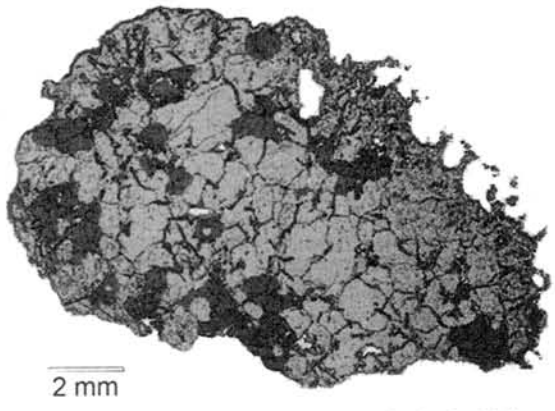

Fig. 2. Mineral distribution map of Dhofar 836. Green: olivine; red: pigeonite.

Highly siderophile elements in silicate clast of Mount Padbury. M. Tamaki[1], A. Yamaguchi[1,2], K. Misawa[1,2], M. Ebihara[3], [1] Grad. Univ. Advanced Studies, Tokyo 173-8515, Japan. [2] National Institute of Polar Research, Tokyo 173-8515, Japan. [3] Grad. School of Sci., Tokyo Metropolitan University, Hachiouji, Tokyo, 192-0372, Japan. (E-mail: tamaki@nipr.ac.jp)

Introduction

Mesosiderites are stony-iron meteorites composed of almost equal proportions of silicates and Fe-Ni metal [1-3]. The original bulk composition of the metal mixed with silicates is most comparable to that of the IIIAB irons which thought to have originated in the core of an asteroidal body [4-5]. Silicate clasts in mesosiderite comprise suites of basalts and gabbros, and are similar to eucrites. However, silicate clasts show systematic difference in siderophile element abundances. Previous studies showed that the Ir/Ni ratio was significantly lower in silicate clasts than in metallic portion [6-8].

We performed petrological and geochemical studies of a clast in Mount Pudbury to elucidate origin of siderophile element abundances in mesosiderite silciates. Based on the petrological observation and chemical compositions of silicate clast, we discuss the origin of metallic phases in the clast.

Sample and analytical technique

We have selected a basaltic clast (BCMtP) from the least metamorphosed type of mesosiderite, Mount Padbury. The PTSs were examined optically and with a scanning electron microscope (SEM) (JEOL JSM-5900). Chemical compositions of minerals were determined with electron microprobe analyzers (EPMA) (JEOL JXA-8800 and 8200). Major, minor and trace element abundances of bulk samples were determined by neutron-induced prompt gamma-ray analysis (PGA) and by instrument neutron activation analysis (INAA). Abundances of platinum group elements (PGE) were determined by isotope dilution mass spectrometry and external calibration method (only for Rh) using inductively coupled plasma mass spectrometry (ICP-MS) combined with a fire assay preconcentration technique. The isotopic compositions were measured with ICP-MS (VG Plasma Quad3) in Tokyo Metropolitan University.

Results

Texture and Mineralogy

Petrographic descriptions and modal abundances of minerals in the clast are given in [9] and we present a synopsis and new results obtained as part of this work.

The clast shows a relict basaltic texture and is composed predominantly of pyroxene and plagioclase. Minor and trace minerals include Ca-phosphate, silica, chromite, ilmenite, troilite and Fe-metal. We focus on the occurrence of Fe-metal which is likely to be a carrier phase of siderophile elements. Two types of Fe-metals are observed. One occurs as a fine-grained droplet coexisting with troilite, which occurs throughout the silicates. The other occurs as an angular shape grain coexisting with chromite. There are systematic differences in Ni contents among the Fe-metals. The Fe-metals together with troilite show higher Ni contents (typically 20-30 wt.%).

Bulk Geochemistry

Fig. 1 shows Ni and Co contents of BCMtP together with other silicate clasts of mesosiderite and eucrites. BCMtP is plotted in the same region of other basaltic clasts in mesosiderite, but significantly higher than the average value of basaltic eucrite (Ni=20 ppm, Co=6.5 ppm [10]). Fig. 2 shows CI-normalized siderophile element abundances of BCMtP. The abundance pattern of siderophiles is extremely fractionated. The abundances of Os and Ir are below the detection limit (0.01ppb). The CI-normalized Co/Ni (= 1.3) ratio is similar to that of mesosiderite metallic portion (= 1.17). However, the CI-normalized Pt/Ni (= 0.0096) ratio (i.e., highly siderophile element/Ni ratio) is different from that of mesosiderite metallic portion (= 1.19)[5].

Discussion

The siderophile element abundances of BCMtP are significantly higher than those of basaltic eucrites. As shown in Fig. 1, Ni and Co contents of silicate clasts in mesosiderites are higher and more variable than those of eucrites. The high abundances of siderophile elements in silicate clasts of mesosiderite could not be explained by igneous processes. Thus, the enrichment could be explained by contamination of other components from mesosiderite metallic portion after the mixing of metals and silicates.

Metallic phases could be major carrier phases of siderophile elements. Ni-poor metals are associated with chromite and ilmenite, and may have formed by breakdown of Cr-ulvöspinel as a result of subsolidus reduction [11,12]. Small rounded grains of Ni-rich metal may have formed by different process because metallic phases produced by the decomposition of spinel would have low Ni contents. The BSE images show curvilinear trails of tiny Fe-Ni metal and troilite grains. These trails may have been formed by injection of molten metal from mesosiderite metallic portion. The low Fe-FeS eutectic temperature (988 °C) causes the metal and sulfide to be readily melted and mobilized during impact heating as observed in shocked ordinary chondrites [13]. An obvious

potential source of the metal and sulfide is mesosiderite metallic portion. If this is the case, siderophile element pattern in BCMtP could be parallel to that of mesosiderite metallic portion. However, the CI-normalized siderophile element pattern of BCMtP is quite different from those of mesosiderite metallic portions, which show relatively flat patterns with a very limited compositional range of ~10 x CI-chondrite [5] (Fig. 2).

If metallic portion underwent low-degree of partial melting, abundances of highly siderophile element in S-rich melts should be quite low. Partitioning of siderophile elements (Re, Os, Ir, Ge, Co, and Ni) between solid metal and liquid metal-sulfide is markedly dependent on the S contents [14-16]. The solid metal/liquid metal-sulfide partition coefficients of highly siderophile elements are more than three orders of magnitude greater than that of Ni. Extremely fractionated siderophile element pattern observed in BCMtP could be derived from such a partial melting process.

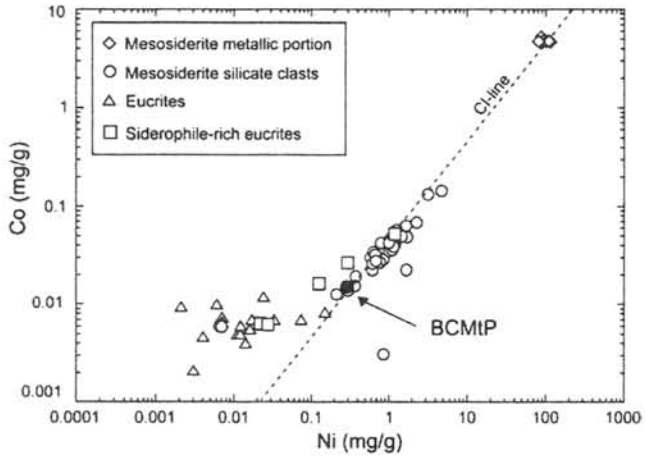

Fig 1. Ni vs. Co plot for mesosiderites and eucrites. Data are from [5-8, 17-19].

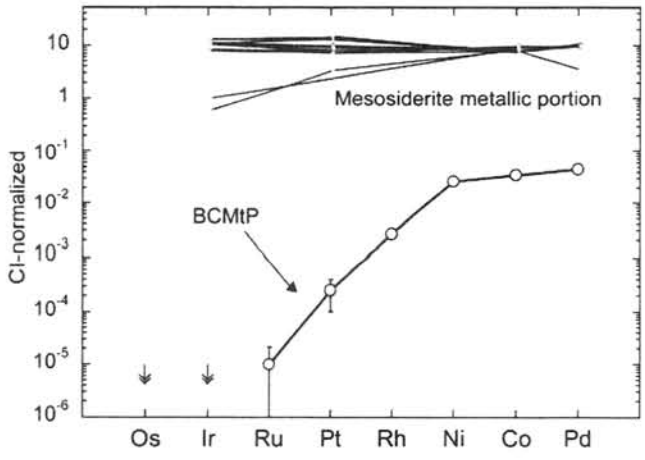

Fig. 2. CI-normalized siderophile element patterns of BCMtP. Os and Ir are below detection (<1 ppb). Data of mesosiderite metal nodules are from [5].

References

[1] Powell, B. N. (1971) *Geochim. Cosmochim. Acta* **35**, 5-34. [2] Floran, R. J. (1978) *Proc. Lunar Planet. Sci. Conf.*, **9th**, 1053-1081. [3] Delaney, J. S. et al. (1981) *Proc. Lunar Planet. Sci. Conf.*, **12th**, 1315-1342. [4] Wasson, J. et al. (1974) *Geochim. Cosmochim. Acta* **53**, 735-744. [5] Hassanzadeh, J. et al. (1990) *Geochim. Cosmochim. Acta* **54**, 3197-3208. [6] Rubin, A. E. and Jerde, E. A. (1987) *Earth Planet. Sci. Lett.* **84**, 1-14. [7] Rubin, A. E. and Jerde, E. A. (1988) *Earth Planet. Sci. Lett.* **87**, 485-490. [8] Kimura, M. et al. (1991) *Proc. NIPR Symp. Antarct. Meteorites*, **4**, 263-306. [9] Tamaki M. et al. (2004) *Antarctic Meteorites* **XXVIIII**, 85-86. [10] Kitts, K. and Lodders, K. (1998) *Meteoritics* **33**, A197-A213 [11] El Goresy, A. and Ramdohr, P. (1975) *Proc. Lunar Planet. Sci. Conf.*, **6th**, 729-745. [12] Yamaguchi, A. et al. (2001) *Geochim. Cosmochim. Acta* **65**, 3577-3599. [13] Rubin, A. E. (1992) *Geochim. Cosmochim. Acta* **56**, 1705-1714. [14] Jones, J. H. and Malvin, D. J. (1990) Metall. Trans. **21B**, 679-706. [15] Fleet, M. E. and Stone, W. E. (1999) *Geochim. Cosmochim. Acta* **63**, 2611-2622. [16] Chabot, N. L. et al. (2003) *Meteoritics* **38**, 181-196. [17] Ikeda, Y. et al. (1990) *Proc. NIPR Symp. Antarct. Meteorites*, **3**, 99-131. [18] Rubin, A. E. and Mittlefehldt, D. W. G. (1992) *Geochim. Cosmochim. Acta* **56**, 827-840. [19] Okamoto, C. et al. (2004) *Antarctic Meteorites* **XXVIIII**, 68-69.

Experimental study on growth kinetics of metallic iron in vacuum. K. Tatsumi, S. Tachibana, H. Nagahara and K. Ozawa, Department of Earth and Planetary Science, University of Tokyo, 7-3-1 Hongo, Tokyo 113-0033, Japan. E-mail: tachi@eps.s.u-tokyo.ac.jp.

Introduction:

Condensation is a fundamental process to form solids under low-pressure conditions as in the primitive solar nebula. For instance, isolated large (>100 μm) Fe-Ni metal grains in CH chondrites are thought to have kinetically condensed in the solar nebula [1]. In order to understand timescales and physical conditions for formation of such condensates, it is important to know condensation kinetics in detail.

The condensation rate from vapor is proportional to $(\alpha_c p - \alpha_e p^{eq})$, where p is a vapor pressure near the substance, p^{eq} is the equilibrium vapor pressure, and α_c and α_e are called the condensation and evaporation coefficients that express kinetic hindrances for evaporation and condensation ($0<\alpha_c$, $\alpha_e \leq 1$), respectively. Condensation occurs when $p^{eq}<p$ (oversaturation), while evaporation takes place when $p^{eq}>p$ (undersaturation). When $p^{eq}=p$, the substance and vapor coexist in equilibrium. Many experimental studies have been clarified evaporation kinetics (α_e) of minerals and melts in vacuum without back reactions ($p^{eq} \gg p \sim 0$). On the other hand, in spite of its importance, few experimental studies on condensation have been carried out so far because it is difficult experimentally to control physical parameters (p, temperature of gas and the substance) of an oversaturated condition, where condensation takes place.

In this study, we have performed condensation experiments of metallic iron on a substrate in order to examine growth kinetics of metallic iron and to apply it to growth of metallic iron under the protoplanetary disk conditions.

Experiments: The condensation experiments were carried out in a vacuum chamber with a tungsten mesh heater. The chamber was continuously evacuated by a turbo molecular pump. Gaseous iron was produced by heating a metallic iron plate, set at the center of the heater, at ~1170°C. The iron gas condenses on a molybdenum substrate set apart from the gas-source plate. The temperature of the substrate varies depending on the distance from the source (~1020-~415°C). It should be noted that the temperature of substrate is not independently controlled, and therefore, the flux incoming to the substrate surface varies depending on the distance from the source as well as temperature; the incoming flux is larger for the substrate closer to the source.

The weights of the iron source and the substrate were measured before and after experiments. The weight losses of the source and weight gains of the substrate were converted to evaporation and condensation rates, respectively, by dividing by the experimental duration and by the surface area of the source and condensable area of the substrate, respectively. Condensates were observed with a field-emission scanning electron microscopy (FE-SEM) for surface morphology, analyzed with energy-dispersive spectroscopy (EDS) for chemical composition, and with electron backscatter diffraction (EBSD) for the crystallinity and phase identification.

Results:

Analyses by EDS and EBSD showed that the condensates were metallic iron under all the experimental conditions. No other phase was detected. Figure 1 shows surface textures of condensed layers. The structure of the condensed layer varies with temperatures of the substrate. Condensates formed a compact layer at ~600-1020°C, while a porous layer of granular condensates were formed on the substrate at ~415°C.

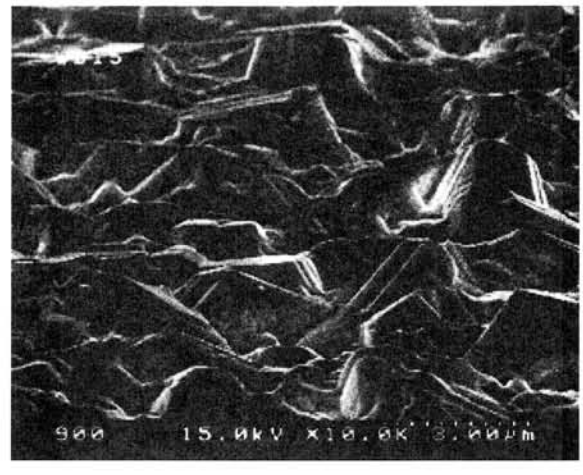

Fig.1. SEI images of condensed metallic iron on a molybdenum substrate at ~1020°C (top).

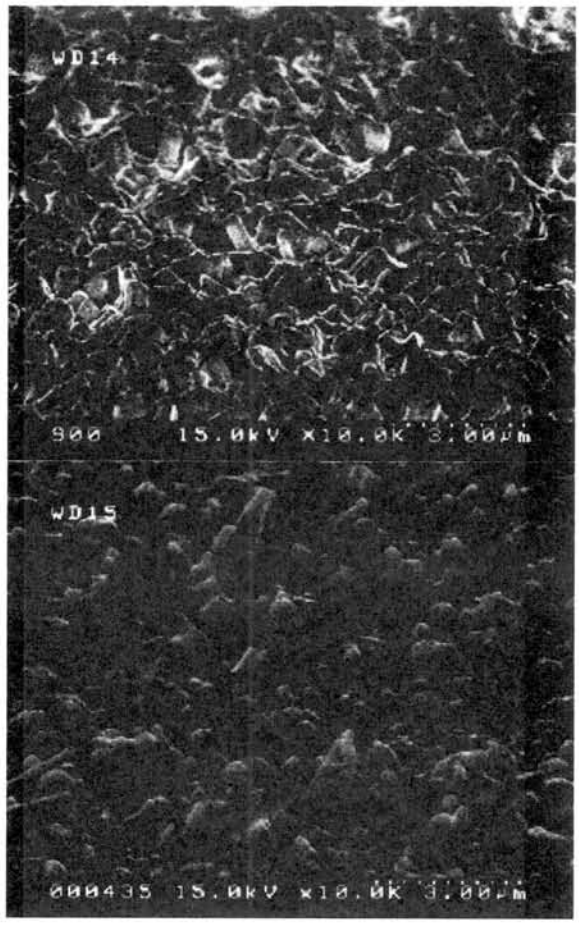

Fig.1 (*cont.*). SEI images of condensed metallic iron on a molybdenum substrate at ~750°C (top) and ~415°C (bottom).

The weight of the condensates and the thickness of the condensed layer increased linearly with heating duration. The iron plate source lost its weight linearly with time, and its evaporation rate was consistent with previous evaporation experiments of metallic iron [2].

Discussion:

Condensation coefficients of metallic iron (α_c) were calculated based on weight changes of the source and the substrate. The obtained α_c are close to unity at temperatures of ~1020°C and <~600°C, while they are smaller than unity at temperatures of 750-900°C. Although this may indicate temperature dependence of α_c, the degree of supersaturation (p/p^{eq}>>1) also varies with temperatures of the substrate in the experimental setting in this study. So, the apparent temperature dependence of α_c might also be explained by dependence on supersaturation.

The condensation coefficient of almost unity at high temperatures (~1020°C) may be due to thermal roughening of the surface of condensates. On the other hand, at lower temperatures (<~600°C), α_c is close to unity probably because of the extreme high degree of supersaturation.

The obtained α_c under supersaturated conditions is compared with α_e of metallic iron evaluated by [2], in which the dependence of α_e on p/p^{eq} was obtained in the temperature range of ~1450-1070°C. At ~1070°C, α_e is ~0.5 for p/p^{eq} =0 (free evaporation) and becomes smaller for a larger p/p^{eq}. On the contrary, α_c is ~1 for p/p^{eq} =~3-4 in this study, suggesting that kinetic hindrance for evaporation and condensation depends on supersaturation and that one cannot assume α_e=α_e for non-equilibrium conditions.

Although further detailed investigation is required, α_c for temperature conditions of condensation of metallic iron in the early solar system might be smaller than unity. This may imply that the timescale of kinetic condensation may be a little longer than that estimated with α_c=1 [1].

References:

[1] Meibom, A. et al. (1999) JGR, 104, 22053. [2] Tachibana, S. et al. (2001) LPS XXXII, abstract #1767.

Classification of Antarctic Micrometeorites based on their Abundance Patterns

Y. Tazawa[1], T. Fukuoka[2], Y. Fukushi[2, 3], Y. Saito[4], H. Sakurai[5], Y. Suzuki[5], T. Noguchi[6] and T. Yada[7]
[1]Department of Physics and Astrophysics, Graduate School of Science, Kyoto University, Kyoto 606-8502 (tazawa@cr.scphys.kyoto-u.ac.jp), [2]Department of Environmental Systems, Faculty of Geo-Environmental Science,Rissho University, Kumagaya 360-0914, [3]Department of Earth and Planetary Sciences, Tokyo Institute of Technology, Tokyo 152-8551 (Present Address), [4]Radio Isotope Laboratory, College of Science and Engineering, Aoyama Gakuin University, Sagamihara 229-8551, [5]Department of Physics, Faculty of Science, Yamagata University, Yamagata 990-8560, [6]Department of Materials and Biological Science, Ibaraki University, Mito 310-8512, [7]Department of Earth and Planetary Science, University of Tokyo, Tokyo 113-0033.

Introduction

Micro particles thought to be of cosmic origin and collected from the Earth's environments have survived from the heating and the weathering during their Atmospheric entry and their residence on the Earth. Most of them have lost their inherent features and have altered into fully molten droplets, *e.g.*, "Cosmic Spherules (CSs)"[1]. Since three decades, a large number of scarcely altered extraterrestrial particles have been collected from the Stratosphere [2, 3] and the Polar Regions [4, 5]. Typical of them are fragile aggregates of chondritic constituents; *i.e.*, "Interplanetary Dust Particles (IDPs)" thought to be of cometary origin [2], and "Antarctic Micrometeorites (AMMs)", especially "Unmelted MMs (UMMs)" [4]. AMMs have been collected and investigated widely in recent years [6, 7, 8, 9, 10] because they may be unique samples of primitive Solar System materials unknown in either IDPs or tiny constituents of conventional meteorites. We report several types of AMMs so far investigated by Instrumental Neutron Activation Analyses (INAA) [11, 12, 13].

Samples and Experimental

AMMs studied here are thirty-one MMs; an I-type spherule, fourteen S-type spheres or spheroids, and sixteen S-type UMMs (irregular shape), provided by National Institute for Polar Research (NIPR), which were collected from deposits in a water tank at the Dome Fuji Station (DF:77° 19' S, 39° 42' E, JARE -37/38)[6], bare ice near the Kuwagata Nunatak (KN: 72° 06' S, 35° 15' E) and south of Minami-Yamato Nunataks (MY: 72° 26' S, 35° 20' E) at Yamato Mountains (JARE-39)[7], and bare ice near Tottuki Point on the Soya Coast (TP: 68° 55' S, 39° 51' E, JARE-41)[8]. Assortments and preliminary investigations of the AMMs have been also performed by the AMM initial examination team organized by NIPR [6].

INAA were performed on the individual MMs and tiny chips of standard materials; *i.e.*, glass made from Japanese Standard Rock (basalt), JB-1, for lithophile elements (LPEs) and metal wire, Al-Au (0.1%) (IRMM-530) and Pt (SRM-680a), for siderophile elements (SPEs). Each of the samples was weighed by an electro microbalance prior to the INAA. The procedures were applied after [14] and seen in [11, 12, 13], and as follows:

INAA for short half-life nuclides(SL series): Each of the MMs and the standards was heat-sealed in each small (ca. 2x2 mm) bag made with ultra pure polyethylene sheet and irradiated by neutron for 10 min at 20 MW ($2x10^{13}$ neutrons/cm^2/sec) in the pneumatic pipe (PN-3) of the reactor JRR-3M, the Japan Atomic Energy Research Institute (JAERI). The first counts were done for 400 sec, after 2~10 min cooling using a gamma-ray counting facility at JRR-3M. The second counts were done for 1000 sec at 1~6 hr after the first counts using a facility at the Inter–University Labo- ratory for the Joint Use of JAERI Facilities, Research Center for Nuclear Science and Technology (RCNST, Tokai br.), University of Tokyo.

INAA results of selected MMs collected from Dome Fuji, Minami-Yamato Nunataks, Kuwagata Nunatak and Tottuki-Point

Sample		F96CI004	F96CI019	F97AG008	IB004	IB005	IB007	K5100030	K5100035	K5100040	ND7	NJ5	NR6
wt	μg	3.0	10.7	1.9	3.3	5.8	9.4	3.8	2.1	1.2	20.5	4.7	13.3
Na	%	0.32	0.017	0.77	0.42	0.005	0.002	0.42	0.58	0.50	0.03	0.03	–
Mg	%	7.63	20.6	15.0	11.2	11.5	–	15.3	10.8	9.36	18.5	15.0	30.6
Al	%	1.2	0.87	1.52	1.64	1.64	0.037	0.92	1.58	2.06	1.34	1.75	0.415
Ca	%	0.46	0.68	1.70	1.01	2.30	–	0.49	0.89	–	1.41	–	0.458
Ti	%	–	0.54	–	0.20	0.26	–	0.27	0.16	0.11	0.10	–	–
Sc	ppm	7.12	5.28	15.1	7.78	8.64	0.17	14.0	10.7	10.9	11.2	11.6	13.9
V	ppm	48	46	86	68	80	2.4	126	95.6	100	93.1	115	164
Cr	ppm	2140	149	4370	4980	3800	2800	6480	4260	4070	3540	3900	726
Mn	%	0.19	0.72	0.28	0.43	0.20	0.01	0.36	0.21	0.23	0.510	0.217	0.134
La	ppm	0.39	0.21	–	0.25	0.22	–	–	0.43	–	0.28	0.62	0.13
Sm	ppm	0.08	0.143	0.320	0.20	0.20	–	–	0.227	0.415	0.199	0.332	0.065
Yb	ppm	0.35	0.31	0.15	0.26	0.32	–	–	0.13	–	0.256	0.269	0.154
Lu	ppm	0.12	0.09	0.048	0.07	0.03	–	0.032	0.033	0.031	0.038	0.052	0.036
Fe	%	22.4	11.7	26.2	26.4	27.4	88.6	10.9	27.8	24.9	13.00	19.60	3.13
Co	ppm	620	57.0	531	435	255	150	15.3	293	175	245	127	40.9
Au	ppb	333	264	80	202	15	33	–	110	47	19.8	2.2	–
Ir	ppb	775	107	3.79	640	308	34	21.7	6.65	4.18	7.04	13.6	2.73

INAA for long half-life nuclides(LL series): After the SL series, the samples were picked out from the polyethylene bags and encased again individually in ultra-pure synthetic quartz vials. Then they were activated again all together for 100 hr at 20 MW ($1x10^{14}$ neutrons/cm^2/sec) in a hydraulic rabbit irradiation facility HR-1 of the JRR-3M. They were counted repeatedly in accordance with their half-lives and activities, using gamma-ray counting facilities of the Institute for Cosmic-Ray Research, University of Tokyo and Aoyama Gakuin University. Counting durations and cooling times were about for 2~12 hr after 4~8 days, for 6~24 hr after 2~3 weeks, 1 day ~1 week after more than 1 month, respectively.

Results

As listed in Table and shown in Figures, results are; *i.e.*, a) Abundance patterns normalized to CI, Mg (LPEs: Al, Ti, Ca, Mg, Cr, Mn, Na) and Fe (SPEs: Ir, Cr, Mn, Fe, Co, Au) of the MMs illustrate their features similar to chondrites (except Na, Ir, Au are more or less depleted in 2/3 of the MMs) rather than achondrites. b) They are classified into six types (5 S-types and 1 I-type) based on their abundance patterns of LPEs and SPEs. c) REE (Sc, La, Sm, Yb, Lu) abundances also show the patterns; *i.e.*, unfractionated ones similar to chondrite (12 MMs), a little fractionated ones (9 MMs) and fairly fractionated ones (10 MMs). d) In contrast to Deep Sea Spherules, AMMs do not so much deplete Na and Au.

References:

[1] Murray J. and Renard A. F. (1883) *Proc. Roy. Soc. Edinburgh, 12,* 474–495. [2] Brownlee D. E. et al. (1976) *NASA Tech. Mem., TMX-73152,* 1-42. [3] CDPET (1981-1997) *Cosmic Dust Catalog,* NASA/ JSC, Vol 1-15. [4] Maurette M. et al. (1986) *Science, 233,* 869-872. [5] Maurette M. et al. (1991) *Nature, 351,* 44-47. [6] Nakamura T. et al. (1999) *AMR, 12,* 183-198. [7] Fukuoka T. et al. (1999) *Ant. Met. XXIV,* 24-25. [8] Yada T. and Kojima H. (2000) *AMR, 13,* 9-18. [9] Iwata N. and Imae N. (2002) *AMR, 15,* 25-37. [10] Noguchi T. et al. (2000) *AMR, 13,* 270-284. [11] Fukuoka T. et al. (2000) *Ant. Met. XXV,* 10-11. [12] Tazawa Y. et al. (2003) *Internatl. Symp. Evolution of Solar System Materials,* 138-139. [13] Fukushi Y. et al. (2004) *Ant. Met. XXVIII,* 12-13. [14] Fukuoka T. and Tazawa Y. (1996) *Ant. Met. XXI* 33-34.

Figure 1. Abundances normalized to CI, Mg (LPEs) and Fe (SPEs)

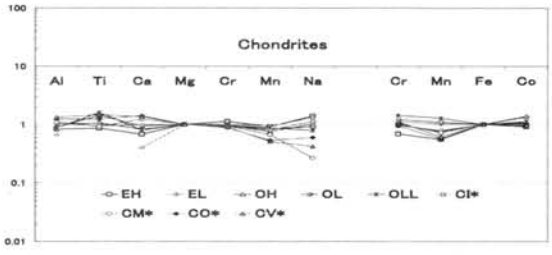

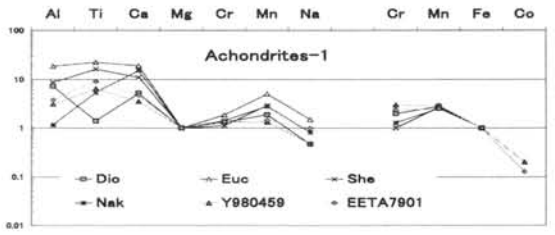

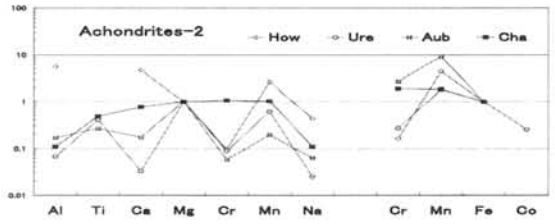

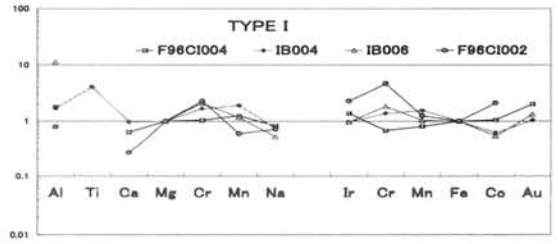

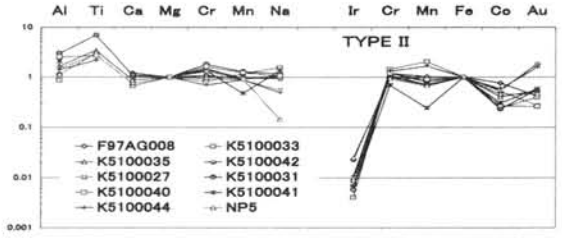

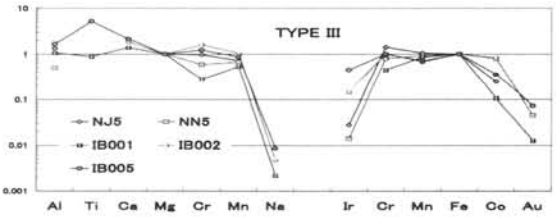

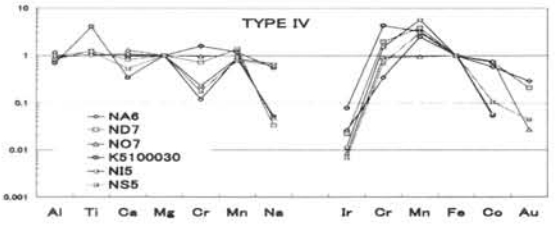

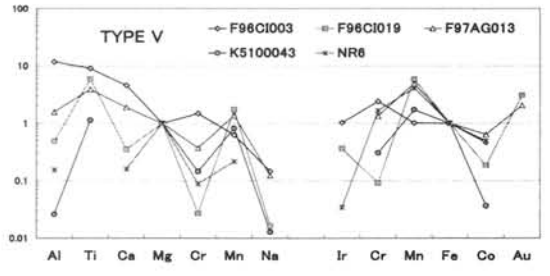

In-situ U-Pb dating of phosphates in lunar basaltic breccia EET87521 and EET96008

K. Terada[1,2]* and Y. Sano[3], [1]Department of Earth and Planetary Systems Science, Hiroshima University, Higashi-Hiroshima 739-8526, JAPAN (terada@sci.hiroshima-u.ac.jp), [2]MIRAGE Project Center, Hiroshima University, Higashi-Hiroshima 739-8526, JAPAN, [3]Center for Advanced Marine Research, Ocean Research Institute, The University of Tokyo, Nakano-ku 164-8639, JAPAN.

Introduction:

The lunar meteorites have been valuable sources for understanding the origin and evolution of the Moon, as they could potentially provide a new insight into the thermal history of unexplored regions of the Moon. For example, the predominance of low-Ti and Very-Low-Ti (VLT) basaltic materials in the lunar meteorites contrasts with their scarcity among lunar samples returned by the six Apollo and three LUNA missions [1-3]. In spite of their scientific interests, chronological studies of brecciated lunar meteorites have proved to be difficult, since they are mixtures of materials with different origins. In this paper, U-Pb systematics of phosphates in the brecciated lunar meteorite Elephant Moraine 87521 (hereafter abbreviated as EET 87521) and EET 96008, which are considered to be paired and are classified into VLT basalt [4-13], were investigated using the Sensitive High Resolution Ion MicroProbe (SHRIMP) installed at Hiroshima University, JAPAN. (Although our coworker Anand et al. [14] have already published the chronological data of EET 96008, we just compiled them for the comparison with EET 87521). Our in-situ analysis techniques attain high sensitivity at high mass resolution of ~5800 (e.g. more than 10 cps/ppm/nA for ^{206}Pb on apatite; [15]), providing the following advantages in comparison with conventional TIMS analyses: (1) a much smaller amount of sample is required, (2) the mineralogy of the phosphates and textural relationships with other minerals can be investigated, (3) U-Pb systematics in various phases are independently investigated, and (4) following the U-Pb analysis, other elements such as rare earth elements (REEs) can be measured in the same grain. This in-situ U-Pb dating method has been successfully applied to extraterrestrial phosphates in some Martian meteorites [16-18] and some ordinary chondrites [19, 20]. The purpose of the present work is to investigate the U-Pb systematics of phosphates in EET 87521 and EET 96008, independently, and to constrain the thermal history of VLT sources.

Sample and Analytical Methods:

At first, the polished thin sections were carbon-coated and back-scattered electron images were obtained, with the major chemical components being analyzed by an Electron Probe Micro Analyzer (EPMA), in order to identify the location and mineralogy of phosphates. Ten phosphate grains (5 whitlockites and 5 apatites) and eight phosphate grains (5 whitlockites and 3 apatites) were observed in the single thin section of EET 87521 and EET 96008, respectively, whose sizes range from 10 to 30 μm. The location and chemical composition of melt glass phases are also investigated for EET 87521. The textures of phosphate are homogeneous except for some cracks. In contrast, the textures of glass phase are inhomogeneous on 1~10 μm scale. For SHRIMP analysis, the area of grain was selected so as free from such inclusions or cracks.

After EPMA analysis, the thin sections were polished slightly using 0.25 μm diamond paste. Then, following cleaning to minimize surface contaminant Pb, it was gold-coated to prevent charging of the sample surface during SHRIMP analyses. The thin sections were evacuated in the sample lock overnight in order to further reduce the already very small $^{x-1}PbH^+$ interference on the $^{x}Pb^+$ peaks. Before the actual analysis, the sample surface was rastered for 3 minutes in order to remove possible contaminants.

An ~ 1 nA O_2^- primary beam with acceleration voltage of 10kV was focused to sputter an area ~ 10 μm in diameter on the phosphates and positive secondary ions were extracted with 10 kV. The mass resolution was set to ~ 5800 at ^{208}Pb for U-Pb analyses. The magnet was cyclically peak-stepped from mass 159 ($^{40}Ca_2{}^{31}P^{16}O_3^+$) to mass 254 ($^{238}U^{16}O^+$), including background, all Pb isotopes, and masses 238 and 248 for ^{238}U and $^{232}Th^{16}O$. No significant isobaric interferences were detected in this mass range for the phosphates (e.g. the mass peak of ^{159}Tb (158.925 AMU) is clearly separated from that of $^{40}Ca_2{}^{31}P^{16}O_3^+$ (158.884 AMU) by the mass resolution of 5800). The abundance ratios of ^{238}U to ^{206}Pb were obtained from the observed $^{238}U^+/^{206}Pb^+$ ratios using an empirical quadratic relationship between the $^{206}Pb^+/^{238}U^+$ and $^{238}U^{16}O^+/^{238}U^+$ ratios of standard apatite PRAP dated at 1156 Ma. Experimental details of the U-Pb analysis and the calibration of the data were given in [15, 16]. The analyses and calibration of glass phase are analogous to those of phosphate, in exception that matrix peak is 104 ($^{28}Si_2{}^{16}O_3^+$) instead of 159 ($^{40}Ca_2{}^{31}P^{16}O_3^+$) and NIST SRM610 is used as a referenced standard [21].

Results and Discussion:

Analyses of three whitlockite and five apatite from EET 87521 give a $^{204}Pb/^{206}Pb$ – $^{207}Pb/^{206}Pb$ isochron age of 3503 ± 140 Ma (95% confidence limit), while apatite analysis alone gives a $^{238}U/^{206}Pb$ – $^{204}Pb/^{206}Pb$ isochron age of 4325 ± 930 Ma (95%

confidence limit). Thus, we define the formation age of phosphates in EET 87521 is 3521 ± 138 Ma as a weighted mean age of these two. On the other hand, The $^{204}Pb/^{206}Pb$ – $^{207}Pb/^{206}Pb$ isochron age of apatite and whitlockites for EET 96008 is 3538 ± 80 Ma (95% confidence limit), consistent with those of EET 87521 (3503 ± 140 Ma). The observed U/Pb and Pb/Pb ratios for EET 96008 were well presented by *PLANAR* regression rather than *LINEAR* regression in the $^{238}U/^{206}Pb$ - $^{207}Pb/^{206}Pb$ - $^{204}Pb/^{206}Pb$ 3D space, and the best-fitted *PLANAR* regression intercepts the concordia curve on the $^{238}U/^{206}Pb$ - $^{207}Pb/^{206}Pb$ plane at 3569 ± 100 Ma and 100 ± 130 Ma (2σ) as shown in Figure 15 of [14]. The upper intercept age of 3569 ± 100 Ma for EET 96008 agrees well with those of 3531 ± 110 Ma for EET 87521. Thus, all these results indicate that the observed age of about 3.55 Ga defines the phosphates formation age in their parent mare basalt. This is quite distinct from previous chronological studies on the VLT mare basalt of 3.2-3.3Ga for LUNA 24 [22, 23], extending the VLT magmatism 200 m.y. prior to the known age. Vogt et al. [24] showed that EET 87521 was launched from the Moon < 10^5 yr ago and arrived on the Earth between 15~50 x 10^3 yr ago, and Nishiizumi et al. [25] suggested that the exposure history of EET 96008 is compatible with that of EET 87521. Taking into account these results and the lower intercept age of 100 ± 130 Ma recorded in the EET 96008 phosphates, it is likely that the discordance found in the $^{238}U/^{206}Pb$ ratios of EET 96008 is attributable to a shock metamorphism occurred at 100 ± 130 Ma, when the meteorite was launched to the Earth. It should be noted that the observed $^{238}U/^{206}Pb$ ratios of whitlockites grains in EET 96008 range from 2.2 to 7.8, indicating that whitlockites are more influenced by shock events than apatites (see Figure 15 in [14]). For EET 87521, only one whitlockite grain, #6 among five whitlockite grains is similarly discordant. The observed ratios of grain #6 ($^{238}U/^{206}Pb$ = 2.13, $^{207}Pb/^{206}Pb$ = 0.311 and $^{204}Pb/^{206}Pb$ = 0.0002) are very similar to those of the least influenced whitlockite grain #38.05 in EET 96008 ($^{238}U/^{206}Pb$ = 2.15, $^{207}Pb/^{206}Pb$ = 0.325 and $^{204}Pb/^{206}Pb$ = 0.0007), suggesting that phosphates in EET 87521 were less influenced than in EET 96008. The reason is not well understood at present.

In contrast to U-Pb systematics of phosphates, those of glass phases in EET 87521 are so complicated that the conclusive age could not be determined possibly due to local heterogeneous texture on 1~10 μm scale. If their origins of glass phase were the same (in other words, the parent materials had same initial Pb compositions) and they were disturbed by a single event, the observed data of glass phases should be plotted on a discordia *PLANE* in the $^{238}U/^{206}Pb$-$^{207}Pb/^{206}Pb$-$^{204}Pb/^{206}Pb$ 3D space (for details see [26, 27]). However, observed U-Pb data show considerable scatters and the significant correlations could not be found. This result indicates that glass phases were formed from different origin materials by single or more shock events. In contrast, phosphates grains in EET 87521 might be derived from the same origin and might not be affected by such a shock event possibly due to their high closure temperatures. In addition, it should be emphasized that U and radiogenic Pb in glass phases are not negligible. This means that chemical leaching techniques for bulk U-Pb system might lead an invalid age assessment for this kind of samples.

Acknowledgments

The polished thin sections of EET 87521 and EET96008 were provided by NASA and Dr. L. A. Taylor from the University of Tennessee, respectively. We are also appreciate Dr. T. Arai, Dr. I. Williams and Dr. N. Kita for valuable discussions.

References:

[1] Lindstrom M. M., Martinez R. R. and Lipschutz M. E. (1991) *LPS XXII*, 817-818. [2] Lindstrom M. M. et al. (1991) *AMR 4*, 12-32. [3] Warren P. H. and Kallemeyn G. W. (1991) *AMR 4*, 91-117. [4] Delaney, J. S. (1989) *Nature 342*, 889-890. [5] Warren P. H. and Kallemeyn G. W. (1989) *GCA 53*, 3323-3330. [6] Delaney et al. (1991) *LPS XXII*, 301-302. [7] Takeda H., Mori H. and Saito J. (1992) *LPS XXII*, 355-364. [8] Arai T., Takeda H. and Warren P. H. (1996) *M&PS 31*, 877-892. [9] Arai T. and Warren P. H. (1999) *M&PS 34*, 209-234. [10] Snyder G. A., Taylor L. A. and Patchen A. (1999) *LPS XXX*, #1499. [11] Snyder G. A. et al. (1999) *LPS XXX*, #1705. [12] Warren P. H. and Ulff-Møller F. (1999) *LPS XXX*, #1450. [13] Mikouchi T. (1999) *LPS XXX*, #1558. [14] Anand M. et al. (2003) *GCA 67*, 3499-3518. [15] Sano Y. et al. (1999) *Chem. Geol. 153*, 249-258. [16] Sano Y. et al. (2000) *M&PS 35*, 341-346. [17] Terada K., Monde T. and Sano Y. (2003) *M&PS 38*, 1697-1703. [18] Terada K. and Sano Y. (2004) *M&PS 39*, 2033-2041. [19] Terada K. and Sano Y. (2002) *GRL 29*, 98-1~4. [20] Terada K. and Sano Y. (2003) *Applied Surface Science 203/204*, 810-813. [21] Terada et al. (2002) *LPS XXXIII*, #1481. [22] Nyquist L. E. and Shih C.-Y. (1992) *GCA 56*, 2213-2234. [23] Nyquist L. E., Bogard D. D. and Shih C. –Y (2001). Radiometric chronology of the Moon and Mars, chapter 55, pp. 1325-1376. [24] Vogt S. et al. (1993) *GCA 57*, 3793-3799. [25] Nishiizumi K. et al. (1999) *LPS XXX*, #1980. [26] Wendt I. (1984) *Chem. Geol. 46*, 1-12. [27] Wendt I. (1989) *EPSL 94*, 231-235.

Transmission electron microscopy of experimentally shocked Murchison CM chondrite.

N. Tomioka[1], K. Tomeoka[1], K. Nakamura[2], [1]Department of Earth and Planetary Sciences, Faculty of Science, Kobe University, Kobe 657-8501, Japan, [2] NASA, Johnson Space Center, Houston, Texas, 77058, USA

Introduction:

A large population of dust particles (micrometeorites) falling to the Earth's surface has characteristics related to hydrated, porous meteorites. However, such meteorites comprise only a very small population (2.8%) of recovered falls [1]. It has been widely believed that hydrated, porous meteorites are so friable that they are mostly broken up into dust particles during atmospheric passage [2]. Recently, Tomeoka et al. (2003) conducted shock recovery experiments of anhydrous (Allende CV) and hydrated (Murchison CM) carbonaceous chondrites and found that high-density fractures are produced in the hydrated meteorite shocked at 25-30 GPa, but such fractures are not produced in the anhydrous meteorite shocked at pressures even higher than 30 GPa [3]. Thus, they suggested that hydrated asteroids would readily be explosively dispersed by impacts and produce dust particles during collisions at a much higher rate than anhydrous asteroids [3].

Previous studies [4, 5] indicated that most micrometeorites have been significantly altered or melted by heating. The effects of heating have previously been mainly ascribed to aerodynamic drag during atmospheric entry. If the model described above [3] is valid, the effects of heating in micrometeorites should also be ascribed to impact-induced shock on their parent bodies. However, effects of heating in shocked hydrated meteorites and their relationship to micrometeorites have remained to be more studied. Here we report the results of transmission electron microscopy (TEM) study of the matrix of Murchison experimentally shocked at a pressure range of 10-49 GPa.

Experimental Methods:

Small pieces of matrix (~50 μm in size) were removed from the Murchison samples shocked at 10, 21, 30, 36 and 49 GPa and embedded in epoxy. They were processed to thin foils of 55-70 nanometers in thickness using an ultramicrotome. The thin foils were mounted on Cu grids covered with microgrid and formvar/carbon film. ATEM observations and analyses were performed using a JEOL JEM-2010 equipped with an energy dispersive spectrometer, operated at 200 kV. The details of shock experiments and the results of petrographic and mineralogical studies of recovered samples are described in Tomeoka et al. (1999) [6].

Results:

The matrix of unshocked Murchison consists mainly of Fe-rich serpentine and tochilinite. In the samples shocked at 10 and 21 GPa, Si-rich glass is the dominant phase. In places, coarse grains (<0.7-5.5 μm in size) of serpentine having an interlayer spacing of ~0.7 nm are embedded in Si-rich glass. Tochilinite is absent. Si-rich glass contains numerous rounded and subrounded inclusions (< 200 nm) of Fe-O-rich phase and Fe-S-rich phase, which are probably Fe-oxide (or –hydroxide) and Fe-sulfide, respectively. Fe-sulfide inclusions are heterogeneously distributed.

In the sample shocked at 30 GPa, the matrix consists of abundant fine grains (0.2-1 μm) of Mg-rich olivine ($Fo_{99\pm1}$) embedded in Si-rich glass. The Si-rich glass contains numerous rounded inclusions (<150 nm) of Fe-sulfide, Fe-oxide and minor amounts of low-Ca pyroxene ($En_{95\pm2}$) (0.2-1.0 μm in size). In places, relatively coarse-grained serpentine (0.1-0.5 μm) occurs.

In the sample shocked at 36 GPa, Si-rich glass is the dominant phase. It contains numerous vesicles (< 500 nm) and rounded inclusions (< 150 nm) of Fe-oxide and Fe-sulfide as well as minor amounts of Mg-rich olivine ($Fo_{95\pm3}$) (0.5-1.5 μm) and low-Ca pyroxene ($En_{89\pm14}$) (1-2 μm). Serpentine is absent.

In the sample shocked at 49 GPa, Fe-rich olivine grains ($Fo_{57\pm9}$; 0.3-2.5 μm in size) are abundant. They commonly contain Fe-Cr-rich inclusions (< 50 nm) that are probably derived from the stainless steel container. Low-Ca pyroxene grains (0.2-0.5 μm; $En_{51\pm23}$) are more abundant than in the matrix shocked at 36 GPa. Si-rich glass occurs in the interstices of olivine and low-Ca pyroxene grains. The Si-rich glass commonly contains numerous vesicles (< 600 nm) and Fe-Ni-metal and Fe-Ni-sulfide (70-300 nm).

Discussion:

Our study revealed that tochilinite is completely absent in the samples shocked at 10 GPa and above, and serpentine is completely absent in the samples shocked at 36 GPa and above. In all the samples studied, Si-rich glass containing numerous inclusions of Fe-oxide and Fe-sulfide occurs as the dominant phase, and the amount of Si-rich glass increases with increasing shock pressure. From these results, we interpret that the Si-rich glass with Fe-oxide inclusions was produced by the breakdown of Fe-rich serpentine and the Si-rich glass with Fe-oxide and Fe-sulfide inclusions was produced by the breakdown of serpentine and tochilinite.

The breakdown of these hydrous minerals gives some constraints on the temperatures to which the samples were heated at given shock pressures. It is known that tochilinite is sensitive to heat and

easily decomposed to Fe-sulfide at 245 °C [7]. Our study suggests that Murchison shocked at 10 GPa was heated to at least 245 °C. Heating experiments of Murchison [8] indicated that serpentine is decomposed at 700 °C. Thus, the post-shock temperature of Murchison shocked at 36 GPa probably reached at least 700 °C.

Abundant fine fragments of olivine and low-Ca pyroxene occur in the sample shocked at 30 GPa. They are very Fe poor and homogeneous in composition, and are compositionally similar to olivine and pyroxene in type I chondrules of natural Murchison [7]. We suggest that the fine-grained olivine and pyroxene have been mostly derived from impact-induced fragmentation of olivine and low-Ca pyroxene crystals in chondrules.

At 49 GPa, olivine and low-Ca pyroxene are the dominant phases, and they are coarser-grained and more heterogeneous in Fe content than those in the samples shocked at lower pressures. Many of the olivine and pyroxene grains were probably derived from fragmentation of olivine and pyroxene in chondrules, as in the sample shocked at 30 GPa. Mg-rich olivine may have been enriched in Fe by solid-state diffusion during strong post-shock heating. We infer that it is also possible that part of olivine and low-Ca pyroxene grains, especially those containing Fe-Cr-rich inclusions, were crystallized from shock-induced melts that were produced from Fe-rich serpentine and tochilinite.

Previously Greshake et al. (1998) conducted flash heating experiments of the hydrated CI chondrites to simulate the effects of atmospheric entry of hydrated interplanetary dust and examined heated samples by a TEM [9]. In the CI samples heated at > 800 °C, phyllosilicates were mostly decomposed, and the dominant phases are olivine and pyroxene with interstitial Si-rich glass. The mineralogy and texture of the heated CI samples are very similar to those of the matrix of shocked Murchison presently studied.

Recently, many unmelted micrometeorites collected in Antarctica were characterized by synchrotron X-ray diffraction and ATEM studies and mineralogically classified into three classes; phyllosilicate-rich, olivine-rich and pyroxene-rich classes [5]. The mineralogy and texture of the shocked Murchison matrix have close similarities to those of the micrometeorites. If hydrated asteroids are among the main sources of micrometeorites, the effects of heating in micrometeorites could also be explained by impact-induced shock on their parent bodies. This indicates that heating effects of extraterrestrial impacts on dust particles could be overprinted on those of atmospheric entry. Therefore, we believe that the thermal history of dust particles needs to be further re-evaluated.

References:

[1] Sears D.W.G and Dodd R.T. in *Meteorites and the Early Solar System* (eds Kerridge J.F. & Mathews M.S.) 3-31 (Univ. Arizona Press, Tuscon, 1988). [2] *e.g.* Baldwin B. & Sheaffer Y. (1971) *J. Geophys. Res.* **76**, 4653-4668. [3] Tomeoka K. et al. (2003) *Nature* **423**, 60-62. [4] *e.g.* Kurat G. et al. (1994) *Geochim.Cosmochim. Acta* **58**, 3879-3904; Genge M.J. et al. (1997) *Geochim.Cosmochim. Acta* **61**, 5149-5162; England C. & Maurette M. (1998) *Meteorit. Planet. Sci.* **33**, 565-580. [5] Nakamura T. et al. (2001) *Geochim.Cosmochim. Acta* **65**, 4385-4397; Noguchi T. and Nakamura T. (2000) *Antarct. Meteorite Res.* **13**, 285-301. [6] Tomeoka K. et al. (1999) *Geochim. Cosmosim. Acta* **63**, 3683-3703. [7] Fuchs L.H. et al. (1973) *Smithson. Contrib. Earth Sci.* **10**, 1-39. [8] Akai J. (1992) *Proc. NIPR symp. Antarc. Meteorites* **5**, 120-135. [9] Greshake A. et al. (1998) *Meteorit. Planet. Sci.* **33**, 267-290.

Formation process of compound chondrules in primitive solar nebula. M. Uesugi[1] and M. Sekiya[2], [1]Department of Earth and Planetary Sciences, Graduate School of Sciences, 33 Kyushu University, Hakozaki, Fukuoka, 812-8581, Japan [2]Department of Earth and Planetary Sciences, Faculty of Sciences, 33 Kyushu University, Hakozaki, Fukuoka, 812-8581, Japan.

Abstract:

We focused our attention on the compound chondrules that consist of different-texture chondrules. In order to form such compounds, very small scale of thermal energy distribution on the space is required, because the difference of chondrule textures is considered to depend on the difference of thermal history of the chondrules.

We examined the possibility of the formation of compound chondrules by nebular shock wave, which is thought as one of the most probable process of chondrule formation. Our examinations show that chondrules with different sizes have very large relative velocities. So, for the nebular shock wave model, the sticking between chondrules only those have almost same radius could occur because collisions with relative velocities less than several m/s could form compound chondrules. However, the chondrules those have similar radii would experience similar thermal histories in a shock wave, because the degrees of drag heating are almost same for such chondrules throughout the shock heating. So, the results of our calculations shows that the chondrules in a compound chondrule would have similar textures, if they formed by nebular shock wave heating.

Introduction:

Compound chondrules, which consist of two or more chondrules sticking each other, are occasionally found in natural chondrites. Figure 1 shows the compound chondrules that classified as "independent", which consists of chondrules with different type of textures [1]. We investigated the possibility for the sticking of chondrules with different textural types, especially compound chondrules those consist of non-porphyritic "secondary chondrules" (lost spherical shape due to sticking). In such case, the non-porphyritic chondrules, which require total melting and rapid cooling, must stick to another chondrule before their resolidification. Such independent type compound chondrules could form, if the thermal histories between the chondrules are different enough, and also those chondrules with different thermal history have enough possibility of sticking.

Nebular shock wave model:

Nebular shock wave heating model is thought as one of the most probable models of chondrule formation. Recent studies shows that the temperatures of chondrules in a nebular shock heating mainly depend on the radiation from surrounding materials, and then the thermal histories of chondrules in a nebular shock wave are similar irrespective of other physical quantities of chondrules in the optically thick environment [2-3]. The thermal history of chondrules is very important for the variation of chondrule textures. Thus, compound chondrules, which classified as independent, are difficult to form in such environment.

However, in an optically thin environment, the thermal histories of chondrules mainly depend on the drag heating, which is the function of chondrule radius. Thus, the compound chondrules, which are classified into "independent", could form in the optically thin nebula and by the collisions between the chondrules with different size, because they could experience different thermal histories in a nebular shock wave[4].

We calculated the motion of chondrules in a shock wave using the models shown by previous studies [2], and investigated the possibility of sticking of chondrules that have different textures.

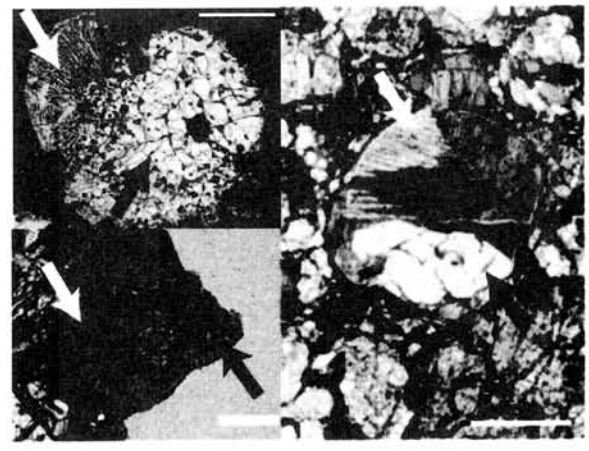

Fig. 1 Images of compound chondrules that have non-porphyritic "secondary" chondrules. White scales measure 300 μm. **Upper left:** A Barred olivine chondrule (a white arrow) sticks on a porphyritic chondrule (a black arrow). **Lower left:** A radial pyroxene chondrule (a white arrow) sticks on a porphyritic pyroxene chondrule (a black arrow). **Right:** A barred olivine chondrule (a white arrow) sticks on a large olivine crystal (a black arrow)

Results:

Figure 2 shows an example of results showing kinetic energy variations of chondrules that have 5% to 40% differences in their radii in the shocked

nebular gas flow, which is normalized by the total surface energy of melted chondrules. We ignore the energy dissipation due to viscosity of molten silicates at the time of collisions, because the viscosity of a totally melted chondrule is low enough (< 10 poise; [5]). The values of physical parameters used for this calculations are, nebular gas mass density far upstream of nebular shock ρ_g=10^{-9} g cm^{-3}, the initial temperature of nebular gas T_g=500 K, the shock velocity v_s=9 km s^{-1}, the surface tension of melted chondrule τ_c=400 dyn cm^{-1}, the mass density of melted chondrule ρ_c=3.4 g cm^{-3}, the mass ratio of chondrules to nebular gas is 0.01, which is determined by the solar abundance of solid material. Our model consists of three populations of chondrules that have characteristic radius, 0.17, 0.3 and 0.42 mm for simplicity. The radii of chondrules are taken from the average radius of chondrules in ordinary chondrites and its standard deviation [5].

Figure 2 shows that the kinetic energy between chondrules that have 10% difference of radius are extremely large after a several tens seconds of passage of the nebular shock front, around 10^3-10^5 times total surface energy of melted chondrules, even after the stopping time. This means that the collisions of chondrules in the time around stopping time would lead to the disruption of them, not to sticking. In order to make it possible to stick at the stopping time, the incident and target chondrules must have almost same radii (within 10% difference in radii). However, if the radii of chondrules are too much close each other, the difference of textures cannot be established between the chondrules, because the thermal histories of chondrules are also almost same for such chondrules.

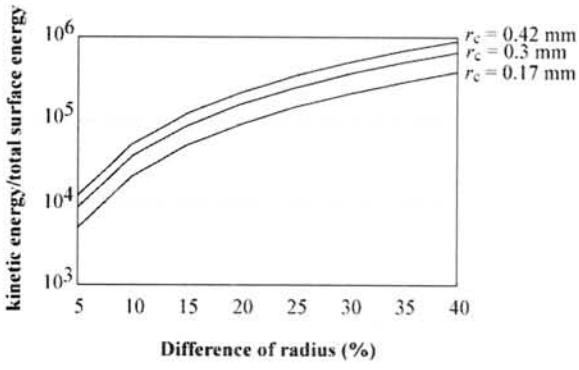

Fig. 2 The kinetic energies of chondrules at the stopping time with various case of radius difference. Even for the case of 5% difference, the kinetic energy of collision at the stopping time is 10^4 times total surface energy of melted chondrule.

The difficulty might be overcome by considering other effects that make the difference of textures of chondrules, such as the dust seeding [6]. If the difference of chondrule texture does not depend on the thermal history so largely, sticking could occur at far downstream of the nebular shock wave, where the collisions are not so destructive. However, there are some examples that could not be explained by such effects. Right part of Fig. 1 shows a totally melted chondrule (barred olivine chondrule) sticks on a large olivine crystal. The olivine crystal is clearly unmelted, although it has almost same chemical composition of the secondary BO chondrule. Hence the difference of melting degree suggests that their size is largely different, if the compound chondrule is formed by the nebular shock wave heating. However, the crystal must melt partially or totally from the surface and took spherical shape due to the radiative heating from the surroundings, if the sticking occurred far downstream of a shock wave in the high density region of solar nebula. In order to maintain the lithic shape, the secondary BO chondrule must rapidly melt and stick to the olivine crystal before the melting of the crystal. Thus, this compound chondrule indicates that very short duration between the total melting of secondary BO chondrule and sticking, suggesting they form in the region where very near to the nebular shock front, if they form due to a nebular shock wave.

The presence of compound chondrules that consist of chondrules with different textural types probably indicates that the length scale of thermal inhomogeneity of the chondrule formation region is very small.

References:

[1] Wasson J. T. et al. (1995) *GCA, 59,* 1847–1869. [2] DeschS.J.andConnollyH.C.Jr. (2002) *MAPS., 37,* 183-207. [3] Ciesla F. J. and Hood L. L. (2002) *Icarus, 158,* 281-293. [4] Iida A. et al. (2001) *Icarus, 153,* 430-450. [5] Uesugi et al., (2003) *Earth. Planet. Space., 55,* 493-507. [6] Connolly H. C. Jr. and Hewins, R. H., (1995) *GCA, 59,* 3231-3246.

Evidence for the shock metamorphism of GRV 99027. D. Wang and M. Chen. Guangzhou Institute of geochemistry, Chinese Academy of Sciences, 510640 Guangzhou, China

Introduction:
Martian meteorites found include several types of igneous rocks, which consist of basalt, peridotitite (lherzolite and harzburgite), clinopyroxenite, orthopyroxenite and dunite, respectively. It was reported that all these Martian meteorites were strongly shock-metamorphosed during the impact event on the Mars, and most important evidence for the shock metamorphism includes the formation of melting silicate pockets, melting silicate veins, shock-produced maskelynite, polysynthetic mechanical twins in pyroxene, mosaic texture in olivine and pyroxene, and high-pressure minerals [1-6]. The GRV 99027 meteorite is an lherzolitic shergottite recovered in the Grove Mountains region, Antarctica, by the 16th Chinese Antarctic Research Expedition in 1999/2000. This meteorite was considered to derive from Mars, and its petrology, mineralogy and rare earth elementary geochemistry were studied [7,8]. Here we reported preliminary results on the investigation of shock metamorphism on this meteorite.

Methods:
Polished thin sections of the GRV 99027 meteorite were studied by optical microscopy, scanning electron microscope in mode of back-scattered electron, and Raman spectroscopy. Chemical compositions of minerals were investigated by using X-ray energy dispersive spectrometer (EDS) and electron microprobe (EPMA).

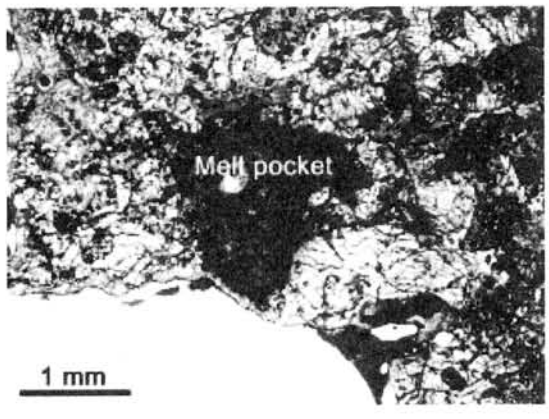

Fig.1. A recrystallized polymineralic melt pocket in the non-poikilitic areas. Plane polarized light.

Results and Discussion:
The meteorite consists of two distinct lithologies with both poikilitic and non-poikilitic areas, respectively. Poikilitic areas consist of millimeter-sized pyroxene (pigeonite) oikocrystals enclosing other minerals olivine, chromite and ilmenite as inclusions. The non-poikilitic areas are composed of olivine, pigeonite and augite with interstitial plagioclase, and accessory minerals chromite, ilmenite and whitlockite. Pigeonite both from poikilitic and non-poikilitic areas locally contains exsolution lamellae of augite.

Shock melt pockets: Several melt pockets up to 1 mm in diameter were observed in the non-poikilitic areas. These melt pockets are mainly composed of fine-grained silicate assemblage mainly consisting of olivine and pyroxene with interstitial plagioclase. Olivine and pyroxene in the melt pockets have lath-like morphology from 5 by 20 μm to 20 by 200 μm(Fig.1). Although a silicate glass was reported by other investigators [8], we did not observe such glass phase. It shows recrystallizing texture in these shock-induced melt pockets.

Mechanical deformation: Olivine and pyroxene in non-poikilitic areas are with mosaic texture. Weak undulatory extinction was developed in olivine and pyroxene in both poikilitic and non-poikilitic areas. Mechanical twins were observed in the pyroxene, which appears as shock-induced polysynthetic mechanical twin lamellae.

Shocked plagioclase: Although this meteorite was shock-metamorphosed and contains silicate melt pockets, all shocked plagioclase is still crystalline. We investigate many grains with plagioclase composition and no maskelynite has been found. Most plagioclase contains lamellae of olivine and pyroxene and show branches intruding regular fractures of the neighboring pyroxene and olivine (Fig.2). Olivine and pyroxene fragments enclosed in plagioclase also show jagged surface. The formation of such tooth or jagged surface shows evidence of dissolving of olivine and pyroxene into plagioclase liquid. It suggests that the lamellae of olivine and pyroxene in plagioclase were formed because of exsolution from a plagiolcae melt with small amount of dissolved olivine and pyroxene. Olivine and pyroxene neighboring these plagioclase grains were locally transformed from single crystal into fine-grained polycrystalline aggregate typical for a recrystallization texture. Obviously, plagioclase was reheated into a liquid during an impact event, and the temperature in the liquid was high enough for the melting of olivine and pyroxene. The shock-produced plagioclase liquid was subsequently recrystallized due to a lower cooling rate.

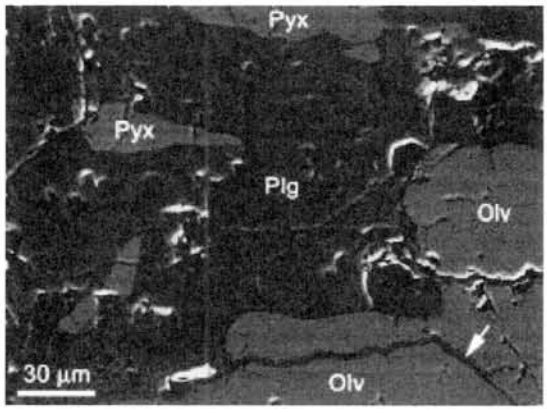

Fig. 2. Back-scattered electron image of a plagioclase grain showing pyroxene fragments and oriented lamellar inclusions or intergrowths. The arrow indicated a plagioclase branch intruding fractures of the neighboring olivine. Pyx-pyroxene; Olv-olivine; Plg-plagioclase.

Conclusions:

Our preliminary study indicates that the meteorite was locally shock-metamorphosed to a temperature up the melting point of olivine and pyroxene, probably more than 1600 °C, which correspond to a peak shock pressure above 45 GPa[9]. At such shock-induced high temperature, both material with whole rock composition and all plagioclase were locally melting, which results in the formation of melt pockets with bulk rock composition and plagioclase melt, following with recrystallization of these two kinds of silicate melt at a lower cooling rate. In comparison to other Martian meteorites, this meteorite could have been heated by shock to a higher temperature following subsequently slow cooling.

References:

[1] Stöffler D. et al (1986) *Geochim. Cosmochim. Acta* 50: 889-903. [2] Ikeda Y. (1997) *Antarctic Meteorit. Res.* 10: 13-40. [3] Malavergen V. et al. (2001) *Meteorit. Planet. Sci.* 36: 1297-1305. [4] Sharp T. G. et al. (1999) *Science* 284: 1511-1513. [5] El Goresy A. et al. (2000) *Science* 288: 1632-1634. [6] Walton E. L. and Spray J. G. (2003) *Meteorit. Planet. Science* 38: 1865-1875. [7] Lin Y.et al. (2003) *Chinese Science Bulletin* 48: 1771-1774. [8] Hsu W. et al. (2004) *Meteorit. Planet. Sci.* 39: 701-709. [9] Stöffler D. et al. (1991) *Geochim. Cosmochim. Acta* 55: 3845-3867.

The stellar origins of presolar silicates discovered in Antarctic micrometeorites. *T. Yada[1,2,3], F. J. Stadermann[1], C. Floss[1], E. Zinner[1], C. T. Olinger[1,4], G. A. Graham[5], J. P. Bradley[5], Z. R. Dai[5], T. Nakamura[6] and T. Noguchi[7]. [1]Lab. Space Sciences, Phys. Dept., Washington Univ., St. Louis, MO 63130-4899, USA. [2]Dept. Earth Planet. Sci., Grad. Sch. Science, Tokyo 113-0033, Japan. [3]Inst. Astron. Astrophys., Academia Sinica, Taipei 106, R.O.C. [4]Los Alamos Nat. Lab., Los Alamos, NM 87545, USA. [5]Inst. Geophys. Planet. Phys., Lawrence Livermore Nat. Lab., Livermore, CA 94550, USA. [6]Dept. Earth Planet. Sci., Grad. Sch. Sci., Kyushu Univ., Fukuoka 812-8581, Japan. [7]Dept. Material. Biol. Sci., Ibaraki Univ., Ibaraki 310-8512, Japan. **Present address:* Materials Sci. Div., Argonne Nat. Lab., Argonne, IL 60439, USA (yada@anl.gov).

Introduction: Presolar grains, which formed in the stars existed before the solar system, have given us valuable information about stellar nucleosynthesis and the origin of the solar system [1]. In these years, presolar silicates have been discovered in interplanetary dust particles (IDPs) and chondrites, which indicates that presolar grains existed more ubiquitously in the early solar nebula than previously considered [2,3]. As reported before, presolar silicates were discovered also in Antarctic micrometeorites (AMMs), using NanoSIMS [4,5]. This discovery tells us that parent bodies of the AMMs preserve a primary feature since their accretions in the early solar nebula. Here we review the discovered presolar silicates and discuss about their stellar origins.

Samples and Methods: Seven AMMs from Cap Prudhomme in West Antarctica (AWU01-3, -9, -11, -14, -16, -24 and -25) and five from Tottuki Point in East Antarctica (T98-G6, -H3, -H5, -NF2 and TT54B397) were used for this study [6-8]. They were analyzed by a scanning electron microscope equipped with energy dispersive X-ray spectrometry (SEM-EDS) and identified as AMMs based on their EDS spectra, which showed chondritic chemical compositions. The former seven AMMs were divided into two pieces; one was used for ion microprobe measurement and the other for noble gas measurement [9,10]. All AMMs except for one (TT54B397) were pressed into Au foils for the ion microprobe and NanoSIMS measurements. For NanoSIMS measurement, ~1nA primary Cs+ ions of Ø100nm in beam size were accelerated with 16kV to raster over the samples. Extracted negative ions were accelerated with 8kV to go through double-focusing mass spectrometer and detected by a multiple collectors system. The mass resolving power was ~6,000. $^{12}C^-$, $^{13}C^-$, $^{16}O^-$, $^{17}O^-$, and $^{18}O^-$ (lately $^{28}Si^-$ and $^{24}Mg^{16}O^-$ instead of $^{12}C^-$ and $^{13}C^-$) were simultaneously detected by five electron multipliers. The AMMs were analyzed in isotopic imaging mode with repeated scans over a 20x20μm^2 area for each analysis.

Results: In total, a ~37000μm^2 surface area of twelve AMMs was analyzed with NanoSIMS. Six presolar grains were discovered in three AMMs, AWU01-16, T98-H5, and TT54B397, based on their oxygen isotopic anomaly (Fig. 1). Three grains, T98-H5 grain 1-P1, 5-P1 and 15-P1 fall into the composition of Group 1 presolar oxide grains [11]. Although AWU01-16 grain C3-P1 also plot on the Group 1 composition, it cannot be classified as any Group of presolar oxide grains, because its original isotopic composition may be higher than the Group 1 compositions, which is estimated based on the fact that the surrounding area shows gradation in oxygen isotopic ratio and the possibility that the isotopic gradation results from a diffusion of the presolar isotopic oxygen from the grain C3-P1. TT54B397 grain 2-P1 and 2-P2 plot on the region of Group 4 presolar oxide grains. The sizes of these six grains ranges ~1μm to 200nm. All the presolar grains except for T98-H5 grain 15-P1 were also analyzed by the SEM-EDS to be identified as silicates. Although T98-H5 grain 15-P1 was consumed by the NanoSIMS measurement, it was also identified as a silicate because of the detection of certain amounts of $^{28}Si^-$ and $^{24}Mg^{16}O^-$ from the grain. A focused ion beam (FIB) section of AWU01-16 grain C3-P1 was further observed with transmission electron microscope (TEM). The grain consist of poorly crystallized ferromagnesian silicate containing aggregates of a few tens nm Fe-Ni metal/oxide grains (Fig. 3). AWU01-16 grain C3-P1 was also analyzed for Mg isotopes with NanoSIMS, however, no isotopic anomaly was detected. T98-H5 grain 1-P1, 5-P1 and 15-P1, and TT54B397 grain 2P-1 and 2P-2 were analyzed also for Si isotopes, but no obvious isotopic anomaly out of the range of the solar isotopic composition was observed.

Discussion: The three Group 1 presolar silicates are supposed to have formed in the stellar outflow wind from low-mass, high-metallicity red giants or asymptotic giant branch (AGB) stars [11]. For Group 1 presolar oxide grains, their stellar origins have been consistently predicted by theoretical studies, related their oxygen isotopic compositions with masses and metallicities of the RG or AGB stars [11]. As three Group 1 silicates plot on the oxygen three isotope diagram of red giants and AGB stars by theoretical prediction, T98-H5 grain 1-P1, 5-P1 and 15-P1 overlap with a star of >1.5 solar mass and Z~0.023, >1.5 solar mass and Z~0.018, and ~1.35 solar mass and Z~0.023, respectively (Fig. 4). This indicates that they have a different stellar source each other.

For Group 4 presolar oxide grains, their stellar sources are still under discussion. One possible source is ^{18}O produced in the He burning shell of AGB stars might have been dredged up in the early

thermal pulse [11]. Second possibility is that AGB stars with higher metallicity (subsequently ^{18}O-enriched) than the sun may have formed Group 4 grains. The third is Type II supernovae (SNII), which could have generated ^{18}O-rich oxide grains [2]. Each possible source has inconsistency, thus their stellar sources are still unclear. In this study, two Group 4 presolar silicates were also analyzed for Si isotopes, however, no obvious anomaly was detected. In contrast, type X SiC grains that are consistently supposed to originate from SNII show ^{28}Si enrichments [1]. This may indicate they would not originate from SNII, although SiC and oxide grains should have condensed at different regions in SNII.

Because AWU01-16 grain C3-P1 might originally have much higher $^{17}O/^{16}O$ and $^{18}O/^{16}O$ ratios than other Group 1 presolar oxide grains, its plausible stellar source cannot be proposed so far. If all excesses ^{17}O and ^{18}O in surrounding regions could have been diffused from the grain, its original $^{17}O/^{16}O$ and $^{18}O/^{16}O$ ratios are calculated to be $1.5x10^{-2}$ and $5.6x10^{-3}$, respectively. Wolf-Rayet stars, the first dredge-up of very low metallicity AGB stars, and novae could have reached such high $^{17}O/^{16}O$ ratios, although they should have extreme ^{18}O depletions [12-14].

References: [1] Zinner E. (1998) *Annu. Rev. Earth Planet. Sci.*, **26**, 147. [2] Messenger S. et al. (2003) *Science*, **300**, 105. [3] Nguyen A. N. and Zinner E. (2004) *Science*, **303**, 1496. [4] Yada T. et al. (2004) In *Chondrites and the Protoplanetary Disk, Abstract Volume*, 223. [5] Yada T. et al. (2005) *Lunar Planet. Sci.*, **XXXVI**, #1227. [6] Maurette M. (1991) *Nature*, **351**, 44. [7] Yada T. and Kojima H. (2000) *Antarct. Meteorite Res.*, **13**, 9. [8] Iwata N. and Imae N. (2002) *Antarct. Meteorite Res.*, **15**, 25. [9] Stadermann F. J. and Olinger C. T. (1992) *Meteoritics*, **27**, 291. [10] Olinger C. T. *et al.* (1989) *Earth Planet. Sci. Lett.*, **100**, 77. [11] Nittler L. R. (1997) In *Astrophysical implication of the laboratory study of presolar materials*, p59. [12] Prantzos N et al. (1986), *Astrophys. J.* **304**, 695. [13] Boothroyd A. I. and Sackmann I.–J. (1999) *Astrophys. J.* **510**, 232. [14] Fox C. et al. (2004)*Physical. Rev. Lett.* **93**, 807.

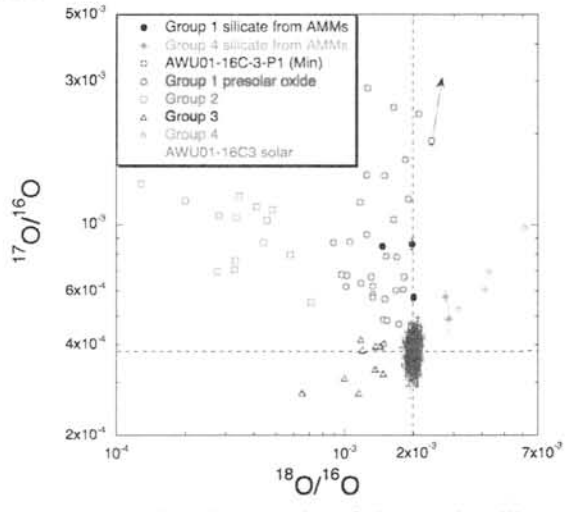

Fig. 1. Oxygen three isotope plot of six presolar silicates discovered in AMMs. Four Groups of presolar oxide grains plot for comparison [11].

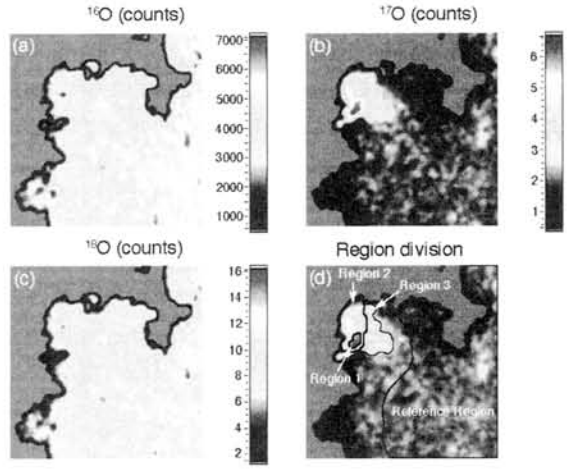

Fig. 2. Oxygen isotopic images of AWU01-16 grain C3-P1. The size of each image is $20x20\mu m^2$. Upper left area of this image is obviously enriched in ^{17}O compared to ^{16}O and ^{18}O. Since it shows a gradation in isotopic ratio, the isotopic anomalous area is divided into three regions, and region 1 is considered as an original presolar grain so far.

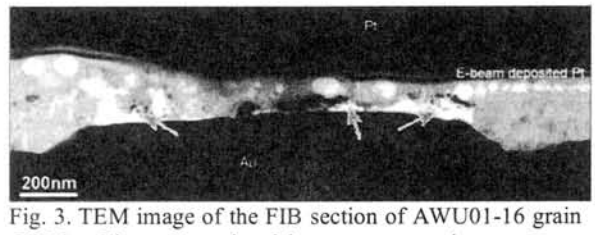

Fig. 3. TEM image of the FIB section of AWU01-16 grain C3-P1. The areas pointed by arrows contain aggregates of a few tens nm Fe-Ni metal/oxide grains.

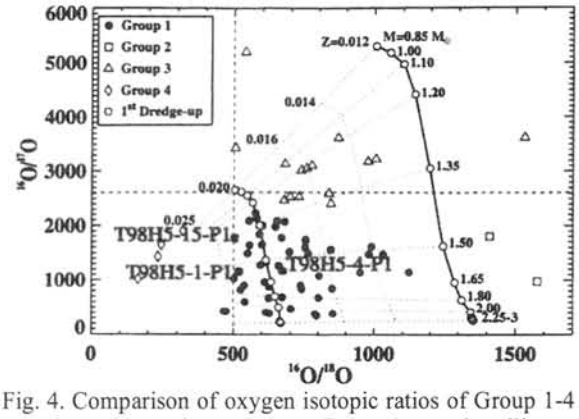

Fig. 4. Comparison of oxygen isotopic ratios of Group 1-4 presolar oxide grains and three Group 1 presolar silicates with those predicted for red giants or AGB stars of each mass and metallicity. This graph is based on the Fig. 3 of [11].

Yamato-86032 Lunar Meteorite: Implication for Impact History of the Highland Crust.

A. Yamaguchi[1], H. Takeda[2], Y. Karouji[3], M. Ebihara[1,3], L.E. Nyquist[4], D.D. Bogard[4], C.-Y. Shih[5], Y. Reese[5], [1]National Institute of Polar Research, Tokyo 173-8515, Japan, yamaguch@nipr.ac.jp, [2]Research Institute, Chiba Institute of Technology, Narashino 257-0016, Japan, [3]Department of Chemistry, Tokyo Metropolitan University, Hachioji, Tokyo 193-0397, Japan. [4]NASA Johnson Space Center, Houston, TX77058, USA. [5]Mail Code JE-23, ESCG/Jacobs Sverdrup, Houston, TX77058, USA.

Introduction:

Yamato- (Y) 86032 is a large lunar meteorite (648 gram) and a breccia composed of a variety of highland lithologies [1-3]. The low contents of Th and Fe suggest that this meteorite was derived from some distance away from the Apollo landing sites, perhaps, the far-side of the Moon [1-5]. One ferroan anorthosite (FAN) clast in Y-86032 has a very old Ar-Ar age of ~4.35-4.4 Ga [6]. The negative ε_{Nd} of this clast may suggest a direct link with the primordial magma ocean [7]. Thus, Y-86032 provides us with a unique opportunity to study highland lithologies not sampled by Apollo and Lunar missions.

We identified white (W), light gray (LG), dark gray (DG), and impact melt (IM) lithologies in a large slab (5.2 x 3.6 cm x 3-5 mm) of Y-86032 [3] Samples representing the three main lithologies were allocated for petrologic, geochemical, and isotopic studies. Results of the isotopic works are presented in a companion abstract [7].

Polished thin sections (PTSs) were made from representative portions adjacent to the separates for chemical and isotopic studies, and were examined by optical microscope, SEM, and EPMA. The bulk chemistries of the lithologies were analyzed by INAA and ICP-MS.

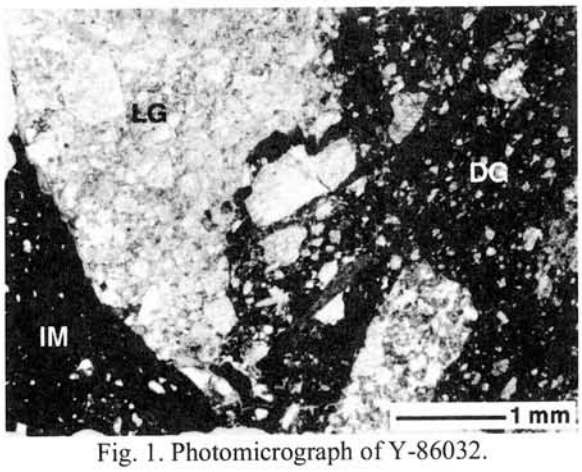

Fig. 1. Photomicrograph of Y-86032.

Texture and mineral chemistry:

Fragments of W lithology (clast) occur in the DG lithology (~5 vol%). The light-gray (LG) lithology (~20 vol %) occurs in the DG lithology with diffuse boundaries due to shear deformation. The black impact melt (IM) (~20-30 vol%) vein cuts both the LG and DG lithologies (Fig. 1). The breccia is well-lithified and has very low porosity.

The W lithology occurs as rounded or subrounded clasts (up to 3 mm in size) of anorthosite with minor mafic minerals (<1-5 vol%). The W lithologies include a variety of feldspathic clasts such as granulitic clasts, clasts similar to white portions in the LG lithology, and an ancient FAN clast described previously (e.g., ,116) [6,7].

The LG lithology is a breccia mostly composed of fragments of anorthosite (94.5%) with minor amounts (~5%) of pyroxene, olivine, silica minerals, and chromite. Olivine compositions are mostly $Fo_{78.1-82.4}$. There are some relatively Fe-rich olivine grains ($Fo_{66.4-64.6}$). Compositions of pyroxene vary significantly: low-Ca (<5 mol% Ca) pyroxenes have mg' (= Mg/(Mg+Fe) x 100) = 41.0-81.3. Plagioclase compositions range from $An_{\sim 85.4}$ to $An_{\sim 96.6}$ with two peaks at $An_{\sim 88.5}$ and $An_{\sim 93}$. There is a grain of AlMg-chromite ($Usp_{2.2}Sp_{42.5}$) (mg'=41.6). We also found a moderately, brecciated clast, composed of plagioclase ($An_{88.9}$) and Fe-rich augite grains ($Wo_{39-4}En_{31-39}$) (<0.2 mm in size). The augite grains have fine planar exsolution lamellae of low-Ca pyroxene. On the An versus mg' diagram, this clast plots outside the regions of pristine nonmare rock groups, probably forming a different suite of igneous rocks [3]. The LG lithology may be composed of fragments from augite-bearing anorthosites with plagioclase of $\sim An_{88.5}$ plus anorthosites with more An-rich plagioclases and more Mg-rich mafic minerals. The rocks thus represented may form a single suite of igneous rocks.

The DG lithology is a dark matrix composed of a variety of clast types: fragments of feldspathic clast (W lithology), glassy (impact melt) clast, granulitic clasts, basalts, and mineral fragments. Olivine compositions vary from $Fo_{8.7-83.3}$, and the mg' of pyroxenes, varies in the range 38.3-81.2. Plagioclase compositions are $An_{68.8-97.9}$. On the An versus mg' diagram, two granulitic clasts plot between the FAN and Mg-suite fields, like those found in the Apollo granulites [9]. The grain boundaries of clasts and mineral fragments are cemented by thin, vesiculated intergranular melts.

There is a basaltic clast (0.4 x 0.38 mm in size) composed of plagioclase and pyroxene with minor amount of silica minerals and Ti-rich phases. The pyroxenes are widely zoned ($Wo_{4.7}En_{71.3}$-$Wo_{24.5}En_{14.8}$) and show a strong correlation between

Fe/(Fe+Mg) (Fe#) and Ti/(Ti+Cr) (Ti#), overlapping the range of VLT basalt [10]. There are also fragments of mafic minerals that could be derived from mare basalts.

The IM vein is a dark glassy matrix with various kind of lithic and mineral fragments similar to those in the DG lithology.

Bulk chemistry:

The chemical data are mostly consistent with the previous data of Y-86032 [e.g., 2,4,11], except for Na, Al, V, Cr, Mn, and HREEs. The FeO content of the LG breccia (2.37 wt%) is lower than other lunar highland meteorites [11]. The Na/Ca and Fe/Mg may reflect the degree of geochemical evolution. Na/Ca in LG is higher than in DG and IM, while Fe/Mg in LG is lower than in the other lithologies. Also, the abundance of REEs in DG and IM are similar to value obtained in previous analyses of Y-86032, but those in LG are lower (x 0.5-0.6 except Eu) (Fig. 2). This may be due to contributions of minor basaltic components, as indicated by textural observations. The abundances of Ir in DG and IM are 5.7 and 9.3 ppb, respectively, while that of LG is lower (2.7 ppb).

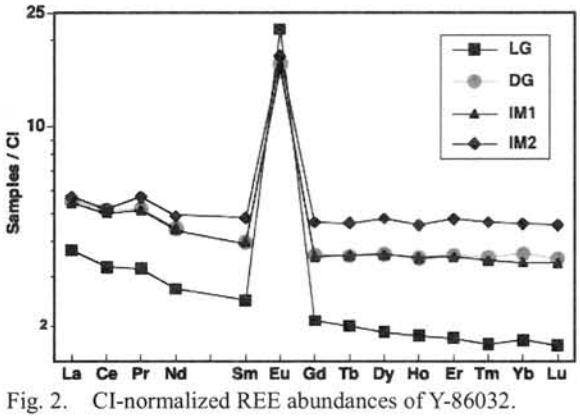

Fig. 2. CI-normalized REE abundances of Y-86032.

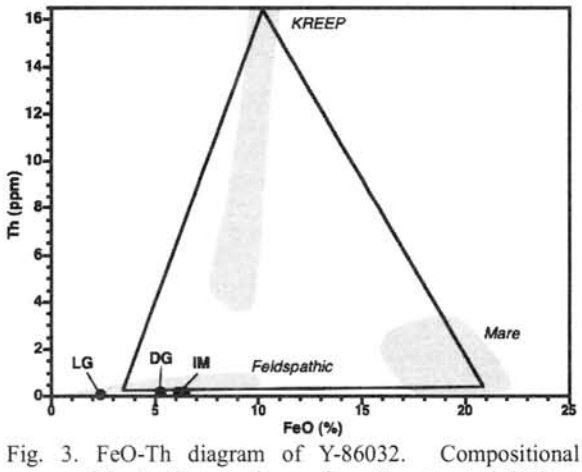

Fig. 3. FeO-Th diagram of Y-86032. Compositional ranges of the Apollo samples are from Korotev et al. [11].

In spite of evidence of impact mixing, Th (0.0765-0.191 ppm) and U (0.0258-0.056 ppm) are very low, confirming the absence of KREEP components. Coupled with the low FeO data these data imply that a majority of matrix components originated from the far-side of the Moon (Fig. 3).

Discussion:

Textural observations suggest that Y-86032 is a complicated breccia resulting from multiple impacts (at least two) on the lunar highland crust. The range of Ar-Ar ages of the lithologies also implies multiple impact heating events [7]. The LG breccia was incorporated into the DG matrix. Both lithologies are shear-deformed and were cut by IM veins. The presence of intergranular melts in the DG and IM lithologies suggests peak shock pressures of ~10-15 GPa [10]. The temperatures were locally more than ~1600°C, but the bulk temperatures were no more than several hundreds °C. The breccia was shocked again after initial formation, and impact melt veins (~20-30 vol%) formed locally. After thermal equilibration, the bulk temperature would have increased to >400°C. These shock events could explain partial resetting of Ar-Ar ages [7].

Despite evidence of multiple impact and mixing, including fragments of more evolved rocks and possibly mare basalts, the Th and Fe contents are extremely low in the Y-86032 breccia, indicating that mixing was mostly limited on the lunar highland crust. The Sm-Nd age of 4.43±0.03 Ga from mineral separates from the DG and LG lithologies suggests that most of the rocks of the protolithic suite were cogenetic [7]. The old age was preserved because the Sm-Nd system is difficult to reset by shock heating at several hundred °C. Although the LG lithology contains a restricted suite of rocks, it is nevertheless a mixture of similar and apparently related compositions that have not been found in previous studies, either of the Apollo samples or of other lunar meteorites. Although Y-86032 appears to contain a restricted set of primary lithologies, the wide variety of clasts also reflects additional igneous, impact, and metamorphic processes occurring on the lunar highland crust.

References: [1] Takeda H. et al. (1990) *Proc. Lunar Planet. Sci. Conf. 20,* 91-100. [2] Palme H. et al. (1991) *GCA 55,* 3105-3122. [3] Yamaguchi A. et al. (2004) *LPS-XXXV* (CD-ROM #1474). [4] Koeberl C. et al. (1989) *Proc. NIPR Symp. Antarct. Meteorites 2,* 15-24. [5] Karouji Y. et al. (2004) *Antarct. Meteorites* XXVIII, 29-30. [6] Bogard D.D. et al. (2000) *LPS-XXXI* (CD-ROM #138). [7] Nyquist L.E. et al. (2005) *Antarct. Meteorites,* this volume. [8] Nyquist L.E. et al. (2002) *LPS-XXXIII* (CD-ROM #1289). [9] Lindstrom M.M. and Lindstrom D.J. (1986) *Proc. Lunar Planet. Sci. Conf. 16,* D263-D276. [10] Nielsen R.J. and Drake M.J. (1978) *Mare Crisium: The View from Lunar 24.* 419-428. [11] Korotev R.L. et al. (1996) *MAPS 31,* 909-924.

Drastic changes of mineralogy and noble gas compositions in carbonaceous chondrite Ningqiang during experimental aqueous alteration. Y. Yamamoto[1], R. Okazaki[2] and T. Nakamura[2], [1]Laboratory for Earthquake Chemistry, Graduate School of Science, University of Tokyo, Hongo, Bunkyo-ku, Tokyo 113-0033, Japan. [2]Department of Earth and Planetary Sciences, Faculty of Sciences, Kyushu University, Hakozaki, Fukuoka 812-8581, Japan.

Introduction:

At the early stage of the solar system formation, asteroids had formed from the gas and dust in the solar nebula. There would be abundant water in asteroids, and then, aqueous alteration could have commonly occurred. Aqueous alteration is thought to be the earliest chemical reaction in hydrous asteroids because of their lower reaction temperatures than those of thermal metamorphism. In order to elucidate the evolution of materials in the early solar system, it is important to gain better understanding the effects of aqueous alteration on materials in primitive asteroids.

Carbonaceous chondrites are one of the most primitive materials in the solar system and contain large amounts of volatile elements such as noble gases. Q gas, one of the components of primordial noble gases trapped in carbonaceous material called phase Q [1, 2], is contained commonly in carbonaceous chondrites. Varieties of mineralogy and noble gas contents in chondrites could be inferred from the different extents of aqueous alteration experienced in parent bodies. Ar-rich gas, so-called subsolar gas, has $^{36}Ar/^{132}Xe$ and $^{84}Kr/^{132}Xe$ ratios higher than Q gas [3] and is contained in some anhydrous carbonaceous chondrites [e.g., 4, 5]. The $^{36}Ar/^{132}Xe$ and $^{84}Kr/^{132}Xe$ ratios are variable between meteorites, and thus the unique composition of Ar-rich gas has not been defined. In contrast to some anhydrous carbonaceous chondrites, carbonaceous chondrites that suffered extensive aqueous alteration are absent in Ar-rich gas, whereas they contain Q gas [6]. It would be expected that Ar-rich gas had been released during aqueous alteration.

The Ar-rich gas in Ningqiang was removed by light acid etching, accompanied by loss of amorphous rims around fine-grained olivine and pyroxene [7]. This result suggests that Ar-rich gas is located in the amorphous rims. To compare with the light acid etching experiment, experimental aqueous alteration by neutral water performed in this study is more suitable to reproduce the condition of hydrous asteroids. In earlier work, we revealed that major part of primordial noble gases lost during experimental aqueous alteration [8]. In this study, we report the relation between the extent of aqueous alteration and the contents of primordial noble gases.

Sample and experimental method:

Ningqiang is a type-3 carbonaceous chondrites that consists entirely of anhydrous minerals. Texturally it resembles CV3 chondrites such as Allende. Chemically it is an ungrouped carbonaceous chondrite because of low abundances of refractory lithophile elements and high abundances of olivine aggregates [9]. But this chondrite has been classified as a CV- [9, 10] and CK-anomalous [e.g., 11] chondrites because of some similarities to CV and CK chondrites. Ningqiang contains large amount of Ar-rich gas as well as Q gas [7].

A piece of Ningqiang sample including chondrules and matrices weighing 600mg was crushed into μm-sized particles and loaded into a pressurized vessel together with 10 g neutral liquid water. Sample and water were kept at 200°C. Estimated internal water vapor pressure is 15 atms. After 0.5, 1, 2, 5, 10, and 20 days, 100mg of the sample was recovered and the rest of the sample was kept being soaked for another days. Natural and altered samples were analyzed for mineralogy and noble gas compositions.

Mineral compositions before and after alteration of Ningqiang samples were analyzed by powder X-ray diffraction method with Rigaku RAD-IIA at Kyushu University and synchrotron radiation X-ray diffraction method at KEK-PF, Tsukuba. Detailed configurations of noble gas analyses are given in earlier work [8]. Noble gases were extracted at the temperatures of 300, 700, 1000, 1300 and 1850°C. The concentrations and isotopic ratios of the noble gases were determined with a mass spectrometer (modified MM5400) at Kyushu University.

Results and Discussion:

Mineralogical analyses show that the natural Ningqiang sample consists of olivine, low-Ca pyroxene, magnetite and iron sulfide. In the altered samples, olivine, low-Ca pyroxene and iron sulfide were decomposed, and serpentine and hematite were formed. Serpentine appears to have formed from the elements supplied by the decomposition of olivine and pyroxene. The serpentine / (olivine + low-Ca pyroxene) of integrated intensities of diffraction peak increases from the 0.5-day alteration sample to the 5-day one, but remains constant after the 5 days. These results indicate that a large portion of serpentine formed in the early stage of experimental aqueous alteration.

Experimental aqueous alteration drastically changed noble gas composition in Ningqiang. 84%, 73% and 70% of ^{36}Ar, ^{84}Kr and ^{132}Xe, respectively, were removed from natural Ningqiang during only the 5-day alteration, while the losses of ^{4}He and ^{20}Ne were 42% and 41%, respectively. These indicate that the altered phases contain greater amounts of Ar,

Kr and Xe than those remaining in the 5-day sample. Altered portions of both olivine and pyroxene lose cosmogenic ^{21}Ne because alteration products such as serpentine are formed via reconstruction of atoms in initial phases such as olivine. Therefore, ^{21}Ne concentrations in the experimentally altered samples could be a measure of the extent of the aqueous alteration reactions. As the alteration proceeds, the concentrations of primordial noble gases decrease steeply while those of ^{21}Ne decreases slowly (Fig. 1), suggesting that even low degrees of aqueous alteration removes great amounts of primordial noble gases. In the sample altered over 5 days, noble gas concentrations are basically similar to those of the 5-day sample, thus indicating that the loss of primordial noble gases completed within the 5-day alteration. Among primordial noble gases, Ar-rich gas was lost in the largest amounts by the experimental aqueous alteration (Fig. 1). The ^{36}Ar/^{132}Xe and ^{84}Kr/^{132}Xe ratios of the noble gases remained in altered samples fall gradually as the alteration progresses from 0.5 to 5 days. The calculated elemental ratios of the noble gases lost from samples are higher than those of the natural Ningqiang sample, indicating that the noble gases removed during the alteration are enriched in Ar-rich gas. This result suggests that Ar-rich gas is located in materials that are very susceptible to aqueous alteration. In contrast, heavy primordial noble gases remaining in the samples after aqueous alteration are close to Q gas based on elemental and isotope compositions [12], indicating that the trapping phase of Q gas is much more resistant to aqueous alteration than the host phases of Ar-rich gas. The results of our study confirm that chondrites experienced aqueous alteration, like CM chondrites, do not have Ar-rich noble gases, although it has large amounts of Q gas.

As well as primordial noble gases, radiogenic noble gases were also significantly removed during the experimental aqueous alteration. Almost all of ^{129}Xe, which is generated by the β decay of ^{129}I, was lost by the 10-day alteration (Fig. 1). This result suggests that not only thermal metamorphism but also aqueous alteration could disturb radiometric ages, and it is therefore thought that the ^{129}I-^{129}Xe age reflects the timing when the aqueous alteration has finished in hydrous asteroids.

The results of this study suggest that the major portion of heavy noble gases could have been lost from primitive asteroids during low-temperature aqueous alteration at the early stage of the solar system evolution. We experimentally revealed that ^{129}I-^{129}Xe age of hydrous chondrites does not correspond to the formation age of the asteroids but rather it would imply the timing of aqueous alteration.

References:

[1] Lewis R. S. et al. (1975) *Science, 190,* 1251-1262. [2] Phinney D. et al. (1976) *LPS VII,* 691-693. [3] Wacker J. F. and Marti K. (1983) *Earth Planet. Sci. Lett., 62,* 147-158. [4] Schelhaas N. et al. (1990) *Geochim. Cosmochim. Acta 54,* 2869-2882. [5] Miura Y. N. et al. (2002) *Proc. NIPR Symp. Antarct. Meteorites, 27,* 96-97. [6] Nakamura T. et al. (1999) *Geochim. Cosmochim. Acta, 63,* 241-255. [7] Nakamura T. et al. (2003) *Meteorit. Planet. Sci., 38,* 243-250. [8] Yamamoto Y. et al. (2004) *Proc. NIPR Symp. Antarct. Meteorites, 28,* 91-92. [9] Rubin A. E. et al. (1988) *Meteoritics, 23,* 13-23. [10] Koeberl C. et al. (1987) *LPS XVIII,* 499-500. [11] Kallemeyn G. W. (1996) *LPS XXVII,* 635-636. [12] Busemann H. et al. (2000) *Meteorit. Planet. Sci., 35,* 949-973.

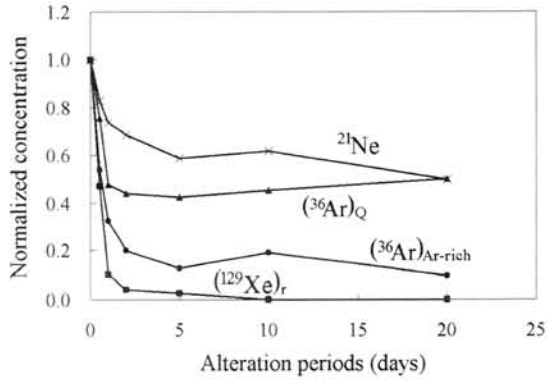

Fig. 1. The changes of ^{21}Ne, $(^{36}Ar)_Q$, $(^{36}Ar)_{Ar\text{-}rich}$ and radiogenic ^{129}Xe, $(^{129}Xe)_r$, concentrations that are normalized to those in the natural sample.

Chromium isotopic study of mesosiderite and ureilite: evidence for $\varepsilon^{54}Cr$ deficit in differentiated meteorites. K. Yamashita[1], T. Ueda[2], N. Nakamura[1,2], N. Kita[3] and L.M. Heaman[4]. [1] Department of Earth and Planetary Sciences, Kobe University, Nada, Kobe 657-8501, Japan, [2] Graduate School of Science and Technology, Kobe University, Nada, Kobe 657-8501, Japan, [3] Department of Geology and Geophysics, University of Wisconsin Madison, 1215 W. Dayton Street, Madison, WI 53706-1692, USA. [4] Department of Earth and Atmospheric Sciences, University of Alberta, Edmonton, AB T6G 2E3, Canada.

Introduction

The relatively short half-life of ^{53}Mn makes the Mn-Cr chronometer an ideal tool to unravel the age of various igneous events in the early solar system. The general approach when measuring the $^{53}Cr/^{52}Cr$ ratio of geological samples by TIMS is to correct for mass fractionation using a terrestrial $^{50}Cr/^{52}Cr$ ratio. However, Lugmair and Shukolyukov [1] have demonstrated that the precision of the data can be improved significantly by further correcting for mass fractionation using the $^{54}Cr/^{52}Cr$ ratio (i.e. a second order fractionation correction). This correction assumes that $^{54}Cr/^{52}Cr$ ratio of the sample is normal (or indistinguishable from the terrestrial value). While this correction may be applied to some meteorites, it has recently been suggested that the $^{54}Cr/^{52}Cr$ ratio of some igneous meteorites deviate from the terrestrial value [2]. Here we report further evidence for the presence of ^{54}Cr anomaly in differentiated meteorites.

Analytical procedure

Our analytical procedure for Cr isotope study is similar to that of Lugmair and Shukolyukov [1], except a Si-Al-boric acid mixture was used as an activator. All measurements were made using a Finnigan MAT262 mass spectrometer in single collector peak-jumping mode. A typical sample analysis consists of sixteen sets of 300 ratios taken from four separate filament loads, and the standards were treated in the same manner. All presented uncertainties are $2\sigma_m$. Ratios are normalized to $^{50}Cr/^{52}Cr$ of 0.051859 using an exponential law and no second order fractionation corrections were made. The Mn/Cr ratios were measured using ICP-AES.

Results and discussion

(*Ordinary chondrite and SNC meteorite*)

In order to test the quality of our data, we have undertaken a Cr isotopic study of one ordinary chondrite Y793241 (host and igneous inclusion) [3] and one Nakhlite Y000593. These results are shown in Figure 1. All of these samples show systematic shift towards positive $\varepsilon^{53}Cr$ but show no clear evidence for isotopic anomaly on ^{54}Cr.

(*Carbonaceous chondrite*)

To further confirm that our data are comparable to those previously published in the literature, we have measured the Cr isotopic composition of carbonaceous chondrite Tagish Lake. In this case, an isotope anomaly on ^{54}Cr is expected so a second order fractionation correction using terrestrial $^{54}Cr/^{52}Cr$ ratio cannot be made. In order to overcome this problem, we have made three repeated analyses of this meteorite, resulting in total of 48 sets of 300 ratios. These results are also shown in Figure 1. The range of variation seen in the three analyses is broadly similar to that of the terrestrial standards without the second order fractionation correction (external reproducibility of the standard = $\pm 0.33\varepsilon$ and $\pm 0.60\varepsilon$ for $\varepsilon^{53}Cr$ and $\varepsilon^{54}Cr$, respectively). This indicates that the uncertainty reported for each analysis (that is, sixteen sets of 300 ratios) is probably underestimating the true uncertainty that includes the effect of residual mass fractionation. However, when all of these analyses are combined to calculate the average Cr isotopic composition of Tagish Lake ($\varepsilon^{53}Cr$=+0.25 ± 0.10, $\varepsilon^{54}Cr$=+1.34 ± 0.19), and the result is plotted on an isochron diagram (measured $^{55}Mn/^{52}Cr$ = 0.67), the data plots on the isochron defined by other carbonaceous chondrites (Figure 2.) [4, 5]. Since the data from [4, 5] were also obtained from a large number of repeated measurements in order to eliminate the effect of residual mass fractionation, an excellent agreement of these data demonstrates that; (1) by increasing the number of measurement, a reliable Cr isotopic composition can be achieved without the use of second order fractionation correction and (2) our data are comparable to those previously published in the literature. It is also noteworthy that the Cr isotopic signature of Tagish Lake closely resembles that of CM chondrite Murray.

(*Mesosiderite*)

For the Vaca Muerta silicate matrix, eight analyses were conducted from three separate sample dissolution (VM#1 Pyroxene, Chromite, Chromite-rpt, Silicate, VM#2 whole rock, VM#3 Chromite, Silicate, Whole rock) and the results are summarized in Figure 1. These data show systematic shifts toward positive and negative $\varepsilon^{53}Cr$ and $\varepsilon^{54}Cr$ values, respectively. Although the external reproducibility of $\varepsilon^{54}Cr$ is estimated to be ~0.60ε, we propose that the $\varepsilon^{54}Cr$ deficit seen in Vaca Muerta is true for the reasons outlined below. (1) Chromite is an ideal mineral to investigate in detail because it is resistant to secondary alteration. During the course of this study, we made three analyses of chromite. By combining the data from these three analyses, we obtain average $\varepsilon^{53}Cr$ and $\varepsilon^{54}Cr$ values of +0.21 ± 0.07 and -0.59 ± 0.14, respectively (49 sets of 300 ratios). As demonstrated by the result of Tagish Lake, increasing the number of measurements to ~48 can

provide a reliable $\varepsilon^{54}Cr$ value without using a second order fractionation correction. (2) As is the case with the repeated measurements of the standards, there is a strong correlation between the $\varepsilon^{53}Cr$ and $\varepsilon^{54}Cr$ values of Vaca Muerta (not shown), and the slope of this correlation is similar to that of the standards. This suggests that the $\varepsilon^{53}Cr$ variation seen in Vaca Muerta is a result of a residual mass fractionation effect rather than decay of ^{53}Mn. Such an isotopic equilibration was also documented from the silicate clasts of Vaca Muerta [6]. Assuming the isotopic signatures of silicate and chromite are in equilibrium, we can calculate the $\varepsilon^{53}Cr$ and $\varepsilon^{54}Cr$ values of the Vaca Muerta matrix by combining all of the measurements. The values calculated in this way are $+0.25 \pm 0.05$ and -0.55 ± 0.09 for $\varepsilon^{53}Cr$ and $\varepsilon^{54}Cr$, respectively.

(*Ureilite*)

In order to further explore the possible existence of a $\varepsilon^{54}Cr$ anomaly in differentiated meteorites, we have measured the Cr isotopic signatures of two ureilites, ALH77257 and Y791538. Only a few tens of milligrams of these samples were dissolved so their $\varepsilon^{53}Cr$ may not be representative. However, because they are igneous meteorites, their $\varepsilon^{54}Cr$ values in different phases are expected to be in equilibrium. Our preliminary $\varepsilon^{53}Cr$ and $\varepsilon^{54}Cr$ values for ALH77257 and Y791538 are $+0.32 \pm 0.12$ and -0.65 ± 0.22, and $+0.14 \pm 0.08$ and -0.97 ± 0.16, respectively. While these numbers are still preliminary and further measurements are required, the available data strongly hints towards the presence of a $\varepsilon^{54}Cr$ anomaly in ureilites.

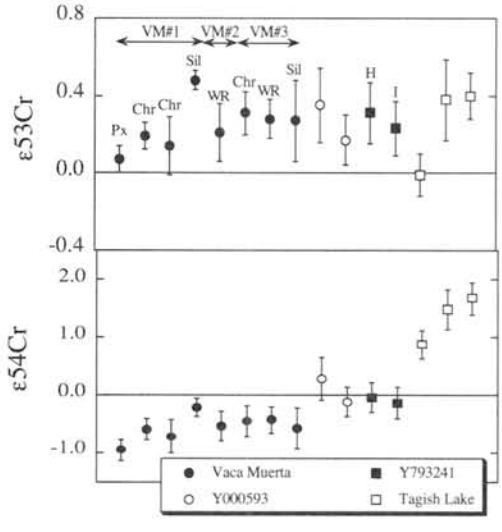

Figure 1. Results for the Cr isotopic analyses of Mesosiderite (Vaca Muerta), SNC meteorite (Y000593), ordinary chondrite and its igneous inclusion (Y793241) and carbonaceous chondrite (Tagish Lake). Each point typically represents an average of sixteen repeated measurements taken from four independent filament loads. WR: Whole Rock, Chr: Chromite, Sil: Silicate, H: host, I: igneous inclusion.

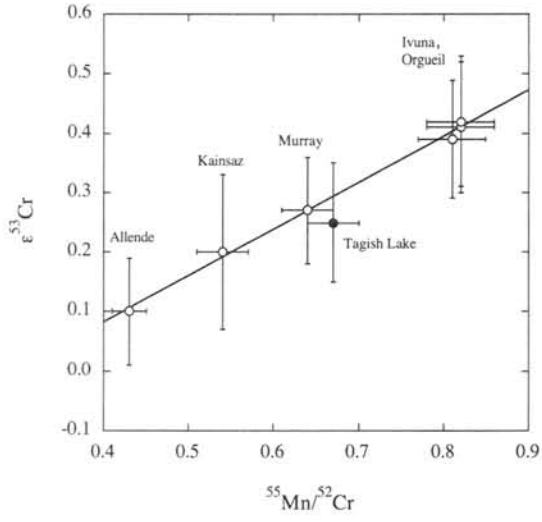

Figure 2. Isochron diagram of carbonaceous chondrites. Data for samples other than Tagish Lake were taken from Schukolyukov et al. [4, 5]. The uncertainties on $^{55}Mn/^{52}Cr$ ratios for these samples were assumed to be ~5%.

Summary

Through detailed investigation of a mesosiderite and two ureilites, we have confirmed the existence of ^{54}Cr anomaly in differentiated meteorites.

Our results for mesosiderite are in good agreement with the recently published result by Trinquier et al. [7]. However, the reason for the lack of such an anomaly in the Vaca Muerta silicate clasts studied by Wadhwa et al. [6] is not clear at this stage.

Negative $\varepsilon^{54}Cr$ in Vaca Muerta may suggest that the reservoir from which the mesosiderite parent body evolved from is isotopically distinct from those of Earth, Mars and even some of the chondrites. However, an alternative way to produce such an anomaly may be the partial melting of materials which contain phases with both positive and negative $\varepsilon^{54}Cr$ values at a micro scale, such as CI-CM chondrites [8]. If phases with negative $\varepsilon^{54}Cr$ are preferentially melted relative to those with positive $\varepsilon^{54}Cr$ during the partial melting event(s), the $\varepsilon^{54}Cr$ value of the resulting melt may become negative even if the $\varepsilon^{54}Cr$ value of the bulk starting material is positive.

References:

[1] Lugmair, G.W. and Shukolyukov A. (1998) *GCA, 62,* 2863–2886. [2] Trinquier A. et al. (2003) *Geophys. Res. Abstract.*5, 05916. [3] Nakamura N. et al. (1994) *Antarct. Meteorites, 7,* 125–143, [4] Shukolyukov A. and Lugmair, G.W. (2001) *Meteoritics&Planet. Sci. 26,* A188, [5] Shukolyukov A. and Lugmair, G.W. (2003) *LPS XXXIV,* abstr. #1279, [6] Wadhwa, M. et al. (2003) *GCA, 67,* 5047-5069. [7] Trinquier A. et al. (2005) *LPS XXXVI,* abstr. #1259. [8] Rotaru et al. (1992) Nature, 358, 465-470.

AUTHOR INDEX

Anand M. ····17
Arai T. ····1
Bartoschewitz R. ····69
Bérczi Sz. ····3, 5, 19
Bischoff A. ····55
Bobrov A. V. ····37
Bogard D. D. ····57, 96
Bradley J. P. ····94
Bridges J. ····17
Brückner J. ····10
Buchanan P. C. ····7
Burbine T. H. ····7
Chen M. ····8, 92
Chokai J. ····32
Dai Z. R. ····94
Dreibus G. ····10, 27
Ebihara M. ····80, 96
El Goresy A. ····8
Fagan T. J. ····12
Floss C. ····94
Franchi I. A. ····17
Fritz J. ····14
Fukuoka T. ····84
Fukushi Y. ····84
Gánti T. ····3
Gesztesi A. ····3
Gillet P. ····8
Grady M. M. ····16, 17
Graham G. A. ····94
Granovsky L. B. ····37
Greshake A. ····14
Grossman J. N. ····28
Gucsik A. ····25
Hargitai H. I. ····19
Heaman L. M. ····100
Herrmann S. ····53
Honda M. ····21, 49
Horvath A. ····3
Ikeda Y. ····23
Imae N. ····23, 55
Ishida Y. ····25
Ishii T. ····78
Jagoutz E. ····10, 27
Jotter R. ····27
Józsa S. ····5
Kaiden H. ····43
Karouji Y. ····96
Kato T. ····45
Keil K. ····34
Kereszturi A. ····3
Kimura M. ····28, 55, 69
Kita N. ····1, 100
Kobayashi S. ····30
Koizumi E. ····32, 41
Kojima H. ····36
Komatsu M. ····34
Kovács Zs. ····5
Krot A. N. ····30, 34
Kubny A. ····27
Kusakabe M. ····36, 67, 69
Lukács B. ····5
MacPherson G. J. ····12
Marakushev A. A. ····37
Maruyama S. ····36
McKay G. ····39, 41
Mikouchi M. ····32
Mikouchi T. ····41
Misawa K. ····43, 80
Miura Y. ····45
Miyamoto M. ····32, 34, 41
Miyamoto T. ····67
Morishita Y. ····1
Nagahara H. ····47, 82
Nagao K. ····21, 49, 69
Nagashima K. ····12, 30
Nagy B. ····3
Nakajima H. ····28
Nakamura K. ····88
Nakamura N. ····100
Nakamura T. ····53, 55, 63, 67, 94, 98
Nakamuta Y. ····51
Nakashima D. ····53
Naraoka H. ····59
Ninagawa K. ····25

Nishido H. ·····25
Noguchi T. ·····53, 55, 84, 94
Nyquist L. E. ·····57, 96
O'Brien K. M. ·····7
Oba Y. ·····59
Ohnishi I. ·····61
Okazaki R. ·····63, 69, 98
Olinger C. T. ·····94
Osawa T. ·····55
Otsuki M. ·····78
Ott U. ·····53
Owaki R. ·····51
Ozawa K. ·····47, 82
Ozima M. ·····65, 75
Ozono Y. ·····67
Park J. ·····69
Pearson V. ·····17
Pócs T. ·····3
Reese Y. ·····57, 96
Rost D. ·····12
Rubin A. E. ·····71, 73
Saito Y. ·····84
Sakamoto M. ·····25
Sakamoto N. ·····30
Sakurai H. ·····84
Sano Y. ·····86
Schwandt C. ·····39
Seki K. ·····75
Sekiya M. ·····90
Shih C.-Y. ·····57, 96
Shimoda H. ·····1
Shinagawa H. ·····75
Sik A. ·····3
Stadermann F. J. ·····94
Stöffler D. ·····14
Sugiura N. ·····77
Suzuki Y. ·····84
Szakmány Gy. ·····5
Szathmary E. ·····3
Tachibana S. ·····82
Takeda H. ·····51, 57, 78, 96
Tamaki M. ·····80
Tatsumi K. ·····82
Tazawa Y. ·····84
Terada K. ·····86
Terada N. ·····75
Tomeoka K. ·····61, 88
Tomioka N. ·····88
Tomomura S. ·····47
Tonotani A. ·····30
Toyoda S. ·····25
Trigo-Rodríguez J. M. ·····73
Ueda T. ·····100
Ueda Y. ·····41
Uesugi M. ·····90
Verchovsky A. B. ·····17
Vicenzi E. P. ·····12
Wang D. ·····92
Wasson J. T. ·····73
Weisberg M. K. ·····28
Wright I. P. ·····16
Yada T. ·····84, 94
Yamaguchi A. ·····43, 57, 78, 80, 96
Yamamoto Y. ·····98
Yamashita K. ·····100
Yurimoto H. ·····12, 30
Zartman R. ·····27
Zinner E. ·····94
Zinovieva N. G. ·····37